International
Progress Report

IPR-04-50

Äspö Hard Rock Laboratory

Complex gas-water processes in discrete fracture-matrix system

Upscaling, mass-conservative discretization and efficient multilevel solution

Volker Reichenberger, Peter Bastian

Heidelberg University

Hartmut Jakobs, Rainer Helmig,
Jennifer Niessner

Stuttgart University

June 2003

Svensk Kärnbränslehantering AB
Swedish Nuclear Fuel
and Waste Management Co
Box 5864
SE-102 40 Stockholm Sweden
Tel 08-459 84 00
+46 8 459 84 00
Fax 08-661 57 19
+46 8 661 57 19

Report no.
IPR-04-50

No.
F50K

Author
Volker Reichenberger
Hartmut Jakobs
Peter Bastian
Rainer Helmig
Jennifer Niessner

Date
June 2003

Checked by

Date

Approved
Christer Svemar

Date
2004-12-07

Äspö Hard Rock Laboratory

Complex gas-water processes in discrete fracture-matrix system

Upscaling, mass-conservative discretization and efficient multilevel solution

Volker Reichenberger, Peter Bastian

Heidelberg University

Hartmut Jakobs, Rainer Helmig,
Jennifer Niessner

Stuttgart University

June 2003

Keywords: Degassing, Hydrogeology, Two-phase flow, Geostatistics, Henry coefficient, Capillary pressure

Complex Gas-Water Processes in Discrete Fracture-Matrix Systems

Upscaling, Mass-Conservative Discretization and Efficient Multilevel Solution

Volker Reichenberger[1], Hartmut Jakobs[2], Peter Bastian[1], Rainer Helmig[3] and Jennifer Niessner[3]

[1] Universität Heidelberg, Interdiszipliäres Zentrum für Wissenschaftliches Rechnen, Im Neuenheimer Feld 368, 69120 Heidelberg

[2] Universität Stuttgart, Institut für Wasserbau, Lehrstuhl für Hydromechanik und Modellierung von Hydrosystemen, Pfaffenwaldring 61, 70550 Stuttgart, Germany. Now at: DaimlerChrysler AG, PBE/DAM, HPC B209, 70546 Stuttgart, Germany

[3] Universität Stuttgart, Institut für Wasserbau, Lehrstuhl für Hydromechanik und Modellierung von Hydrosystemen, Pfaffenwaldring 61, 70550 Stuttgart, Germany.

Die diesem Bericht zugrunde liegenden Arbeiten wurden mit Mitteln des Bundesministeriums für Wirtschaft und Arbeit (BMWA) unter dem Förderkennzeichen FKZ 02E 9370 gefördert. Die Verantwortung für den Inhalt der Veröffentlichung liegt allein bei den Autoren.

Sammanfattning

I denna rapport presenteras ett nytt sätt att utveckla kunskap om hur avgasningsprocessers mekanismer påverkar hydrauliska egenskaper hos sprickor i granit i närheten av ett slutförvar, liksom en tvärvetenskaplig väg till numerisk simulering av flerfasflöde i sprickiga, porösa medier.

För att garantera att undersökningen tar hänsyn till tillräckligt stora sprickvidder genereras dessa med hjälp av geostatistiska verktyg. Vid användande av log-normalfördelning uppstod dock problem med överskattning av sannolikheten för stora sprickvidder. Problemet löstes med hjälp av en lämplig omvandlingsfunktion för sannolikheten för stora sprickvidder, baserad på faktiska observationer. Samtidigt bibehålls den rumsliga kovariansen för sprickors vidder.

I mikroskala kan resultaten från Jarsjö och Geller (1996) reproduceras. Detta har observerats för den visuella representationen av gasmättnad liksom för en minskning av transmissiviteten med 50%, såsom anges i experimentet för en initiell, volymetrisk koncentration på 14%. Med det omnormaliserade angreppssättet har det visats att en representativ elimentarfas kan hittas. Här ger det valda omnormaliserade angreppssättet information om inte bara minsta storlek på den representativa elementarfasen utan också om variationerna som är resultat av olika geostatistiskt genererade sprickvidds-realiseringar.

Den representativa elementarfasen är huvudsakligen beroende av korrelationslängden för den beaktade sprickvidden. Ju mindre stoppkriterium för medelvärdesbildnings-proceduren, desto större blir den minsta yta över vilken den medelvärdesbildade storheten behöver beaktas. Till följd av den monotoniskt minskande variationen hos den beaktade effektiva parametern kan en representativ fas för avgasningsprocessen alltid hittas vid de beaktade modellantagandena.

Avgasningsprocessen simuleras för olika i vatten lösta gaser med den omnormaliserade perkolationsmodellen. Här framgår betydelsen av Henry-koefficienterna för avgasningsprocessen. För koldioxid observerar vi en stark avgasning redan vid låga tryck- och temperaturändringar; för kväve och vätgas är avgasningsprocessen mycket mindre beroende av temperatur, och inträffar endast vid större tryckminskningar.

Analys av kapillärtrycksgradienten har visat att gasfasen inte kan mobiliseras ens för vertikala sprickor. Emellertid skulle den distribueras annorlunda, så att den effektiva parametern skulle kunna ändras beroende på placeringen av sprickan. Minskningen av vattenfasens effektiva permeabilitet som resultat av avgasningsprocessen bestäms som en funktion av tryck och temperatur. Denna minskning är möjlig under de beaktade experimentella förhållandena, eftersom volymen hos den genom avgasning bildade gasen, och därmed också mättnaden, enbart är beroende av tryck och temperatur. Detta är ett resultat av den begränsade mängd vatten som mättats med gas, och är inte allmänt giltigt. Emellertid avstod vi från att redovisa resultateftersom inga experimentella data finns för validering.

Simuleringen av fältförsöken visar god överensstämmelse med resultaten från Jarsjö och Destouni (2000). Den svaga underskattningen av den relativa permeabiliteten kan ha olika orsaker. Den kan bero på en felaktig uppskattning av vattenfilmens betydelse eller vara ett resultat av antagandet om termodynamisk jämvikt, för att nämna två möjligheter. Även om en kalibrering av parametrarna skulle vara enkel att göra har det inte gjorts i vårt arbete. Det presenterade resultaten erhölls direkt från överföring av parametrar från mikro till representativ elementärvolymskala (REV-skala). Avvikelser hos de simulerade resultaten från de experimentella resultaten är ett tecken på osäkerheten hos modellantagandena. En kalibrering av parametrarna i syfte att få en bättre anpassning av de experimentella resultaten skulle emellertid inte bidra med någon bättre informationom kvaliteten på modellantagandena. Härigenom skulle inte mer utan mindre information erhållas.

För numerisk simulering av vätskeflöde och transport i sprickiga medier valde vi det diskreta modelleringssättet i vilket diskreta sprickor modelleras separat, och ett kontinuum antas råda i sprickorna och det omgivande porösa mediet. Detta val har fördelen framför ekvivalensmodellering att inga artificiella parametrar – såsom utbytestermer mellan spricka och matris i dubbelporositetsmodellen – behöver användas. Vi antog att en REV förekommer i matrisen och att sprickan, från vilken vi kan utveckla en flerfasflödesutvidgning av Darcys lag, och antog också att kapillära tryckfunktioner och relativa permeabilitetsfunktioner efter Brooks-Corey gäller för sprickorna. Funktionen vid gränssnittet spricka-matris och allmänna diskontinuiteter modelleras av de utökade kapillära tryckförhållandena hos van Duijn et al. (1995). Den stora roll det kapillära trycket spelar har länge varit känd och utgör en betydelsefull komponent i modellen.

Vi beaktar två scheman, ett vertex-centrerat finit volymschema och den diskontinuerliga Garlekinmetoden från Baumann och Oden. Den senare befinner sig i en mindre mogen fas och har ännu ej applicerats på flerfasvätskeflöden i heterogena medier. Vi använde metoden på vätskeflöde med en enskild fas i heterogena medier och presenterade en multigridmetod för den effektiva lösningen av grundvattenekvationen. Multigridmetoden visar h-oberoende konvergens för homogen och heterogen permeabilitetdistribution och fungerar betydligt mycket bättre än finita volymsscheman vid problem med full regularitet. Den cache-effektiva egenskapen hos de små, täta blocken som uppstår i den diskontinuerliga Garlekinmetoden gör den speciellt lämplig för modern datorarkitektur. Vi jämför också den diskontinuerliga Garlekinmetoden med den vertex-centrerade finita volymschemat för ett problem med en enskild spricka. I detta exempel beaktar vi också sprickgeometrins betydelse för lösningen, vilken har en inverkan i det fall sprickor modelleras som volymetriska element. Beroende på formen hos elementen vid sprickans ändar ändras hastighetsfältet betydligt mellan de olika realiseringarna. Vi fann också god överensstämmelse mellan finita volymmetoden med sprickelement av lägre dimension, den volymetrisk finita volymmetoden och den diskontinuerliga Garlekinmetoden för fallet med en kvadrupel-lateral sprickände.

För tvåfasflödesekvationen presenterade vi en metod baserad på en tryck-mättnadsformulering. Metoden behandlar tvåfas sprickmatrissystemet fullt kopplat, för att på ett adekvat sätt fånga betydelsen av samverkan mellan spricka-matris. Metoden baseras på ett vertex-centrerat finit volymschema som implementerar sprickelement med lägre dimension. Tack vare användandet av den utökade kapillärtryckfunktionen är det möjligt att uppnå den fysikaliskt relevanta, diskontinuerliga mättnaden vid noder som delas av spricka och matris i en anpassad finit elementmiljö. De diskretiserade icke-linjära ekvationerna har lösts med en inexakt Newtonmetod med linjesökning, de linjeariserade ekvationerna har lösts med en parallell multigridmetod med speciella trunkerade restriktionsoperander. Implementeringen av datorprogrammet baseras på det så kallade UG-ramverket. Flerfasflödesproblem i porösa medier är idealiska för adoptiv förfining; deras komplexa geometrier erfordrar icke-strukturerade gridmetoder, och problemens komplexitet erfordrar att datorberäkningarna görs på parallell-datorer. Vi kunde demonstrera att metoden kan användas för simulering av komplexa sprick-matrissystem med flera miljoner okända storheter. Mjukvaran för simuleringen inpassedes i en miljö av domängeneratorer, gridgeneratorer och visualisering, vilka behövde anpassas till lågdimensionella elementrepresentationer.

De utvecklade verktygen erbjuder en god bas för simulering av gas-vattenprocesser i ett sprick-matrissystem. Även om många frågor fortfarande är öppna utgör det arbete som presenteras i rapporten ett steg framåt på vägen mot en bättre förståelse av de komplexa processerna.

Summary

In this book, we present a new approach to understanding the mechanisms of degassing processes of the hydraulic properties in granite fractures in the vicinity of repositories, and an interdisciplinary approach to the numerical simulation of multiphase flow in fractured porous media.

To guarantee an investigation of sufficiently large fracture aperture fields, these are generated using geostatistical tools. Here, we encounter the problem of overestimating the probability of large fracture apertures by the logarithmic normal distribution. The problem is solved by adapting the probability of large fracture apertures to the measurements, using an appropriate transformation function. At the same time, the spatial covariance of the fracture apertures is preserved.

On the microscale, the results of Jarsjö and Geller (1996) can be reproduced. This has been observed for the visual representation of gas saturation as well as for the reduction of transmissivity by around 50%, as stated in the experiment for an initial volumetric concentration of 14%. With the renormalization approach, it has been shown that a representative elementary face can be found. Here, the chosen renormalization approach provides information not only on the minimum size of the representative elementary face but also on the variations resulting from the different realizations of the fracture aperture field generated by geostatistical methods.

This representative elementary face is mainly dependent on the integral length of the considered fracture aperture field. The smaller the stopping criterion for the averaging procedure, the larger the minimum area for which the averaging property has to be considered. Due to the monotonically decreasing variation of the considered effective parameter, a representative face for the degassing process can always be found under the considered model assumptions.

The degassing process is simulated for different gases dissolved in water with the renormalization–percolation model. Here, the importance of the Henry coefficients for the degassing process can be seen. For carbon dioxide (CO_2), we already observe a strong degassing for low pressure and temperature changes; in the case of nitrogen (N_2) and hydrogen (H_2), degassing processes depend much less on temperature and occur only for higher pressure decrease.

The analysis of the capillary pressure gradient has shown that the gas phase could not be mobilized even for vertical fractures. However, it would be distributed differently so that the effective parameters could change depending on the location of the fracture. The reduction of the effective permeability of the water phase resulting from the degassing process is determined as a function of pressure and temperature. This reduction is possible in the context of the experiments considered here as the volume of the degassing gas and thus also the saturation is only dependent on pressure and temperature. This results from the limited amount of water saturated with the gas component and is not generally valid. However, we refrained from showing results as no experimental data are available for validation.

The simulation of the field experiment shows a good accordance with the results from Jarsjö and Destouni (2000). The slight underestimation of the relative permeabil-

ity can have different causes. It can be due to the wrong estimation of the influence of the water film or a result of assuming a thermodynamic equilibrium, to mention only two possible reasons. Even though a calibration of the parameters would easily be possible, it is not done in our work. The presented results were obtained directly via the transfer of the parameters from the micro- to the REV-scale. The deviation of the simulation results from the experimental results are a sign of the uncertainty of the model assumptions. A calibration of the parameters for a better adaptation of the experimental results would not permit any better information on the quality of the model assumptions. Thus, not more information would be given, but less.

For the numerical simulation of fluid flow and transport in fractured media, we chose the discrete modeling approach in which discrete fractures are modeled separately and a continuum in the fractures and the surrounding porous media is assumed. This has the advantage over equivalence models that no artificial parameters—such as exchange terms between fracture and matrix in the double porosity model—have to be employed. We assumed the existence of a representative elementary volume (REV) in the matrix and the fracture, from which we can derive a multiphase flow extension of Darcy's law, and also assumed that capillary pressure functions and relative permeability functions according to Brooks-Corey are valid in the fractures. The behavior at the fracture-matrix interface and general media discontinuities is modeled by the extended capillary pressure conditions of van Duijn et al. (1995). The large role of the capillary pressure has long been recognized and is an important component of the model.

We considered two schemes, a vertex-centered finite volume scheme and the discontinuous Galerkin method of Baumann and Oden. The latter is in a less mature state and has not seen application to multiphase fluid flow in heterogeneous media yet. We applied the method to the fluid flow of a single phase in heterogeneous media and presented a multigrid method for the efficient solution of the groundwater equation. The multigrid method shows h-independent convergence for homogeneous and heterogeneous permeability distributions and performs dramatically better than a finite volume scheme in the case of problems with full regularity. The cache-efficient nature of the small dense blocks arising in the discontinuous Galerkin method makes it especially suitable for modern computer architectures. We also compared the discontinuous Galerkin method to the vertex-centered finite volume scheme for a problem with a single fracture. In this example, we also considered the influence of fracture geometries on the solution, which is an issue if fractures are modeled as volumetric elements. Depending on the shape of the element at the fracture ends, the velocity field changes considerably between the different realizations. We also found good agreement between a finite volume method with lower-dimensional fracture elements, the volumetric finite volume method and the discontinuous Galerkin method in the case of a quadrilateral fracture end.

For the two-phase flow equation, we presented a method based on a phase pressure–saturation formulation. The method treats the two-phase fracture-matrix system in a fully coupled way in order to capture the effects of fracture-matrix interaction adequately. The method is based on a vertex-centered finite volume scheme which implements fracture elements of lower dimension. Due to the incorporation of the ex-

tended capillary pressure function, it is possible to achieve the physically relevant discontinuous saturation at nodes shared by fracture and matrix in a conforming finite element setting. The discretized nonlinear equations are solved by an inexact Newton method with line search, the linearized equations are solved by a parallel multigrid method with special truncated restriction operators. The implementation of the computer program is based on the framework UG. Multiphase flow problems in porous media are ideally suited for adaptive refinement; their complex geometries require unstructured grid methods and the complexity of the problems requires that the computations are run on parallel computers. We were able to demonstrate that the method can be employed for simulations in complex fracture-matrix systems with several million unknowns. The simulation software was embedded in an environment of domain generators, grid generators and visualization, which had to be adapted for the lower-dimensional element representation.

The developed tools provide a good basis for the simulation of gas-water processes in fracture-matrix systems. Although many questions are still open, the work presented here is a further step on the road to gaining a better understanding of the complex processes.

CONTENTS

1 Introduction

1.1 Motivation

The urgent need for sites for the disposal of radioactive waste has directed interest towards the possible use of rock dumping sites, because they are considered to be virtually impermeable in many cases. However, natural barriers formed by rock material are usually interlaced with fractures and shear zones which are generally interconnected over long distances. In view of the latter, flow processes may indeed occur, even if they are slow. The escape of polluting materials from disposal dumps or rock caverns leads to instance of pollution, which, particularly in view of the desirable long–term safety of the disposal sites concern, must be taken into consideration.

Degassing effects may occur in fractures in the vicinity of deep radioactive-waste-disposal sites as a result of a pressure drop. These effects play an important role in the investigation of the hydraulic conditions in the near field of the disposal sites. The assumption of single-phase conditions may lead to the misinterpretation of experimental data as degassing leads to two-phase conditions and to a reduction of the effective permeability.

The aim of this book is to contribute to the understanding of non-isothermal behavior of water–gas systems in the near field of atomic waste disposal sites in fractured porous media.

We distinguish between sub-REV effects within single fractures and effects due to super-REV heterogeneities which result from the fracture–matrix system. We assume to have undisturbed physical conditions as reported from the Äspö Hard Rock Laboratory in Sweden, i.e.:

- a fully water-saturated system
- a hydrostatic pressure of 5 million Pa.

Degassing processes can be caused by a drop of pressure or by a rise of temperature. The investigation of the corresponding phase change from a one-phase-system to a two-phase-system plays a central role for this work. The hydraulic properties in the near field of a disposal site may be strongly affected by degassing processes.

Therefore, the laboratory experiments published by Jarsjö (1998) and the field experiments published by Jarsjö and Destouni (2000) are investigated in detail. We compare their experimental results with simulation results on the laboratory as well as on the field scale. Using this method we can quantify the error made by the simulation models and the upscaling method.

For the simulation on the laboratory scale we use a percolation model. To transfer the information from the laboratory scale to the field scale we use a renormalization scheme. On the field scale we use a numerical simulator which solves the multiphase flow equations based on the extended form of Darcy's law. In order to investigate the limits of our models we analyze the importance of the forces taken into account, i.e. capillary forces, gravity forces, and viscous forces. This method allows us to quantify the constraints of our models.

Furthermore, we investigate the influence of strong parameter heterogeneities caused by the fracture–matrix system on the flow behavior of gas and water. We consider in particular the influence of the large difference between the entry pressures of matrix and fracture on the migration of the gas phase from the fracture system into the matrix system.

For simulating flow and transport processes in fractured rock, a major prerequisite is the possibility of coupling discrete (fractures, shear zones) and continuous (rock matrix) model elements. The model described in this report employs the concept of a *porous medium* in conjunction with a *discrete fracture system*. The numerical model based on a *finite volume method* or a new *discontinuous Galerkin Method* for elliptic problems is presented for simulating gas water processes under the special conditions pertaining to a fractured porous medium.

The physical description and the discretization techniques for these processes within porous media are provided by the simulation software MUFTE (**MU**ltiphase **F**low, **T**ransport, and **E**nergy). Fractured media lead to complicated domains which demand the use of unstructured grids. The numerical simulation toolbox UG offers sophisticated numerical tools such as multigrid methods and adaptive refinement for unstructured grids on workstations and parallel computers. efficient toolbox for the simulation of multiphase multicomponent processes within porous media.

We would like to thank the *Gesellschaft für Anlagen– und Reaktorsicherheit* **(GRS)**, the *Bundesanstalt für Geowissenschaften und Rohstoffe* **(BGR)** and the *Svensk Kärnbränslehantering* **(SKB)** for the fruitful discussions. We are grateful to Jerker Jarsjö from the Division of Water Resources Engineering **(WRE)**, Kungl Tekniska Hägskolan Stockholm for ideas he shared with us and for the excellent exchange of knowledge and data. The authors thank W. Steininger and W. Bechthold, *Forschungszentrum Karlsruhe, Abteilung Projektträgerschaft Entsorgung* **(PTE)** for the cooperation within this project and for their review, whose comments greatly improved this book. This work was funded by the *Bundesministerium für Wirtschaft und Arbeit* **(BMWA)**.

1.2 Fracture Models

1.2.1 Overview of Fracture-Matrix Models

It is very difficult to understand the topology of fracture–aquifer systems. This is due to the fact, that fractures occur on a variety of length scales which can be taken from Figure 1.1. If fractures can be found on the whole range of scales, it is reasonable to describe

them using fractal models, as shown by Bonnet et al. (2001). A fractal set is according to Mandelbrot (1982) a "set without a characteristic length scale". This definition, however, is weakened, for the consideration of natural systems. For natural systems, we always have limits, if we only choose the characteristical length sufficiently small, respectively sufficiently large. According to the definition of Mandelbrot (1982), however, it is sufficient, if these limits do not occur on the observed scales. For this reason, we have to take into account not only the influence of the fractures on the considered scale, but also the influence of the fractures on the lower scales.

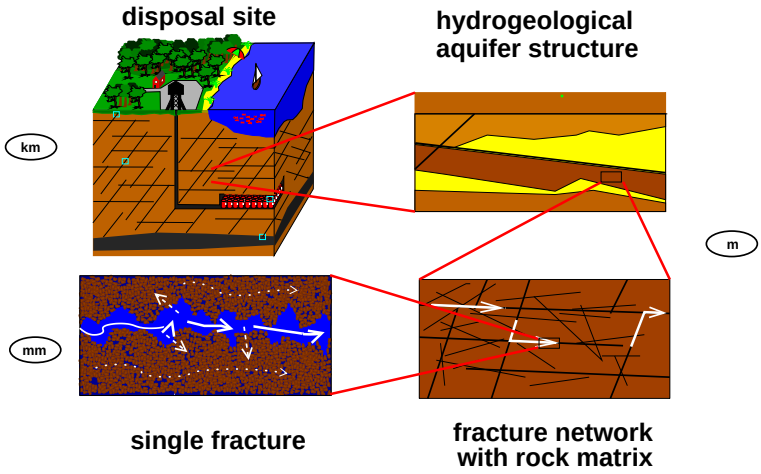

Figure 1.1: Fractures can occur on different scales (from Silberhorn-Hemminger (2002))

According to Singhal and Gupta (1999a), a fracture is generated in a process of cracking where the coherence (cohesion) in the rock is annihilated. Here, no significant macroscopically detectable change of location of the blocks of rock separated by the fracture occurs. Considered in more detail, a fracture consists of two complementary faces created by the cracking process, the fractured surfaces, with an opening in between. The creation of this opening results in a small dilatation of the fractured rock body perpendicular to the fractures. The process of cracking within the rock is caused by tensions. These tensions can have various reasons:

- deformation of the rock by tectonic tensions
- shrinkage evoked by cooling processes of magma or by the process of drying of sediments
- displacement processes at the surface, e.g. movement of glaciers, landslides
- discharge processes caused by erosion
- weathering processes

Generally we can divide a fracture–aquifer system into the components fracture and matrix as schematically shown in Figure 1.2. The rock matrix, consisting of crystalline

rock, has a porosity of 0.1% to 1% and a very low permeability. The fracture system on the other hand has a comparatively high permeability. Even though the porosity of the rock matrix is very small, the storage capacity of the rock matrix is higher than the storage capacity of the fracture system. This is due to the fact that the total volume of the rock matrix is in general much higher than the total volume of the fracture system. In summary, a fractured porous medium represents a system, that principally consists of two components with contrary properties:

- The fracture system has a high permeability, a high porosity (if one can assume a porosity to open fractures), a low total volume, and a low storage capacity.
- The rock matrix has a low permeability, a low porosity, a high total volume, and a high storage capacity.

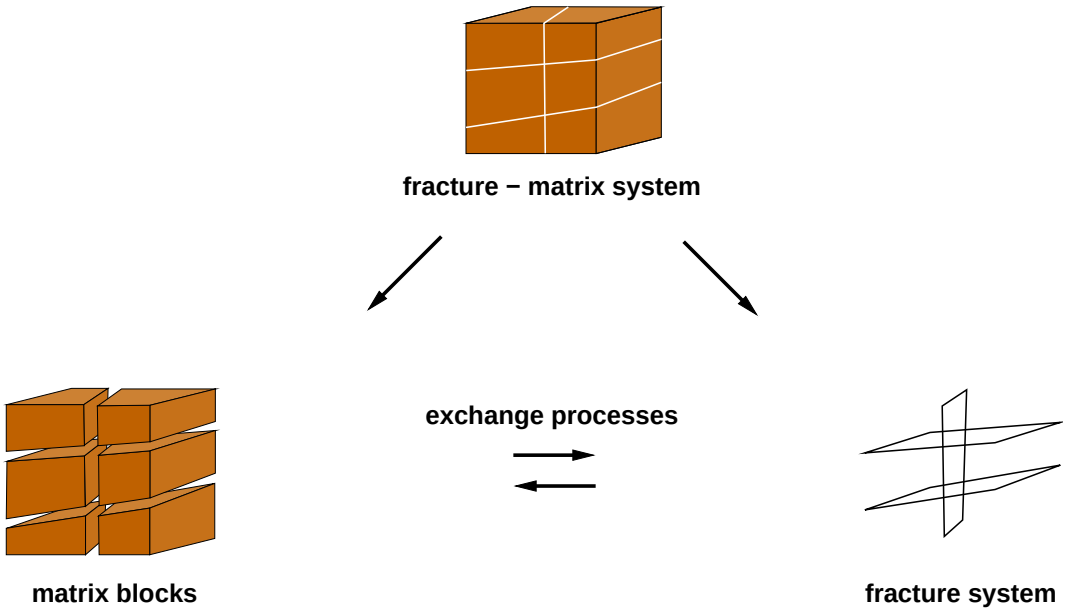

Figure 1.2: Fracture–matrix systems have high demands on simulation tools

Because of these significant differences, the requirements for a model of the fracture system are absolutely different from those for a model of the rock matrix. The discontinuities of the rock matrix resulting from the fractures can be regarded as a special case of heterogeneities, where the fracture has totally different properties than the rock matrix.

For gas–water processes, the different properties can lead to the fact, that the fractures are filled with gas, whereas the matrix is still entirely water-saturated. In this case, the fractures act as a barrier for the water flow, which in this case only takes place over the contact points of the rock matrix (see Unger and Mase (1993)).

Due to the low thermal conductivity of air, the fractures can additionally act as thermal isolators in such a case. In this work, we will neglect these blocking properties of

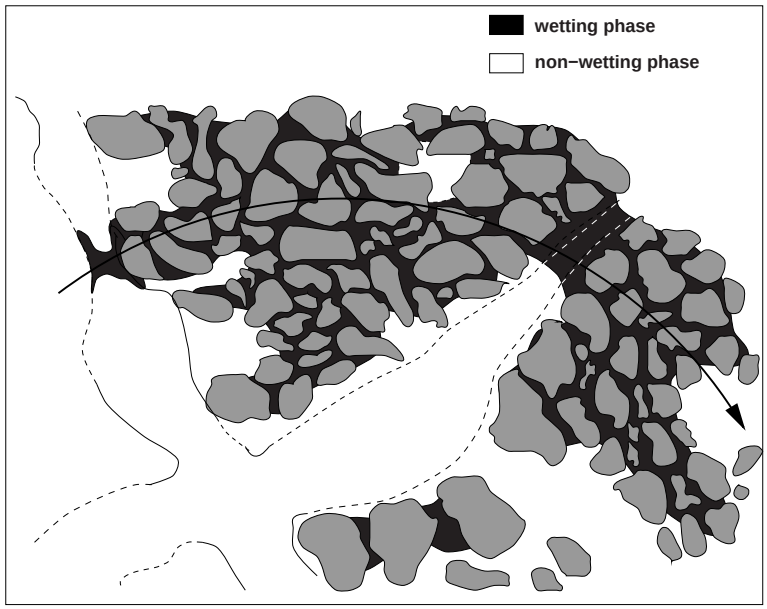

Figure 1.3: Gas can act as a barrier for water flow in a fracture. (see Wang and Narasimhan (1985))

fractures.

Due to the strong differences in material properties, fractures can be regarded as discontinuities in the rock. Depending on size and formation of these discontinuities, we can classify different types:

- ▷ faults,
- ▷ shear zones,
- ▷ bedding planes,
- ▷ joints,
- ▷ fissures.

In the frame of this work, the term fracture is synonymously applied to faults, shear zones, bedding planes, joints and fissures, even though the above mentioned discontinuities occur on different scales (see Figure 1.1).

Fractures are described by a variety of different properties. In Table 1.1 the most important properties are briefly explained. A detailed description of these parameters can be found in the work of Hemminger et al. (2000). Most of these properties (coplanarity, persistence, distance, intensity, termination behaviour) are properties of bands of fractures. Fractures can be absolutely disordered. However, it is mostly possible to determine main directions. Position, form, and orientation mark the location of a fracture in the system matrix. Fracture aperture and roughness are properties which

concern the inner structure of a fracture. A lot of these properties are highly correlated. For example, taking a smaller distance and a higher intensity, more fracture intersections will occur than taking a higher distance and a lower intensity. Bonnet et al. (2001) indicate, for example, the existence of a correlation between fracture length and fracture aperture.

Property	Description
form	The form of the fracture, i.e. the outer border, can be assumed as being polygonal, circular, elliptic or irregular. The block formation of the surrounding matrix often gives a hint on a polygonal form of the fractures. However, also elliptic forms can be observed. In laboratory experiments, circular fractures could additionally be produced by hydraulic fracturing.
aperture	Perpendicular distance between corresponding fracture faces
roughness	Measure for the deviation of the separating surfaces from the assumed area.
fracture dimension/ extension	The extension of the fracture can either be described by the trace length ($[m]$), which can be detected using outcrops or by the surface extension ($[m^2]$) of single fractures.
coplanarity	We speak of coplanarity if there are several fractures in the same plane.
persistence	A measure for the ratio of the sum of the fracture traces l_i over the length L of the colinear reference line, respectively the ratio of the sum of the fracture surfaces a_i over the area A of the coplanar reference face.
position/ location	Specifying a fracture in space can often only be done indirectly, taking the distance of one fracture to the other or taking the fracture density.
distance	Perpendicular distance between the directly neighbored fractures in a main direction.
intensity/ density	We specify the intensity taking the number of fractures per volume unit or by taking the total trace length of the fractures per unit area, respectively the total fracture area per unit volume.
orientation	The orientation of fractures in space is described using the terms strike and fall.
termination behaviour	It is analyszed whether fractures terminate at intersection points/ lines with other fractures or in the intact rock, or if they fan or branch out at the ends.
connectivity	Intersection behaviour of the fractures.

Table 1.1: Geometrical characterization of fractures (taken from Silberhorn-Hemminger (2002) according to Dershowitz and Einstein (1988), completed by entries from Singhal and Gupta (1999a))

As described in Chapter 2 it is desirable to integrate as few structural information of length scales smaller than the considered one as possible into the model. This means in this respect, that only those discontinuities which occur on the observed scale should be captured as structure by the geometric model. The influence of smaller discontinuities should be detected with the help of effective parameters, if possible. In Figure 1.4, taken from Kröhn (1991), a model with fractures on different scales is presented. The chosen cut-outs are described by different models.

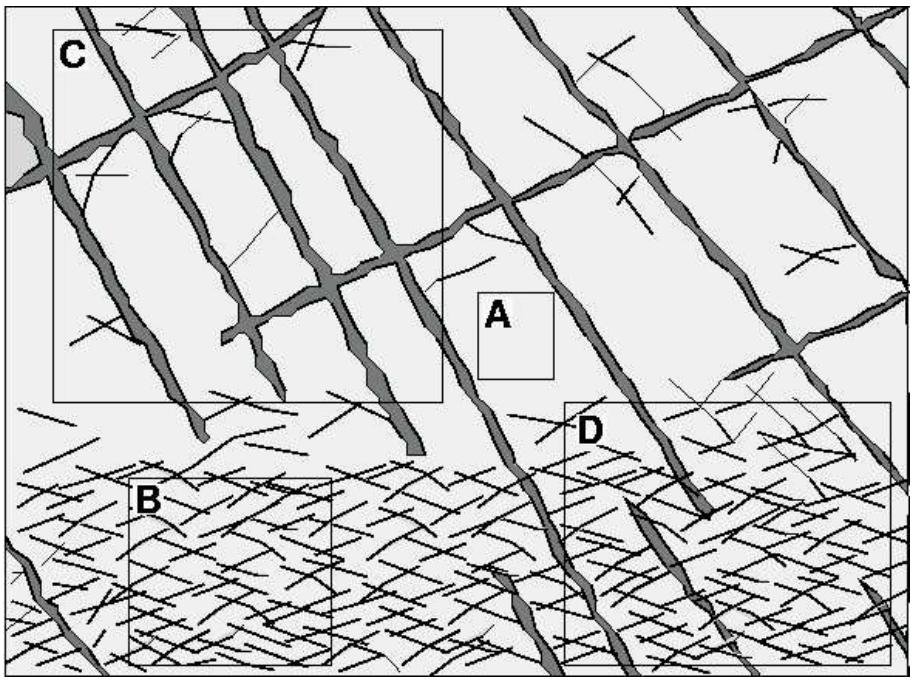

Figure 1.4: Fractured groundwater aquifer with different discontinuities (taken from Kröhn (1991))

cut-out A This cut-out contains the undisturbed rock matrix. It can be described as a porous medium in the model.

cut-out B Besides the rock matrix, we have a high percentage of so-called fissures in the investigation area. The connected fissures contribute to the increase of total permeability. If the definition of an REV is possible over the whole cut-out, this cut-out can be regarded as a substituting porous system with equivalent flow and transport properties.

cut-out C The rock matrix is pervaded by a connected network of fractures of large aperture. Besides, we have shorter fractures with a very small aperture which, however, do not form an interconnected network. For investigations using models, the discrete modelling is appropriate. In dependence of the flow and transport properties of the matrix, either a bare fracture network or a fracture–matrix

system is considered. If we additionally succeed in identifying an REV over the fracture network, we have the possibility to represent the cut-out in the model by a continuum model.

cut-out D The single non-connected fractures with large aperture are considered as being discrete fractures in the model. The rock matrix which is pervaded by fissures can be included into the model by an equivalent substituting matrix according to cut-out B. The creation of the model leads to a discrete fracture–matrix system.

Thus, we can principally distinguish the following fracture–matrix models:

- ▷ *Discrete Models:* The fractures are considered as discrete structures. The condition therefore is the investigation of the fracture parameters, listed in Table 1.1. With such a model, we have the possibility to model flow and transport processes very similarly to nature. In the work of Hemminger et al. (2000), the possibility is explained how to use geostatistically generated data additionally to deterministic data taken from experiments. This is especially appropriate, if the fracture data is taken from two-dimensional cuts of the area, even if we want to carry through a three-dimensional simulation. As the fracture aperture is very small compared to the extension of the rock blocks and as the flow velocities in the fractures are much higher than in the rock matrix due to the higher permeability, the modelling of flow in fractured porous media is very difficult. It is possible to model fractures equidimensional (3D fractures in 3D space) or to take fractures of a lower dimension (2D fractures in 3D space). An equidimensional model implies very high demands on net generation and the numerical tools for solving the resulting equation system (see Neunhäuserer (2002)). Modeling using fractures of a lower dimension is much easier on the other hand. However, one has to keep in mind that modeling of flow perpendicular to the fracture orientation is not possible.

- ▷ *Multi-continua models:* Using multi-continua models, we have to make the assumption that an REV cannot only be obtained for the porous medium—the rock matrix—but also for the fractured system. It is principally possible to use different flow and transport models for the two continua. In practice, however, we mostly use the same models with different parameter sets. Exchange terms describing the interaction between the matrix system and the fracture system (see Figure 1.5) are very important using multi-continua models. Narasimhan and Pruess (1988) describe a multi-continua model for multiphase flow processes in fractured porous media. For multi-continua models, we use averaged parameters for rock matrix and fracture system. Mostly, we additionally have measuring results at hand which give us the possibility of an integral consideration. The inspection of the correctness of a multi-continuum model is extremely difficult especially for complex multiphase flows, as the single parameters can strongly correlate like for example in inverse modelling.

- ▷ *Hybrid Models:* Hybrid models represent a combination of the two model types explained above. For this model, we consider the fractures on the observation scale

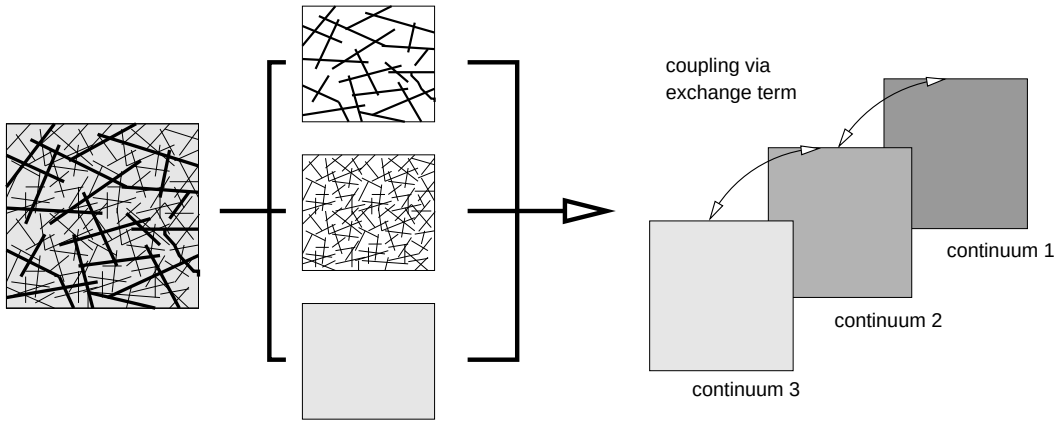

Figure 1.5: Procedure for the multi-continuum model

discretely and the fractures on the lower scales with the help of continua models. Assuming fractal properties of the fracture system with respect to all relevant scales, the hybrid model is the only one which is appropriate. Unfortunately, combining the two above mentioned models, also combines their uncertainties. In addition to the difficulties in representing the discontinuities on the observation scale, we have uncertainties of the model using the multi-continua approach. In spite of these difficulties, Wu and Pruess (2000) have used this approach to model radio nuclid transport in partially saturated fractured rock.

In this work, we deal with gas-water processes in the near field of a repository. The aim is to gain a fundamental understanding of the processes. For this reason, we do not assume the existence of a representary elementary volume from the beginning on. The choice of the REV has to be carried out in different ways for different model approaches. For discrete models, we need an REV for the internal structure of the fracture as well as the matrix. For the fracture, we have to consider fracture aperture and roughness, for the rock matrix we have to consider the pore distribution. As fractures as well as the matrix are taken into account in a discrete manner, the exchange processes result from the geometry and the chosen model. For this reason, it is not necessary for the discrete model to calculate an REV for the exchange processes. For multi-continua models, we need a proof of the existence of an REV for the total system. This means, that we need an REV for the fracture bands, the system matrix and for the exchange processes.

The model concept chosen here is discrete, i.e. the fractures are taken into account directly by geometry. We assume that the position and form of the fractures is known. From the properties of Table 1.1, we need only those concerning the internal structure of a fracture: the fracture aperture and the roughness. In the following section, we will deal with these properties of the fractures in more detail.

Multi-continua models and therefore also hybrid models assume that the calculation of an REV is possible for fractured systems. The proof of the existence of an REV is,

however, rarely given and even not always posssible. Often, a proof is only given for a single property which is then assumed to guarantee the possiblity of the calculation of an REV for the total system. However, this is not correct. Formally, the REV has to be calculated for each of the considered processes. This can either be put into practice directly or by proofing the correctness of the direct derivation. For this proof, you have to show, that the calculation of the REV of one variable implies the calculation of the REV for other variables.

In this work, we have temperature, pressure, and gas saturation as primary variables. All the other variables are secondary variables.

For temperature distribution in geological systems, we can normally state that we have a low influence of heterogeneities on the temperature distribution. This is due to the fact that thermal conductivity smoothens the variation of temperature due to jumps of parameters.

The main heterogeneities on a considered scale have an influence on the pressure distribution in a geological system. However, the pressure distribution is not very much influenced by heterogeneities on lower scales.

For transport processes, the results are not only dependent on large-scale but also on smaller-scale heterogeneities because flow channeling occurs. Tsang and Neretnieks (1998) define flow channeling as the phenomena describing the fact that a fluid in a geological system with heterogeneities mainly flows along certain flow paths. These flow paths are called *paths of minimum resistence* by Tsang and Neretnieks (1998), while Neretnieks (1987) and others call them *main flow paths*. The effect of these main flow paths is highly increased when considering gas–water flow and transport.

In Tsang and Neretnieks (1998), you can find an overview of experiments in fracture–matrix systems on spatial scales from the micro scale to the field scale. This causes problems for the simulation of flow and transport processes in fracture–aquifer systems, as main flow paths on all considered scales represent a strong hint against the possibility of finding a representative elementary volume for the considered process. In Table 1.2, you can find the experiments carried through by Tsang and Neretnieks (1998).

scale	*type of experiment*	*reference*	*comment*
		laboratory experiments	
5.2 cm	Wood's metal is injected into the fracture plane and its flow path is observed.	(Pyrak-Nolte et al., 1987)	Wood's metal flows in a limited area in the fracture plane.
12 cm	Colored water is injected into the core center of a fracture. The outflow is observed at the border of the core.	(Gentier, 1986), (Gentier et al., 1989)	The outflow of colored water is very irregular.
19.5 cm	Tracer is injected into a core with a fracture along its axes. Breakthrough curves are measured.	(Neretnieks et al., 1982), (Moreno et al., 1985)	Tracer breakthrough curves cannot be described by advective - dispersive equations
41 cm	Flow through a fracture along the main axes; detailed measurements of fracture opening width.	(Hakami and Larsson, 1996)	Irregular flow as a function of the normal tensions on the fracture.

	small-scale field experiments		
2.5 m	Five bore holes in the fracture plane in granite; bore holes in distance of 7 cm; over-cross pressure test.	(Bourke, 1987)	Only about 20 percent of the fracture plane are water permeable.
1.95 m	2 bore holes in a fracture plane, each hole is packed with 5 cm sections; over-cross tracer test (so called channeling experiment).	(Abelin et al., 1988), (Abelin et al., 1990)	Flow and transport are strongly channelized.
5-10 m	Bore hole within a fracture cut by a drift. Flow and tracer outflow along the cut-out of the fracture drift are investigated (so called stripa 2D experiment).	(Abelin et al., 1985)	Flow and transport are highly irregular; hydraulically active fracture opening width is highly different from the fracture opening width active for the transport process.
20 m	A shear zone is cut by a drift and 8 bore holes. Measurements of flow and transport in the bore holes in the fracture plane (so called MI experiment)	(Frick, 1992), (Eikenberg et al., 1994), (Hadermann and Heer, 1996)	Tracer breakthrough curves have a steep increase, a long tail and in some cases several points. Flow properties in the fracture plane are very irregular. Matrix diffusion can be observed.
10-20 m	Drift and bore holes cut a fracture zone of a width of 6 cm. The drift wall is divided into areas	(Birgersson et al., 1993)	Flow is dominated by only some large flow paths. One of the 60 areas is responsible for more than 50 percent of the flow.
10.6-29.8 m	A single fracture. Dipole and radial, convergent flow field and pulse - tracer injection.	(Novakowski et al., 1985), (Raven et al., 1988)	The data can be fitted with an ”instationary” storage model with mobile and stagnating flow zones in the fracture.
	large-scale field experiments		
25-27 m	Drift of 100 m and 3 bore holes from the drift to the fractured rock. Tracer is injected into the bore holes with appropriate tacker systems. Flow and tracer transport are observed at the drift wall in collective areas (so called stripa 3D experiment).	(Neretnieks, 1987), (Abelin et al., 1987)	Flow and tracer breakthrough are very irregular. Tracer breakthrough curves cannot be described by advective - dispersive equations.
25-100 m	Drift of 100 m with radial bore holes in highly fractured rock. Injection flows are measured in appropriate packer systems in the bore holes; tracer is injected by packer systems and collected in sections of the drift (so called Fanay-Augères experiment)	(Calmels et al., 1986), (Barbreau et al., 1987)	Data are used for calibration of a model with stochastic methods (appropriate distribution).

150-200 m	Injection and extraction boring in fracture zones in 100-260 m below the surface. Flow and transport experiments were carried through. The latter contain convergent single borings as well as dipole experiments (so called Finnsjön experiment)	(Andersson et al., 1988), (Andersson et al., 1989), (Andersson et al., 1990)	Several tracers were used. Many breakthrough curves, all with long tails and some with several points.
50-150 m	Shafts and bore holes in three fracture system; tracers were injected by packed sections and collected in the shafts (URL, pinawa, Manitoba, Canada).	(Frost et al., 1992), (Frost and Davison, 1995)	Tracer breakthrough curves vary - some of them are describable with the advective - dispersive equations, others have long tails and several points.
1000 m	In a tunnel and silo system in fractured rock at the east sea near Forsmark we can observe the invasion of water in a tunnel system.	(Neretnieks, 1994)	The invasion of water is highly spotted over the rock walls; we have a strong variability of flow rates.

Table 1.2: Experiments with occuring main flow paths (*flow channeling*)

1.2.2 Geometrical Models for Single Open Fractures

Depending on the orientation of a fracture, we can define a (x,y) plane parallel to this orientation. A straight line perpendicular to this (x,y) plane cuts the two border faces of the fracture. The distance between these two points is defined as the aperture of the fracture. We define accordingly the fracture aperture functions illustrated in Figure 1.6. When constructing our fracture model, the information of the roughness of this fracture is not considered. Tiedemann (1983) calls this *macro roughness*, but often it is also called *out-of-plane-tortuosity*. In Figure 1.7 the idealization of describing a fracture is schematically illustrated. In neglecting the tortuosity of the fracture perpendicular to its orientation we overestimate the permeability in our model.

The function of the fracture aperture can also only be described in idealized form. Inspite of today's precision instruments, measurements of fracture aperture still are pointwise measurements. The values between these points have to be interpolated (see Figure 1.7(b)). Depending on the distance of the points, we have an additional micro roughness which cannot be captured by our model and which also leads to an overestimation of fracture permeability. However, modern measurement strategies decrease this error. Demny et al. (2000) reached a resolution of 2 mm using the 3D scanning method, and a resolution of about 0.5 mm using the adsorption method. Bertels et al. (2001) reach a pixel size of 0.3 mm using the computer tomography scanning method. As they use smoothing over five pixel, they present the resolution of their results as being about 1.5 mm.

The more important errors in measuring fields of fracture apertures occur as they depend on the rock pressure—the lythostatic pressure—on the fracture planes. This

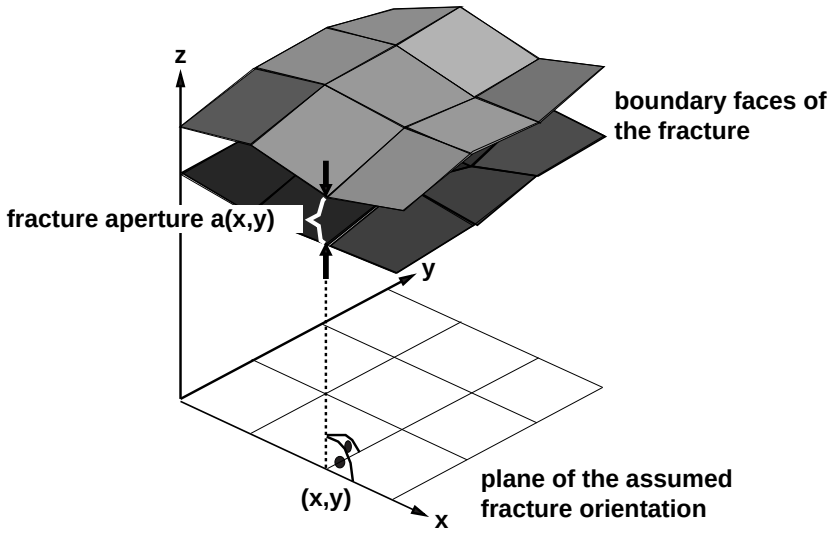

Figure 1.6: Definition of the fracture aperture taken from Demny et al. (2000) according to Hakami and Larsson (1996)

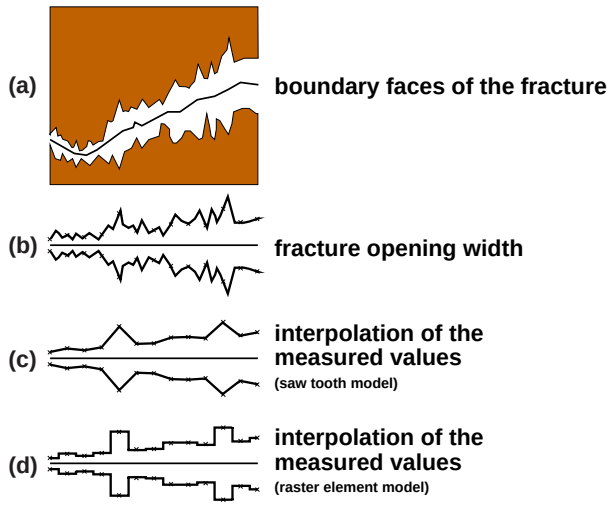

Figure 1.7: Idealisation of the function of the fracture aperture

makes the investigation of the real aperture very difficult because taking a bore core leads to pressure exoneration. For lythostatic pressures occuring in deep mountains, we can observe an elastic deformation of the fracture planes, even in granite as illustated by Wong et al. (1989). For the contact points, respectively faces, we have according to the above mentioned definition, a fracture aperture of zero. The majority of the faces which are hydraulically not or hardly active, increase the effect of main flow paths within the fracture. In order to investigate this effect, Pyrak-Nolte et al. (1987) used "Wood's metal" to get prints of natural fractures under various lythostatic pressures. With the help of these prints, the change of empty spaces and contact regions was shown in dependence of the different pressures.

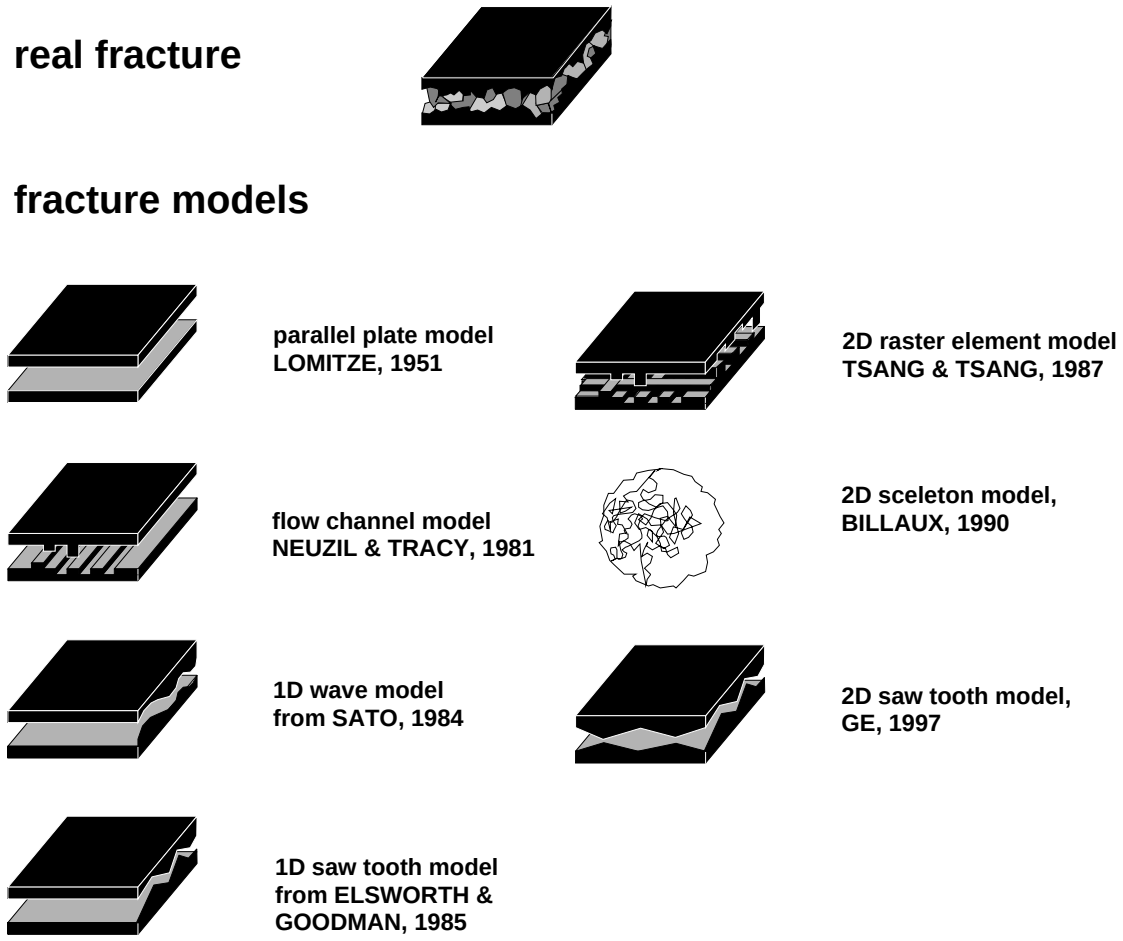

Figure 1.8: Overview over models for single fractures (according to Demny et al. (2000))

For the description of flow and transport processes a variety of geometric models has been developed. Demny et al. (2000) give an overview of the most important approaches. These are illustrated in Figure 1.8. In general, they distinguish between three

model categories where combinations of these categories are possible.

- ▷ The parallel plate model has first been introduced by Lomize (1951). This model takes into account neither the macro nor the micro roughness.
- ▷ The model of Neuzil and Tracy (1981) tries to model the observed flow channels by one-dimensional channels.
- ▷ With the 1D saw tooth model taken from Elsworth and Goodman (1985) and the wave model taken from Sato et al. (1985) topology models are extended by the direct modeling of macro roughness.
- ▷ Billaux (1990) models the flow channels as one-dimensional paths in the two-dimensional space.
- ▷ Taking the 2D raster model of Tsang and Tsang (1987) and the 2D sceleton model of Ge (1997), models are developed which simulate the effects of micro roughness up to a certain degree. The flow channels in the fracture plane are modeled as property resulting from the field of fracture aperture.

With the models of Lomize (1951), Neuzil and Tracy (1981), Elsworth and Goodman (1985) and Sato et al. (1985) the formation of main flow paths in a single fracture cannot be represented. The model of Billaux (1990) is also not appropriate for an investigation of gas–water processes: The gas occupies the larger pores, so that they no longer serve as flow paths for water.

Demny et al. (2000) conclude that the raster model of Tsang and Tsang (1987) is most adequate to imitate micro scale flow processes as it is most widely spread and gives the best results in a comparison. Moreover, the 2D raster model is especially easy to implement, as for the assumption of a value to a measured fracture aperture only the respective value is necessary. Like this, it is also taken as a basis for the consideration of gas - water flow in single fractures. However, we assume that under the assumption of a 2D saw tooth model according to Ge (1997), flow in single fractures can be better simulated than with the 2D raster model. This assumption is based on the simple fact that the 2D saw tooth model is an interpolation of 1st order of the measured fracture aperture, whereas the 2D raster element model is an interpolation of 0th order. For the approximation of the volume of a measured fracture aperture, for example, we would have to take nine values into account in the 2D saw tooth model (the value itsself and its eight neighbors) whereas under the assumption of the 2D raster model, we only have to take into account the fracture aperture itsself. As the uncertainties in the model assumptions are already large (see Section 2.2.3), we abstain from the somewhat more detailed interpolation of the fracture aperture of the 2D saw tooth model.

1.3 Literature Overview

This work deals with different topics and stresses different aspects within one topic which are used for the simulation of non-isothermal gas–water processes in fractured

porous media. At this point, we abstain from an overview of the state of research for all these topics. Instead, we will refer to certain works where we can find such an overview.

The theory and model formation for multiphase flow processes and multiphase–multicomponent flow and transport processes is presented in detail by Helmig (1997) for fractured porous media. This work is an extension of the work of Helmig (1993) in which first approaches for the treatment of multiphase flow processes in fractured porous media are presented.

Multiphase–muliticomponent flow and transport processes are presented in detail by Emmert (1996) for two phases and two components and by Class (2001) for three phases and three components. Class (2001) emphasizes the effect of non-isothermal phase transfer processes in the model. Especially in the work of Class (2001), there is a good overview of the continuum models and the constitutive relationships for non-isothermal multiphase–multicomponent processe in porous media.

The presentation of the numerical model used within this work and of the interface condition presented in Chapter 2 can be found in more detail in Bastian (1999b). There, one can find further presentations which show the possibilities of the simulation program MUFTE-UG used for this work.

The implementation of the fracture discretization in MUFTE-UG is described in Chapter 4 and in Reichenberger (2004). Besides the description of the basic discretization, we will explain the coupling of the fracture generator of Fuchs (1999) with the simulation program MUFTE-UG for the simulation of threedimensional fractured systems. A presentation of the fracture discretization can also be found in the project report of Helmig et al. (2000).

An overview over different upscaling techniques for porous media is given by J.H. Cushman (2002). This overview contains besides renormalization techniques also further possibilities of homogenizing heterogeneous porous media. Especially for permeability, Renard and de Marsily (1997) give a broad overview of different methods with practical examples. Stauffer and Aharony (1995) give a fundamental introduction into percolation and renormalization theory. Applications of the percolation theory for flow and transport processes in fractured porous media can be found in the work of Berkowitz and Balberg (1993). Upscaling techniques are explained in the works of Braun (2000) and Neuweiler (1999). Especially Neuweiler (1999) deals with gas migration processes for single fractures and shows that for the processes considered there, the continuum approach is questionable.

An overview over the present state of the research in the fields of flow and transport processes in fractures is given by Wang (1991) and by Berkowitz (2002). These works give an overview for fractured systems as well as for single fractures. Singhal and Gupta (1999a) have a closer look on the geological problems in relation to fractured systems. They also give an overview over the hydrological methods for the parameter identification of fractured systems. An overview over the description of fractured systems with the help of geostatistical and deterministic data can be found in the work of Silberhorn-Hemminger (2002). In the works of Oron and Berkowitz (1998), Demny et al. (2000), and Tsang (1992), the hydraulic properties of fractures are dis-

cussed in detail. Here, we can also find explanations about the fields of aperture of single fractures as well as the resulting flow processes.

The experiments for the degassing mentioned within this work, are found in Jarsjö (1998). There, laboratory experiments as well as field experiments are presented. We also find an upscaling approach there, describing the fracture system in a highly simplified manner.

2 Physical and Mathematical Model Concepts

2.1 The Averaging Process

In Chapter 1 we have already introduced the concept of the Representative Elementary Volume (REV) and of scales.

In Bear (1972) it is shown how averaging over the molecular movements can lead from the molecular consideration to the consideration as a continuum. By the averaging process, we receive new parameters like density or viscosity of a fluid. These parameters are not appropriate for the description of single movements of the molecules. By averaging, we gain new relationships, for example the Navier-Stokes equations.

On the micro scale, the flow movements of a single fluid can still be directly captured. Here, we have to have an exact knowledge of the pore space. For larger domains, however, this procedure is not feasible. On the one hand, the computer simulation even of relatively small systems would take a very long time, on the other hand, the gain of information over structure and geometry of single pores would be much too elaborate and too variable.

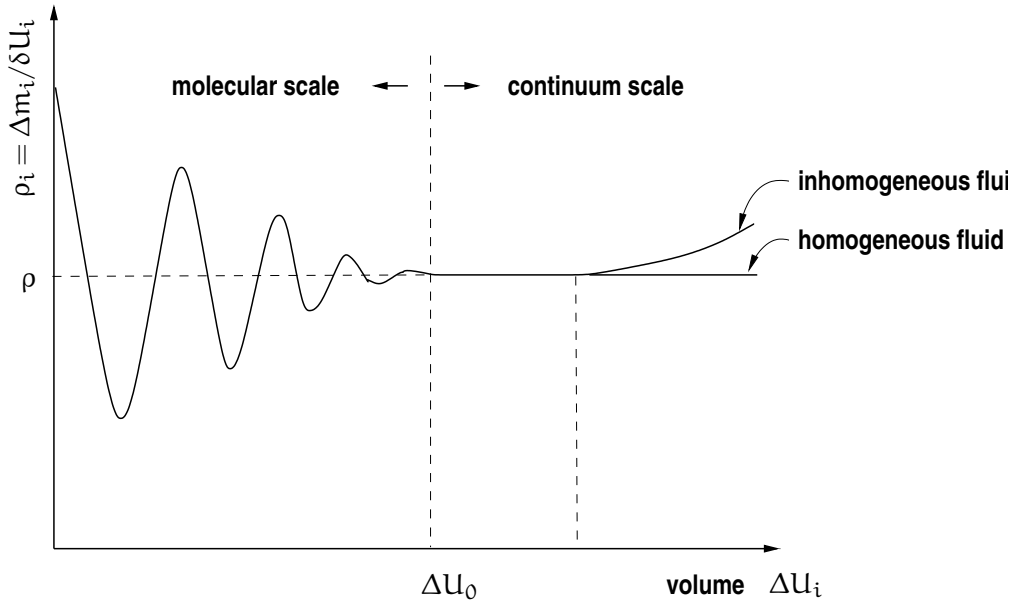

Figure 2.1: Averaging of density

Like this, the following citation taken from Chilès and Delfiner (1999), describes very clearly the difficulty in defining a porous medium in an exact manner.

> *Ghislain de Marsily started the defense of his hydrogeology thesis by showing the audience a jar filled with fine sand and announced "here is a porous media". Then he shook the jar and announced "and here is another one", shook it again "and yet another one". Indeed at the microscopic scale the geometry is defined by the arrangement of thousands of individual grains with different shapes and dimensions, and it changes as the grains settle differently each time. Yet at the macroscopic scale we tend to regard it as an ingenious illustration of the notion of a random function in three–dimensional space.*

The pore space will indeed change every time the sand is shaken. For many problems, however, we are not interested in the exact fluid movements within the pore space. So for certain problems, we do not have to preassume the exact description of the pore space. We assume that all porous media generated by shaking—called realisations in the following—can be described in the same way "on average". We assume that all these realizations can be described with the help of geostatistic parameters, i.e. that we can give a distribution function with mean value and variance as well as a spatial distribution (see Bardossy (2002)). Here, we can average over many realisations, but we can also divide a very large realisation again and again. (That these two procedures are equivalent is made clear by the idea that we get a larger realisation in stringing together the smaller realisations.)

For this reason, it is sufficient to subdivide the pore space into corresponding volumes which are meant to be systems in the sense of our definition. For these systems, it is important that they are chosen so large that an averaging of properties over the system is reasonable. They have also to be chosen so small that these properties do not vary within the system. For the section where these two properties are fulfilled, we can calculate the so-called representative elementary volume which can be taken from Figure 2.2 (see Bear (1972)).

The averaging concept for the transition from the micro to the macro scale can be clarified by considering an REV, Figure 2.3. Instead of describing the distribution of the fluid phase and the gas phase as well as the pore matrix exactly, only the ratio of their volumes is taken into account. Under the assumption of a phase distribution which is continuous and homogeneous within the REV, this will lead to the definition of new system parameters on the macro scale, for example the effective saturation.

As already explained in Section 1.2.1, pressure distribution and temperature distribution are not dependent on small-scale heterogeneities. As a logical consequence, the calculation of the REV is easily possible for the parameters determining pressure and temperature distribution.

Transport processes, however, are not dependent on the heterogeneities of all length scales which can be taken from Table 1.2. From this, it follows that a calculation of the REV is much more difficult for transport processes as the length of the REV is a multiple of the characteristic length of the heterogeneity, in other words, that the variance is large for the averaging over smaller volumes.

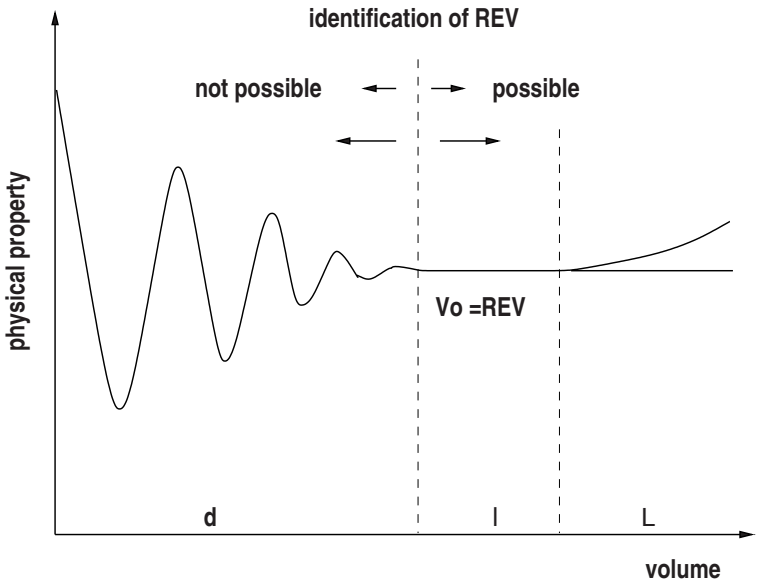

Figure 2.2: Identification of the representative elementary volume (REV).

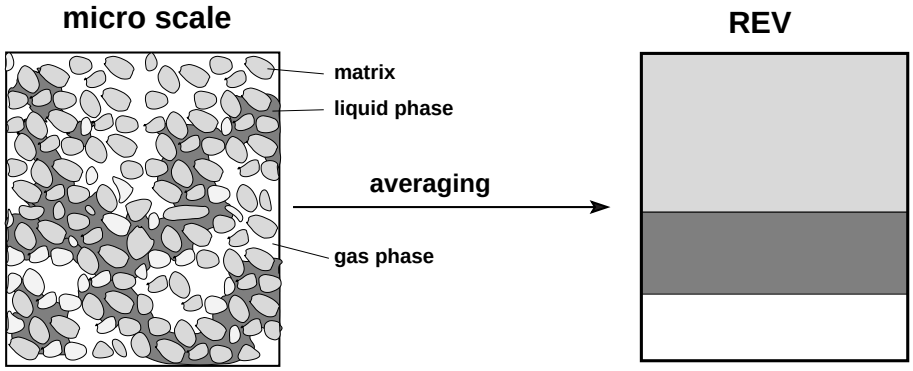

Figure 2.3: Consideration of the averaged pore space.

Additionally to the averaging properties, we have further requirements for our REV: we assume a chemical, thermal and quasi-mechanical equilibrium.

The requirement for chemical equilibrium means in our case that all phase transitions are already finished. After a pressure or temperature change, we first have a state of inequilibrium which approaches the equilibrium state exponentially. It depends on a variety of factors how fast the phase composition approaches the equilibrium. For example, the velocity of degassing is dependent on the number of crystallization points. For our model consideration, we assume that the time until the equilibrium is reached is small compared to the considered time. Similar assumptions hold for the thermal equilibrium. Here we assume that the heat transfer within the considered system (between the phases within the system) is fast compared to the other considered processes.

We demand that the pressures in the single phases differ only by a certain value within the REV. Here we assume that the non-wetting phase has already occupied the larger pores which can be entered by this phase. This is indeed a process which can take several weeks dependent on the considered sample. Here, the demand of an equilibrium is also a precondition which cannot be neglected.

2.1.1 Transition to the Local Scale

For the transition from the molecular scale to the minimum continuum scale we average—at least theoretically—over all molecular collisions. From this averaging process we get new state variables like pressure and temperature as primary variables and parameters depending on these primary variables, like viscosity functions and the density function as secondary variables. When modeling a sufficiently large number of atomic, respectively molecular movements, this functions should be deductible. Indeed, these models only exist for those approaches and cases where we cannot assume a continuum, as for example for the modelling of gas dynamic processes in the outer earth's atmosphere.

For the transition from the continuum scale to the local scale, we proceed in the same way. Here, we calculate the average over the parameters relevant for flow. The difference of the transition from the molecular to the minimum continuum scale lies in the fact that pressure and temperature of the variables are preserved. As a new variable, we have the saturation S_α of phase α. This saturation is calculated as the ratio of the volume of the respective phase within the REV over the total pore volume in the REV:

$$S_\alpha = \frac{\text{Volume of phase } \alpha \text{ within the REV}}{\text{Volume of the pore space within the REV}} \,. \tag{2.1}$$

All the other parameters depend on these variables (the pressure of the phases, the temperature of the phases, the pore space and the distribution of the pore space among the phases). They will be described in the next chapters. Unfortunately, these functions are not always defined in a unique way. This is due to the fact that the saturation does represent the pore space only insufficiently. Some functions are not only dependent on the saturation—that is the volume ratios—but also on the class of distribution

which can be different depending on the considered processes. This is called hystereses within the pore space as the effect of imbibition (infiltration of the pore space by the wetting phase) or drainage (infiltration of the pore space by the non-wetting phase) still continues when these processes are finished. A detailed description of these processes and their effects on the parameter distributions can be found in Sheta (1999).

Later approaches deal with the calculation of REVs on the meso scale. Ataie-Ashtiani et al. (2002) and Braun et al. (2002), for example, derived anisotropic relative permeability functions on the meso scale where models on the local scale are used and the heterogeneities are first modeled directly. In these works, it is assumed that for a model on the scale of a multiple of the characteristic length of these heterogeneities, an averaging over these effects is possible. A critic which can often be heard is that a repeated, cascade-like averaging does not always lead to the same average as a single averaging. This objection is certainly not wrong assuming an irregular distribution of heterogeneities or processes, for which small-scale heterogeneities are relevant. That means that we have to have certain preconditions for the system in order to calculate an REV in multiple steps. With respect to this criticism, we often forget that the cascade-like averaging is in any case already part of the total model. The first average has already lead from the molecular scale to the continuum scale. Consequently, you should be able to average directly from the molecular scale to the REV scale when rejecting the cascade-like averaging.

2.1.2 The REV for Fracture–Matrix Systems

Singhal and Gupta (1999a) explain that it is not possible to receive a constant value when calculating the REV for fracture–matrix systems, but that certain fluctuations remain (see Figure 2.4). They weaken the preconditions for the formulation of an REV in a way that they admit an "insignificant" fluctuation in the averaging process. Additionally, they introduce the conditions that the averaged parameter only encounters slight changes when enlarging or reducing the considered volume and that the averaging parameter can be calculated independently of the direction.

Singhal and Gupta (1999a) indicate that for the identification of a REV of a fracture–matrix system a sufficiently large number of section boundaries of the fractures has to be captured in order to receive an appropriate averaging of the parameters relevant for flow mechanics. This means that the REV has to be much larger than the average fracture length of the considered system. If the fracture length is large compared to the considered system, the identification of a REV is not possible. For this reason, models being based on the REV identification of fracture–matrix systems cannot be applied in such a case and the fractures have to be included directly into the system.

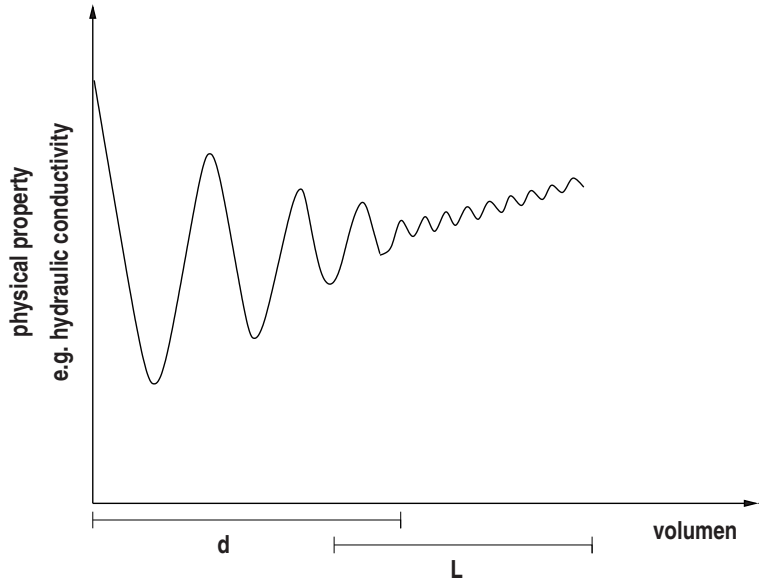

Figure 2.4: The calculation of a REV for a fracture–matrix system is not always possible (taken from Singhal and Gupta (1999a)).

2.2 Effective Parameters

2.2.1 Porosity

Porosity is defined as

$$\phi = \frac{\text{Volume of the pore space within the REV}}{\text{Volume of the REV}} . \tag{2.2}$$

Taking this equation, we assume that the whole pore space is accessible to flow and that it is either occupied by the gas or by the water phase. The pore space is in principal also dependent on the primary variables pressure and temperature, for swelling porous media like clay or smectite also on saturation. In this work, we assume that the solid phase, and thus also porosity, does not change. For open fractures, porosity is equal to one, of course. For a two-dimensional consideration of a single fracture, a reference thickness of 1 meter is assumed by the numerical model. In these cases, we can include the real fracture aperture for the calculation of fluxes by adjusting porosity.

2.2.2 Conductivity, Permeability and Darcy's Law

The proportionality constant K_f in Darcy's law

$$\boldsymbol{v} = \frac{Q}{A} = -K_f \nabla h \tag{2.3}$$

with $Q\left[\frac{m^3}{s}\right]$ as the volumetric flux, $A[m^2]$ as decisive area, $\boldsymbol{v}[\frac{m}{s}]$ as Darcy velocity and $h[m]$ as the water level is called hydraulic conductivity. About 100 years after the dis-

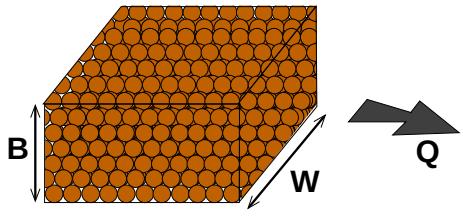

Figure 2.5: Hubbert used packings of uniform glass spheres for the investigation of the hydraulic conductivity.

covery of this relationship by Darcy, Hubbert conducted several investigations with fluids of different densities and dynamic properties with packings of uniform glass sheres of diameter $d[m]$.

In the frame of these experiments, Hubbert found out, that the hydraulic conductivity K_f is proportional to $\frac{d^2 \cdot \rho_f \cdot g}{\mu_f}$. This means, that the hydraulic conductivity can be written as

$$K_f = \frac{N d^2 \rho_f g}{\mu_f}. \tag{2.4}$$

N denotes a proportionality factor depending on the way of the packing of the spheres.

The intrinsic permeability is part of this expression which is fluid independent, as it is only defined by the solid phase. It is defined as

$$K = N \cdot d^2. \tag{2.5}$$

While the hydraulic conductivity characterizes the ability of a porous medium to conduct water under standard condition, the intrinsic permeability can in theory be applied to every fluid.

While Darcy's and Hubbert's original experiments described one-dimensional problems, the anisotropy of porous media and consequently the anisotropy of permeability became interesting issues for research later on. This anisotropy occurs especially in layered porous media whose permeability in horizontal direction is much larger than in the vertical direction. This permeability is described by matrices of a rang according to the considered dimension.

$$K = \begin{pmatrix} k_{xx} & k_{xy} & k_{xz} \\ k_{yx} & k_{yy} & k_{yz} \\ k_{zx} & k_{zy} & k_{zz} \end{pmatrix} \tag{2.6}$$

While layers as presented in Figure 2.6 can lead to highly different values in the primary diagonals ($k_{xx} < k_{yy}$), effective permeabilities of fracture - matrix systems can lead to dominant entries in the secondary diagonals (k_{xy}, k_{yx}) if the main fracture directions differ highly from the chosen main flow directions.

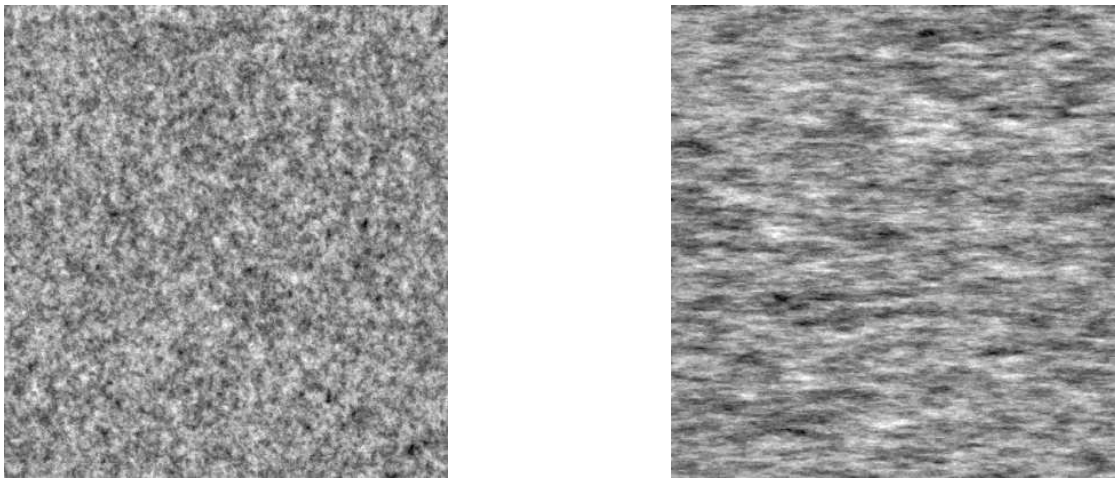

Figure 2.6: Layers lead to strong anisotropy; on the left hand side an isotropic, on the right hand side an anisotropic permeability field.

Renard and de Marsily (1997) give an overview over the possibilities to conclude from small single volumes with isotropic permeability—called cells in the following—to a possibly anisotropic effective permeability for a larger volume.

In principle, there are three main types of averaging which also play a role for the averaging of permeability, the arithmetic, the harmonic and the geometric one.

The arithmetic average is applied if the areas to be averaged over are "connected in parallel", i.e. if the pressure gradient is parallel to the boundaries of the partial domains. The arithmetic mean is defined as

$$\mu_a = \frac{\sum_{i=1}^{n} k_i}{n}. \tag{2.7}$$

The harmonic average is used if the areas to be averaged over are "connected in series", i.e. if the pressure gradient is perpendicular to the boundaries of the partial domains. The basic types of averaging are the arithmetic average of permeability perpendicular to the pressure gradient and the harmonic average parallel to the pressure gradient.

The harmonic average and the arithmetic average also represent the limits for the investigation of an effective permeability k_{eff} of a permeability field with isotropic permeabilities $k_i, i \in \{1, ..., n\}$: $\mu_a < k_{eff} < \mu_h$.

According to Renard and de Marsily (1997), the rule of the geometric mean is one of the few exact results in the investigation of the effectivepermeability of a permeability field. It was derived by Matheron (1967). This method is based on the fact that in the two-dimensional space a 90° rotation transforms a gradient vector to a conservative vector and vice versa. Under the condition that the permeability field $k(x, y)$ and its inverse function $k' = \frac{1}{k}$ are random functions with the same probability distributions and that these functions are invariant to a 90° rotation, the effective permeability can be expressed in the following way:

$$K = \mu_g = exp\,(E\,[\log k]) \tag{2.8}$$

These conditions are fulfilled for the special case of an isotropic medium if the permeability is log-normally distributed. Equation (2.8), however, is only valid for a parallel flow field and not, for example, for a radial flow field. Matheron (1967) shows that at least for large distances, the harmonic mean is valid for radial flow fields in porous media with an isotropic log-normal k distribution.

2.2.3 Laws for Flow in Fractures

As already explained in Section 1.2.2, we take the 2D raster model of Tsang and Tsang (1987) as a basis for flow and transport models for single fractures. For the derivation of a flow velocity, we first consider a single raster element (see Figure 2.7).

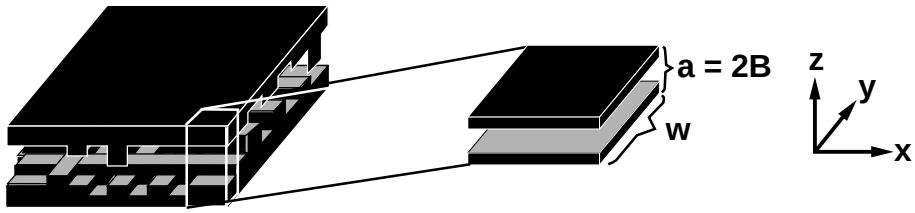

Figure 2.7: We consider fracture surfaces as plane plates.

Deriving the laws for flow in fractures we make the following assumptions:

- ▷ incompressible fluid
- ▷ constant temperatures
- ▷ stationarity
- ▷ small absolute velocities
- ▷ small changes of convective velocities
- ▷ negligibly small velocity components v_z perpendicular to the fracture plane – and thus also to the flow plane
- ▷ small second derivatives of velocities (laminar flow behaviour)
- ▷ hydraulically smooth walls of the separating surfaces.

Under these assumptions, we can calculate the flow velocities between two fixed plates as a consequence of a pressure gradient. Here we assume that the velocities are

parallel to the pressure gradient, that means we assume a one-dimensional consideration. The simplified and transformed Navier-Stokes equations give for the x component of the velocity vector $\boldsymbol{v} = v_x, v_y, v_z$:

$$v_x = -\frac{a^2}{8\mu}\frac{dp}{dx}\left(\frac{4z^2}{a^2} - 1\right) \tag{2.9}$$

The integration from 0 to $\frac{a}{2}$ over the half (for reasons of symmetry) of the fracture aperture gives:

$$\int_{z=0}^{z=\frac{a}{2}} v_x \, dz = \left[-\frac{a^2}{8\mu}\frac{dp}{dx}\left(\frac{1}{3}4y^3a^2 - z\right)\right]_0^{\frac{a}{2}} = \frac{a^3}{24\mu}\frac{dp}{dx}$$

Thus, the integration over the whole fracture aperture a gives:

$$\int_{z=0}^{z=a} v_x \, dz = a \cdot v_x(z) = \frac{a^3}{12\mu}\frac{dp}{dx} \tag{2.10}$$

Let $a = 2b$ be the fracture aperture, and w the width of the considered fracture segment. Thus, the flux Q is equal to

$$Q = Av_x = wav_x(z) = -w\frac{a^3}{12\mu}\frac{dp}{dx} \tag{2.11}$$

This relationship is called "cubic law" as the fracture aperture a occurs to the third power.

To show the relationship of this equation to the Darcy's law, we consider once more the calculation of flux in porous media:

$$Q = Av_x = A(-K_f \cdot \nabla h) = wa(-K_f \cdot \nabla h) \tag{2.12}$$

From $h \hat{=} \frac{p}{\rho g} + z$ it follows in combination with Equation (2.11) for the flux between two fixed plates:

$$\begin{aligned} Q &= wa\frac{a^2\rho g}{12\mu}\frac{d\frac{p}{\rho g}}{dx} \hat{=} wa\frac{a^2\rho g}{12\mu}\frac{dh}{dx} \\ \Rightarrow K_f &\hat{=} \frac{a^2\rho g}{12\mu} \end{aligned}$$

As for the intrinsic permeability the relation $K \hat{=} K_f\frac{\mu}{\rho_f g}$ holds; it follows

$$K = \frac{a^2}{12}. \tag{2.13}$$

Often, single fractures are computed with the help of 2D simulation programs. Here, we have to multiply again with the fracture aperture to identify the flux correctly:

$$K = \frac{a^3}{12}. \tag{2.14}$$

As explained at the beginning of this section, many assumptions hold for the flux. Additionally, the plates are assumed to be absolutely smooth. Al-Yaarubi et al. (2001) stated that the simulation under the assumption of the "cubic law" highly overestimates the flux when comparing a simulation under the assumption of the Navier-Stokes equations with one under the assumption of the "cubic law". Oron and Berkowitz (1998) explain that such an overestimation results from the negligence of the micro roughness. Therefore, they use dimensional analysis which will be shown in the following.

As generally known and explained for example in Jischa (1982), the Navier-Stokes equations describe flow under most of the conditions for which a corresponding continuum has to be assumed. Equation (2.15) gives the equation for the conservation of impulse which forms together with the mass conservation equation a basis for the Navier-Stokes equations.

$$\frac{\partial \boldsymbol{v}}{\partial t} + (\boldsymbol{v}\nabla)\boldsymbol{v} = \frac{1}{\rho}\left[-\nabla p + \mu \boldsymbol{v}\right] \tag{2.15}$$

Now we assume, that the fluid is incompressible and that the flux does not change in time. Moreover, we only consider the flux in direction of the pressure gradient assuming, that this is the x-direction. With these assumptions, the Navier-Stokes equations give us the following equation:

$$\left(v_x \frac{\partial v_x}{\partial x} + v_z \frac{\partial v_x}{\partial z}\right) = -\frac{1}{\rho}\frac{\partial p}{\partial x} + \frac{u}{\rho}\left(\frac{\partial^2 v_x}{\partial x^2} + \frac{\partial^2 v_x}{\partial z^2}\right) \tag{2.16}$$

Assuming the fact that fractures are in general parallel, we will now define some characteristic numbers. Here, L is a "typical segment" of the fracture. As we are working with the 2D raster model of Tsang and Tsang (1987), it is a good idea to set L equal to the length of the edges of a raster element. V_x is a typical velocity in the x-direction, V_z is a typical velocity in the y-direction. Moreover, $B = \frac{a}{2}$ is valid.

$$\delta = \frac{B}{L} \qquad \gamma = \frac{V_z}{V_x} \tag{2.17}$$

Already by the choice of these parameters (mainly the choice of B), we assume a certain homogeneity of the topology of the fracture walls. Here, we have to assume that within the raster element of length L, the fracture aperture does not strongly differ from the aperture defined for this element.

Moreover, we assume that the roughness of the fracture is not too large. We take this as a condition for the variance of the function of the fracture aperture. Assuming that we define the plane of fracture orientation (x, y) in the center of a fracture, one of the idealized fracture walls lies in a distance of B above this plane and the other idealized fracture wall in a distance of B below this plane. Computing the distances of the non-idealized faces being the boundaries of a fracture from this (x, y) plane, we define with

$$\sigma_o = \sqrt[2]{\frac{\int_0^L \int_0^L (f_o(x,y) - B)^2 \, dx \, dy}{L}} \tag{2.18}$$

the square root of the averaged roughness of the upper wall and with

$$\sigma_u = \sqrt[2]{\frac{\int_0^L \int_0^L (f_u(x,y) + B)^2 \, dx \, dy}{L}} \tag{2.19}$$

the square root of the averaged roughness of the lower wall (see also Figure 2.8). In this way, we can define by ε a measure for the roughness and postulate that this measure has to be small enough according to Equation (2.20). In other words, we postulate that for a fracture segment the real faces being the boundaries of a fracture do not differ too much from the idealized ones.

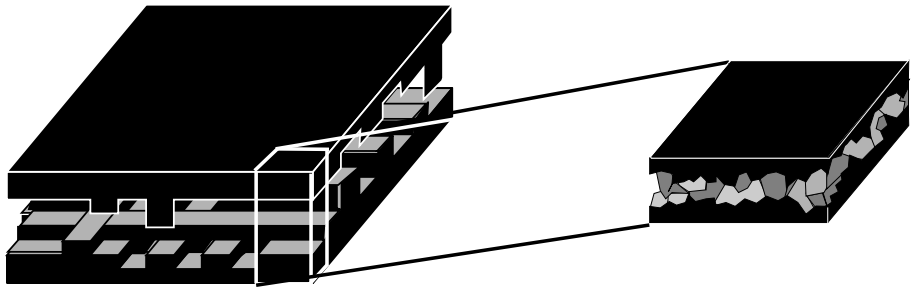

Figure 2.8: Illustration of the micro roughness of a segment.

$$\varepsilon = \max\left(\frac{\sigma_u}{B}, \frac{\sigma_1}{B}\right) << 1 \tag{2.20}$$

Now, we can evaluate the following non-dimensional characteristic numbers:

$$\begin{aligned}
v_x^* = \tfrac{v_x}{V_x} \quad &\Rightarrow \quad v_x = V_x v_x^* \\
v_z^* = \tfrac{v_z}{V_z} \quad &\Rightarrow \quad v_z = V_z v_z^* \quad \Rightarrow \quad v_z = v_z^* \gamma V_x \\
\tfrac{\partial^*}{\partial x^*} = \tfrac{\partial}{\partial x} L \quad &\Rightarrow \quad \tfrac{\partial}{\partial x} = \tfrac{1}{L}\tfrac{\partial^*}{\partial x^*} \quad \Rightarrow \quad \tfrac{\partial}{\partial x} = \tfrac{\gamma}{B}\tfrac{\partial^*}{\partial x^*} \\
\tfrac{\partial^*}{\partial z^*} = \tfrac{\partial}{\partial z} B \quad &\Rightarrow \quad \tfrac{\partial}{\partial z} = \tfrac{1}{B}\tfrac{\partial^*}{\partial z^*}
\end{aligned} \tag{2.21}$$

With $h = \frac{p}{\rho g} + z$ and G as a "typical" gradient of water level we can replace the pressure gradient by the dimensionless form of the water level:

$$\frac{\partial^* h^*}{\partial x^*} = \frac{\frac{\partial h}{\partial x}}{G} \Rightarrow \frac{\partial p}{\partial x} = \rho G g \frac{\partial^* h^*}{\partial x^*} \tag{2.22}$$

Now we can plug the so-defined terms into Equation (2.16):

$$V_x v_x^* \frac{\delta}{B}\frac{\partial^*}{\partial x^*}(V_x v_x^*) + \gamma V_x w^* \frac{1}{B}\frac{\partial^*}{\partial z^*}(V_x v_x^*) = \tag{2.23}$$

$$-gG\frac{\partial^* h^*}{\partial x^*} + \frac{\mu}{\rho}\left(\frac{\delta^2}{B^2}\frac{\partial^{*^2}}{\partial x^{*^2}}(V_x v_x^*) + \frac{1}{B^2}\frac{\partial^{*^2}}{\partial z^{*^2}}(V_x v_x^*)\right) \tag{2.24}$$

A further simplification of the equation gives:

$$\frac{V_x^2}{B}\left(\delta v_x^*\frac{\partial^* v_x^*}{\partial x^*} + \gamma w^*\frac{\partial^* v_x^*}{\partial z^*}\right) = -gG\frac{\partial^* h^*}{\partial x^*} + \frac{\mu V_x}{\rho B^2}\left(\delta^2\frac{\partial^{*^2} v_x^*}{\partial x^{*^2}} + \frac{\partial^{*^2} v_x^*}{\partial z^{*^2}}\right) \tag{2.25}$$

We can write this equation without superscript $*$ in the following way:

$$\delta v_x\frac{\partial v_x}{\partial x} + \gamma w\frac{\partial v_x}{\partial z} = -\frac{gGB}{V_x^2}\frac{\partial h}{\partial x} + \frac{\mu}{\rho V_x B}\left(\delta^2\frac{\partial^2 v_x}{\partial x^2} + \frac{\partial^2 v_x}{\partial z^2}\right) \tag{2.26}$$

and with the definition of the *Reynolds*-number

$$Re = \frac{\rho V_x B}{\mu} \tag{2.27}$$

we get

$$\delta v_x\frac{\partial v_x}{\partial x} + \gamma w\frac{\partial v_x}{\partial z} = -\frac{gGB}{V_x^2}\frac{\partial h}{\partial x} + \frac{1}{Re}\left(\delta^2\frac{\partial^2 v_x}{\partial x^2} + \frac{\partial^2 v_x}{\partial z^2}\right) \tag{2.28}$$

.

To get the "cubic law", further simplifications are necessary. The left hand side of the equation has to be negligibly small so that we can assume it to be equal to zero. Moreover, $\delta^2 \frac{\partial^2 v_x}{\partial x^2}$ has to be negligibly small compared to $\frac{\partial^2 v_x}{\partial z^2}$. As a result, we obtain:

$$0 = -\frac{gGB}{V_x^2}\frac{\partial h}{\partial x} + \frac{1}{Re}\frac{\partial^2 v_x}{\partial z^2} \tag{2.29}$$

A transformation of the dimensionless expressions gives:

$$\frac{\partial^{*^2} v_x^*}{\partial^* z^{*^2}} = \frac{\rho V_x B}{\mu}\frac{gGB}{V_x^2}\frac{\partial^* h^*}{\partial x^*} \tag{2.30}$$

$$\frac{1}{B^2}\frac{\partial^{*^2}}{\partial^* z^{*^2}}(V_x v_x^*) = \frac{\rho g}{\mu} G \frac{\partial^* h^*}{\partial x^*} \tag{2.31}$$

$$\frac{\partial^2 v_x}{\partial z^2} = \frac{\rho g}{\mu}\frac{\partial h}{\partial x} \tag{2.32}$$

$$\mu\frac{\partial^2 v_x}{\partial z^2} = \gamma\frac{\partial h}{\partial x} \tag{2.33}$$

Additionally to the geometric condition for the roughness in equation (2.20) two other conditions have to be valid to derive the cubic law from the non-dimensional form of the Navier-Stokes equations. These assumptions lead to the following restrictions:

To be able to neglect $\delta^2 \frac{\partial^2 v_x}{\partial x^2}$, $\delta^2 \ll 1$ has to be valid as $\frac{\partial^2 v_x}{\partial z^2}$ and $\frac{\partial^2 v_x}{\partial x^2}$ have about the same order of magnitude.

Transforming the non-dimensional equation (2.28) into the following form

$$\delta v_x \frac{\partial v_x}{\partial x} + \gamma v_z \frac{\partial v_x}{\partial z} = \frac{1}{Re}\left\{-\frac{\rho}{\mu}\frac{gGB^2}{V_x}\frac{\partial h}{\partial x} + \left(\delta^2\frac{\partial^2 v_x}{\partial x^2} + \frac{\partial^2 v_x}{\partial z^2}\right)\right\} \tag{2.34}$$

we get as a result that the left hand side is negligibly small if $Re \cdot max(\delta, \gamma) \ll 1$.

Oron and Berkowitz (1998) refer to the fact that Wang (1978) and Munson et al. (1985) explained that for small Reynolds numbers the effect of roughness on flow velocities can be written as an asymptotic series dependent on ε:

$$v_x = v_{x,0} + \varepsilon v_{x,1} + ... \tag{2.35}$$

$$v_z = 0 + \varepsilon v_{z,1} + ..., \tag{2.36}$$

where $v_{x,0}$ is the parabolic velocity profile of the Poiseulle flow (see Equation (2.9)). Independent of the derivation, this representation is also intuitively clear: In a first approximation, the deviation of the Poiseulle flow profile is a linear function of roughness.

For this reason $\gamma = \frac{V_z}{V_x} \approx \varepsilon \frac{v_{z,1}}{v_{x,1}}$ is valid and with $\frac{v_{z,1}}{v_{x,1}} \approx 1$, we get $\gamma \approx \varepsilon$. With this equality, we can formulate three conditions which can be taken for checking the validity of the cubic law in a segment:

$$1. \quad \varepsilon = \max\left(\frac{\sigma_u}{B}, \frac{\sigma_l}{B}\right) << 1 \tag{2.37}$$

$$2. \quad \delta^2 << 1 \tag{2.38}$$

$$3. \quad Re \cdot \max(\delta, \varepsilon) << 1 \tag{2.39}$$

Moreover, this gives us a rough estimate for the Reynold's number of the system:

$$Re = \frac{\rho V_x B}{\mu} \tag{2.40}$$

Considering equation (2.34) and assuming that the left hand side is negligibly small, it follows under the condition that all variables and derivatives are in the order of one, and that the magnitudes can be transferred to the characteristic numbers:

$$\frac{1}{Re} \approx \frac{gGB}{V_x^2}, \tag{2.41}$$

and then:

$$V_x \approx \frac{\rho g}{\mu} B^2 G. \tag{2.42}$$

This is a dimensionless form of writing the cubic law. Remember, that Equation (2.13) said that $K = a^2/12$. Consequently,

$$v_x = -\frac{\rho g}{\mu} \frac{B^2}{3} \nabla h.$$

Thus, the dimensionless derivation of the flow laws overestimates the average velocity by a factor of three and the maximum velocity of the Poiseulle flow by a factor of two. For rough approximations, made in the course of the derivation of the Reynold's number, this is not astonishing any more. It is important in this respect that the dimensionless form provides computable equations for the Reynold's number:

$$Re \approx \frac{\rho^2 gGB}{\mu}. \tag{2.43}$$

As for water, the condensed terms for dynamic viscosity, density and gravity lie in an order of magnitude of about 10^7 and a "typical" hydraulic gradient within a fracture lies in the order of one-tenth of a percent, the fracture aperture has to lie in the range of millimeters. This follows from the condition (2.39) for the case of small ε and δ, i.e. for small micro roughnesses and segments that are much larger than their average aperture.

ε and δ are actually dependent on one another. The longer the segment, i.e. the smaller δ, the larger gets ε as the derivations of the fracture walls from the average value get larger.

To sum up, we can derive the following conditions for our topology model:

- ▷ The segment length of the 2D raster model should be a multiple of the average fracture aperture. If possible, it should even be larger than the maximum fracture aperture in order to guarantee a small δ.
- ▷ The segment length should be definitly smaller than the correlation length of a single fracture in order to guarantee a small ε.

2.2.4 Capillary Pressure - Saturation Relationship

The capillary pressure plays an essential role in the description of gas–water flow in fractured porous media. The capillary pressure described on the macro scale is dependent on the exact distribution of the water phase and the gas phase in the pore space (respectively on the distribution of the fracture aperture). The best known approaches only take into account the dependency of the capillary pressure on the saturation, wheras the exact form of the capillary pressure–saturation function is dependent on the pore space.

Actually, the capillary pressure is dependent on a variety of other factors. The occupation of the pore space is not unique, even if we take the modified mechanical equilibrium as a basis (see Section 2.1). It is much more important, if the considered process is a drainage of an imbibition process, i.e. if the wetting or the non-wetting phase is entering the pore space. Moreover, it plays a role how often the pore space is imbibed and drained. This behaviour is also called hysteresis effect. Hysteresis effects are explained in detail in the work of Sheta (1999). There, the respective scaling and the implementation of hysteresis effects into a numerical model are presented.

One of the most important hysteresis effects is the entrapment of a fluid. This effect consists of the fact that when one phase is replaced by another, a part of the first phase is completely enclosed by the second. Fluid properties can occur on different scales. We consider the entrapment of a fluid on the micro scale whose effect has to be captured by effective parameters on the REV scale. On the micro scale the fluid entrapment results from the fact that the non-wetting phase occupies the larger pores, and the wetting phase the smaller pores. If thus during a drainage process the non-wetting phase occupies a region of small pores encircled by larger pores, the phase enclosed in this region is cut off and thus immobile. On the other hand, the non-wetting phase can get trapped

in a region with larger pores. The phases trapped in this way that they are present even in a fully drained, respectively imbibed, pore space, are called residual saturations of the respective phase as they remain in the pore space even for an extreme increasement of the pressure gradient (see also Section 2.4).

Besides the fluid entrapment, there exist further micro-scale hysteresis effects, e.g. the inkbottle effect which occurs where the pore space enlarges after a bottle-neck and decreases again thereafter up to the original diameter. For this reason, we have several saturation states for the capillary pressure. Moreover, there is the so-called bypassing effect which has to do with the different diameters of two flow paths. For the flow path with the least flow resistance, the fluid phase will move quicker and thus entrap the phase with the higher flow resistance. Further descriptions for the micro-scale reasons of hysteresis can be found in Sheta (1999).

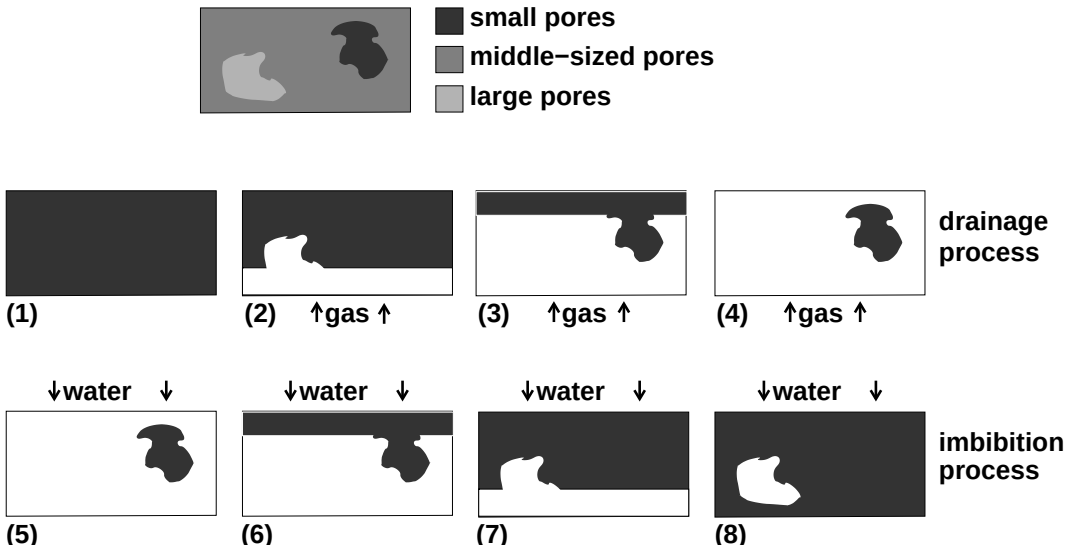

Figure 2.9: Drainage and imbibition lead to hysteresis effects.

The main issue of this work is to get an understanding of the processes for the relevant physical/ thermodynamical processes using the model concept implemented in MUFTE-UG and to investigate the influence of different numerical methods. Taking into account hysteresis effects would already lead to the fact that the difficulty of identifying single processes would increase. Moreover, a quantitative identification of hysteresis curves is not available for the experiments simulated in the frame of this work.

The influence of temperature differences on capillary pressure was only investigated in a couple of works. Leverett (1941) proposes to scale the capillary pressure - saturation relationships with the help of temperature-dependent surface tensions.

Of the numerous capillary pressure–saturation relationships which were developed in the last decades, the ones of Brooks and Corey (1964)—called BC in the following—and of van Genuchten (1980)—called VG in the following—are most widely used. Both

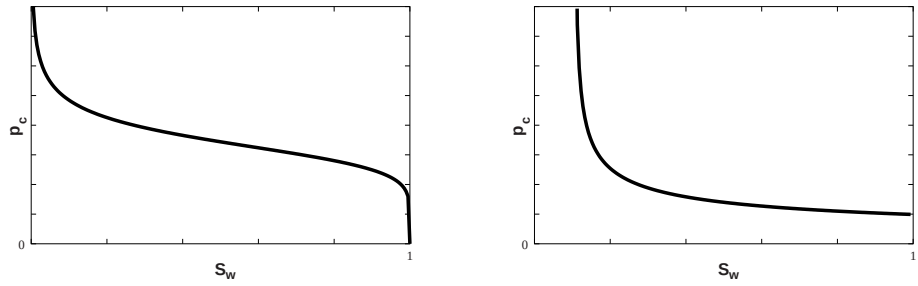

Figure 2.10: Comparison of the capillary pressure–saturation functions according to Brooks and Corey (1964) and van Genuchten (1980)

approaches use parameterized functions and describe the capillary pressure–saturation behaviour in a more or less similar way. Equation (2.44) describes the BC functions in dependence of the effective saturation S_e. S_e is calculated from the water saturation S_w as in Equation (2.46), where S_{wr} and S_{gr} are the residual saturations of the water and the gas phase.

$$p_c = p_d S_e^{-1/\lambda} \tag{2.44}$$

$$p_c = \frac{1}{\alpha}\left(S_e^{-1/m} - 1\right)^{1/n} \tag{2.45}$$

$$\text{with} \quad S_e = \frac{S_w - S_{wr}}{1 - S_{wr} - S_{gr}} \tag{2.46}$$

$$m = 1 - \frac{1}{n} \tag{2.47}$$

The BC parameters p_d and λ as well as the VG parameters α, m, and n have to be found by fitting the curves to experimental data. Both functions represent the capillary pressure–saturation function mainly in the same way. The main difference occurs for a function if the water saturation has reached a value of one. While the BC function of a fully water-saturated soil has a capillary pressure higher than one, the VG function decreases down to zero as can be seen from Figure 2.10.

Experiments for the evaluation of capillary pressure–saturation relationships are often carried out with the so-called controlled outflow cell technique, which is described by Lorentz et al. (1992), for example. Such a series of measurements is shown in Figure 2.11. The respective values are represented by filled squares. The form of the measurement series is schematically shown in Figure 2.12. One can recognize that the form of the measurement series resembles the VG capillary pressure–saturation relationship. Measurements taken using the controlled outflow cell technique support the model of van Genuchten (1980). A further proof for the validity of the VG relationships is the fact that the capillary pressure is equal to zero for full water saturation, i.e. $p_c(S_w = 1) = 0$, as presented in Schubert (1982).

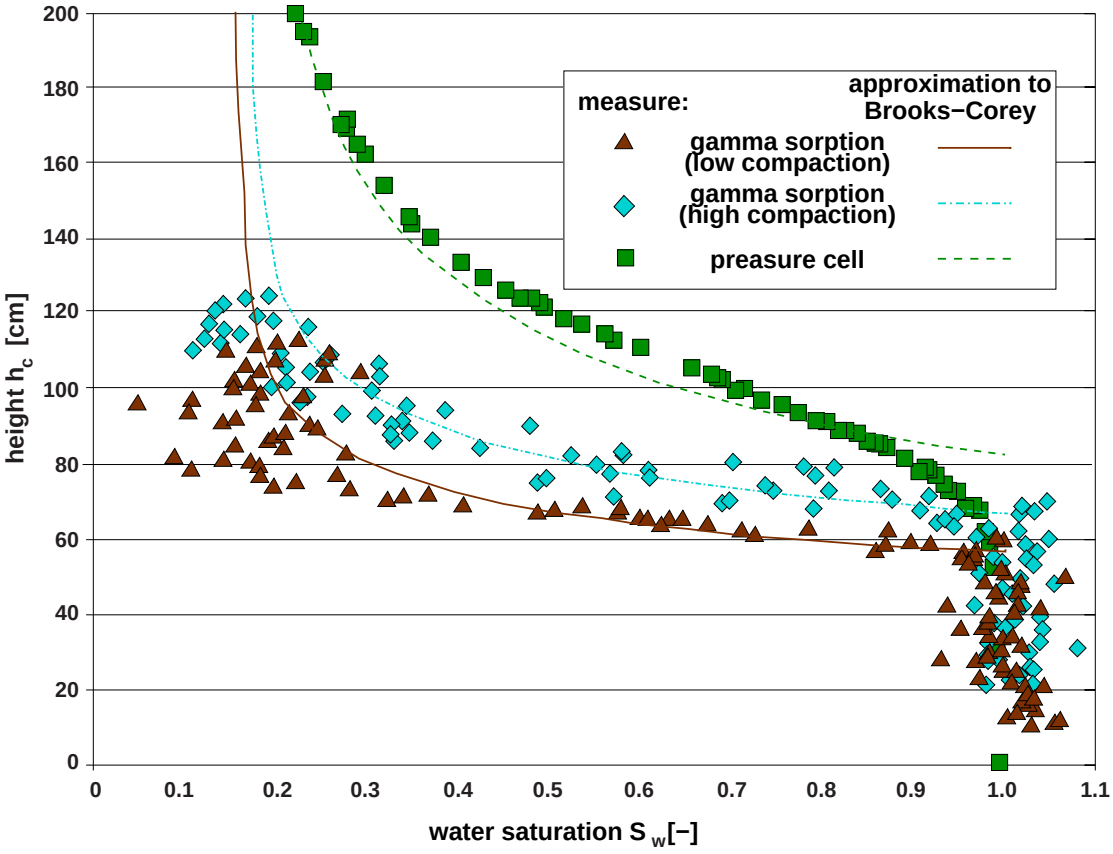

Figure 2.11: Capillary pressure–saturation relationships with the gamma ray technique and the cell technique of controlled outflow (after Winkler (2002)).

A modern measuring technique is the gamma ray system technique which is described by Färber and Betz (1995), for example. This technique allows an exact resolution of the information, i.e. the averaged region is much smaller. Moreover, measurements do not necessarily need a pressure as high as for the cell technique of controlled outflow. In Figure 2.11, the measurements received by the gamma ray technique are compared, on the one hand for a high compaction of the sand (represented by non-filled diamonds), on the other hand for a low compaction of the sand (represented by filled triangles). As can be seen, the decrease of the adjusted BC curve for low compaction for values close to S_{wr} is higher than for the adjusted BC curve for the compaction. For higher values of S_w, however, the decrease is much lower. By the compaction, the pore space is diminished and gets more irregular. Thus, the form parameter λ describing the pore behaviour has to be larger. For the values received by the pressure cell technique we get a much higher value of λ for the adjustment of the BC curve. Taking the pressure cell technique, the irregularity of the pore space is highly overestimated because of the strong compaction of the porous medium.

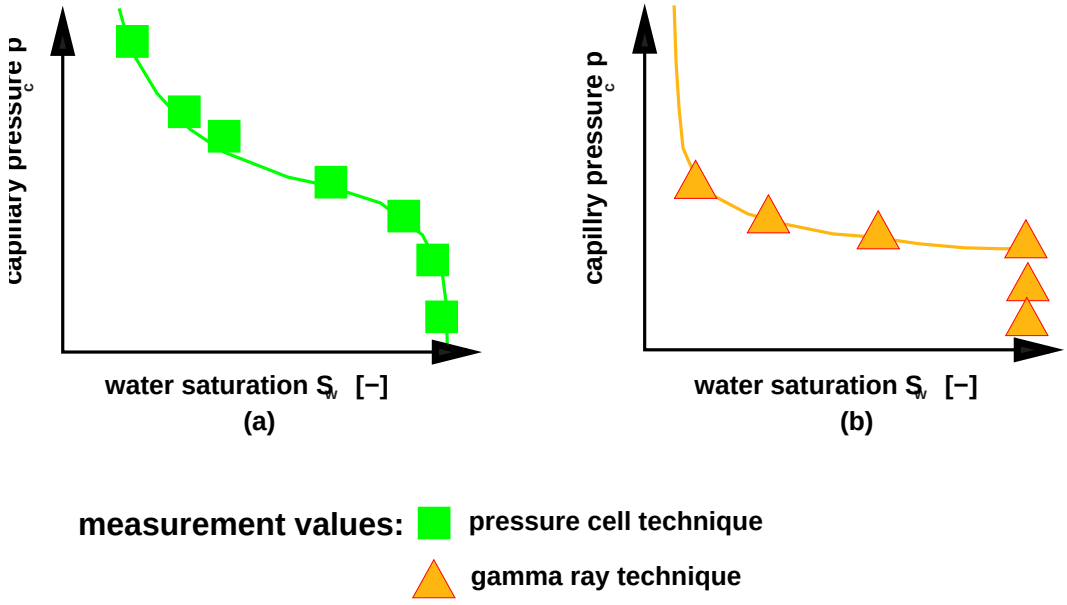

Figure 2.12: Capillary pressure - saturation relationships with the gamma ray technique and the cell technique of controlled outflow (after Winkler (2002)).

More interesting in the frame of this work is the behaviour of the curves at $S_w = 1$. Figure 2.12 emphasizes this effect schematically, Figure 2.12(a) shows values for the pressure cell technique. The curve in Figure 2.12(a) looks like a typical VG curve, the capillary pressure tends to zero for $S_w = 1$. Figure 2.12(b), however, shows that the capillary pressure for $S_w = 1$ first goes down to a capillary pressure larger than zero and for $S_w = 1$ it goes slowly to zero. For this reason, the capillary pressure–saturation relationship is no function in the original sense as for $S_w = 1$ the "function" assigns all values from 0 up to p_d. The BC functions, however, assign the highest capillary pressure to the fully saturated region, the entry pressure p_d with $p_d = p_c(S_w = 1)$. The other capillary pressures are neglected.

Lenhard et al. (1989a) give a relationship between the BC parameters (p_d, λ) and the VG parameters (α, m, n):

$$\lambda = \frac{m}{1-m}\left(1-0.5^{1/m}\right) \tag{2.48}$$

$$\overline{S}_x = 0.72 - 0.35 \cdot \exp(-n^4) \tag{2.49}$$

$$\alpha = \frac{\overline{S}_x^{\frac{1}{\lambda}}}{p_d}\left(\overline{S}_x^{1/m} - 1\right)^{1-m} \tag{2.50}$$

Besides experiments for evaluating capillary pressure–saturation functions, simulation tools were additionally used in the last years. They capture the processes in the

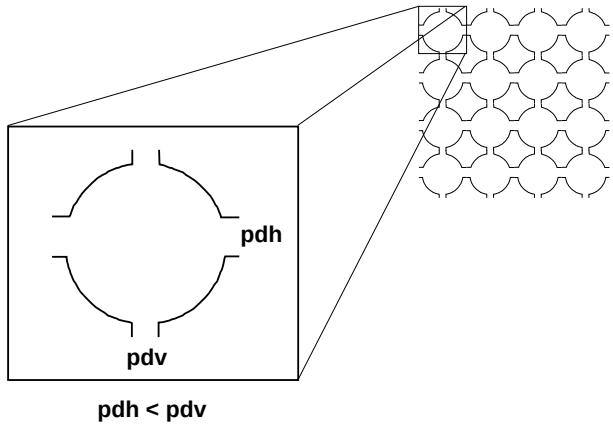

Figure 2.13: With an anisotropic distribution of pore throats, we receive an anisotropic capillary pressure - saturation relationship.

pore space directly or via geostatistical realisations and lead to new results. Jakobs et al. (2003a) found out that layered porous media as resulting for example from sedimentation processes, lead to anisotropic capillary pressure–saturation relationships. This is a concept which can only hardly be captured since pressure as a scalar parameter can not show any anisotropic properties. In Figure 2.13, this effect of anisotropy is schematically presented. It can be seen that the pores are all identical, but the pore throats are anisotropic. Thus, for the entry pressure $p_{d\text{VERTICAL}} < p_{d\text{HORIZONTAL}}$ holds. All in all, such a behaviour leads to a capillary pressure–saturation relationship as given in Equation (2.51).

$$\Pi_{\mathbf{c}} = \begin{pmatrix} p_x(S_w) & 0 \\ 0 & p_z(S_w) \end{pmatrix} \tag{2.51}$$

For to get the scalar properties of the capillary pressure–saturation relationship, $\Pi_{\mathbf{c}}$ is still multiplied by the respective normed vectors. From there, we get for example

$$p_c = \mathbf{n}^T \Pi_{\mathbf{c}} \mathbf{n} \text{ with } \mathbf{n} = \frac{\nabla S_w}{|\nabla S_w|}.$$

The measuring results relevant for this work, for the properties of granite as well as for the inner structure, do not show anisotropic properties. For this reason, we can abstain from an implementation of this approach.

2.2.5 Relative Permeability - Saturation Relationship

As described in Section 2.2.2, the intrinsic permeability $\mathbf{K}$ (dimension of m^2) is the characteristic parameter of a porous medium.

If, however, the pore space is occupied by several fluid phases, they influence each other in their flow behaviour. This means, that the effective permeability $K_{e\alpha}$ for phase

α is significantly smaller than the intrinsic permeability of the porous medium. In order to model this effect, the intrinsic permeability is mulitplied by the relative permeability.

$$K_e = k_{r\alpha} K$$

The relative permeability was considered to be merely a scalar parameter in previous approaches. In these approaches, its value is dependent on the saturation of the respective phase. The boundary conditions for these approaches are $k_{r\alpha}(S_\alpha = 0) = 0$ and $k_{r\alpha}(S_\alpha = 1) = 1$. The first condition can even be intensified: the relative permeability for the residual saturation of a phase has to be equal to zero: $k_{r\alpha}(S_\alpha = S_{\alpha r}) = 0$. Between these values $k_{r\alpha}(S_\alpha = S_{\alpha r}) = 0$ and $k_{r\alpha}(S_\alpha = 1) = 1$ the relative permeability - saturation is strictly monotonously increasing.

The evaluation of the exact shape of the relative permeability–saturation relationship is done either purely empiricly in first approaches or quasi analytically from simplified pore network models, respectively capillary tube models according to the approaches of Burdine (1953) or Mualem (1976), from the capillary pressure–saturation relationships of Brooks and Corey (1964) or van Genuchten (1980). A good representation of these and further approaches can be found in Sheta (1999). Here, the effects of hysteresis on the relative permeability–saturation relationships are further discussed. These are, similarly to the capillary pressure–saturation relationships caused by the fact that saturation is no sufficient description of the occupation of the pore space by the phases.

The BC relative permeability–saturation relationships resulting from the BC capillary pressure–saturation relationships are:

$$k_{rw} = S_e^{\frac{2+3\lambda}{\lambda}} \tag{2.52}$$

$$k_{rn} = (1 - S_e)^2 \left(1 - S_e^{\frac{2+\lambda}{\lambda}}\right) \tag{2.53}$$

According to the VG approach, we get:

$$k_{rw} = \sqrt{S_e}\left[1 - \left(1 - S_e^{1/m}\right)^m\right]^2 \tag{2.54}$$

$$k_{rn} = (1 - S_e)^{\frac{1}{3}}\left[1 - S_e^{1/m}\right]^{2m}. \tag{2.55}$$

In Figure 2.14 the relative permeability–saturation relationships based on BC and VG are plotted in dependence of S_w. The differences result from the different capillary pressure–saturation relationships.

The relative permeability–saturation relationships were also derived on the local scale taking newer approaches from pore network models from the micro-scale to the local scale. There exist numerous approaches (Hilpert et al., 1998, Fischer and Celia, 1999, Hazlett, 1997, Hilpert and Miller, 2000, Jakobs et al., 2003a). Besides, relative permeability–saturation relationships were also derived from the local scale to the

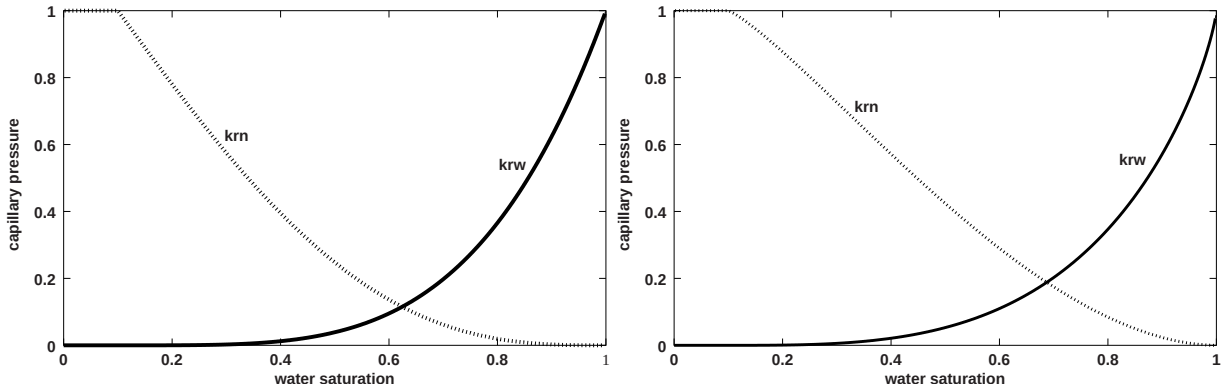

Figure 2.14: Relative permeability–saturation relationship after Brooks-Corey (left hand side) and Van Genuchten (right hand side)

meso-scale. Here, an REV continuum model is used which directly captures the heterogeneities. Based on this model, a new continuum model with an REV on the meso-scale is set up. Ataie-Ashtiani et al. (2002) and Braun et al. (2002) proceeded in this way.

The relationships derived from the micro scale to the local scale as well as from the local scale to the meso scale are highly anisotropic in most of the above-mentioned works. Figure 2.15 shows a system where the non-wetting phase is present as residual saturation. The anisotropy of the relative permeability–saturation relationship results from the anisotropic distribution of pore throats. From the entry pressure, which is lower in horizontal direction, we receive the horizontal spreading of the non-wetting phase and from that the strong decrease of effective permeability for the wetting phase in vertical direction.

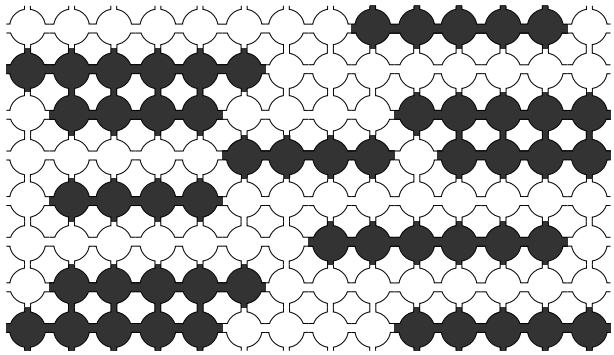

Figure 2.15: From an anisotropic distribution of pore throats, we get an anisotropic capillary pressure–saturation relationship.

For non-isothermal processes it can happen that for the usual approaches the relative permeability of the gas phase with high steam ratio is underestimated. The steam can

condense at the pore water and deliver its enthalpy of evaporation to the pore water. Downstream in the region of lower pressure, evaporation processes can occur again. Due to this process, the relative permeability for steam should be assumed to be significantly higher. Therefore, approaches of Verma (1986) can be taken.

2.2.6 Transition Condition for Two-Phase Flow at Heterogeneities

With the definition of the relative permeability–saturation relationship, we can now transfer Darcy's law to the extended Darcy's law:

$$\boldsymbol{v}_\alpha = -\frac{k_{r\alpha}}{\mu_\alpha} K \cdot (\nabla p_\alpha - \rho_\alpha \mathbf{g}) \tag{2.56}$$

In Section 2.2.4, we have set $p_n = p_w + p_c(S_w)$. Thus, we can define the following velocities for the wetting and the non-wetting phase:

$$\boldsymbol{v}_w = -\frac{k_{rw}}{\mu_w} K \cdot (\nabla p_w - \rho_w \mathbf{g}) \tag{2.57}$$

$$\boldsymbol{v}_n = -\frac{k_{rn}}{\mu_n} K \cdot (\nabla (p_w + p_c(S_w)) - \rho_n \mathbf{g}) \tag{2.58}$$

The decisive question for the modelling of gas migration in fractured porous media is the question if the gas can enter from the fracture into the matrix. This question is of special significance if we represent the fractures as hyper-planes—as lines in the 2D space or as planes in the 3D space. As the flow perpendicular to the fracture cannot be represented in this case, the fracture matrix transition has to be treated separately. The question which we have to pose here is: which conditions have to apply that the non-wetting phase will enter from the high-permeable fracture into the low-permeable rock matrix.

To simplify this problem, we assume a system consisting of water and DNAPL instead of a gas–water system. (DNAPL is short for "dense non-aquous phase liquid" i.e. for a non-wetting fluid phase which is denser than water). The advantages of DNAPL–water systems compared to gas–water systems are the following:

- ▷ The processes can be visualized more easily.
- ▷ The numerical computations converge better as the viscosity difference for DNAPL–water systems is much lower than for gas–water systems.

The effects relevant for us are the same for both systems. We will profit of the advantages of a DNAPL–water system in Section 2.4.

We will determine the effects of heterogeneities on the phase saturations using an example, in which DNAPL is infiltrating a fully water-saturated system. This system consists of a fine-sand lense embedded into ambient coarse sand, see Figure 2.16.

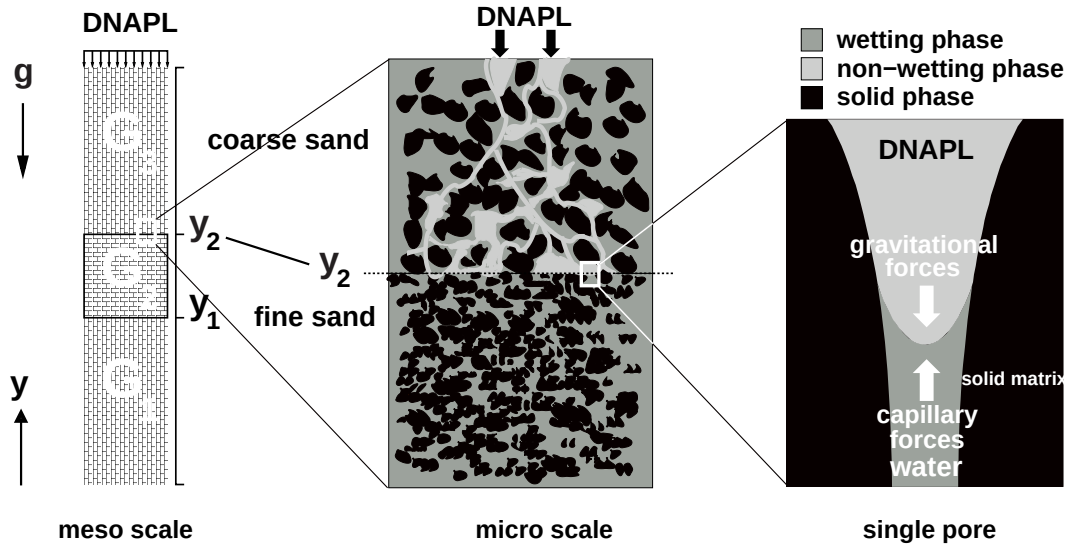

Figure 2.16: Schematic column experiment with fine sand lense, the interfacial region around y_2 is enlarged, and here again the largest pore of the fine sand.

We subdivide the domain of the column into three subdomains G_1, G_2, G_3 with the interfacial lines y_1 and y_2. For the coarse sand domains G_1 and G_3 we use the parameters:

$$\Phi^{G_3}, K^{G_3}, k^{G_3}_{r,we}, k^{G_3}_{r,nw}, p_c^{G_3},$$

and for the fine sand domain G_2 respectively:

$$\Phi^{G_2}, K^{G_2}, k^{G_2}_{r,we}, k^{G_2}_{r,nw}, p_c^{G_2}.$$

We now consider the saturation S_w and the capillary pressure p_c

via y_2 $(\lim_{y \to y_2 + 0} S_w, p_c)$ and
via y_2 $(\lim_{y \to y_2 - 0} S_w, p_c)$,

and we consider only the point of time at which the DNAPL reaches the fine sand lense, i.e. y_2. In Figure 2.16, a cut-out around y_2 is schematically displayed at the micro-scale. It is apparent that the entering of DNAPL into the fine sand is dominated by two forces:

- ▷ the buoyancy forces which are caused by density differences of the fluids, and
- ▷ the capillary forces wich result from the different adhesion forces of the fluids with respect to the rock phase.

Given by the equations (2.57) and (2.58), the entering of the non-wetting phase into the highly permeable domain is governed by the capillary pressure–saturation relationships of the lowly permeable domain and the highly permeable domain.

First we consider the VG capillary pressure–saturation relationships. I.e. that we assume especially $p_c(S_w = 1) = 0$. Looking again at the definition of DNAPL velocity according to the extended Darcy's law (2.56):

$$\boldsymbol{v}_n = -\frac{k_{rn}}{\mu_n} K \cdot (\nabla p_w + \nabla p_c - \rho_n \boldsymbol{g}) \tag{2.59}$$

We see that for no value of y a jump of capillary pressure may occur as otherwise $\nabla p_c(y)$ cannot be defined. It follows, that the flux also cannot be defined. To solve the balance equations for the domain, the capillary equilibrium condition has to hold for the interfacial areas:

$$\lim_{y \to y_2 + 0} p_c(y) = \lim_{y \to y_2 - 0} p_c(y). \tag{2.60}$$

However, we have different capillary pressure–saturation relationships for G_3 and G_2 as can be taken from Figure 2.17. As a jump in capillary pressure is forbidden, a jump in saturation results at the interfacial area y_2.

We can thus define $\lim_{y \to y_2 - 0} S_w$ via the inverse capillary pressure–saturation function of the domain G_2 $Inv_{p_c}^{G_2}(p_c)$:

$$\lim_{y \to y_2 - 0} S_w = Inv_{p_c}^{G_2}(p_c^{G_3}(\lim_{y \to y_2 + 0} S_w)). \tag{2.61}$$

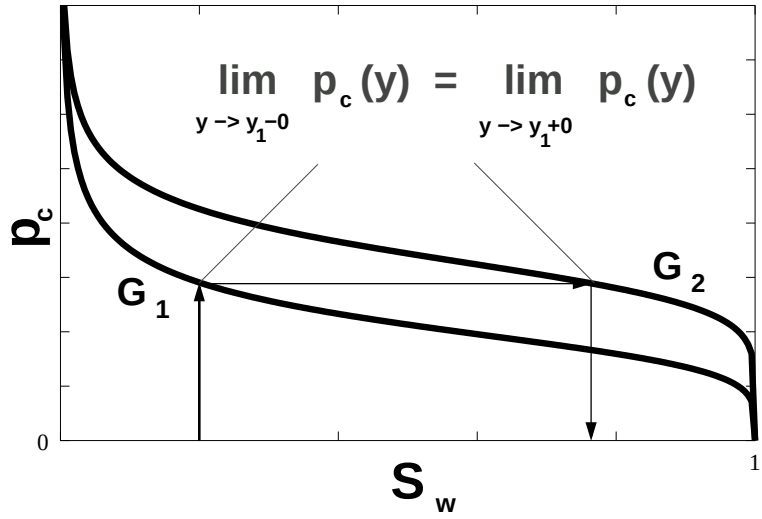

Figure 2.17: Capillary equilibrium condition for capillary pressure—saturation relationships without taking into account the entry pressure.

We now consider the BC capillary pressure–saturation relationships, i.e. functions with $p_c(S_w = 1) = p_e > 0$. As we assume finer sand for G_2, $p_e^{G_3} < p_e^{G_2}$ is valid. For the initially fully water-saturated initial state of the system considered here, we cannot

describe the gradient of the capillary pressure at the interfacial faces y_2 and y_1. This follows for y_2 from $\lim_{y\to y_2+0} p_c(y) < \lim_{y\to y_2-0} p_c(y)$. As however, $\lim_{y\to y_2-0} S_w = 1$ follows from $\lim_{y\to y_2+0} p_c < p_e^{G_2}$, we get $\lambda_n(y_2) = 0$ and from equation (2.56) $v_n = 0$.

From there the extended capillary equilibrium condition as defined by van Duijn et al. (1995) results. Following the notation in this work, we define the critical saturation S_w^* as the saturation which has to be reached within G_3 to reach the entry pressure in G_3. This is made clear in Figure 2.18: $p_c^{G_3}(S_w) = p_e^{G_2}$.

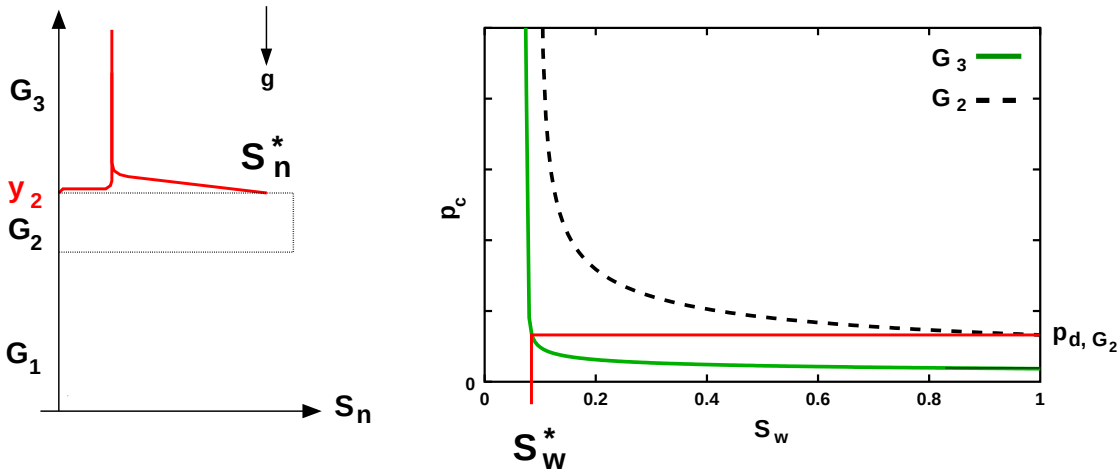

Figure 2.18: Definition of the critical saturation for capillary pressure—saturation relationships taking into account the entry pressure.

Thus, we get for $\lim_{y\to y_2+0} S_w > S_w^*$ and $\lim_{y\to y_2-0} S_w = 1$, for $\lim_{y\to y_2+0} S_w \leq S_w^*$ the indxcapillary equilibrium condition is to be applied (2.61).

Accordingly, we have to make sure for gas–water processes in fractured porous media that the extended capillary pressure condition is fulfilled.

We can now give an answer to the question which sort of capillary pressure–saturation relationship describes the two-phase behaviour at the interface between media with different permeabilities in a better way. In Figure 2.19, we see again the single pore already displayed in Figure 2.16. The DNAPL pools up above this pore, and does not enter as the contact angle is still too high and thus the capillary pressure still too small. Only when the capillary pressure for the coarser sand is reached, the DNAPL can enter the fine sand lense. This concept can only be represented for BC capillary pressure–saturation relationships. Therefore, we will not deal with VG capillary pressure–saturation relationships in this work. However, we always have to keep in mind, that taking the BC capillary pressure–saturation relationships the potential for $S_w = 1$ cannot adequately be described for the total system. This is due to the fact, that the considered system does not assign a certain capillary pressure p_d for $S_w = 1$ but a capillary pressure between 0 and p_d.

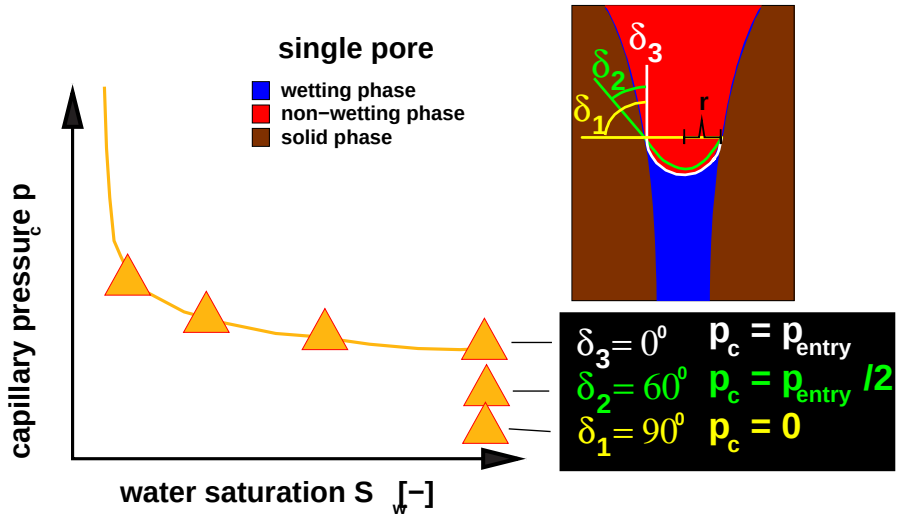

Figure 2.19: Consideration of the contact angle of a single pore from figure 2.16.

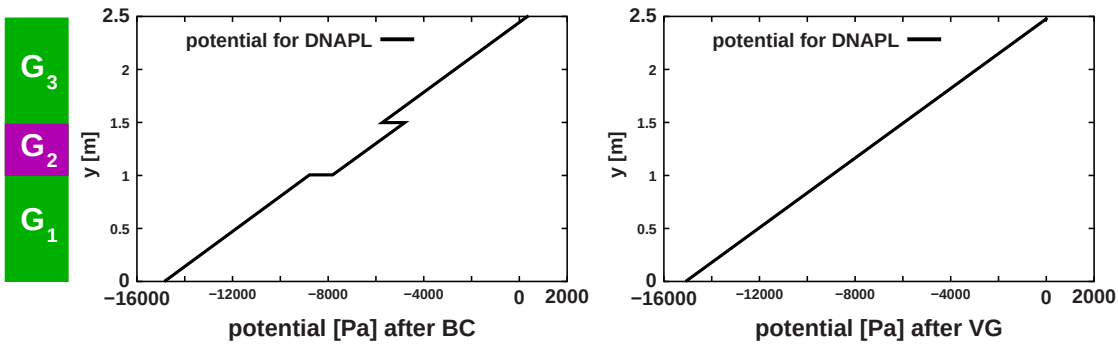

Figure 2.20: Potential for $S_w = 1$ of the system of figure 2.16 under the assumption of BC and VG capillary pressure–saturation relationships.

2.2.7 Dispersion

Dispersion is a macro-scale property which results on the REV scale from sub-REV heterogeneities. The velocity differences which result from the permeability distribution and the tortuosity, contribute much more to the mixing of a phase than the diffusion coefficient. Scheidegger (1961) assumes the mechanical dispersion to be proportional to the average flow velocity. The concentration equalization takes place according to the Fickian law also in this case, with J as the dispersive flux, D as dispersion coefficient and C as concentration of a component of the respective phase.

$$J_D = -D\nabla C \tag{2.62}$$

Important approaches for the upscaling of dispersion parameters are given in Dagan (1989) and in Gelhar (1993). A fundamental description of this approach is presented e.g. in Cirpka (2001).

In case of existence of two phases the tortuosity of the flow paths gets larger for each of the two phases. Using an approach for the dispersion coefficient in a multi-phase system, the dispersion coefficient has to depend additionally on the saturations. The dispersion coefficient is decreasing for increasing phase saturations until at a saturation of one it is equal to the dispersion coefficient coming from the derived dispersion coefficient.

As the phase composition in the model considered here is mainly dependent on the pressure and the temperature distribution, we abstain from an implementation of these approaches. It is however easily possible to replace the dispersion coefficient used is this work by a dispersion coefficient depending on pressure, temperature and saturation.

2.2.8 Thermal Conductivity of the Porous Medium

Thermal conductivity is a material property. For the averaging process, we formulate an equivalent thermal conductivity which results from the volume fractions of the rock phase, the water phase and the gas phase:

$$\lambda_{pm} = \phi \cdot (\lambda_w \phi S_w + \lambda_g \phi S_g) + (1 - \phi) \cdot \lambda_s \tag{2.63}$$

Here, the thermal conductivity of the rock phase has the highest value. The thermal conductivity of the gas phase, on the other hand is so small that it can be neglected. For $S_w = 0$ the transition of thermal energy by thermal conduction takes only place via the connected rock matrix. For a fracture–matrix system, the energy transfer takes mainly place via the rock matrix. This is even valid for filled fractures, as the mostly loose filling material does not have the same thermal conductivity as the rock matrix averaged over an REV.

For increasing S_w, the small pore spaces will first be filled by water. Thus, the faces relevant for energy transfer increase fast. For low water saturations, the average thermal conductivity of a porous medium is accordingly increasing particularly fast.

An air-filled open fracture thus acts as a good isolator which inhibits the transfer of thermal energy via the rock matrix. We cannot represent this effect with our model as the flux is not evaluated perpendicular to the main fracture direction.

For a low-dimensional approach, it is hardly possible to assign another temperature to the fractures than that of the surrounding rock matrix. For the thermal conduction, the gradient of the temperature is needed. For the low-dimensional approach, different temperatures for the same node are needed if the node belongs at the same time to the matrix as well as to the fracture element. Therefore, the temperature gradient cannot be given without problems. To model the isolation of fracture systems, we have to evaluate the energy flux perpendicular to the fracture orientation accordingly. As this is not the aim of our work, we abstain from this.

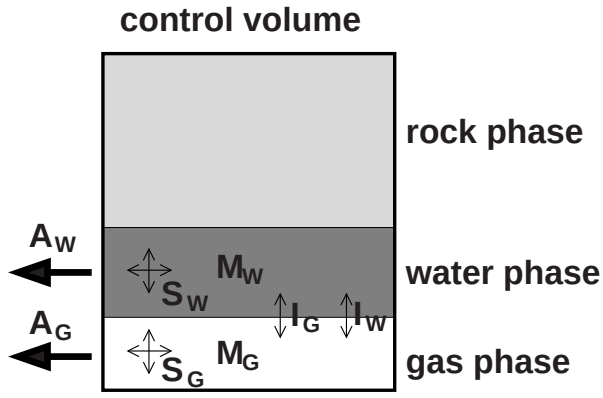

Figure 2.21: Control volume

2.3 General Form of the Balance Equation

Unlike in the deduction of the Navier-Stokes equations where the conservation equations for mass and momentum are set up (see e.g. Jischa (1982)), we consider only the mass balance equations for the phases, respectively the components. There, we will then insert the extended Darcy law as a simplified form of the momentum equation.

A fundamental form of the deduction of the conservation equations for multiphase–multicomponent processes in porous media was first done by Hassanizadeh and Gray (1979b) and further developed in Hassanizadeh and Gray (1980), Hassanizadeh and Gray (1990), Hassanizadeh and Gray (1993), Hassanizadeh and Gray (1997). Here, not only mass, momentum, and energy were balanced, but also entropy. Moreover, not only control volumina are considered, but the balance is also done over the interfacial areas between the single phases, the interfacial lines between three or more phases and the interfacial points between four and more phases. Even though these equations are very helpful for the understanding of multi-phase systems, the resulting equation system turned out to be too complex and the parameters needed were too numerous for simulation models. This could change in the future when the resulting equation system of Hassanizadeh and Gray (1979a) and Hassanizadeh and Gray (1979b) will have been analyzed with respect to the importance of the individual terms.

Figure 2.21 shows a control volume with a gas phase a solid phase and a liquid phase. For the set-up of the mass balance, we consider the change of the mass contained within the system over time. This mass change is denoted by M. It is composed of the transport of the mass out of the system A and the mass sources S within the system. Considering several phases or components, mass can be exchanged. This term is denoted by I_α or I_κ, depending on whether we consider a multiphase system or a multicomponent system. As for the total system no mass change occurs, it is always $\sum_\alpha I_\alpha = 0$, respectively $\sum_\kappa I_\kappa = 0$.

2.3.1 Balance Equations for Multiphase Systems

From the assumptions of the previous section, we get the following general form of the balance equations for phases with infinitesimally small time steps and an infinitesimally small control volume:

$$M_\alpha + A_\alpha - I_\alpha - S_\alpha = 0 \tag{2.64}$$

with

M_α as storage term for the mass of phase α

A_α as inflow term over the boundary of the control volume

I_α as exchange term between the phases

S_α as source and sink term for other inflow/ outflow within the control area

The storage term M_α results from the integral over the control volume over the density ρ_α of phase α multiplied by the volume fraction $\Phi_\alpha = \Phi S_\alpha$ which the phase occupies in the pore space:

$$M_\alpha : \frac{\partial}{\partial t} \int_\Omega \phi_\alpha \rho_\alpha d\Omega \tag{2.65}$$

For the flux term A_α we integrate the inflows over the boundary. For multiphase processes, we only consider the advective flux. This yields:

$$A_\alpha : \int_n (\phi \rho_\alpha \boldsymbol{v}_\alpha) d\Gamma \tag{2.66}$$

Using the Gauss integral theorem

$$\int_\Omega \nabla f d\Omega = \int_\Gamma f \boldsymbol{n} d\Gamma \tag{2.67}$$

we get from (2.66)

$$\int_\Omega \nabla(\phi \rho_\alpha \boldsymbol{v}_\alpha) d\Omega. \tag{2.68}$$

The exchange term is not relevant here, as we do not assume any exchange between the phases for multiphase models:

$$I_\alpha : \int_\Omega i_\alpha d\Omega = 0. \tag{2.69}$$

The storage term is given as follows:

$$S_\alpha : \int_\Omega q_\alpha d\Omega. \tag{2.70}$$

Inserting the terms (2.65), (2.68), (2.69) and (2.70) into equation (2.64) gives:

$$\frac{\partial}{\partial t}\int_\Omega \phi_\alpha \rho_\alpha d\Omega + \int_\Omega \nabla(\phi \rho_\alpha \boldsymbol{v}_\alpha) d\Omega - \int_\Omega q_\alpha d\Omega = 0. \tag{2.71}$$

In differential form, equation (2.71) with $\phi_\alpha = \phi S_\alpha$ reads:

$$\frac{\partial(\phi S_\alpha \rho_\alpha)}{\partial t} + \nabla(\phi \rho_\alpha \boldsymbol{v}_\alpha) - q_\alpha = 0 \tag{2.72}$$

The extended Darcy law for multiphase flow processes is

$$\boldsymbol{v}_\alpha = -\frac{k_{r\alpha}}{\phi \mu_\alpha} K_i (\nabla p_\alpha - \rho_\alpha \mathbf{g}). \tag{2.73}$$

Inserting equation (2.73) into equation (2.72) results in:

$$\frac{\partial(\phi S_\alpha \rho_\alpha)}{\partial t} - \nabla\left(\rho_\alpha \frac{\mathbf{k}_{r\alpha}}{\mu_\alpha} K(\nabla p_\alpha - \rho_\alpha \mathbf{g})\right) - q_\alpha = 0. \tag{2.74}$$

For the water phase and the gas phase we get with the additional constraints $p_g = p_w + p_c$ and $S_g + S_w = 1$:

$$-\phi \rho_w \frac{\partial S_g}{\partial t} - \nabla \cdot \left(\frac{\rho_w \mathbf{k}_{rw}}{\mu_w} \mathbf{K}_i (\nabla p_w - \rho_w \mathbf{g})\right) - q_w = 0 \tag{2.75}$$

$$\phi \frac{\partial(\rho_g S_g)}{\partial t} - \nabla \cdot \left(\frac{\rho_g \mathbf{k}_{rg}}{\mu_g} \mathbf{K}_i (\nabla p_w + \nabla p_c - \rho_g \mathbf{g})\right) - q_n = 0\,. \tag{2.76}$$

2.3.2 Balance Equations for Components

The definition of the terms of Section 2.3.1 can be transferred to the terms treated in the following. Thus, the general balance equation for the components within the system reads:

$$M_\kappa + A_\kappa - I_\kappa - S_\kappa = 0 \tag{2.77}$$

The occupation of the terms is done according to the same principles as for the phases. We also integrate over the control volume for the terms M_κ, I_κ and S_κ. For the computation of the flux term A_κ we integrate over the boundary of the control volume and transfer the boundary integral to a volume integral using the Gauss integral theorem (2.67). Afterwards we can choose a differential intead of an integral consideration. Accordingly, we will abstain from the exact represenation of the procedure in the following and directly give the differential representation.

For the balance of the components, we can balance on the one hand over the components in the respective phases. Thus, we get four balance equations for two phases and two components. On the other hand, we can balance over the total mass of a component. In the first case, we have to consider the exchange terms which we do not have to do in the second case. Therefore, we choose the second procedure and can thus set I_κ to zero. Instead of balancing over mass, we balance over molar mass.

The remaining terms are:

$$M_\kappa: \quad \frac{\partial \sum_\alpha \rho_{mol\alpha} x_\alpha^\kappa S_\alpha}{\partial t} \tag{2.78}$$

$$A_\kappa: \quad \sum_\alpha \nabla(\phi \rho_\alpha^{mol} x_\alpha^\kappa \boldsymbol{v}_\alpha + D_{pm}^\kappa \rho_{mol,\alpha} \nabla x_\alpha^\kappa \tag{2.79}$$

$$S_\kappa: \quad q_\kappa. \tag{2.80}$$

With the extended Darcy law as defined in the previous chapter, we then obtain:

$$\begin{aligned} &\phi \frac{\partial(\sum_\alpha \rho_{mol,\alpha} x_\alpha^K S_\alpha)}{\partial t} \\ &-\sum_\alpha \nabla \cdot \left\{ \frac{k_{r\alpha}}{\mu_\alpha} \rho_{mol,\alpha} x_\alpha^K \mathbf{K}(\nabla p_\alpha - \rho_{mass,\alpha} \mathbf{g}) \right\} \\ &-\nabla \cdot \left\{ D_{pm}^K \rho_{mol,g} \nabla x_g^K \right\} \\ &-q^K = 0 \qquad K \in \{w,a,c\},\ \alpha \in \{w,n,g\}. \end{aligned} \tag{2.81}$$

2.3.3 Balance Equations for Energy

For the energy balance, we integrate over all phases. The balancing over the single phases is certainly possible, but it would be too demanding to be realized. Especially, the question how to set $I_{e\alpha}$ would arise. The exchange takes place via the interfaces which can be very different depending on the pore space occupation. The main argument against a balance of energy for the single phases is, however, that the process of thermal conduction plays a dominant role for very slow flow. It is thus adequate to assume the same temperature within a control volume for all phases. We can thus set I_e to zero. The general form of the energy balance is thus:

$$M_e + A_e - S_e = 0 \tag{2.82}$$

It is balanced over the internal energy. The storage term thus takes into account the

specific internal energy multiplied by the mass density of the respective phases.

$$M_e : \frac{\sum_\alpha \partial(u_\alpha \rho_\alpha)}{\partial t} \tag{2.83}$$

For the deduction of the flux term it is to be taken into account, that besides the thermal energy u, work for a volume change p/ρ can also be transported into the system. Additionally, energy can get into the system via thermal conduction and thermal radiation where thermal radiation can be neglected for our model. In summary we get:

$$A_e : \nabla(\sum_\alpha (\underbrace{\rho u_\alpha \mathbf{q}_\alpha}_{1} + \underbrace{p \mathbf{q}_\alpha}_{2}) - \underbrace{\lambda \nabla \Gamma}_{3}) \tag{2.84}$$

1: Inflow of thermal energy as a transported quantity
2: Inflow of work for a volume change
3: Inflow of thermal energy via thermal conduction.

With the definition of the specific enthalpy $h = u + \frac{p}{\rho}$ we get:

$$A_e : \nabla(\sum_\alpha \rho h \mathbf{q}_\alpha - \lambda \nabla \Gamma). \tag{2.85}$$

The flux over the boundary of the control volume results from the extended Darcy law and the diffusive flux:

$$\mathbf{q}_\alpha = \frac{k_{r\alpha}}{\mu_\alpha} \rho K \nabla p - \rho g - \sum_\kappa D^\kappa \rho \nabla x_\alpha^\kappa. \tag{2.86}$$

With $\rho_{mass,\kappa} = M^\kappa \rho_{mol,\kappa}$ we thus have

$$\begin{aligned}
&\phi \frac{\partial \left(\sum_\alpha \rho_{mass,\alpha} u_\alpha S_\alpha\right)}{\partial t} + (1-\phi) \frac{\partial \rho_s c_s T}{\partial t} \\
&-\nabla \cdot (\lambda_{pm} \nabla T) \\
&-\sum_\alpha \nabla \cdot \left\{ \frac{k_{r\alpha}}{\mu_\alpha} \rho_{mass,\alpha} h_\alpha \mathbf{K} (\nabla p_\alpha - \rho_{mass,\alpha} \mathbf{g}) \right\} \\
&-\sum_K \nabla \cdot \left\{ D_{pm}^K \rho_{mol,g} h_g^K M^K \nabla x_g^K \right\} \\
&-q^h = 0 \qquad K \in \{w,a,c\},\ \alpha \in \{w,n,g\}.
\end{aligned} \tag{2.87}$$

2.4 Scales and Forces

The properties of fractured porous media are heterogeneous over a large range of scales. For this reason, the flow processes of the fluids and the transport processes of the components are quite complex. We have to distinguish between the influences of the heterogeneities which lie above the REV (super-REV heterogeneities) and the heterogeneities lying below the REV (sub-REV heterogeneities).

While the super-REV heterogeneities are directly captured by the geometric model, the influence of sub-REV heterogeneities can only be evaluated with difficulties. A method which seems appropriate is dimensional analysis. With the help of this analysis, we can estimate the dependent dominant forces on each scale. Of course, dimensional analysis does not provide the same possibilities as an exact mathematical model which takes into account the forces on the respective scale—in this case the micro scale. However, it can bring important understanding about the ratio of forces as a function of the respective scale of the considered system.

We apply dimensional analysis here as derived by Hilfer and Oren (1996). There, the effective forces on the fluids were estimated in analyzing the two-phase flow equations (2.75). The forces resulting from this analysis, are the viscous force, the buoyancy force and the capillary force. The respective dimensionless characteristic numbers can be summarized as follows:

$$\text{capillary number} \quad Ca := \frac{\text{viscous force}}{\text{capillary force}} = \frac{\mu \cdot v \cdot L}{K \cdot p_c^*} \tag{2.88}$$

$$\text{Bond number} \quad Bo := \frac{\text{viscous force}}{\text{buoyancy force}} = \frac{\mu \cdot v}{\Delta\rho \cdot g \cdot K} \tag{2.89}$$

$$\text{gravillary number} \quad Gl := \frac{\text{buoyancy force}}{\text{capillary force}} = \frac{\Delta\rho \cdot g \cdot L}{p_c^*}. \tag{2.90}$$

The characteristic numbers show that the effectivity of the forces is dependent on three sorts of parameters:

1. Parameters which describe fluid properties, such as density ρ and the dynamic viscosity μ.

2. Parameters depending on the solid phase, like the intrinsic permeability K.

3. Parameters which describe the interaction between the solid phases and the fluid phases, such as the characteristic capillary pressure p_c^* and a characteristic flow velocity v which is correlated to the effective permeability.

4. A characteristic length L.

2.4.1 Registration of the Forces in an Experiment under Well-defined Conditions

Speaking of "characteristic" capillary pressures, velocities and lengths might cause doubts about the effectiveness of dimensional analysis as a tool for the estimation of forces in a two-fluid-phase system in porous media. To be able to apply dimensional analysis on the two-phase flow process in the nearfield of a repository, we will first control the correctness of its results for an experiment under controlled, well-defined conditions.

In the following, we will present results of an experiment on the meso-scale in a heterogeneous porous medium which was carried out in the VEGAS research facility at the Institute of Hydraulic Engineering, University of Stuttgart. This experiment is explained in more detail by Braun (1996). Figure 2.22 shows the setup of an experiment. The steel reservoir used has a length of 7 m, a height of 3 m, and a depth of 1 m. It has a glass plate in order to make the visualization of the results possible. On the left and the right hand side, the container is equipped with water reservoirs which extend over the whole height and depth of the container. In between, we have the aquifer of 6.35 m. The water reservoir was kept at a constant water level. A water gradient of 1%, from left to right was adjusted.

The dimensions of the heterogeneous system in the container—the actual aquifer—are 6.35 [m] (length) $\times$ 2,4 [m] (height) $\times$ 0,4 [m] (depth). The aquifer consists of coarse sand, middle sand and fine sand. These sand sorts were filled into the exactly defined regions as can be seen in Figure 2.22. They were filled in layers of about 5 cm, moistured and compressed. The main structures of this heterogeneous packing consist of four fine sand lenses, three of which increase with a gradient of 1%, 5% and 10% from left to right and a horizontal layer of middle sand which is confined on the right and the left by vertical fine sand blocks. After saturating the aquifer with water, a basic flow with partially degassed water was established, so that the air entrapped in the aquifer could be solved in the water. Only after that, the infiltration of TCE was started.

According to the definitions of Section 1, this experiment takes place on the meso-scale: The experimental system is sufficiently large to average over micro-scale phenomena and to consider the porous medium as a continuum, however, it is not sufficiently large to average over the fine sand lenses and to consider the system as a double continuum and to resolve the appearing system processes adequately. The parameters for the sands used in this experiment are given in Table 2.1. The properties of the coarse sand with respect to multi-phase flow were measured for a water–TCE system, the properties of the middle and the fine sand for a water–air system. The Brooks-Corey parameters p_d for middle and fine sand are scaled according to Parker et al. (1987) and transferred to a water–TCE system.

The Brooks-Corey parameter λ was received by manual fittung to measured data coming from a sample. Therefore, the so-called controlled outflow cell technique was applied which was described, for example, by Lorentz et al. (1992). In later investigations, however, measurement data were compared, on the one hand side those which were received by the controlled outflow cell technique and those where the

relatively new, so-called gamma radiation system technique—presented for example by Färber and Betz (1995)—was used. These comparisons are already presented in this work in Section 2.2.4. They point out that the controlled outflow cell technique leads to a systematic error in the measurement data. These errors affect besides the already presented error in the capillary pressure–saturation relationship at $S_w = 1$ also the systematic overestimation of λ. With respect to an evaluation of this error, further research would be desirable. For the accuracy needed for dimensional analysis, this error, however, does not play a role.

The confidence intervall of the measurements for *one* sample of each sand type are given in Table 2.2. The results for the hydraulic conductivity and the intrinsic permeability vary between -50% and $+100\%$ of the average for different samples of the respective sand. For the residual saturation of water, no confidence interval can be given. The residual saturation for the non-wetting phase for the drainage process was assumed to be zero; for imbibition, hysteresis effects also have to be taken into account (see Parker and Lenhard (1987), Lenhard et al. (1988), Lenhard and Parker (1989)). Table 2.3 shows the fluid properties. The parameters for water were taken from (IFC, 1967). For TCE, the producer data for 20°C were assumed (see also Häffner product data base). The confidence interval for the measurements is comparatively small ($< 1\%$) and the ambient temperature of the system was kept at 20°C. TCE was coloured with a hydrophob and fluorescing colour in order to visualize the flow behaviour and the residual saturation of TCE.

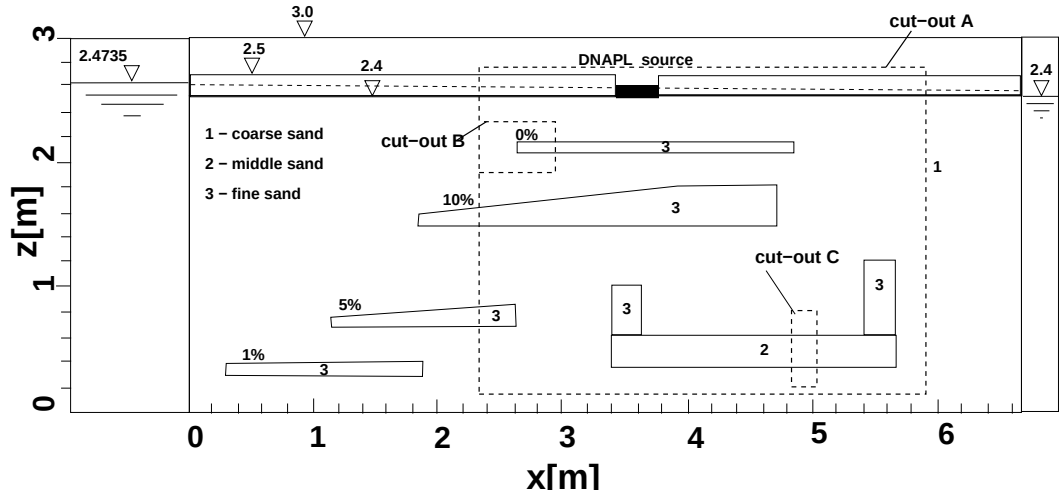

Figure 2.22: Experimental setup of the VEGAS experiment on the meso-scale

The distribution of TCE resulting from the TCE infiltration of a fully water-saturated system was investigated. TCE was infiltrated with a rate of $175[\mathrm{kg/h}] \pm 15\%$ from a region of a length of 0.3 m in the center of the upper side over a time span of 1.5 hours. After that, the TCE spread for another 2 hours and 45 minutes. The flux of water through the system from left to right decreased almost linearly from 210 liters per hour up to

	p_d [Pa]	λ [-]	S_{wr} [-]	K[m^2]	ϕ [-]
Coarse sand (1)	200.0	2.0	0.05	4.6 E-10	0.39
Middle sand (2)	700.0	2.3	0.15	3.1 E-11	0.35
Fine sand (3)	1800.0	3.5	0.18	9.0E-12	0.43

Table 2.1: Parameters of the sands for the VEGAS experiment

	p_d [Pa]	ϕ [-]
Coarse sand (1)	$\pm$10%	$\pm$7%
Middle sand (2)	$\pm$10%	$\pm$10%
Fine sand (3)	$\pm$10%	$\pm$2%

Table 2.2: Confidence intervals for the entry pressure and the porosity of the sands described in Table 2.1

		water	TCE
density, ρ	[kg/m^3]	1000.0	1460.0
dynamic viscosity, μ	[Pa s]	1E-3	5.8E-4

Table 2.3: Fluid parameters for water and TCE

160 liters per hour. After the end of the infiltration, the flux of water increased during the first half of an hour up to 180 l per hour and remained constant from this time on. The results for the TCE saturation are visually observed and measured using the time–domain reflectometry based on the techniques published by Dasberg and Dalton (1985) and Roth et al. (1990). A more detailled analysis of the experiment and appropriate simulations can be found in the work of Sheta (1999).

The final TCE distribution is shown for cut-out A of the total system in Figure 2.23 and for cut-out B in Figure 2.24. The cut-outs are defined in Figure 2.22. Several phenomena can be clearly observed:

- ▷ due to the density difference, the TCE is distributing in vertical direction (Figure 2.23);
- ▷ the residual saturation of TCE gets clear by the relatively equally distributed TCE in Figure 2.23(A)
- ▷ the effect of entry pressure as described in Section 2.2.4 also gets apparent when considering the relatively high TCE saturations above the fine sand lenses. In Figure 2.24 you can see the pooling up of the TCE; in Figure 2.23(B) one can observe how it enters the middle sand lense.

These phenomena result from the following factors:

- ▷ As the TCE is not flowing any more, the capillary force, buoyancy and the viscous force have to be in equilibrium.
- ▷ The large horizontal spreading of TCE allows to conclude that capillarity in the coarse sand is highly variable. This follows from the variability of the pore morphology, i.e. the sub-REV heterogeneities in the coarse sand.
- ▷ The entry pressure of the fine sand lenses in the system is not reached, the entry pressure of the middle pressure in any case.

These experimental results show that the DNAPL migration is not only influenced by block heterogeneities—the super-REV heterogeneities—but especially by the variable properties within the coarse sand which we assume as being homogeneous—the sub-REV heterogeneities. These results are important for decontamination techniques, as described for example by Class (2001). The TCE forms morphologically stable regions above the fine sand lenses as well as in the regions of residual saturation which can only be decaded under high difficulties resulting from the limitations of mass transfer. In the context of this work, however, it is interesting how far dimensional analysis are an appropriate means for the estimation of the forces occuring in the experiment.

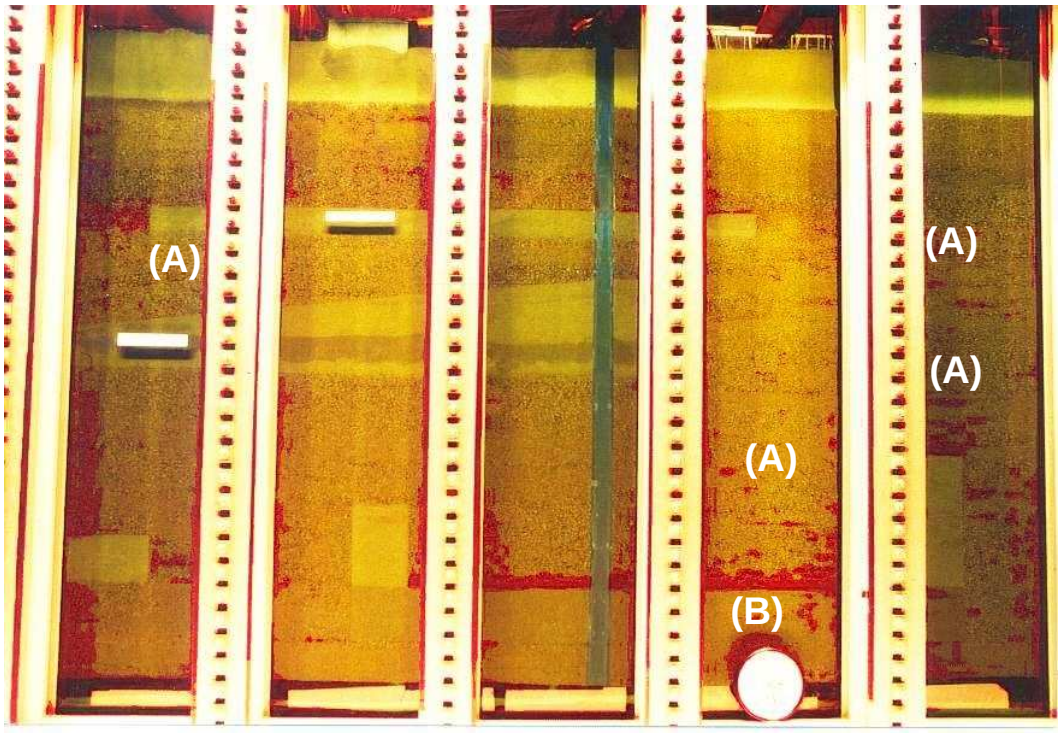

Figure 2.23: TCE distribution for cut-out A (dark grey indicates TCE)

For viscosity and density differences, we take those of a water–TCE system, i.e. we assume the viscosity to be $\mu = 0.001[Pa \cdot s]$, and the density difference as $\Delta\rho =$

Figure 2.24: TCE distribution for cut-out B (dark grey indicates TCE)

460 [kg / m^3]. For the coarse sand, we take the values for the entry pressure and the intrinsic permeability from Table 2.1. We approximate the flow velocity of water in assuming the measured flux as $q_{begin} = 210[l/h]$, $q_{min} = 160[l/h]$ and $q_{end} = 180[l/h]$. Thus, it results $v_{begin} = 6.1E-5[m/s]$, $v_{min} = 4.6E-5[m/s]$ and $v_{end} = 5.2E-5[m/s]$. (The subscripts $begin$, min, and end indicate the begin of the infiltration ($begin$), the end of the infiltration (min)—at this time the flux of water reaches a minimum—and the end of the experiment (end)). Here, we neglect the effects of the lenses on the flow as they only have a subordinate role on the intrinsic permeability besides the high confidence interval: From the hydraulic gradient from left to right and the intrinsic permeability of the coarse sand, we can estimate a flow velocity of water of $v_w = 4.6E-5[m/s]$ ($-50\%, +100\%$). The good agreement between the flow rate on the one hand and the velocity derived from intrinsic permeability and hydraulic gradient on the other hand, shows that the confidence interval for the intrinsic permeability can be taken as being much smaller and the influence on the fine sand lenses can be neglected.

For the time presented in Figures 2.23 and 2.24—i.e. about 2 hours and 45 minutes after the end of the DNAPL infiltration into the system—the flow velocity for the TCE system is effectively zero, $v_n = 0$. For the vertical direction, we can neglect the forces resulting from the water flow. For $v_n = 0$ the capillary forces have to be in equilibrium with the buoyancy forces, i.e. the gravillary number has to be equal to one. This re-

sults in a characteristic length for the coarse sand of $L_{vertical} = 0.044[m]$ $(-10\%, +12\%)$, taking into account the confidence interval of p_d and a confidence interval of 1% for the density difference. Anton and Hilfer (1999) use the length of the NAPL blob as a characteristic length for their dimensional analysis. Thus, it can be seen that the length derived above from the parameters coincides exactly with the length of the TCE blob within the coarse sand (ca. 0.4 [m], see also Figure 2.23(A)). We judge this as a strong sign for the correctness of the dimensional analysis.

Let us consider the forces which act in the horizontal direction: the viscous forces and the capillary forces. As we cannot assume an equilibrium, we take the length of the TCE blob as characteristic length (about 0.15 to 0.2 [m]). Thus, we receive capillary numbers between 0.08 and 0.11, i.e. the capillary force is dominating the viscous force by a factor of ≈ 10. Indeed, we can see from Figure 2.23, that migration of TCE is hardly influenced by the water flow from left to right. The DNAPL spreads almost regularly from the center into the left and the right direction. In this case, the results of the dimensional analysis are also approved.

From the dimensional analysis, one can conclude that the viscous forces have to increase by a factor of 10 in order that the capillary forces are in equilibrium with the viscous forces. For this reason, only for a gradient of 10% of the water potential, parts of the TCE would be carried out of the system. After Anton and Hilfer (1999), the length of the TCE blob will decrease if the viscous forces dominate the capillary forces. Anton and Hilfer (1999) observed a complete discharge of NAPL only for capillary numbers from 10^2 (sphere packing, continuous NAPL) up to 10^5 (sand stone, continuous NAPL), for a discontinuous NAPL phase in a sphere packing $Ca > 10^3$. This would correspond in our case to a gradient of the water potential of 10000%. Of course, we know that the assumptions on which this dimensional analysis is based is not valid for Reynold's numbers resulting from such a gradient. However, the results clearly indicate that a complete discharge of TCE by viscous forces is not practicable for a real case, i.e. by a pump and treat technique.

Figure 2.25 is a plot of the dimensionless numbers Ca, Bo, Gl as a function of the characteristic length L for the coarse sand used for the described VEGAS experiment. The equilibrium between the forces is reached when the respective characteristic number is equal to one. For $Ca < 1$ the capillary forces dominate the viscous forces, for $Ca > 1$ the viscous forces dominate the capillary forces. Analogous relationships hold for Bo and Gl. For small characteristic lengths, the capillary forces are larger, for large characteristic lengths the buoyancy forces are dominating. The importance of buoyancy and capillary forces can very well be derived from the experimental results.

The dimensional analysis cannot be applied to the effects of super-REV heterogeneities: as the dimensional analysis assumes spatial parameter functions which are sufficiently differentiable, effects of block heterogeneities are not taken into account as we have jumps of parameters at block heterogeneities.

The effects resulting from the block heterogeneities are captured by the dimensional analysis. We also made clear the effects of dimensional analysis resulting from the anisotropy of the pore distribution in the coarse sand. Thus, it can be stated, that the dimensional analysis is an adequate tool for the forces occurring in a two-phase sys-

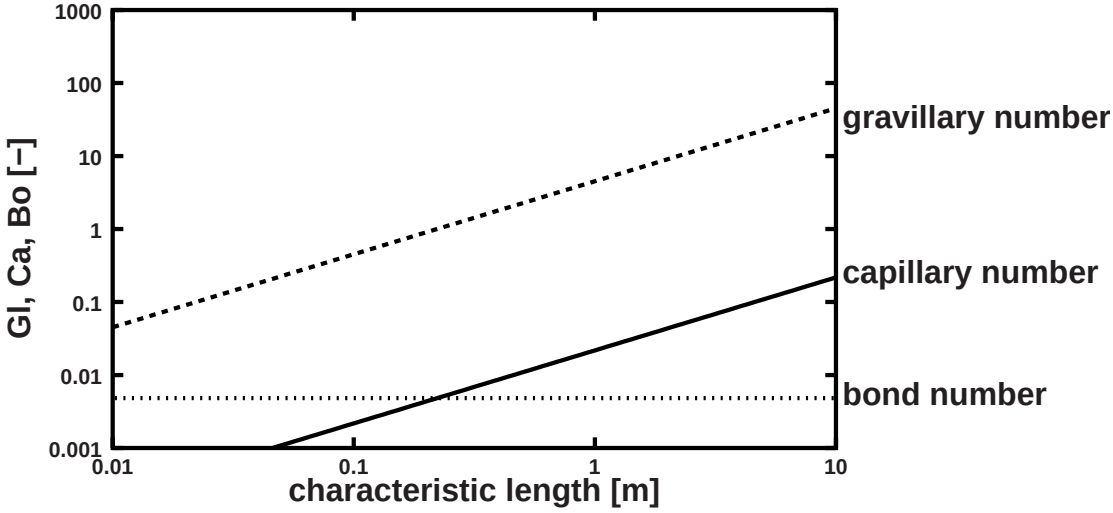

Figure 2.25: Dimensionless characteristic numbers as a function of the characteristic length for coarse sand according to Table 2.1, both axes in logarithmic scale according to Braun (2000)

tem.

3 Upscaling of a Single Fracture

3.1 Fields of Fracture Apertures: Underlying Data and Stochastic Generation

Measurements of the distributions of fracture apertures are expensive and involved. Additionally, we have the basic difficulties that the distributions of the fracture apertures change when taking a drilling core and that drilling cores only represent small regions. Thus, it is very difficult to get information about larger regions. Up to now, only few data sets were published which give all the relevant information on the distribution of the fracture aperture. These contain besides the histogram of the distribution of the fracture apertures—the non-interpreted measured values—also specifications on the measured spatial correlations of these points. Demny et al. (2000) give only an overview of the fitted functions. Jarsjö and Geller (1996) give histograms and fitted probability frequencies, however, their work does not contain any specifications on the spatial covariances. Only the data published by Keller (1997) contains specifications on the measured histogram of apertures as well as on the spatial correlation of the measured values. For this reason, two data sets were taken for this work: the data set of Keller (1997), respectively Keller et al. (1999) due to its completeness and the data set of Jarsjö and Geller (1996) as the degassing experiments were carried out with this data set. The spatial correlation for the data set of Jarsjö and Geller (1996) was estimated from Figure 3.12.

Measured distributions are rarely extensive enough for to make sure, that we are within the super-REV region and have thus already averaged over the sub-REV regions (see section 1). For this purpose, we generated fields using geostatistical methods which represent the properties of the measured distributions of fracture apertures as exactly as possible. Therefore, there exist two common possiblities:

1. The two fracture side walls are generated by fractal models where the values are correlated. Such models are used, for example, by Helmig (1993), Oron and Berkowitz (1998) and Isakov et al. (2001).

   From these models, we get functions of probability frequency for the apertures which ressemble Gaussian curves which are lopped at the top and at the bottom (see Figure 3.1(a)). However, it is difficult to adapt thus generated distributions of fracture apertures to measurements, as those programs need the fractal dimension, the frequency spectrum and the correlations of the boundary faces of the fractures as input parameters.

   From literature, however, we get the histogram, the geometric mean and the semivariogram of the distribution of fracture apertures.

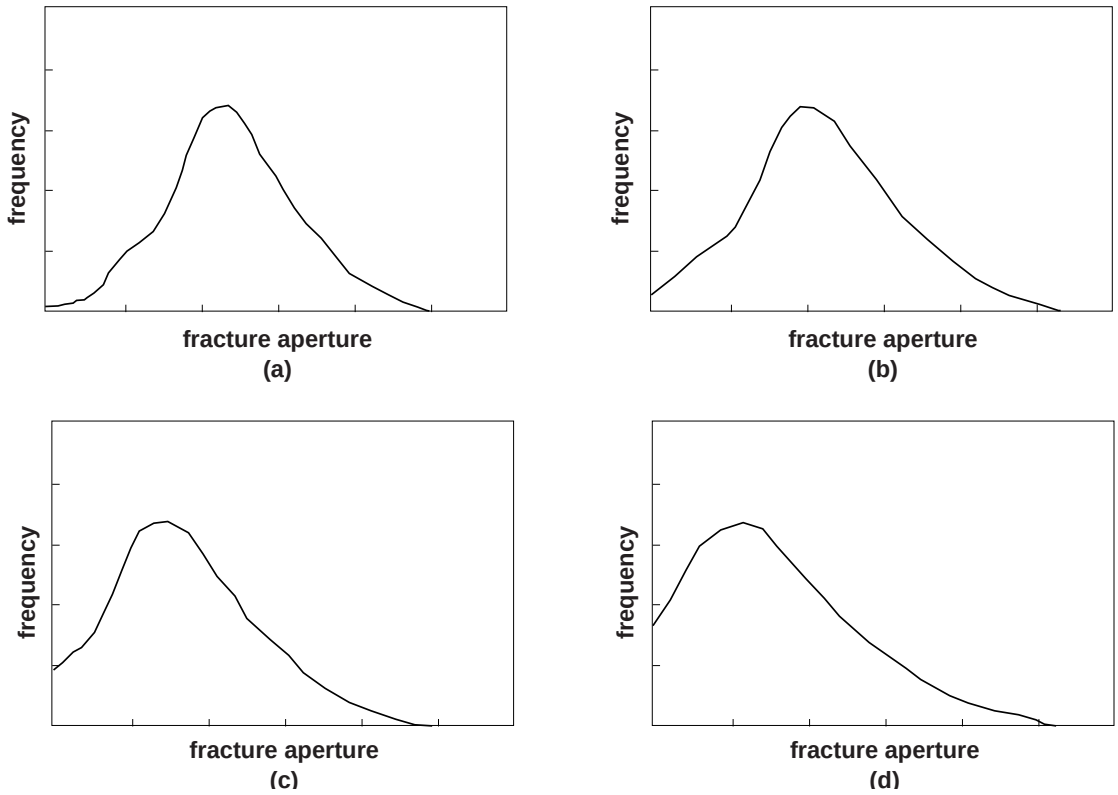

Figure 3.1: Distributions of the fracture apertures for lythostatic pressures increasing from (a) to (d), given by (Oron and Berkowitz, 1998)

2. With the help of geostatistical tools, we can generate distributions of apertures which correspond to the function of probability frequency derived from the histogram. Taking this data, we also get a problem: The histogram is bounded above, i.e. a maximum value exists. The logarithmic normal distributions as given as best adaption to the values of Keller (1997) and Jarsjö (1998) have, however, no upper bounds. The generation of fields leads to the fact that the more values are generated, the more values lie above this maximum measured value.

Oron and Berkowitz (1998) found out that the generation of the fracture walls by fractal methods is appropriate for this problem. They assume that the distribution of the fracture apertures corresponds to the curve of Figure 3.1(a). The asymmetry of many measured curves results according to their argumentation from the lythostatic pressure as shown in Figure 3.1. Oron and Berkowitz (1998) generate these effects in subtracting a fix number from the generated fracture apertures and then setting the negative values to zero. This procedure is made clear in Figure 3.1.

Indeed, their arguments have their advantages: in the case of high lythostatic pressure on the fractures, these are hydraulically inactive. We can suppose that in this case, the contact faces enclose in this case the open areas, so that there does not exist a flow

path through the fracture. Here, however, the elastic deformation of the fractures plays an important role, as presented by Wong et al. (1989).

Moreover, it is correct that filtered log-normal distributions overestimate the probability frequency for large fracture apertures. This can be seen from Figure 3.2.

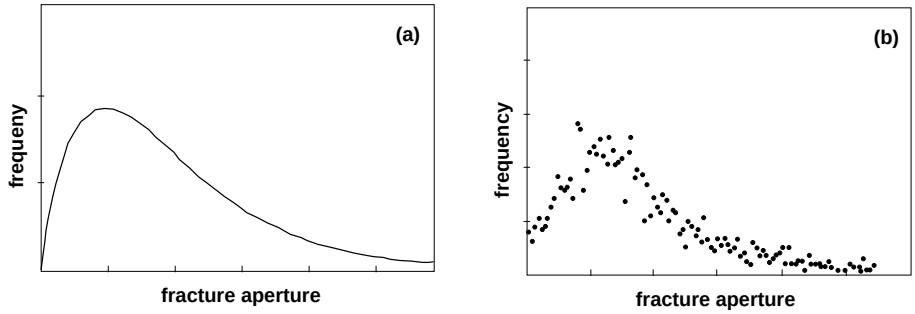

Figure 3.2: Fitted probability frequency – function and histogram given by Tsang and Tsang (1987)

However, taking a method as the one proposed by Oron and Berkowitz (1998) the probability frequencies for small fracture apertures are overestimated as can be taken from Figure 3.7.

All in all we have the problem, that by the use of fractal methods for the generation of the fracture walls and subsequent substraction the number of small fracture apertures is overestimated and that moreover, the literature values cannot be used. What is more, using geostatistical methods and distribution functions fitted to the measurements, we overestimate the high fracture apertures (with respect to the number as well as with respect to the maximum width). For this reason, we use transformation functions here, as described by Cirpka (2002) for to limit the function of probability frequency.

For the generation, an algorithm was modified which had been developed by Kitanidis (1997) and put into practice by Cirpka (2002) in MATLAB. The parameters for the generation of the fields of fracture apertures are presented in Table 3.1. As mentioned at the beginning, the parameters for the spatial covariance model for the distribution of fracture apertures according to Jarsjö and Geller (1996) had to be estimated as no data was published therefore. However, measured fields of fracture apertures make sure that we are dealing with an isotropic exponential covariance model. The nugget effect, however, can only be approximately estimated. The integral length lies at a high probability between 30 and 40 mm. Considering the already high uncertainty of the statistic relevance of measured fields of fracture apertures for by far larger fields of fracture apertures—as we will generate within this work—the uncertainties for the spatial covariance have, however, only a subordinate importance.

The recommendations of Oron and Berkowitz (1998) which we also presented in Section 2.2.3 can only be followed on the basis of the data of Jarsjö and Geller (1996). Here, the length of the raster elements of 4 mm does actually equal ten times the maximum apertures of 0.4 mm. Additionally, the raster element length is significantly below the

assumed integral length of 35 mm. For the fields of fracture apertures on the basis of the data of Keller (1997), we cannot stick to these recommendations, as the maximum fracture aperture of 5 mm and the integral length of 5.7 mm are close to one another. We decided to represent the topology of the fracture in more detail. For this reason, the length of the raster element is chosen smaller than the integral scale and the uncertainty with respect to the cubic law is accepted.

data given by	Keller (1997)	Jarsjö and Geller (1996)
length of raster element Δh	1 mm	4 mm
geometric mean μ_g	0.586 mm	0.087 mm
logarithmic variance	0.746496	0.7644
nugget	0	0.01[1]
integral length	5.7 mm	35 mm[1]
anisotropy	0	0[1]
covariance model	exponential	exponential[1]
max for tf1	5 mm	0.4 mm
max for tf2	15 mm	1.2 mm

Table 3.1: Parameters for stochastically generated distributions of fracture apertures on the basis of the data of Keller (1997) and Jarsjö and Geller (1996)

tf1	tf2
$\frac{e^x \cdot \log(\frac{max}{\mu_g}) - \log(\frac{max}{\mu_g})}{1-e^x}$	$\frac{x}{\frac{x+\lvert x\rvert}{2} + \log(\frac{max}{\mu_g})} \cdot \log(\frac{max}{\mu_g})$

Table 3.2: Transformation functions used for the stochastical generation of the fields of fracture apertures taken from Cirpka (2002)

In Figure 3.4 and 3.8 the transformation function

$$tf1(x) = \frac{e^x \cdot \log(\frac{max}{\mu_g}) - \log(\frac{max}{\mu_g})}{1 - e^x}$$

is presented. max was taken as the maximum of the measured fracture aperture.

Considering the function of probability frequency transformed by tf1 (Figures 3.4 and 3.8), we can see that the maximum probability frequency increases by more than 25 percent.

[1] These values were estimated

We obtain better results taking

$$\mathrm{tf2}(x) = \frac{x}{\frac{x+|x|}{2} + \log(\frac{\max}{\mu_g})} \cdot \log(\frac{\max}{\mu_g})$$

, as can be seen if Figures 3.5 and 3.9. max was taken as being three times the maximum of the measured fracture apertures. This value is purely heuristic. By an automated procedure which maps the maximum of the generated fracture aperture to the maximum of the measured fracture aperture, the probability frequency of large fracture apertures was highly underestimated.

In Figures 3.6 and 3.10, we can recognize the effect of the transformed functions of probability frequency. In the upper pictures, the distribution of fracture apertures on the basis of the non-modified function of probability frequency is illustrated. In the pictures in the center, fields of fracture apertures can be seen which were generated using the functions of probability frequency transformed by `tf1`. The lower pictures show the fields of fracture apertures which were generated by the functions of probability frequency transformed by `tf2`.

You can clearly see that the transformation smoothens the high fracture apertures sticking out like jags. Comparing the generated fields of fracture apertures to the measured field of fracture apertures, we realize that the fields of fracture apertures generated using `tf1` and `tf2` correspond much better to the measured ones than without using the transformation functions. We can also realize this in comparing the functions of probability frequency in Figures 3.3 through 3.5, and 3.7 through 3.9 with the histogram of Figure 3.3, respectively with the measured functions of probability frequency of Figure 3.7.

Fields of fracture apertures given by Keller (1997)

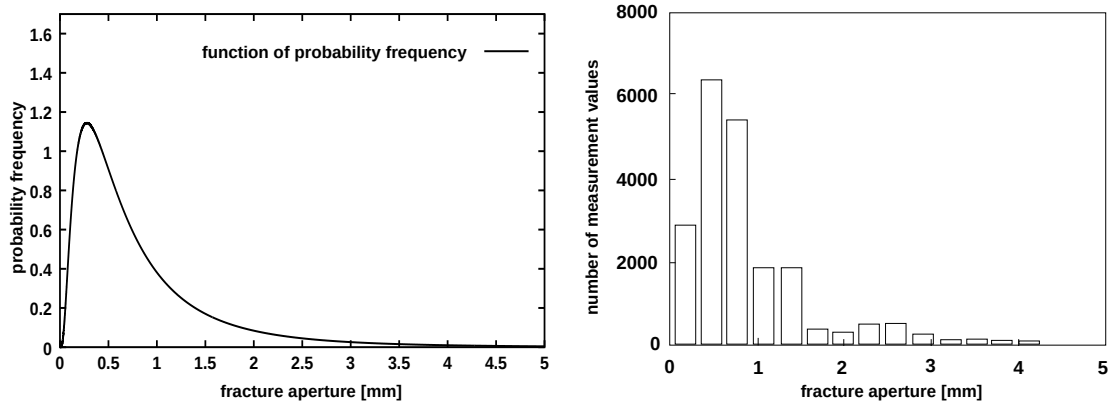

Figure 3.3: Function of probability frequency and histogram given by Keller (1997) with the geometric mean of 586 mm and a variance of 0.2444 mm

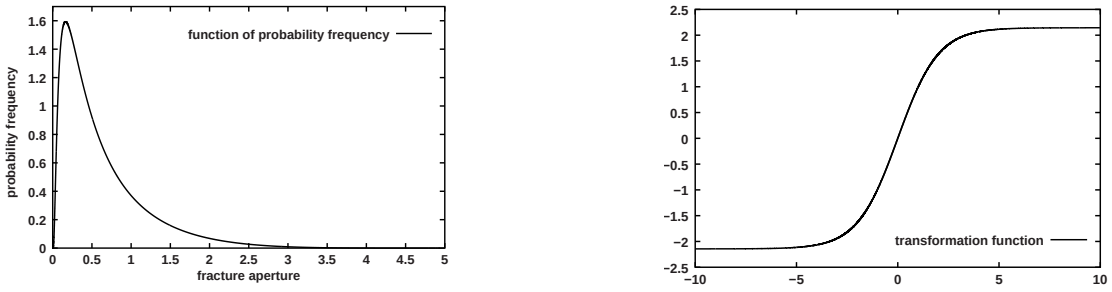

Figure 3.4: Transformed function of probability frequency with max = 5 mm

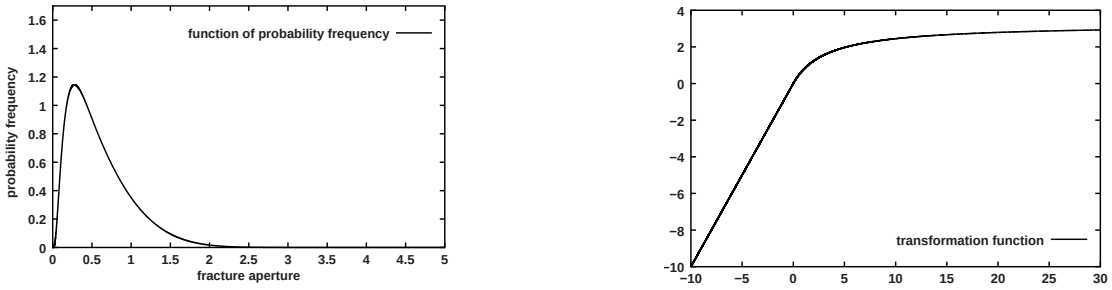

Figure 3.5: Transformed function of probability frequency with max = 15 mm

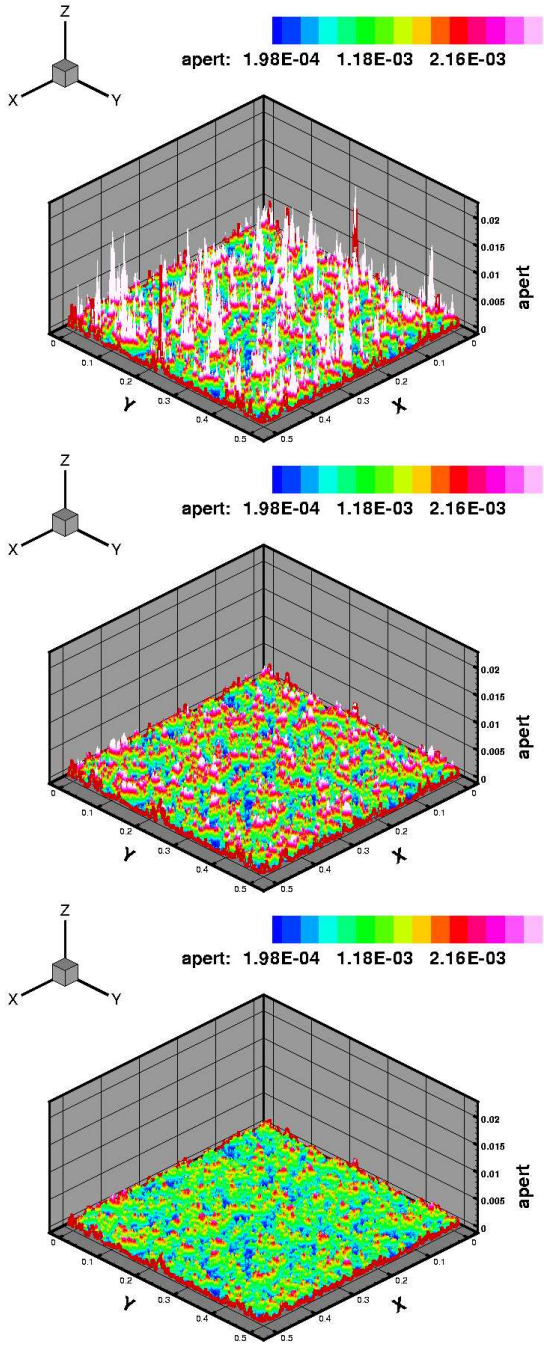

Figure 3.6: Generated fields of fracture apertures given by Figures 3.3 (top), 3.4 (center) and 3.5 (bottom)

Fields of fracture apertures given by Jarsjö and Geller (1996)

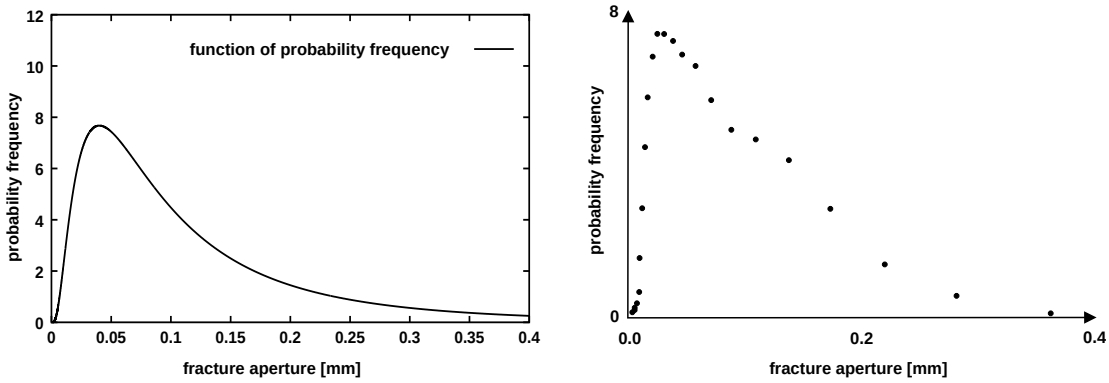

Figure 3.7: Function of probability frequency and histogram taken from Jarsjö and Geller (1996) with a geometric mean of 0.087 mm and a variance of 0.88 m^2

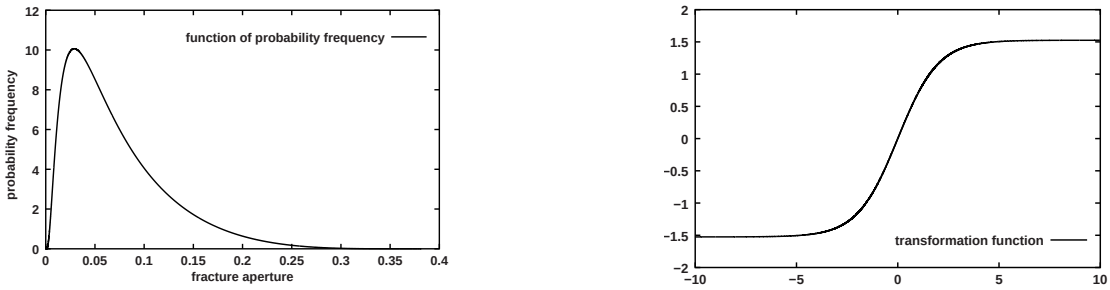

Figure 3.8: Transformed function of probability frequency with max = 0.4 mm

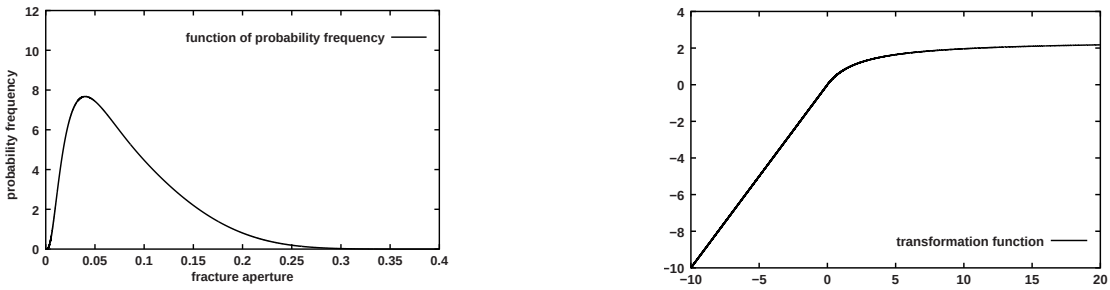

Figure 3.9: Transformed function of probability frequency with max = 1.2 mm

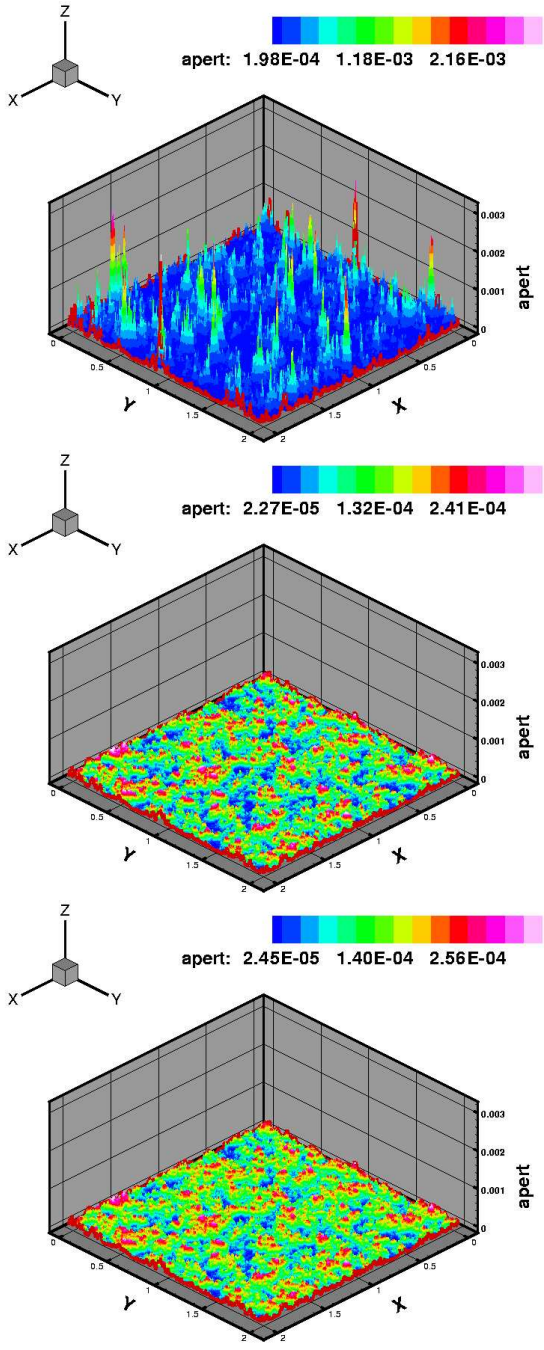

Figure 3.10: Generated fields of fracture apertures taken from Figures 3.7 (top), 3.8 (center) and 3.9 (bottom)

3.2 Model for the Description of the Degassing Process

The extent of a zone around a drilling hole, a shaft or a sheer zone, where degassing effects occur, is limited to the region where the water pressure p_w decreases down to a value below the bubble pressure p_b:

$$p_w < p_b. \tag{3.1}$$

Under the assumption of a thermodynamic equilibrium between the gas phase g and the liquid phase l and under the assumption that the mole fraction of the gas component in the liquid phase is very small, the following relationship holds:

$$\frac{n^a}{n^a + n^w} \approx \frac{n^a}{n^w}, \tag{3.2}$$

where p_g^a [Pa] is the partial pressure of component a, H^a [Pa] the Henry coefficient of component a, and x_l^a [–] the mole fraction of component a in the liquid phase l.

Evaluating experiments, the Henry law is often used in the form

$$p_g^a = \frac{C_l^a}{H^a}. \tag{3.3}$$

In this respect, H^a [$mol/Pa \cdot m^3$] is also called the Henry coefficient. C_l^a [$mol \cdot m^{-3}$] is the molar concentration of component a in the liquid phase l.

Let us first consider the state where there is no gas phase and the system is in equilibrium. For a molar concentration C_l^a, the degassing pressure results from $p_b = C_l^a / H^a$. When decreasing the water pressure p_w below the degassing pressure p_b, the reduction of the molar concentration of the desolved gas component results in

$$\Delta C_l^a = (p_b - p_w) \cdot H^a. \tag{3.4}$$

This reduction of the desolved gas is related to the respective gas volume of the degassed gas:

$$\Delta\theta_g = \frac{\Delta V_g}{V_l}, \tag{3.5}$$

where ΔV_g is the volume of the degassed gas, and V_l the volume of the liquid phase. The volume is averaged using the ideal gas law. Thus, we get

$$\Delta\theta_g = \Delta C_l^a \frac{R \cdot T}{p_w} = (p_b - p_w) \cdot H^a \frac{R \cdot T}{p_w} \tag{3.6}$$

with R [$N \cdot m \cdot K^{-1} \cdot mol^{-1}$] as the ideal gas constant and T [K] as temperature.

In the context considered here, we can assume a density of the liquid phase of $\rho_l = 1000\ kg \cdot m^{-3}$. This corresponds to ca. 55555 $mol \cdot m^{-3}$ with a molar mass of water of $18\ g \cdot mol^{-1}$ and neglecting the molar fraction of the gas component a. Accordingly, we can convert the molar concentration C_a into the mole fraction:

$$x_l^a = \frac{C^a}{55555\ [mol \cdot m^{-3}]} \tag{3.7}$$

experiment	θ_g [%]	molar concentration [mol/m^3]	mole fraction	degassing pressure p_b [Pa]
Äspö-3%a	0.032	34.2477	0.000616458	105221
Äspö-3%b	0.035	34.3703	0.000618666	105586
Äspö-7%	0.07	35.8009	0.000644416	109850
Äspö-15%	0.152	39.1525	0.000704746	119838

Table 3.3: Volume concentration θ_g, molar concentration, mole fraction and degassing pressure of the experiments described by Jarsjö and Geller (1996) for carbon dioxide (CO_2) as desolved gas

.

According to Jarsjö and Destouni (2000), the degassing pressure of the experiments described by Jarsjö and Geller (1996) is given as in Table 3.3.

We have now found an answer to the question which volume of gas degasses in case of a decrease of pressure or an increase of temperature. However, there still remains the question in which form this takes place and what happens with the gas afterwards.

As can be observed when opening a bottle of mineral water and as it is also described in the work of Jarsjö and Geller (1996), gas bubbles form at crystallization points, i.e. at the interface of a solid phase. How many gas bubbles are formed and of which size is dependent on numerous factors, for example on the sort of the crystallization points, on the type of the system state and on the sort of the gas used.

As there do not exist any investigations on the relationship between crystallization points and degassing processes in fractures, this effect cannot be taken into account by a model. For a horizontal position of the fracture, we assume that the gas bubbles move upwards where they are hold at the upper wall by their proper roughness. They unify with other gas bubbles to larger gas bubbles until the gas bubble is in contact with both fracture walls. Then the capillary forces act on this newly formed large gas bubble, so that it migrates in the direction of the gradient of fracture aperture. This process is schematically illustrated in Figure 3.11. A detailed investigation of the spreading of gas due to degassing is carried through in the work of Gale (1999) with the help of experiments. On the one hand, the case is investigated where the gas bubbles block the large fracture apertures. On the other hand, they are dealing with the case that the gas bubbles first migrate through the large fracture apertures and then are retained by the smaller ones. The work of Gale (1999) does not give a unique result.

In case of a vertical fracture the so-formed gas bubble will migrate upwards through the fracture until the fracture gets that thin that the gas bubble touches both fracture walls. If the capillary forces for such a case are larger than the buoyancyforces ($|\nabla p_c| > |(\rho_w - \rho_g) \cdot g|$, the gas bubble gets entrapped. It will then unify with other gas bubbles and move dependent on the capillary and buoyancy forces in the direction of the gradient of the fracture apertures.

The result of these considerations is that the gas will migrate in the largest fracture

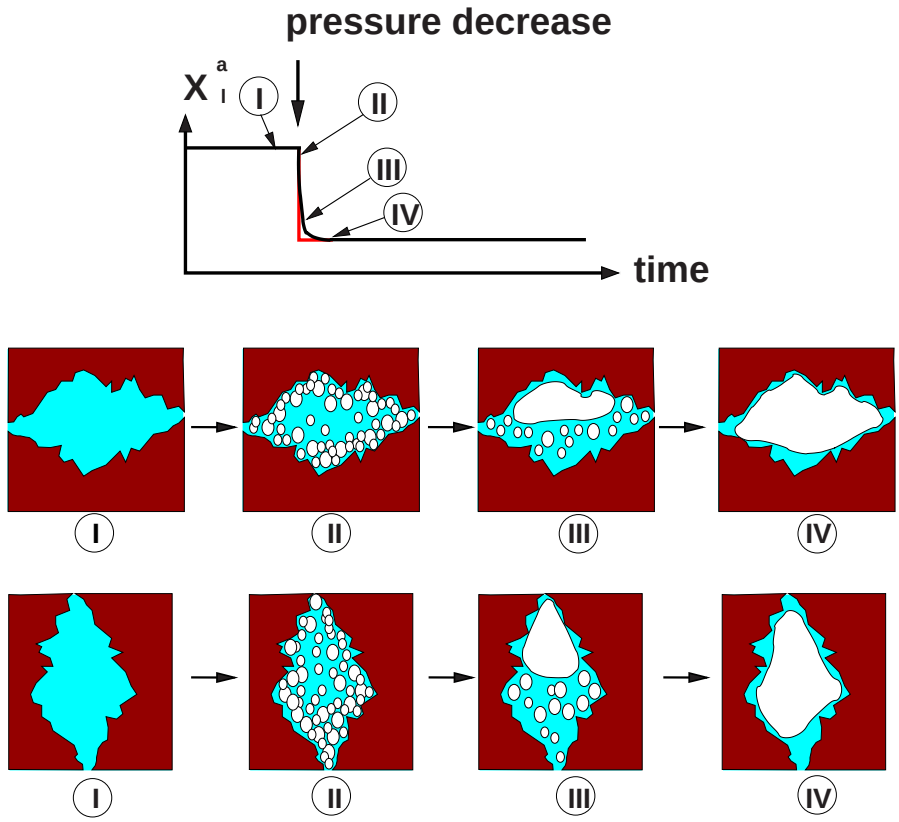

Figure 3.11: Schematic illustration of the degassing process

apertures if capillary forces dominate. According to the considerations of Section 2.4, we can assume dominant capillary forces.

Under the assumption of mechanical quasi-equilibrium, we can assume that the degassed gas occupies the large fracture apertures. For horizontal fractures, however, this is only valid if the gas bubbles are not larger than the smallest fracture apertures as otherwise the capillary forces cannot act.

This model is approved by the experiments of Jarsjö and Geller (1996): in Figures 3.13 and 3.14, we see the degassing process for an initial CO_2 concentration of 7 percent for the epoxide replica of a single fracture whose distribution of fracture apertures is illustrated in Figure 3.12. In Figure 3.16, we see the degassing process for an initial CO_2 concentration of 15 percent for the epoxide replica of a single fracture whose distribution of fracture apertures is illustrated in Figure 3.15. The displayed drilling cores have a diameter of 25 centimeters. Here, darker grey denotes larger fracture apertures. In this experiment, Jarsjö and Geller (1996) directed gas-saturated with CO_2 under overpressure into the fracture replica. The degassing process proceeded under isothermal conditions down to atmospheric pressure due to the pressure decrease. We can clearly see that during the degassing process, the large fracture openings fill with gas. More-

over, we can see from the figures that the capillary forces dominate the gas spreading more and more in the course of the degassing process. We attribute this effect to the already described process that first larger gas bubbles touch both fracture walls and are then influenced by capillary forces.

From these facts, we can derive the following questions:

1. Can we transfer the experimentally observed process, that gas accumulates in the largest fracture apertures, also to larger fracture faces?

2. Is this phenomenon also valid for non-horizontal fractures?

To give an answer to the first question, we have to look at the degassing process for different realisations with different sizes of the faces.

To give an answer to the second question, we use dimensionless characteristic numbers for the estimation of the forces, as explained in Section 2.4.

Therefore, we first construct a model on the micro-scale, which represents the experimentally observed effect that in a degassing process the degassed gas accumulates in the largest fracture apertures. This can be done using a percolation model. Moreover, it has to be investigated, by which extent the properties found out for a micro-scale model, can be transferred to the REV scale. Therefore, we will present a renormalization approach.

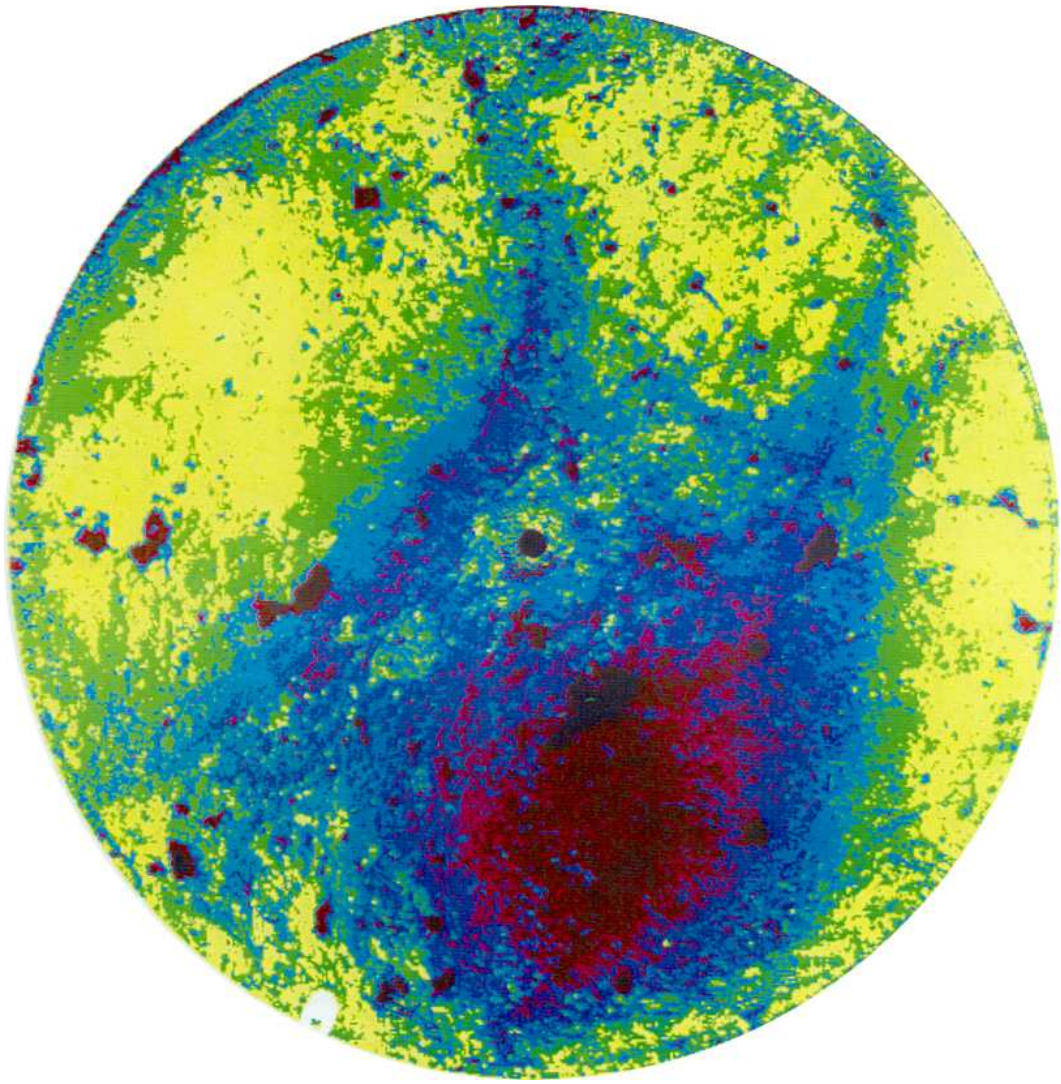

Figure 3.12: Distribution of fracture opening width of drilling core 1 taken from Jarsjö and Geller (1996).

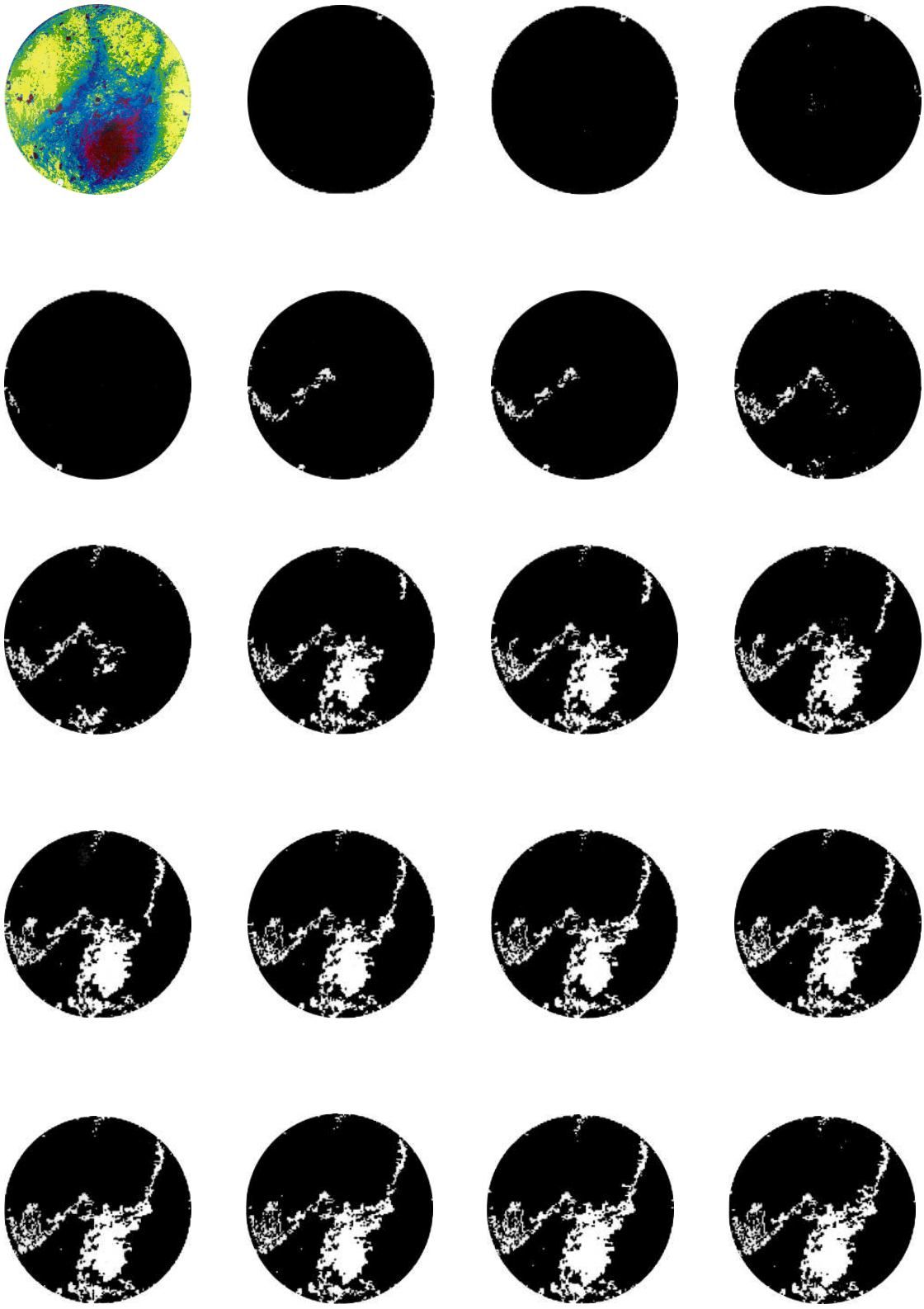

Figure 3.13: Temporal course of the degassing process with an intial CO_2 concentration of 7 percent taken from Jarsjö and Geller (1996) (drilling core 1) (a)

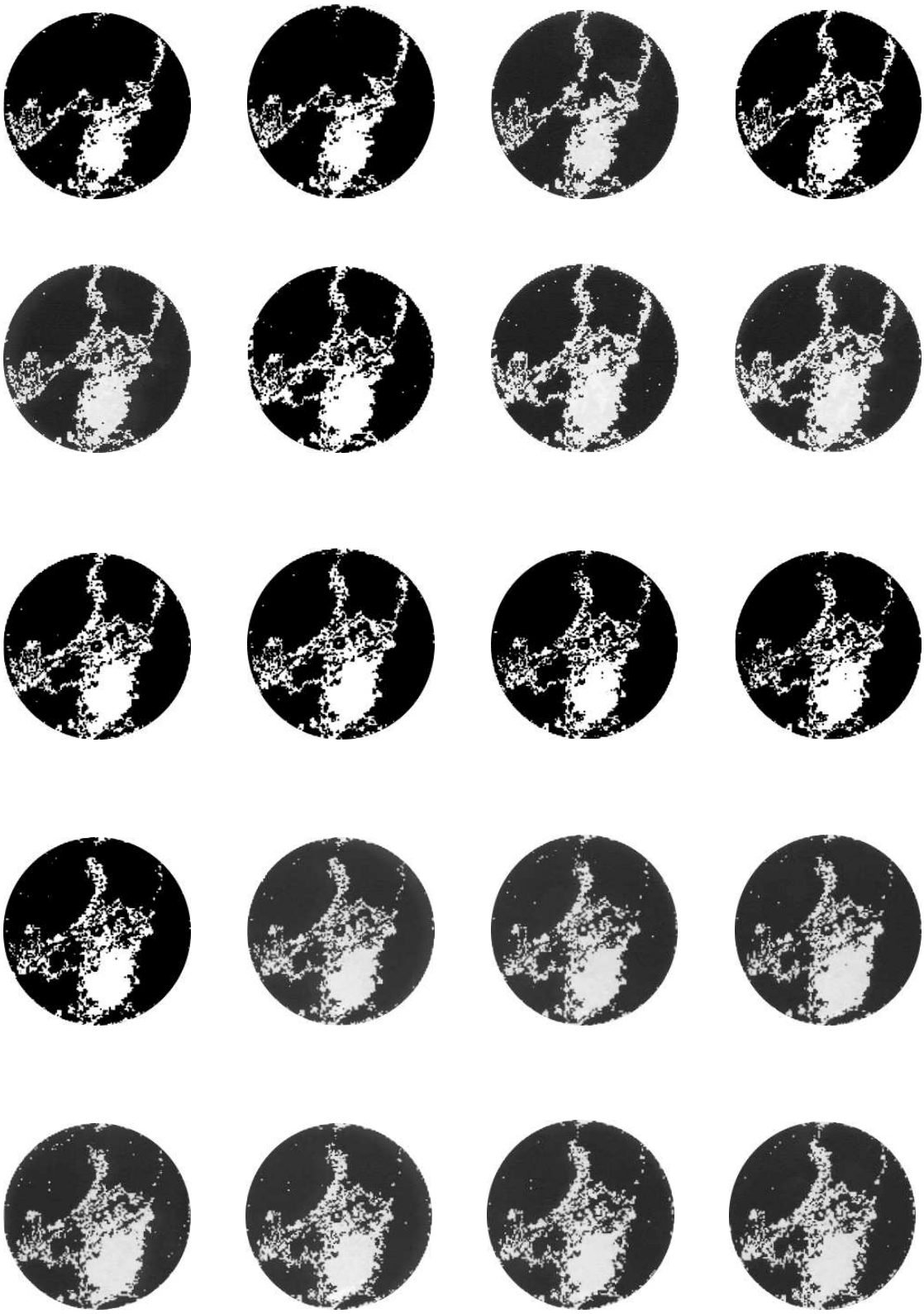

Figure 3.14: Temporal course of the degassing process with an intial CO_2 concentration of 7 percent taken from Jarsjö and Geller (1996) (drilling core 1) (b)

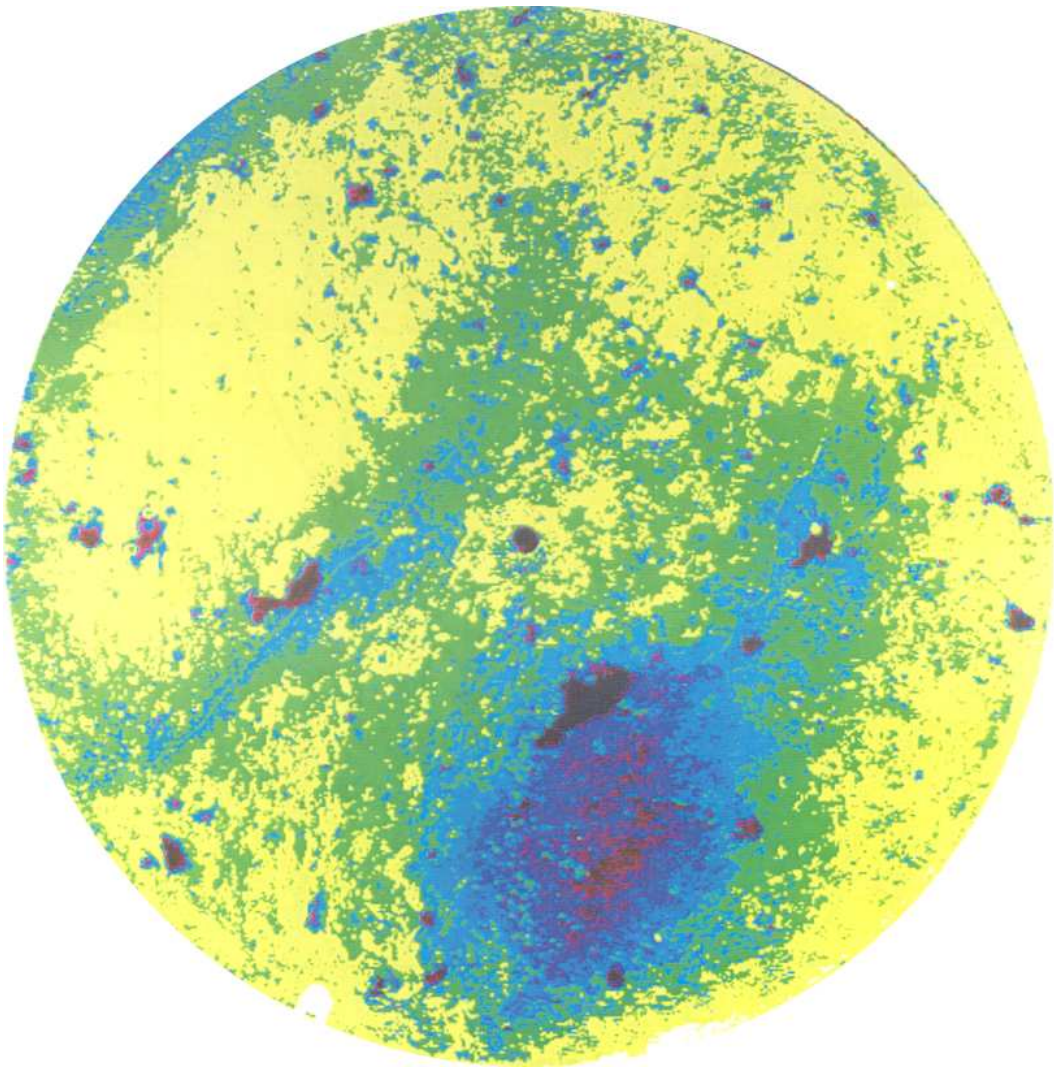

Figure 3.15: Distribution of fracture opening width of drilling core 2 taken from Jarsjö and Geller (1996)

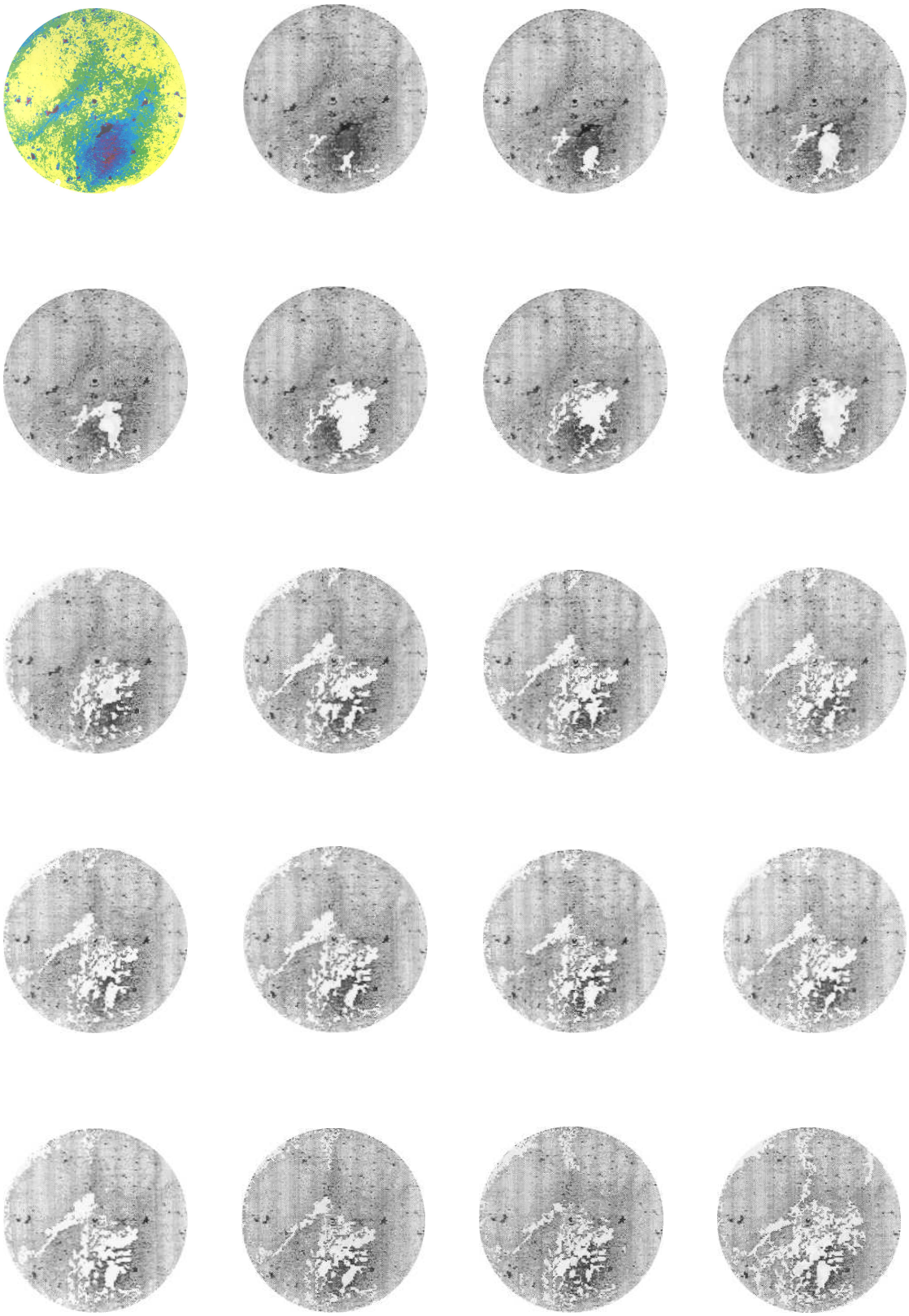

Figure 3.16: Temporal course of the degassing process for an intial CO_2 concentration of 15 procent taken from Jarsjö and Geller (1996) (drilling core 2)

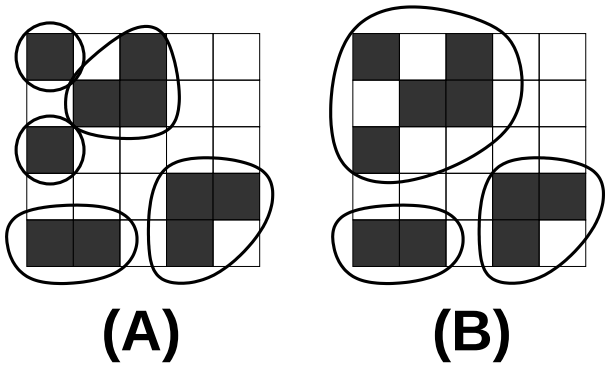

Figure 3.17: Formation of clusters for occupied cells

3.3 Percolation Model

The basis of the percolation theory is according to Stauffer and Aharony (1995) an infinite space which is discretely divided into cells. These cells are occupied with a probability of p and inoccupied with a probability of $(1-p)$. The set of adjacent cells is called cluster. Having a probability of occupation of $p = 0$, non of the cells is occupied, having a probability of $p = 1$ all of the cells are occupied.

In Figure 3.17, we see a quadratic finite mesh. A dark coloured cell is occupied, a light one is unoccupied. In case A, the neighborhood of two cells is defined by the fact that they share a common face. Thus, five clusters result. In case B, the neighborhood of two cells is defined via common nodes. Here, three clusters result. In the percolation theory, the number and the properties of these clusters are considered.

The higher the probability of occupation p, the larger clusters will form. Starting from a certain probability of occupation p_k, a cluster will form which will pervade the whole region. Such a cluster is called percolating. In percolation theory, the occurence of such a cluster is called critical phenomenon. This phenomenon within the percolation theory is described by scale theory.

In Figure 3.18, some possible states of occupation for a mesh of 6×6 cells and $p = \frac{1}{4}$, $p = \frac{1}{3}$ und $p = \frac{1}{2}$ are illustrated. As can be seen, we get a percolating cluster for $p = \frac{1}{2}$.

The examples considered up to now were related to the side percolation, where the single cells are connected by faces. The contrary is the bond percolation where the cells are connected by lines. The connection lines are then open with a probability of p and closed with a probability of $1-p$. The vicinity of cells is defined by open connection lines.

In pure percolation theory, we assume that the cells are not correlated at all. This means, that each cell is occupied with a probability of p independent of the fact whether or not the adjacent cells are occupied. Applying the percolation theory to porous media, we can no longer assume that adjacent cells are not correlated. The spatial correlation of the parameters of the porous medium also has to be taken into account. We can assume that for higher correlation larger clusters will form. The spatial correlation also has a

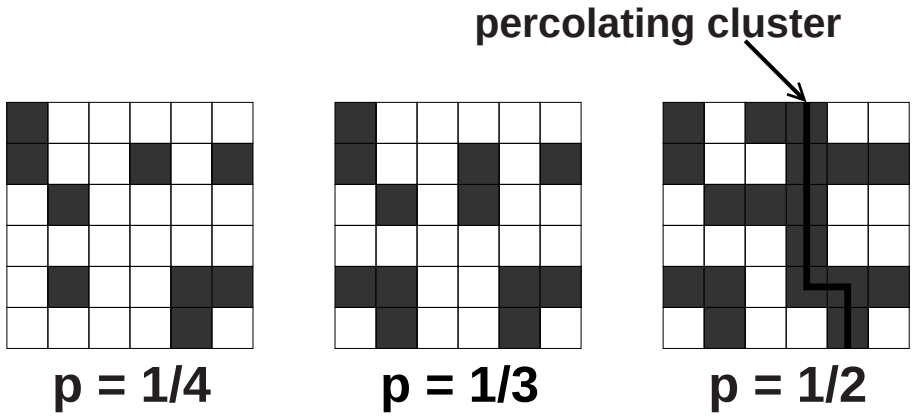

Figure 3.18: Percolating formation of clusters

strong influence of the percolation sill p^k:

While for strongly anisotropic spatial correlation the percolation sill decreases, it increases for isotropic spatial correlation. For this reason, most of the statements which result from percolation theory cannot automatically be transferred to porous media. In the work of Selyakov and Kadet (1996), we find numerous examples of the applications of percolation theory to porous media which base on analytical evaluations with and without consideration of correlation. Berkowitz and Balberg (1993) give also an overview of computer-based applications of percolation theory for groundwater hydrology and point out their limits mentioned above.

A special role for the description of two-phase processes in fractures with dominant capillary forces plays invasion percolation, which is presented by Wilkinson and Willemsen (1983). Assuming that the fracture is completely filled with water and that gas is entering, the gas will always occupy the largest fracture openings which can be reached. Unlike for pure percolation, not all cells can be occupied, but only these cells which are adjacent to the cells which are already occupied. In the course of time of invasion percolation, regions which are filled with water, can be isolated, i.e. that these regions are no longer connected to one of the sides. As water is not compressible, the gas cannot penetrate these regions any more. When the gas has reached the other side of the mesh, we assume that no further cells can get occupied. If gas is replaced by water, we can assume according to Wilkinson (1986) that water also penetrates the isolated gas regions. According to Dias and Payatakes (1986), this sort of invasion percolation can be compared to the normal percolation. Neuweiler (1999) carried through experiments for artificial single fractures and compared them to an invasion percolation model where she found excellent agreement between experiment and invasion percolation.

A further application of percolation theory is described by Braun (2000). In this work, a defined capillary pressure is assigned to the sides of the mesh. Taking the inverse capillary pressure–saturation function, we can calculate a saturation of a cell from this pressure (see also Section 2.2.6). If the specified capillary pressure is smaller than the

entry pressure of a cell, $S_n = 0$ is valid for this cell, and thus also $k_{rn} = 0$ as well as $K_{effn} = 0$.

If we increase the capillary pressure p_c, starting from zero, the percolation sill is reached if a path of adjacent cells between two opposite sides can be found whose entry pressure is below the defined capillary pressure.

Braun (2000) has applied such a percolation model to a strongly anisotropic system, i.e. different percolation sills for the horizontal and the vertical direction. He derived new relative permeability functions by an average over the effective permeabilities which can serve to describe the behaviour of two-phase flow on a larger scale.

As explained in Section 3.2, we can abstract the degassing process in a way that we assume that the escaping gas occupies the largest fracture apertures.

We consider the raster elements of the fracture model given by Tsang and Tsang (1987) as cells of the percolation mesh. We can calculate—as described in Section 3.2—the volume for a defined intitial concentration of desolved gas as a function of pressure and temperature. We will subdivide this volume into cells. Therefore, we start with the largest cells and continue the allocation with the smaller ones until we have reached the volume of the escaping gas. As the water phase stays mobile, we can assume that it is replaced by the gas phase.

The percolation sill is defined by the fact, as described above, that a path between opposite sides can be found. In such a case, the gaseous phase would become mobile, and the water phase immobile. As we assume isotropic conditions, this takes place without taking into account the direction.

3.4 Renormalisation Model and Determination of the REV

As mentioned in Section 3.3, percolation theory is based on an infinite mesh. This can be realized in analytically considering limit values. For computer-based percolation models, however, only finite meshes can be used.

For this reason, it is necessary to extrapolate conclusions from finite to infinite meshes. According to Stauffer and Aharony (1995), it was Wilson (1971) who published the first treatment of critical phenomena using the renormalisation group and who therefore received the nobel prize of physics. At the beginning, the idea was only applied to phase transitions and treated fluctuations in the Fourier space. Later, it was applied to percolation theory and the real location space. The self-similarity of the percolating cluster is the basis for renormalisation theory. In the renormalisation of the location space, several cells are replaced by one super-cell. Here, information is lost. However, for sufficient self-similarity of the structures within the super-cell, this is admitted.

While this self-similarity occurs in the classical percolation theory only for $p = p^k$, we can assume self-similarity for a field of fracture opening width on a certain length scale, if we consider a domain which by far exceeds this integral length scale.

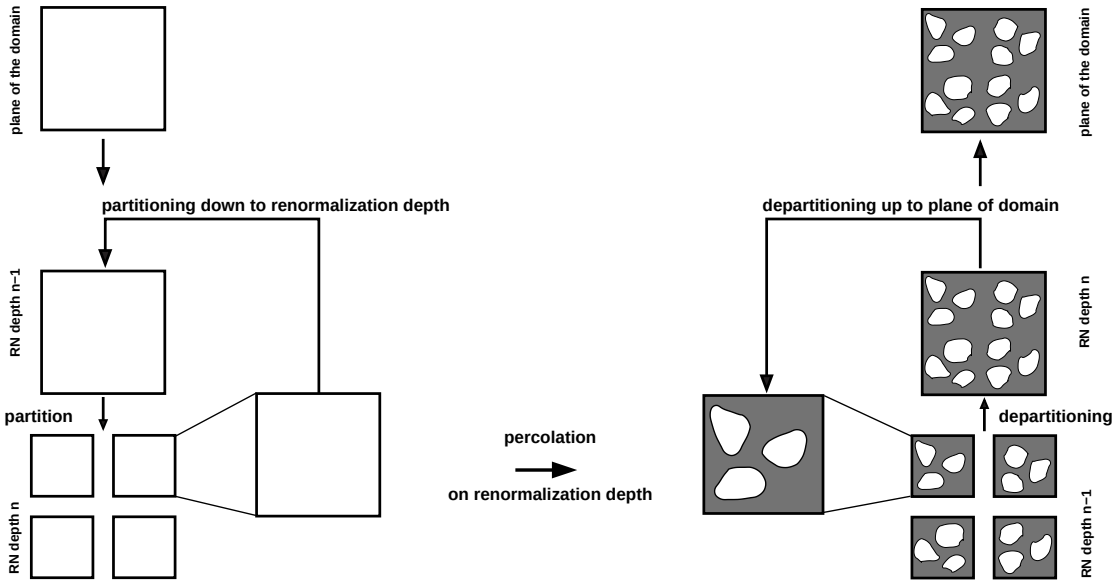

Figure 3.19: Schematic illustration of the algorithm for the renormalisation-perculation model

Thus, the proof needed to transfer information from a finite to an infinite mesh, consists in the proof of self-similarity.

Replacing the mesh by four meshes which are four times smaller and finding the same properties for each mesh, we have guaranteed self-similarity of the larger to the smaller meshes. Dividing the smaller meshes once more, we have a high probability of finding the same properties for even larger meshes.

At the same time, we can be sure that the properties averaged over such a large domain. are representative, i.e. they fulfill the demands of Section 2.1.

In Figure 3.19, the algorithm of renormalization is schematically illustrated.

3.5 Results of the Renormalization–Percolation Model

We will now apply the approaches explained in the previous sections. Therefore, we demonstrate the procedure for two fracture fields, each consisting of 128×128 raster elements. Let us first consider isothermal conditions of 298.1 K and investigate only three pressure states. The first pressure state lies exactly below the assumed degassing pressure. For this pressure, the fracture is still totally water-saturated. The second pressure state is the mean between the degassing pressure and the atmospheric pressure. For each pressure state, we can calculate the volume of the degassed gas for a certain initial concentration, as explained in Section 3.2. In this way, we can also evaluate the

Henry coefficient K^{CO_2}	165564000 [Pa]
temperature	298.15 [K]
initial mole fraction $x_{start^{CO_2}}$	0.000805 [-]
molar mass M^{CO_2}	0.044 [kg]
$Enthsol^{CO_2}$	2400
density of the liquid phase ρ_{fl}	1000 [kg/m^3]
factor for hydraulically active fracture	1.0
thickness of the wetting water film	0.000001 [m]
residual saturation S_{wr} due to fracture roughness	0.2
surface tension for the gas - water system σ_{gw}	0.0727 [Nm]
initial pressure	145000 [Pa]
final pressure	101325 [Pa]
pressure iterations	3
renormalisation depth	4

Table 3.4: Parameters for the renormalisation-percolation model with CO_2 as desolved gas, taken from the experiment of Jarsjö and Geller (1996)

gas saturation of the considered fracture. We destribute the volume of the degassed gas among the largest fracture opening width. For this state of allocation, we derive the effective parameters of the fracture.

The fields of fracture opening width generated with the data of Keller (1997), is illustrated in Figures 3.20 and 3.21.

The degassing states for the different pressure states can be seen in Figures 3.22, 3.25, 3.28 and 3.31 for the renormalization levels 0 to 3.

In Figures 3.23 and 3.24, the parameters can be seen in dependence of the area of the averaging domain. The largest averaging boundary face corresponds to the renormalization level 0, the second largest to the renormalization level 1 and so on.

Due to the renormalization algorithm of Section 3.4, we get 4^i values on renormalization level i. The permeability illustrated on the left hand side in Figure 3.23, is calculated using the geometric mean.

The part of the area occupied by gas (Figure 3.23 on the right hand side) is a rough measure for the self-similarity of the fields on each renormalization level. The relative permeability k_{rw} is calculated in dividing the geometric means of the permeability with and without taking degassing into account.

The capillary pressure results from the smallest fracture opening width occupied by gas.

As can be seen in Figure 3.23 and 3.24, the renormalization model only gives acceptable results for the averaged permeability, if the pressure is higher than the degassing pressure. The results for the part of the area occupied by gas, relative permeability, and capillary pressure on the other hand, are trivial. This changes more and more for lower pressures and correspondingly higher volumes of degassed gas. This can clearly be seen in comparing Figures 3.26 and 3.27 for $p = 1.304 \cdot 10^5$ Pa, 3.29 and 3.30 for

$p = 1.159 \cdot 10^5$ Pa and 3.32 and 3.33 for $p = 1.013 \cdot 10^5$ Pa.

Moreover, it can clearly be seen that the variability decreases with increasing averaging area. From this decrease, we can conclude that the identification of a representative elementary area (REA) is possible starting from a certain area. How large the area for the creation of the REA is, depends on the admitted variablity. We assume arbitarily, that the REA is reached, if the quotient of the values on one renormalization level and of the value on the higher level, lies between 0.9 and 1.1.

The parameter, which is decisive for this work, is the relative permeability of the water phase. This condition is fulfilled for all the examples shown in this section. For stronger conditions (smaller variability, consideration of all parameters), the considered domain has to be correspondingly larger.

Figures 3.34 through 3.47 show the renormalization process described above for a field of fracture openings generated using the data of Jarsjö and Geller (1996). The conditions for a REA are detected for a domain which is 16 times larger, here. This results from the integral length scale, which is 5.7 mm for the field of fracture opening width of Figure 3.20 and 35 mm for the one of Figure 3.34.

Thus, the edge length of the REA is in both cases more than ten times the integral length scale. This value cannot be assigned a high significance, however, as the criteria for the creation of the REA were arbitrarily chosen.

The much higher capillary pressure, which we state for the field in Figure 3.34 in comparison to the field of Figure 3.20 for the same defined system pressure, results from the smaller average of fracture opening width for the field of Figure 3.34 (see also Table 3.1).

Unlike for the capillary pressure, the relative permeability is almost identical for each pressure state for the fields of fracture opening width. Thus, it does not seem to be dependent on the distribution of fracture opening width.

3.5.1 Data from Keller (1997)

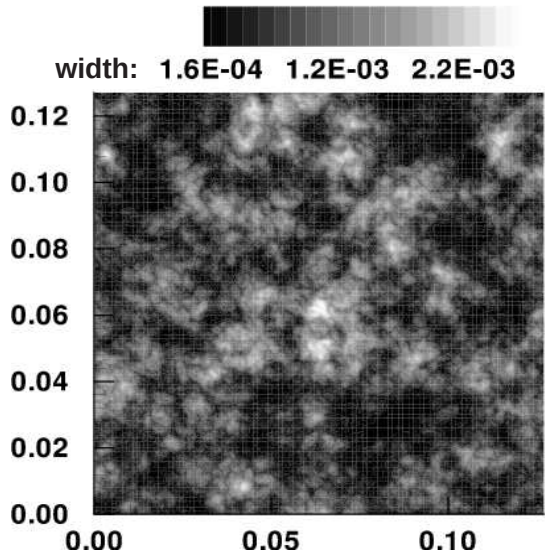

Figure 3.20: Field of fracture apertures from Keller (1997) with 128×128 raster elements

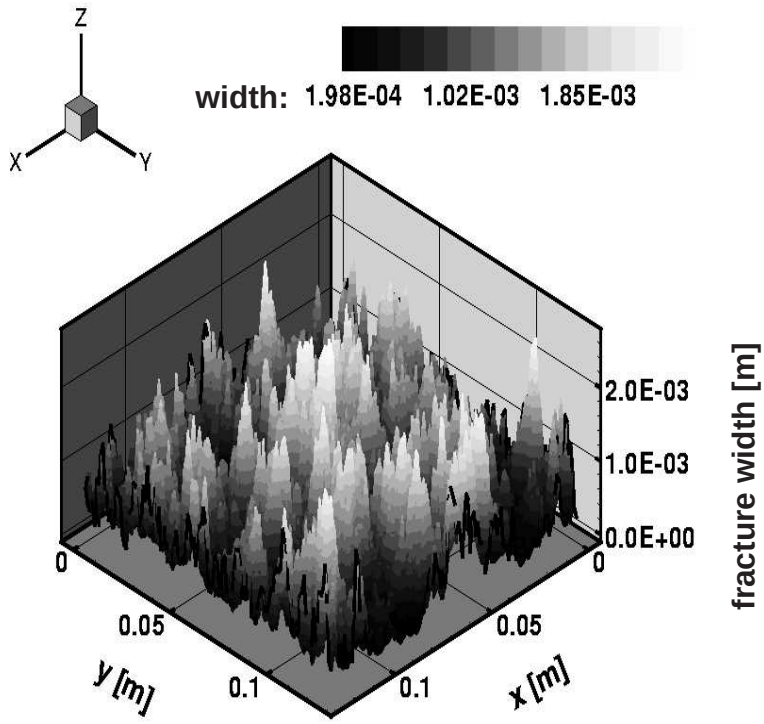

Figure 3.21: Threedimensional representation of Figure 3.20

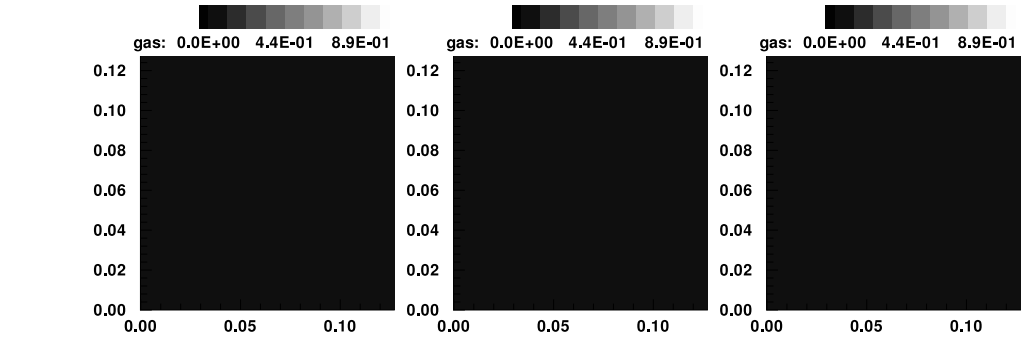

Figure 3.22: Representation of the gas distribution for different renormalisations: renormalisation level 0 (left), renormalisation level 1 (center), renormalisation level 2 (right hand side) (for system state 1 given by Keller (1997))

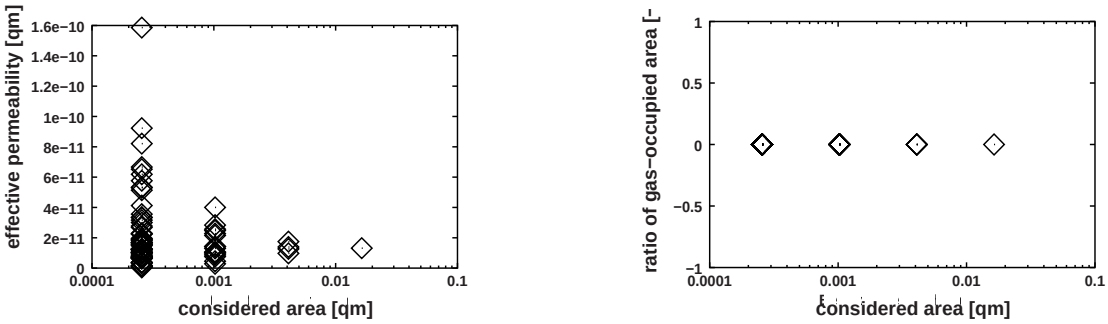

Figure 3.23: Effective permeability and area occupied by gas (for system state 1 given by Keller (1997))

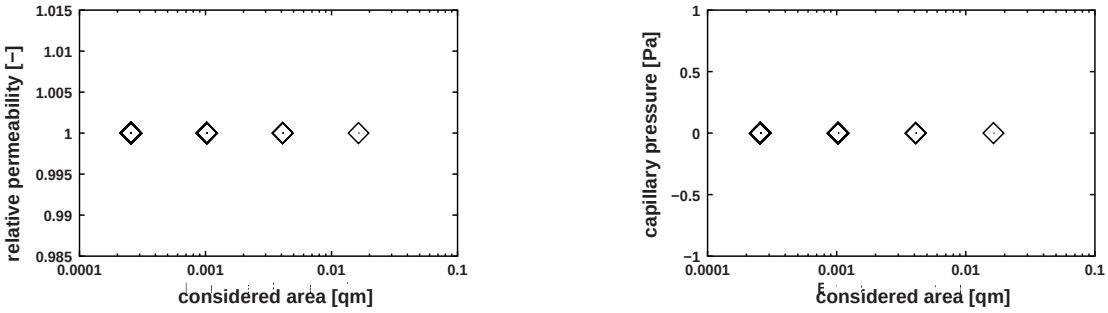

Figure 3.24: Relative permeability and capillary pressure (for system state 1 given by Keller (1997))

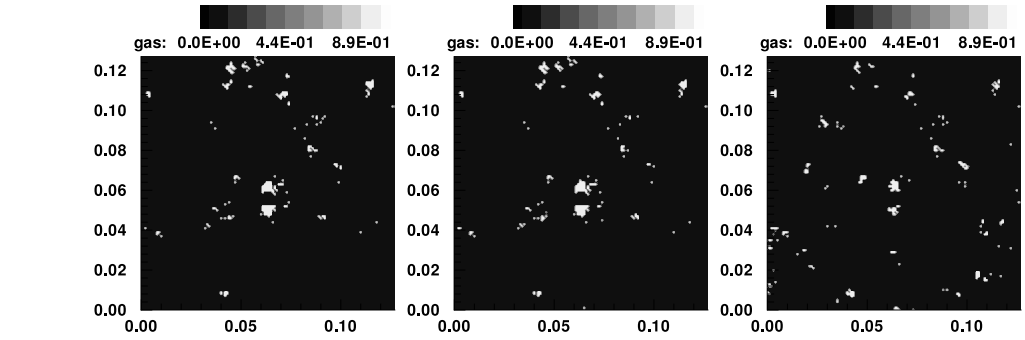

Figure 3.25: Gas distibution for different renormalisations: renormalisation level 0 (left), renormalisation level 1 (center), renormalisation level 2 (right) (for system state 2 given by Keller (1997))

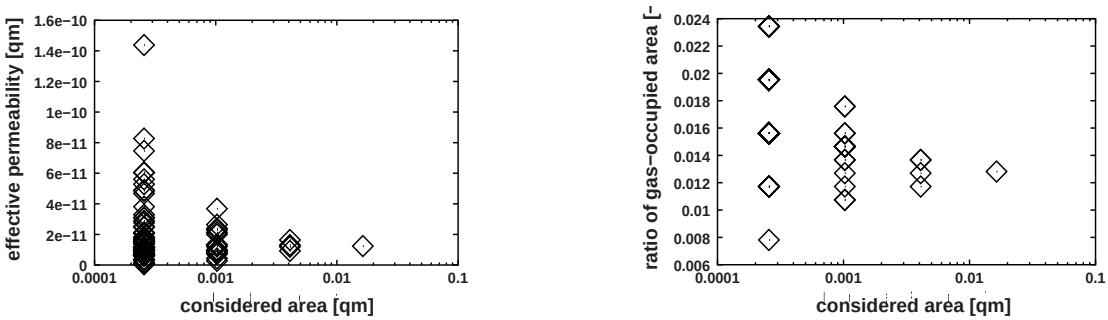

Figure 3.26: Effective permeability and area occupied by gas (for system state 2 given by Keller (1997))

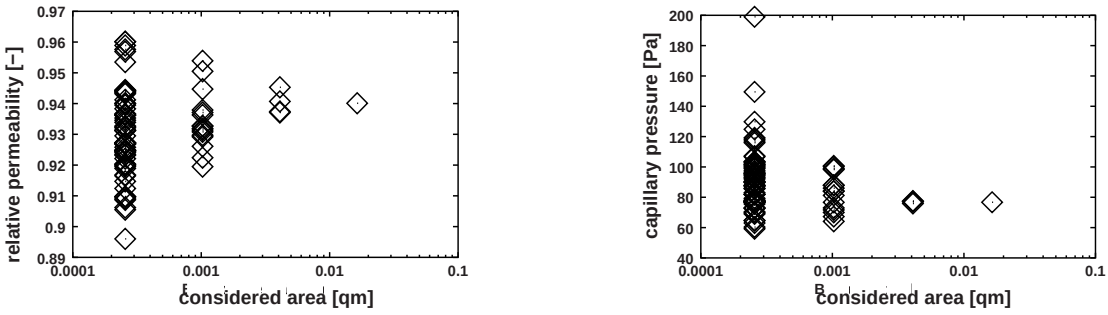

Figure 3.27: Relative permeability and capillary pressure (for system state 2 given by Keller (1997))

System state 3: pressure 1.159e+05 [Pa], temperature 298.1 [K], S_g: 0.1513

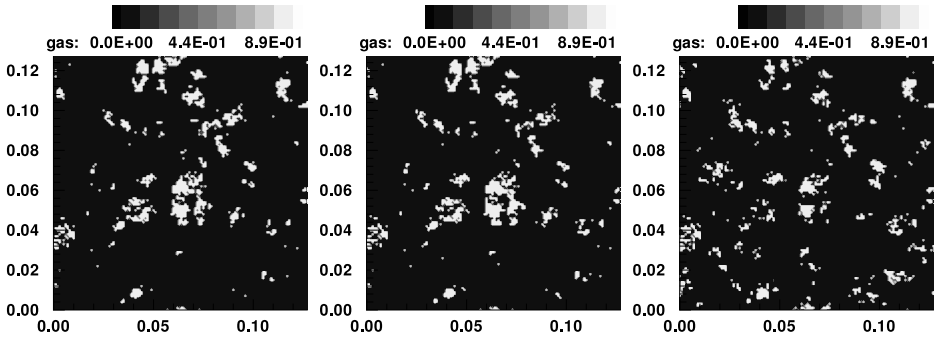

Figure 3.28: Gas distribution for different renormalisations: renormalisation level 0 (left), renormalisation level 1 (center), renormalisation level 2 (right) (for system state 3 given by Keller (1997))

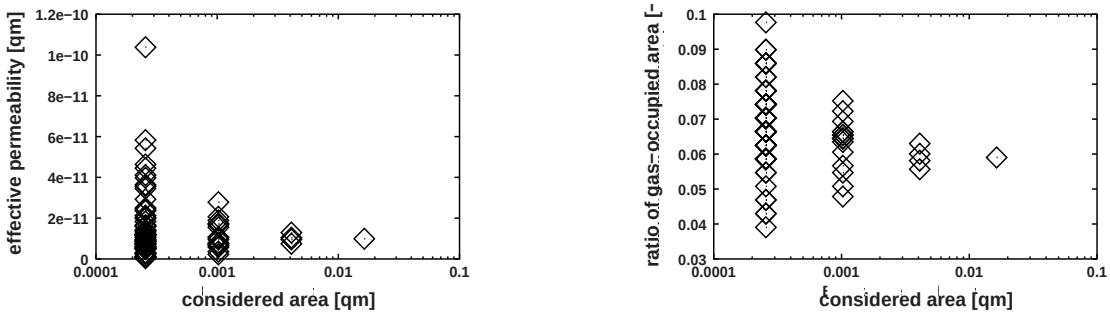

Figure 3.29: Effective permeability and area occupied by gas (for system state 3 given by Keller (1997))

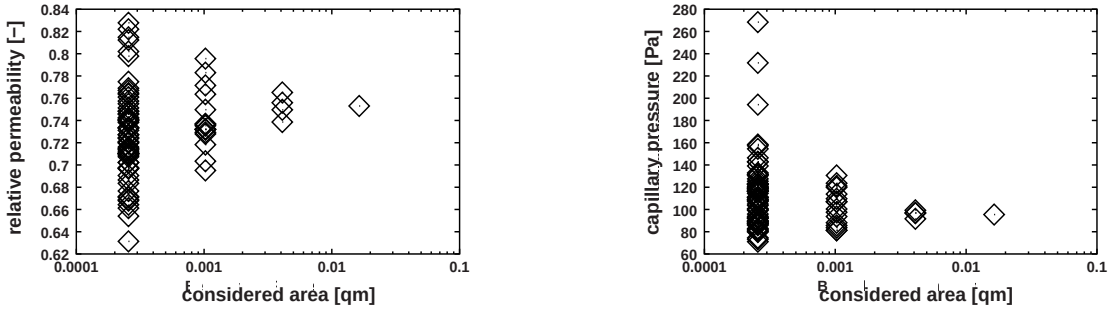

Figure 3.30: Relative permeability and capillary pressure (for system state 3 given by Keller (1997))

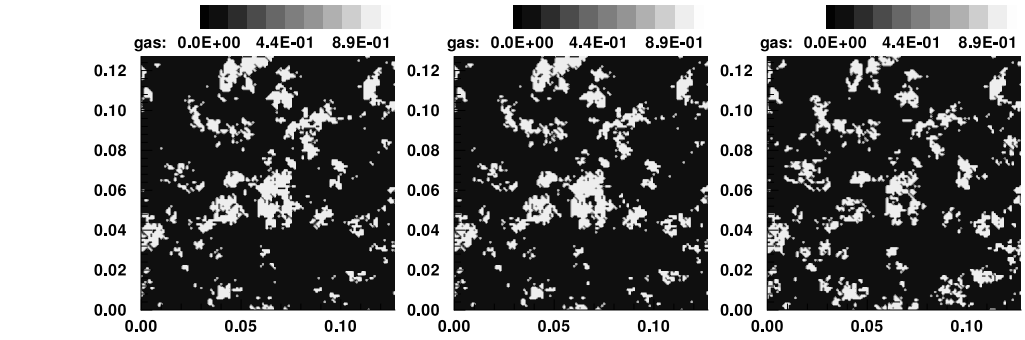

Figure 3.31: Gas distribution for different renormalisations: renormalisation level 0 (left), renormalisation level 1 (center), renormalisation level 2 (right) (for system state 4 given by Keller (1997))

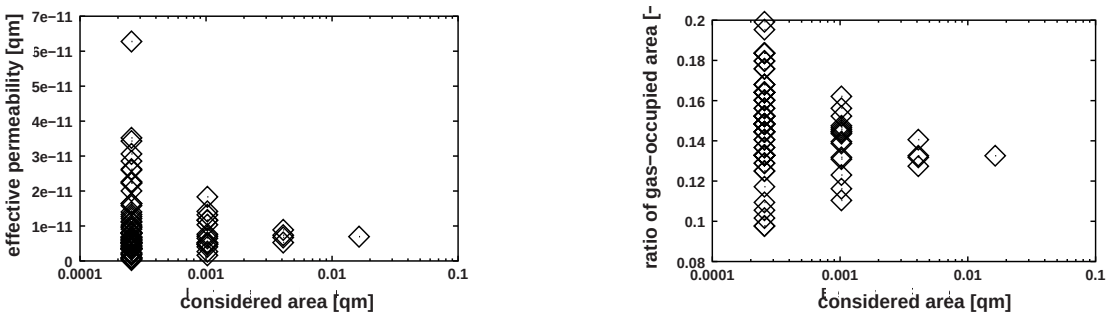

Figure 3.32: Effective permeability and area occupied by gas (for system state 4 given by Keller (1997))

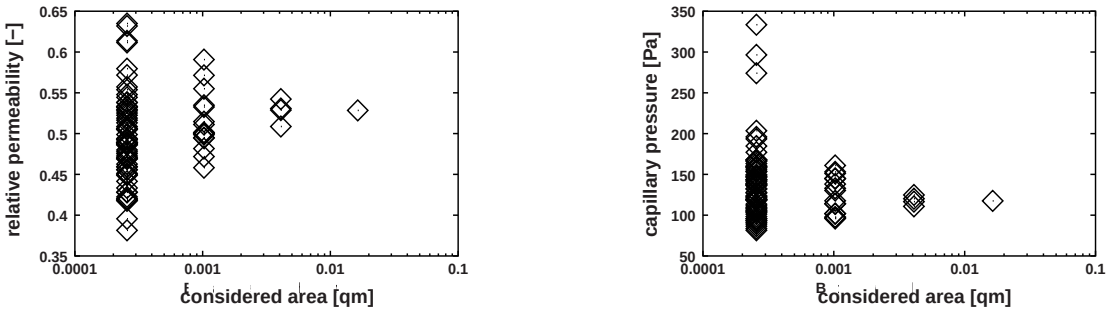

Figure 3.33: Relative permeability and capillary pressure (for system state 4 given by Keller (1997))

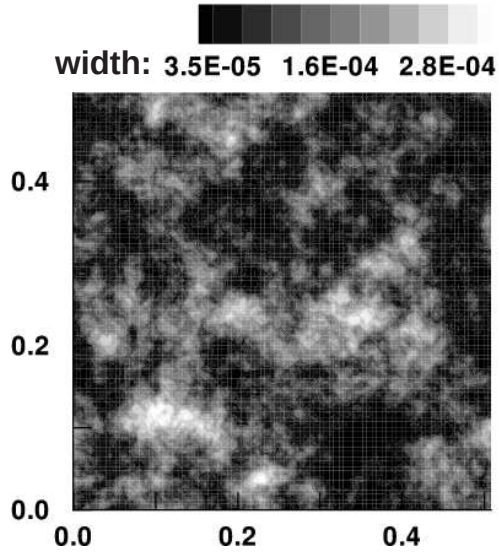

Figure 3.34: Field of fracture opening width from Jarsjö and Geller (1996) with 128×128 raster elements

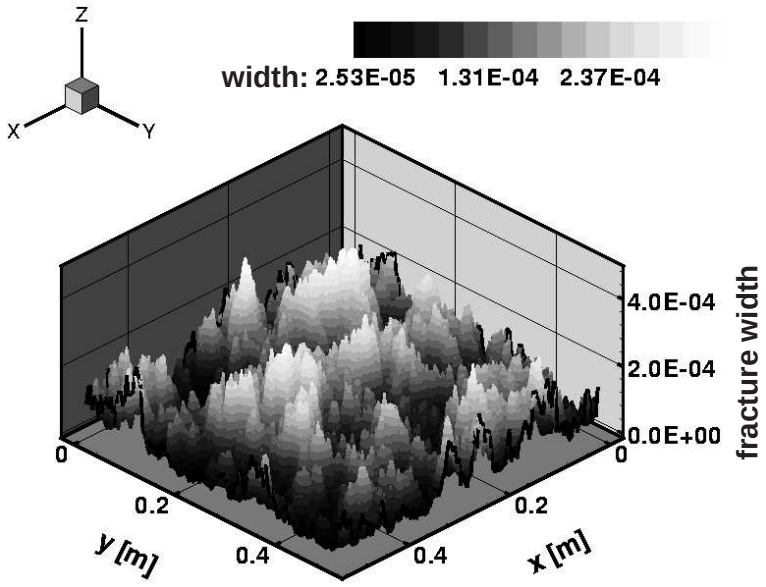

Figure 3.35: Threedimensional representation of Figure 3.34

3.5.2 Data Given by Jarsjö (1996)

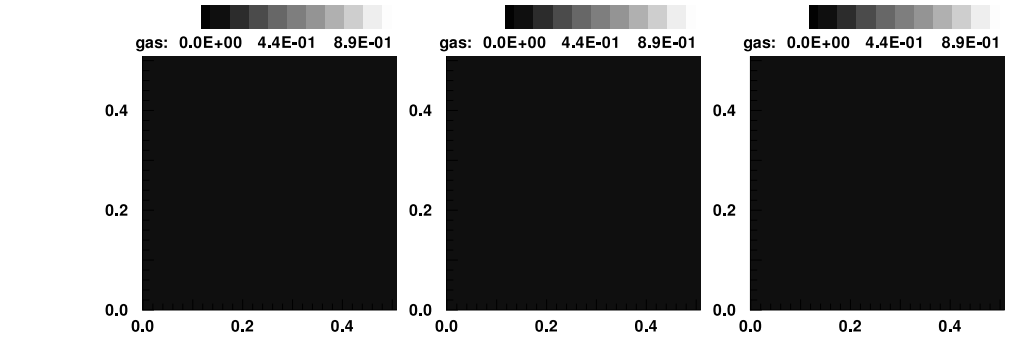

Figure 3.36: Gas distribution for different renormalisations: renormalisation level 0 (left), renormalisation level 1 (center), renormalisation level 2 (right) (for system state 1 given by Jarsjö and Geller (1996))

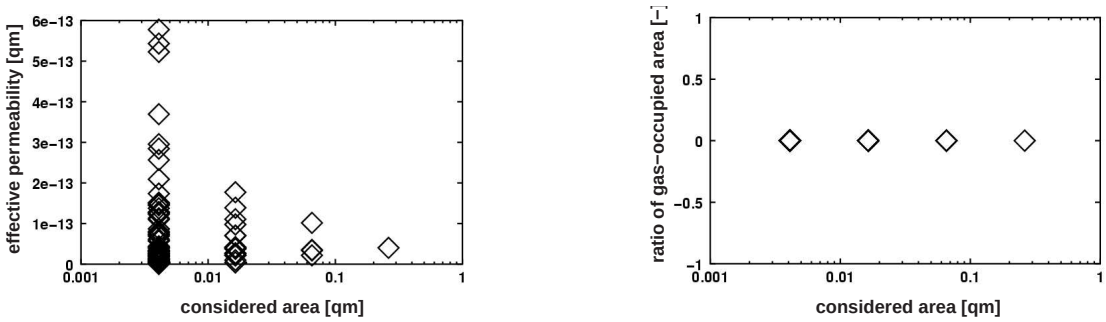

Figure 3.37: Effective permeability and area occupied by gas (for system state 1 given by Jarsjö and Geller (1996))

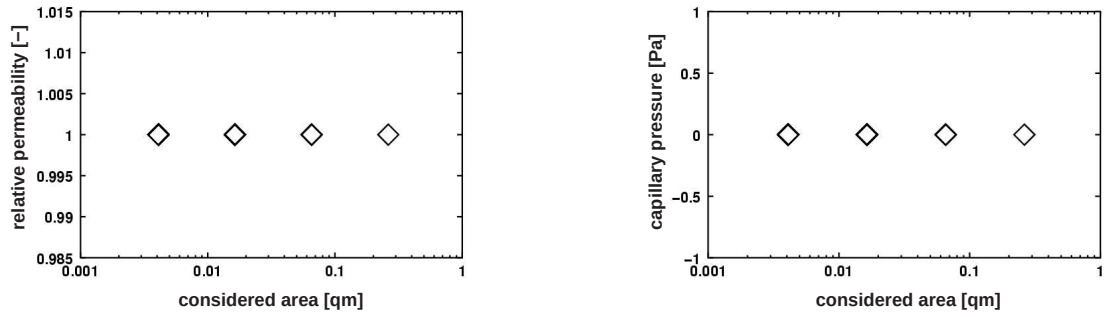

Figure 3.38: Relative permeability and capillary pressure (for system state 1 given by Jarsjö and Geller (1996))

System state 2: pressure 1.304e+05 [Pa], temperature 298.1 [K], S_g: 0.0389

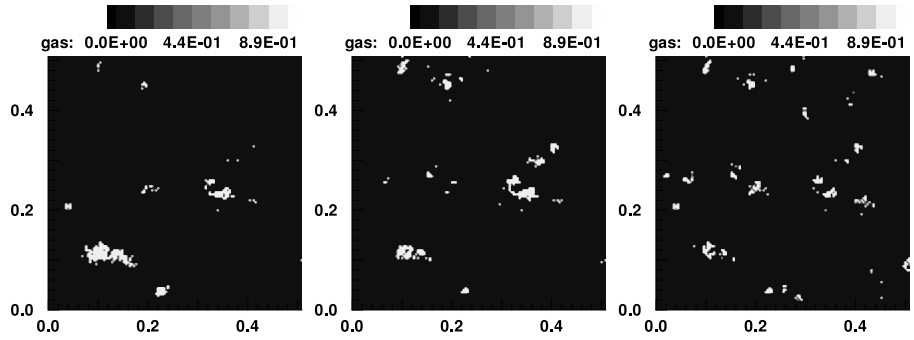

Figure 3.39: Gas distribution for different renormalisations renormalisation level 0 (left), renormalisation level 1 (center), renormalisation level 2 (right) (for system state 2 given by Jarsjö and Geller (1996))

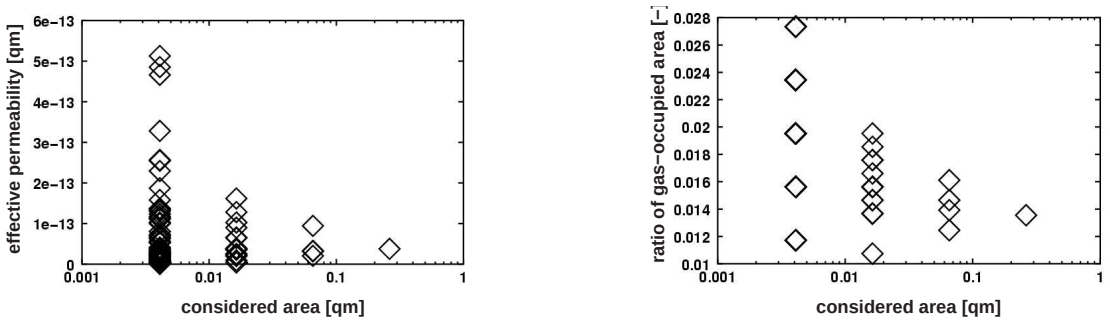

Figure 3.40: Effective permeability and area occupied by gas (for system state 2 given by Jarsjö and Geller (1996))

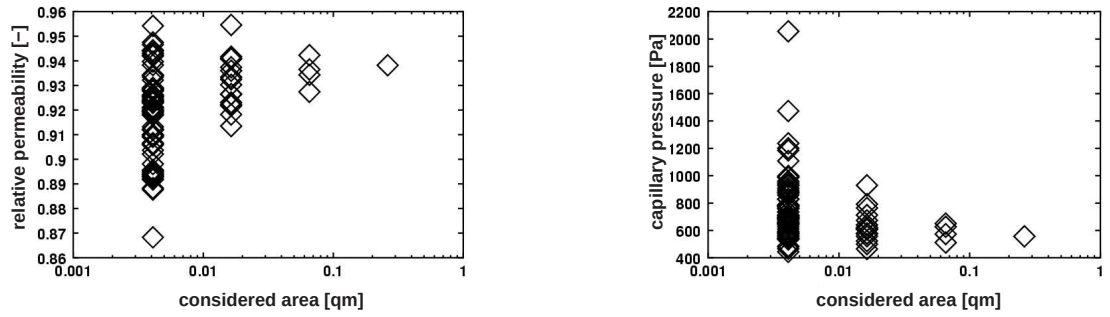

Figure 3.41: Relativen permeability and capillary pressure (for system state 2 given by Jarsjö and Geller (1996))

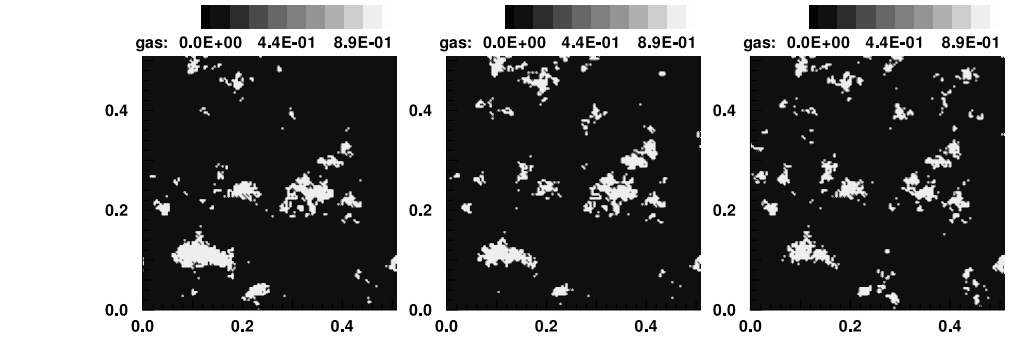

Figure 3.42: Gas distribution for different renormalisations: renormalisation level 0 (left), renormalisation level 1 (center), renormalisation level 2 (right) (for system state 3 given by Jarsjö and Geller (1996))

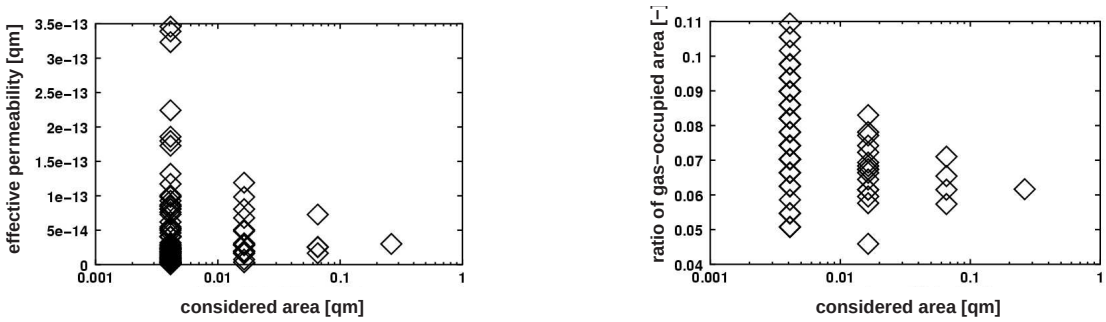

Figure 3.43: Effective permeability and area occupied by gas (for system state 3 given by Jarsjö and Geller (1996))

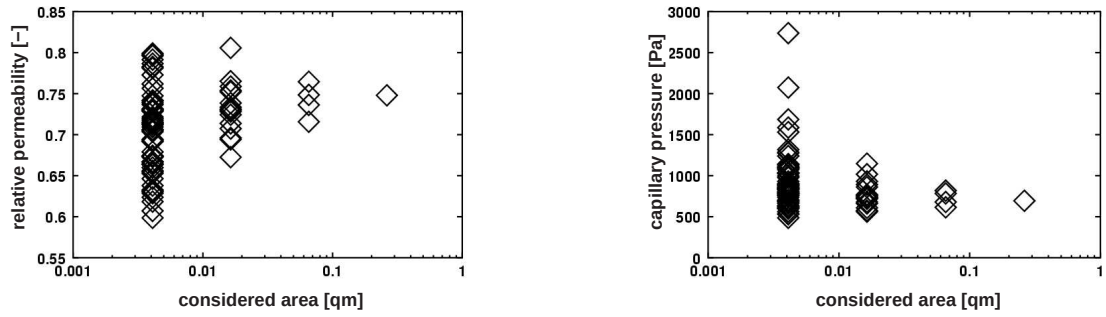

Figure 3.44: Relative permeability and capillary pressure (for system state 3 given by Jarsjö and Geller (1996))

System state 4: pressure 1.013e+05 [Pa], temperature 298.1 [K], S_g: 0.297

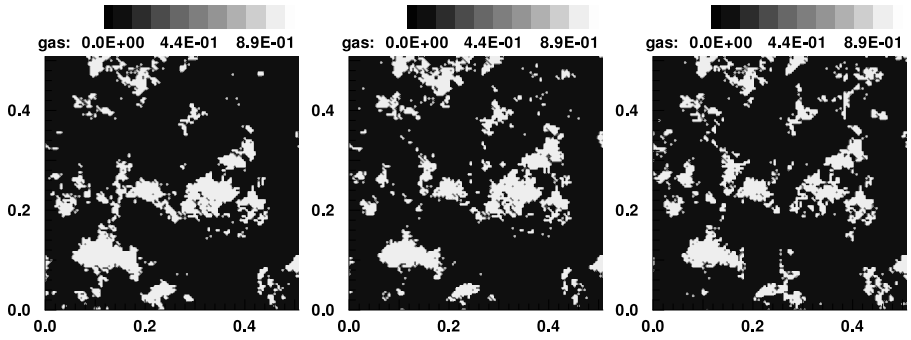

Figure 3.45: Gas distribution for different renormalisations: renormalisation level 0 (left), renormalisation level 1 (center), renormalisation level 2 (right) (for system state 4 given by Jarsjö and Geller (1996))

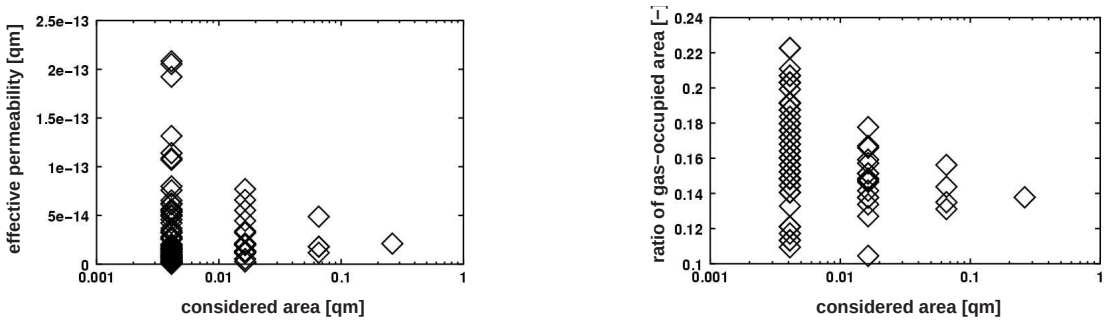

Figure 3.46: Effective permeability and area occupied by gas (for system state 4 given by Jarsjö and Geller (1996))

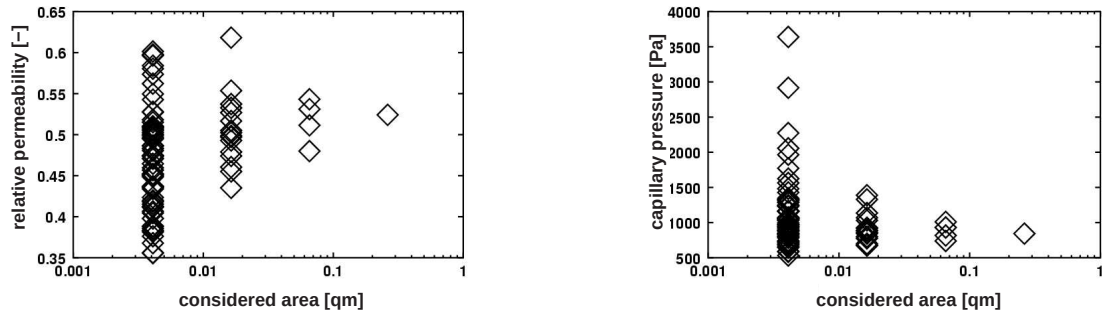

Figure 3.47: Relative permeability and capillary pressure (for system state 4 given by Jarsjö and Geller (1996))

3.6 Identification of Effective Parameters

Having proven that the assumption of the occupation of the largest fracture opening width by the degassed gas can still be upheld for larger fracture faces and that we can assign an REV, respectively an REA (representative elementary area) to this process, we can identify the effective parameters of the process.

Therefore, we vary pressure and temperature. It is important, that we stay above the percolation sill as our model loses its validity at the sill.

For the identification of the effective parameters, we can set the renormalisation depth to 0. This means, that we cannot apply the renormalisation model, as we have already identified the representative elementary face. The other parameters are given in Table 3.5.

We consider a degassing process of CO_2 with an initial molar concentration of 0.00070475. This corresponds to a volume concentration of 0.152 and a degassing pressure of 119837 Pa at 25°C.

This values correspond to the values for the highest gas concentration of Table 3.3.

The data relevant for the percolation algorithm, can be seen in Table 3.5. The Henry coefficient of CO_2 is very small compared to the Henry coefficient of N_2 and H_2. This means, that very small pressure fluctuations already have a significant influence on the concentration of CO_2 desolved in water. Moreover, the enthalpy of solution of CO_2 is very high. Thus, the temperature dependence of the Henry coefficient and because of that also the temperature dependence of the degassing process is very strong.

In Figure 3.49 on the left hand side, we see the gas saturation in dependence of pressure and temperature. The gas saturation corresponds to the volume fraction described in Section 3.2 and is thus not dependent on the considered field of fracture opening width.

The other functions presented here, base on the field of fracture opening width of Figure 3.34. We can clearly recognize the areas in Figure 3.34 where the degassing pressure is not yet reached. For these regions, $S_g = 0$ and the permeability is equal to the maximum value. The decrease of effective permeability of the water phase with decreasing pressure and increasing temperature can clearly be seen.

The course of the relative permeability k_{rw} presented in Figure 3.50 on the left hand side, resembles the course of the effective permeability $K_{eff,w}$. On the right hand side, we see the capillary pressure which jumps up to the entry pressure of a fracture when reaching the degassing pressure and then increases with decreasing pressure and increasing temperature.

In Figure 3.51, we see the maximum capillary pressure gradient on the left hand side, and the minimum capillary pressure gradient on the right hand side. The capillary pressure gradient is defined via the quotient of the difference of the capillary pressures of two adjacent raster elements and the raster element length. Therefore, one of the two elements has to be occupied by water, the other one by gas.

As can be seen from Figure 3.51, the maximum capillary pressure gradient is increasing in the course of degassing, i.e. for decreasing pressure and increasing temperature up to about $\nabla p_c = 600000\ kg/m^2s^2$. The minimum capillary pressure gradient does not

show a monotonic course, but oscillates between 1000 and 3000 kg/m^2s^2. These capillary pressure gradients can be taken in Section 2.4 for $\frac{p_c^*}{L}$ when defining the gravillary number in Equation (2.90). For buoyancy forces, we set $\Delta\rho \cdot g \approx 10000 kg/m^2s^2$.

This behaviour can be explained from Figure 3.48. We see here the maximum degassing state. While the opening width is decreasing to the darker zones, the white regions are connected with one another by "bands" of smaller gradients. With increasing degassing, the gas phase spreads more and more to the darker regions, it is also for this reason that the maximum capillary pressure gradient is increasing. At the same time, the gas phase is also spreading to "bands", therefore the oscillating minimum capillary pressure gradient.

As the darker regions encircle the white ones and the maximum capillary pressure gradients exceeds the buoyancy of the gas by a factor of 60, we can conclude that even for a vertical orientation of the fracture, the gas phase is not mobile. It does, however, distribute differently within the field of fracture opening, as the buoyancy of about 10000 kg/m^2s^2 is three to ten times higher than the minimum capillary pressure gradient.

Table 3.6 gives parameters for the percolation model for degassing of N_2. The initial mole fraction was chosen according to the data published by Jarsjö and Destouni (1998) for their field experiment.

In Figure 3.52, the corresponding gas saturations and the effective permeability are illustrated, in Figure 3.53, the relative permeability and the capillary pressure, and in Figure 3.54 the maximum and the minimum capillary pressure gradient in dependence of pressure and temperature.

Due to the higher Henry coefficient of N_2 in comparison to CO_2, a larger range of pressures is considered. The lower temperature dependence of the Henry coefficient K^{N2} in comparison to the Henry coefficient K^{CO2} of CO_2 is made clear in the figures.

In Table 3.7, the parameters for the percolation model for the degassing of H_2 can be seen. The initial mole fraction was computed for an entry pressure of $5 \cdot 10^6$ Pa and 13°C, the conditions of the Äspö rock laboratory.

From Figures 3.55 through 3.57, it becomes clear that the temperature does hardly play a role for the considered region. A stronger degassing process is only encountered if the pressure decreases below 10^6 Pa.

To sum up, we can say that for the consideration of CO_2 already small pressure and temperature fluctuations play an important role, while for N_2 and H_2, temperature fluctuations have almost no influence and also pressure fluctuations lead only in the range of $5 \cdot 10^6$ Pa to noteworthy degassing effects.

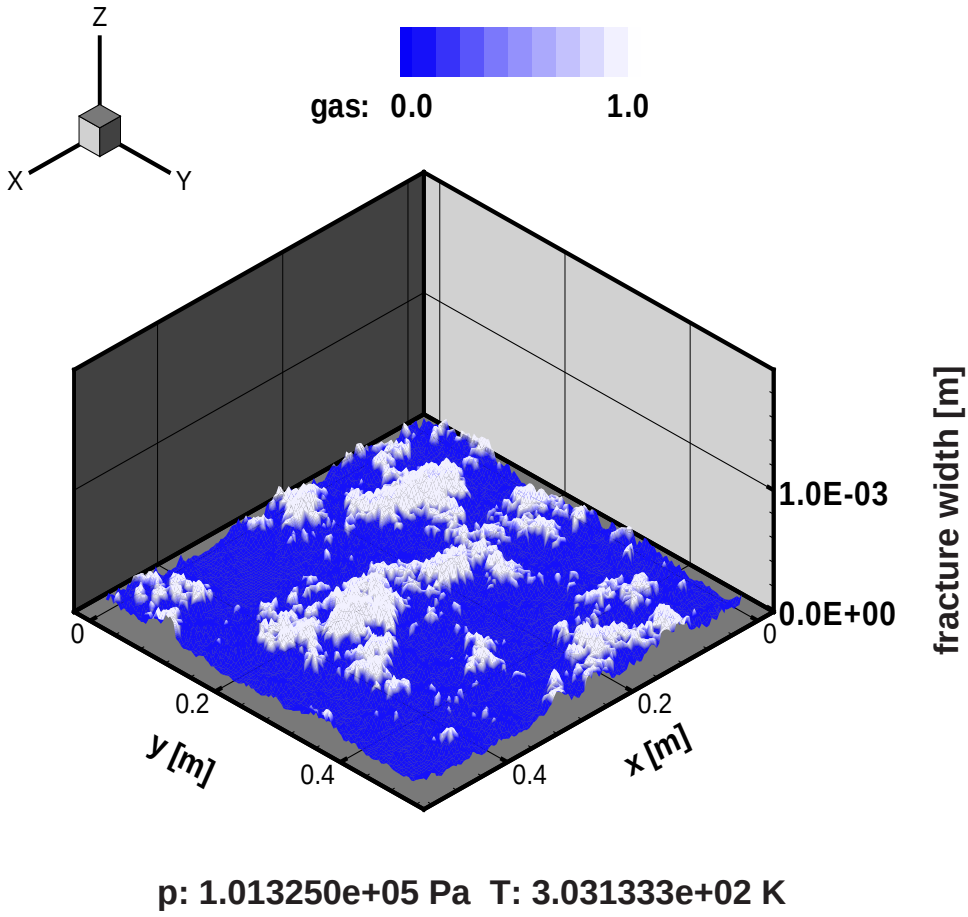

Figure 3.48: State of maximum degassing for p = 101325 Pa und T = 303 K

3.6.1 Carbon Dioxide

Henry coefficient K^{CO_2}	165564000 [Pa]
temperature	298.15 [K]
initial mole fraction $x_{start^{CO_2}}$	0.0007048 [-]
molar mass M^{CO_2}	0.044 [kg]
$Enthsol^{CO_2}$	2400
density of the liquid phase ρ_{fl}	1000 [kg/m^3]
factor for hydraulically active fracture	1.0
thickness of the wetting water film	0.000001 [m]
residual saturation S_{wr} due to fracture roughness	0.2
surface tension of gas - water system σ_{gw}	0.0727 [Nm]
initial pressure	101325 [Pa]
final pressure	125000 [Pa]
pressure iterations	16
initial temperature	283.3
final temperature	304.3
temperature iterations	18

Table 3.5: Parameters for the percolation model with CO_2 as desolved phase according to the experiment of Jarsjö and Geller (1996)

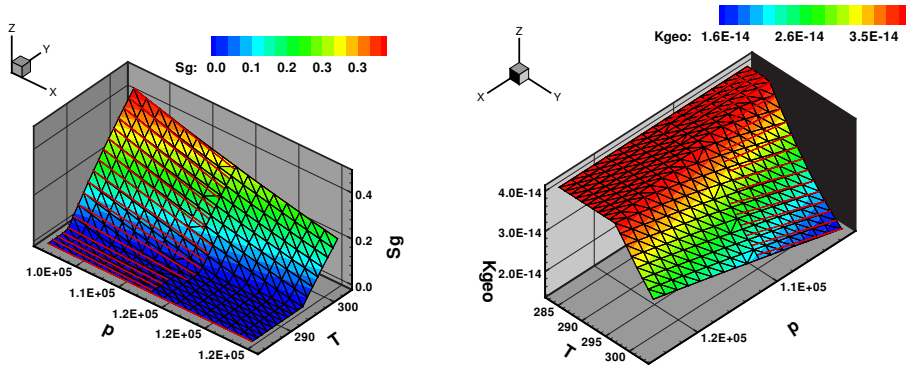

Figure 3.49: Gas saturation and effective permeability in dependence of pressure and temperature for CO_2 as desolved component

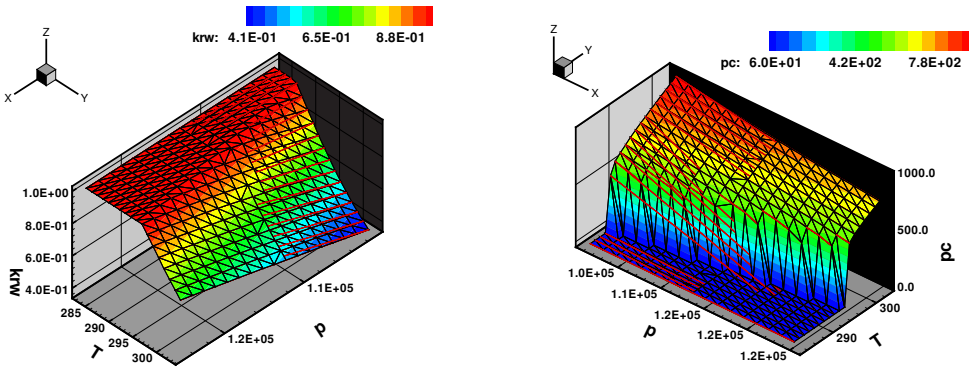

Figure 3.50: Relative permeability and capillary pressure in dependence of pressure and temperature for CO_2 as desolved component

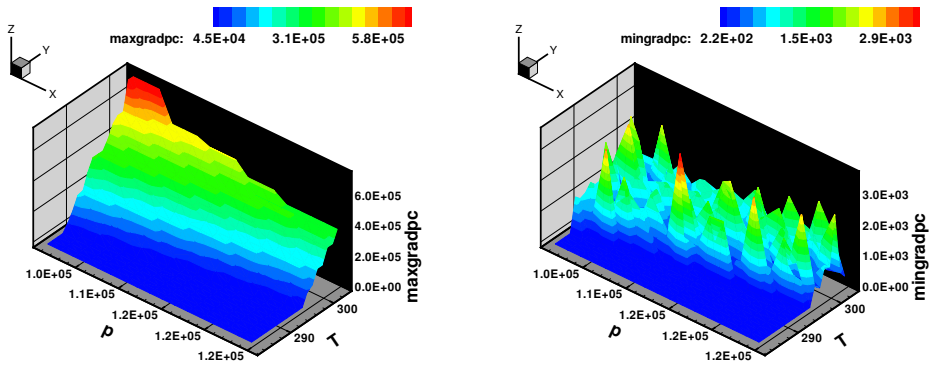

Figure 3.51: Maximum and minimum capillary pressure gradient in dependence of pressure and temperature for CO_2 as desolved component

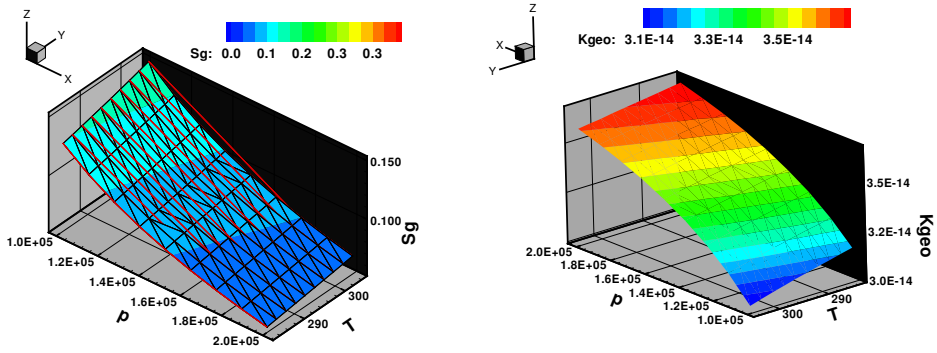

Figure 3.52: Gas saturation and effective permeability in dependence of pressure and temperature for N_2 as desolved component

3.6.2 NITROGEN

Henry coefficient K^{N_2}	9228100000 [Pa]
temperature	298.15 [K]
initial mole fraction $x_{start^{N_2}}$	0.0001124 [-]
molar mass M^{N_2}	0.028 [kg]
$Enthsol^{N_2}$	1300
density of the liquid phase ρ_{fl}	1000 [kg/m^3]
factor for hydraulically active fracture	1.0
thickness of the wetting water film	0.000001 [m]
residual saturation S_{wr} due to fracture roughness	0.2
surface tension for gas - water system σ_{gw}	0.0727 [Nm]
initial pressure	101325 [Pa]
final pressure	200000 [Pa]
pressure iterations	16
initial temperature	283.3
final temperature	304.3
temperature iterations	18

Table 3.6: Parameters for the percolation model with N_2 as desolved gas according to the experiment of Jarsjö and Geller (1996)

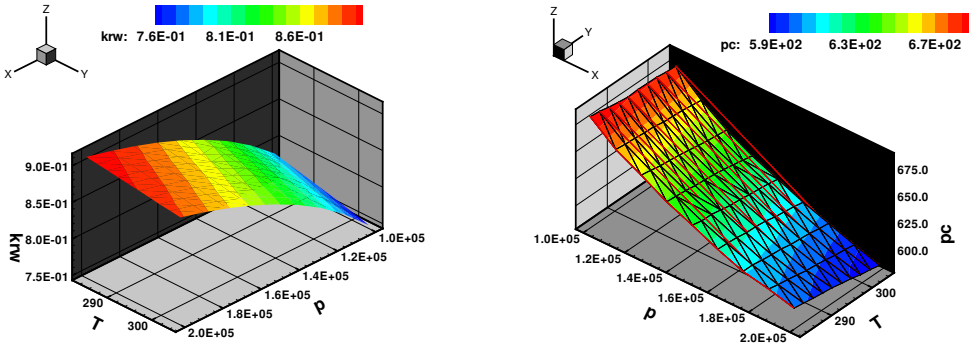

Figure 3.53: Relative permeability and capillary pressure in dependence of pressure and temperature for N_2 as desolved component

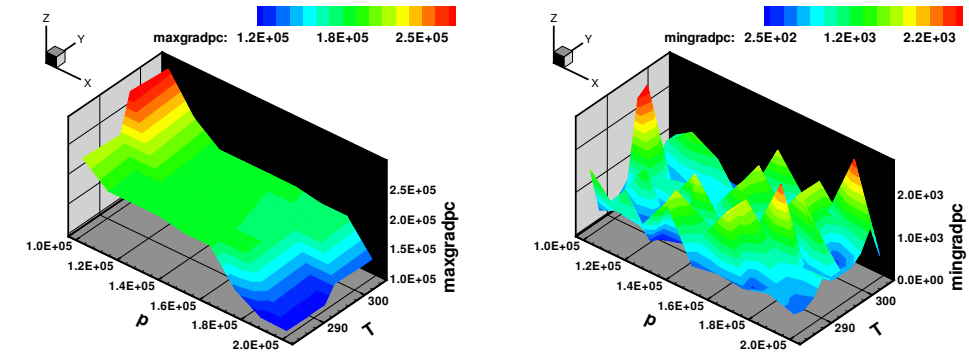

Figure 3.54: Maximum and minimum capillary pressure gradient in dependence of pressure and temperature for N_2 as desolved component

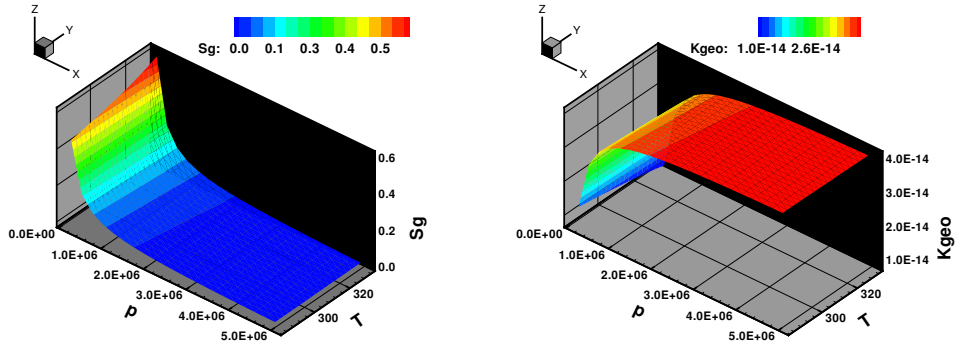

Figure 3.55: Gas saturation and effective permeability in dependence of pressure and temperature for H_2 as desolved component

3.6.3 HYDROGEN

Henry coefficient K^{H_2}	7216900000 [Pa]
temperature	298.15 [K]
initial mole fraction $x_{start^{H_2}}$	0.0007292 [-]
molar mass M^{H_2}	0.002 [kg]
$Enthsol^{H_2}$	500
density of the liquid phase ρ_{fl}	1000 [kg/m^3]
factor for hydraulically active fracture	1.0
thickness of the wetting water film	0.000001 [m]
residual saturation S_{wr} due to fracture roughness	0.2
surface tension for gas - water system σ_{gw}	0.0727 [Nm]
initial pressure	200000 [Pa]
final pressure	5000000 [Pa]
pressure iterations	20
initial temperature	283.3
final temperature	334.3
temperature iterations	20

Table 3.7: Parameters for the percolation model with H_2 as desolved gas according to the experiment of Jarsjö and Geller (1996)

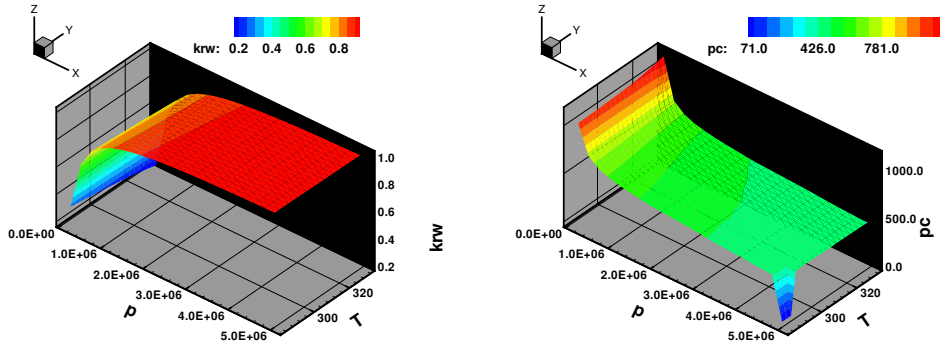

Figure 3.56: Relative permeability and capillary pressure in dependence of pressure and temperature for H_2 as desolved component

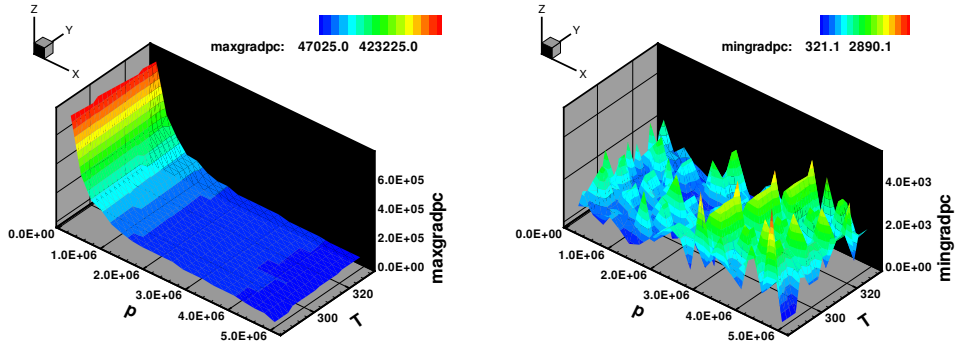

Figure 3.57: Maximum and minimum capillary pressure gradient in dependence of pressure and temperature for H_2 as desolved component

4 Numerical Model Concept

The previous chapters have explained the derivation of the physical and mathematical models. The purpose of this chapter is to present an efficient scheme for the numerical solution of the two-phase flow equations. The chapter is mostly self-contained to make clear what fundamental assumptions underly the numerical model. To device an efficient scheme, we need to determine the nature of the equations, i. e. we need to determine whether the equations are of elliptic, parabolic or hyperbolic type. This classification effects the choice of the discretization method from the broad range of algorithms for spatial and temporal discretization.

The classification is carried out in section 4.1.5, section 4.1.4 gives a short overview over existing schemes for the numerical solution of partial differential equations. After selecting an appropriate formulation in section 4.1.7, we present a fully implicit, fully coupled vertex-centered finite volume method for the two-phase flow equations. This is the main part of this chapter. The remainder of the chapter is concerned with the efficient solution of the systems of equations arising from the discretization by an inexact Newton method and a linear multigrid method.

4.1 Introduction to the Basic Equations

4.1.1 Single-Phase Fluid Flow in Fractured Porous Media

In contrast to the vast amount of competing theories considering different aspects in fluid flow in the subsurface, we are in the fortunate situation that there is only a single approach for the macroscopic momentum equation. The valid equation is by common consent of the porous media community the famous *Darcy's law*. It was found 1856 experimentally by the french engineer Henry Darcy, who investigated the flow of water in vertical homogeneous sand filters Darcy (1856).

We present Darcy's law and then consider under what circumstances Darcy's law is applicable in a single fracture.

4.1.1.1 Darcy's Law for Flow of a Single Fluid Phase in a Porous Medium

Darcy's law states that for the averaged velocity $\boldsymbol{v}$ the equation

$$\boldsymbol{v} = -K_0 \nabla h \tag{4.1}$$

holds, with the tensor of *hydraulic conductivity* K_0 and the piezometric head h,

$$h = \frac{p}{\rho g} + z. \tag{4.2}$$

$p/\rho g$ is the *pressure head* and z is the *elevation head*. The tensor of hydraulic conductivity can be split into

$$K_0 = K\frac{\rho g}{\mu}. \tag{4.3}$$

The quantities introduced in these equations and their units are:

$\boldsymbol{v}(\boldsymbol{x},t)$	The *Darcy velocity*, also called macroscopic apparent velocity. This is the velocity which is observable at the macro-scale, while the velocity in the pore channels is $\boldsymbol{v}/\Phi$.	[m/s]
$p(\boldsymbol{x},t)$	The fluid *pressure*.	$[\mathrm{Pa}] = [\mathrm{N/m^2}]$.
$\rho(\boldsymbol{x},t)$	The fluid *density*. It is either assumed to be constant for incompressible fluids or we employ as the equation of state the ideal gas law $p = \rho RT$ with the temperature T and an individual gas constant R.	$[\mathrm{kg/m^3}]$
$\mu(\boldsymbol{x},t)$	The *dynamic viscosity* of the fluid. We consider only applications where μ is constant.	[Pa/s].
$\boldsymbol{g}$	The gravity vector. It points in the direction of gravity (the z-direction unless stated otherwise) with size g, $\boldsymbol{g} = (0,0,-g)^T = (0,0,-9.81)^T$	$[\mathrm{m/s^2}]$.
$K(\boldsymbol{x})$	The symmetric tensor of *absolute permeability* or *intrinsic permeability*. It depends only on position (for heterogeneous media), not on the fluid, and may introduce anisotropy.	$[\mathrm{m^2}]$.

The form of Darcy's law that we will use is

$$\boldsymbol{v} = -\frac{K}{\mu}(\nabla p - \rho \boldsymbol{g}). \tag{4.4}$$

Despite the consent on the validity of Darcy's law, the proper assumptions for the derivation of Darcy's law from the Navier-Stokes equations are still investigated. We state the incomplete set of assumptions that the flow is laminar (so that inertial effects can be neglected), that the fluid is assumed to be Newtonian, and that a no-slip boundary condition is valid at the microscopic scale at fluid–solid interfaced. For details we refer to Hornung (1997) and Bear (1972).

Equation (4.4) is completed by the equation for macroscopic fluid mass conservation. Let the domain defined by the porous medium under consideration be $\Omega \subset \mathbb{R}^3$. Then

$$\frac{\partial(\Phi\rho)}{\partial t} + \nabla\cdot(\rho\boldsymbol{v}) = \rho q \qquad \text{in } \Omega. \tag{4.5}$$

Here we employ the porosity Φ and source and sink terms q.

$\Phi(\boldsymbol{x})$	The *effective porosity*. Although not considered in this context, the porosity may depend on the fluid pressure p and time and temperature, like in the swelling of clay or in freezing soils (see Ippisch (2001)).	[–]
$q(\boldsymbol{x},t)$	Source and sink term.	[1/s]

Inserting equation (4.4) into equation (4.5) yields

$$\frac{\partial(\Phi\rho)}{\partial t} - \nabla\cdot\left(\rho\frac{K}{\mu}(\nabla p - \rho\mathbf{g})\right) = \rho q \qquad \text{in } \Omega. \tag{4.6}$$

This equation for the unknown p is completed by appropriate initial conditions and boundary conditions at the Dirichlet boundary Γ_D and the Neumann boundary Γ_N, $\partial\Omega = \Gamma = \Gamma_D \cup \Gamma_N$:

$$p(\mathbf{x},0) = p_0(\mathbf{x}) \qquad \text{in } \Omega, \tag{4.7}$$
$$p(\mathbf{x},t) = p_D(\mathbf{x},t) \quad \text{on } \Gamma_D, \tag{4.8}$$
$$\rho\boldsymbol{\nu}\cdot\mathbf{n} = \phi(\mathbf{x},t) \qquad \text{on } \Gamma_N. \tag{4.9}$$

If the fluid is incompressible, ρ is constant and (4.6) reduces to an elliptic equation; if the fluid is compressible, the equation is of parabolic type.

The assumption that only laminar flow takes place (where viscous forces are dominant) is too restrictive in some situations. Especially in fractures with high hydrodynamic conductivity fluid flow can be very fast. According to Sahimi (1995), inertial forces become important for Reynold's numbers Re>10 if we choose the characteristic length of the Reynold's number to $\sqrt{K}$ or $\sqrt{K/\Phi}$; other authors suggest the limit for Re between 1 and 10 Bear (1972). For Re>100 turbulence occurs. Then Darcy's law is no longer valid, as well as for the transition zone between these limits. Alternatives to Darcy's law were proposed by Forchheimer (1901) and Brinkman (1947).

4.1.1.2 Single Phase Fluid Flow in a Fracture

Fluid flow in a filled fracture can be treated by Darcy's law, since a filled fracture is a porous medium. For open fractures, a different situation arises, which has been addressed by many researchers.

A very idealized approximation of an open fracture is the *parallel plate model*, also called *Hele-Shaw analog*. We will comment on the numerous limitations of this model later, but include it despite its flaws since it is the starting point for many models of fluid flow in a fracture. Assuming a setup of two parallel plates arranged at a distance b, we find that the averaged velocity between the plates is

$$\boldsymbol{\nu} = \frac{b^2}{12}\frac{1}{\mu}\nabla h. \tag{4.10}$$

This means that Darcy's law is valid in the opening if we choose $K = b^2/12$.

This relation is often called the *local cubic law*, because the volumetric flux according to equation (4.10) is

$$Q = \frac{b^3}{12}\frac{1}{\mu}\nabla h, \tag{4.11}$$

where the flux Q is proportional to the third power of the fracture width b.

Equation 4.10 can be derived from the Navier-Stokes equations, see Bear (1993). An experimental validation of the cubic law was given by Witherspoon et al. (1980).

In Singhal and Gupta (1999b) several extensions to the parallel plate model are listed. They account for non-parallel flow, turbulent flow, permeable plate walls and for wall roughness. For parallel flow with mostly smooth walls, turbulence occurs for Reynolds numbers $Re > 2400$ according to Lomize (1951), Romm (1966) or $Re > 2300$ according to Louis (1969). For rough wall surfaces, turbulence may start as early as $Re > 300$.

The cubic dependence on the fracture width can quite easily dominate other factors which influence fluid flow. This is an important consideration for laboratory experiments with rock material from great depths, because the fracture width can change considerably in the absence of the large pressure.

See also the review on open questions concerning fluid flow in fractures and fractured media in Berkowitz (2002).

4.1.1.3 Interface Conditions at Media Discontinuities

The governing equations for two-phase fluid flow in porous media are only valid if the media properties are subject to slow and smooth variation. At media discontinuities with sharp changes in properties like permeability or porosity it is necessary to introduce interface conditions which model the correct physical behavior. We adapt the approach of van Duijn, Molenaar and de Neef van Duijn et al. (1995) for the treatment of media discontinuities to the case of fractured media here.

The significant influence of the capillary pressure on the fluid flow especially at media discontinuities has been shown in laboratory experiments (Dawe et al. (1992), Kueper et al. (1989)). These results indicate that it is especially important to capture the effects of the capillary forces in the description of the interface conditions since they are responsible for trapping and pooling at media discontinuities.

The partial differential equations for two-phase flow are of second order in space. An interface condition at an inner boundary does therefore have to consist of two conditions. The first condition is dictated by requiring fluid conservation for our system, so we require continuity of the flux of the wetting phase w and the non-wetting phase n across the interface.

For the derivation of the second condition we consider two parts of the domain, a fracture Ω^f and the matrix Ω^m. (The derivation is the same if we consider lenses or layers of different materials.) We assume a mobile wetting phase in both matrix and fracture, hence we require that p_w is continuous across the fracture-matrix interface Γ. The absolute permeabilities in their respective domains are

$$K(\boldsymbol{x}) = \begin{cases} K^f(\boldsymbol{x}) & \text{if } \boldsymbol{x} \in \Omega^f, \\ K^m(\boldsymbol{x}) & \text{if } \boldsymbol{x} \in \Omega^m. \end{cases} \tag{4.12}$$

Accordingly, the porosity Φ depends on the domain as well as the capillary pressure function $p_c(S_w)$ and the relative permeability functions $k_{r\alpha}$. The capillary pressure functions $p_c(S_w)$ are shaped like the functions in figure 4.1.

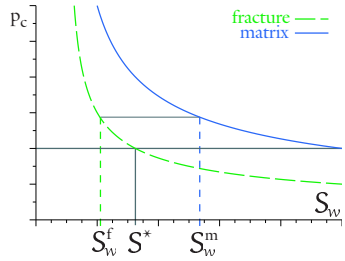

Figure 4.1: Capillary pressure curves in a rock matrix and a fracture according to the Brooks-Corey model.

Two assumptions are essential for our framework: We do not consider blocking fractures (e. g. fractures filled with clay) and assume that

- ▷ the absolute permeability in the matrix is smaller than the absolute permeability in the fractures, $K^m(\mathbf{x}) < K^f(\vec{y})$ for all $\mathbf{x}, \mathbf{y} \in \Omega$, and
- ▷ the capillary pressure function values in the matrix are larger than the capillary pressure function value in the fractures for the same saturation, $p_c^m(\mathbf{x}) > p_c^f(\mathbf{x})$ for $\mathbf{x} \in \Omega$. This implies that the entry pressure of the rock matrix is larger than the fractures.

For the Brooks-Corey capillary pressure relation, the entry pressure is positive, and there is a saturation $S_w^\star$ such that continuity of the capillary pressure can only be achieved if $S_w \leq S_w^\star$. In van Duijn et al. (1995) it is shown for a one-dimensional problem that for $S_w > S_w^\star$ the capillary pressure is discontinuous and that S_w is 1 in the matrix Ω^m. Physically, if the non-wetting phase is not present (i. e. $S_w = 1$ and $S_g = 0$), then p_g is undefined and p_c is discontinuous (p_c is not physically meaningful any more). The proposed interface condition is called extended capillary pressure condition and is

$$S_w^m = \begin{cases} 0 & \text{if } S_w^f > S_w^\star, \\ (p_c^m)^{-1}\left(p_c^f(S_w^f)\right) & \text{else.} \end{cases} \tag{4.13}$$

4.1.2 Multiphase Flow at the Microscopic Scale

The flow of a single fluid phase is driven by pressure forces due to pressure differences and gravitational forces only. If two or more phases are present in the system, a new force is introduced, the *capillary force* at the interface between the fluid phases. The capillary force has a significant influence on the fluid behavior. We will consider the micro-scale to investigate the origin and behavior of the capillary force and will then move to a continuum model on the macro scale in the next section.

4.1.2.1 Capillary Forces and the Shape of the Capillary Surface

To explain the origin of the capillary force we must retract to the the microscopic scale. If we consider a capillary tube with gas and water (figure 4.2, there is an interfacial ten-

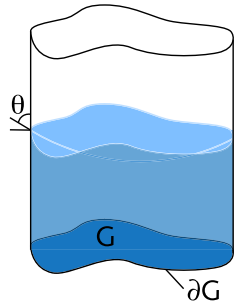

Figure 4.2: Capillary forces in a tube.

sion caused by the cohesive forces which attract molecules in a fluid to each other and adhesive forces between the solid matrix and the fluid phases. The interaction of these forces leads to a specific angle θ between the solid matrix and the interface between the phases. This contact angle depends on the fluids. It also depends on temperature and chemical constituents of the fluids, but these dependencies are neglected here.

If we want to determine the shape of the interface between two phases in a container, we must take into account the adhesive force at the wall and the capillary force at the free boundary which develops because fluid molecules are not surrounded by other fluid molecules. Following Zeidler (1995) the equation for the free surface is

$$z = u(x, y) \quad \text{in } G, \tag{4.14}$$

and u can be determined by the variational problem

$$\underbrace{\sigma \int_G \sqrt{1 + u_x^2 + u_y^2}\, dx\, dy}_{\text{energy stored by deformation}} - \underbrace{\sigma\beta \int_{\partial G} u\, ds}_{\text{work by adhesion}} - \underbrace{\int_G \rho g u\, dx dy}_{\text{work by gravitation}} = \min! \tag{4.15}$$

with the side condition

$$\int_G u\, dx dy = V. \tag{4.16}$$

σ is the surface tension, ρ is the density of the fluid, β is the relative adhesion coefficient, g is the gravitational acceleration and V is the volume of the fluid. We assume that the surface energy is proportional to the surface area and that the adhesion forces at the wall are proportional to the area of the wall wetted by the fluid. Then it is possible to prove that with

$$T := \frac{\nabla u}{|\nabla u|} \tag{4.17}$$

the variational problem satisfies

$$\operatorname{div} T = \kappa u + \lambda \quad \text{in } G, \tag{4.18a}$$

$$T\mathbf{n} = \beta \qquad \text{on } \partial G. \tag{4.18b}$$

$\mathbf{n}$ is the outward unit normal of ∂G, $\kappa = g\rho/\sigma$ is the capillary constant and

$$\lambda = \beta \frac{\text{length}(\partial G)}{\text{meas}(G)} - \kappa \frac{V}{\text{meas}(G)} \quad \text{and} \quad \cos\theta = \beta.$$

Equation (4.18a) can be written as

$$\frac{\partial}{\partial x}\left(\frac{u_x}{\sqrt{1+u_x^2+u_y^2}}\right) + \frac{\partial}{\partial y}\left(\frac{u_y}{\sqrt{1+u_x^2+u_y^2}}\right) = \kappa u + \lambda. \tag{4.19}$$

The outer unit vector to the free surface is

$$N = \frac{\boldsymbol{e}_z - u_x \boldsymbol{e}_x - u_y \boldsymbol{e}_y}{\sqrt{1+u_x^2+u_y^2}} \tag{4.20}$$

with the Cartesian basis $(\boldsymbol{e}_x, \boldsymbol{e}_y, \boldsymbol{e}_z)$. The cosine of the boundary angle θ is defined as

$$\cos\theta = -\mathbf{n}N = T\mathbf{n} \tag{4.21}$$

which implies $\cos\theta = \beta$ by the boundary condition (4.16).

The differential equation (4.15) (without gravity) dates back to papers by Young in 1805 and Laplace in 1806. The heuristic arguments in these works are still employed in the engineering literature. A rigorous approach was proposed by Gauss in 1830, based on the Lagrange multiplier rule. Note that this derivation describes the static situation. If the fluids are moving due to some external driving force, the contact angle is subject to change, as will be discussed in section 4.1.2.4.

The fluid with $\theta < 90°$ is called the *wetting fluid* because of its tendency to adhere to the solid and spread over it. The other fluid is called the *non-wetting fluid*. The *wettability* generally decreases from water over the non-aqueous phase liquid (NAPL) to gas, with water being the wetting fluid w.r.t. NAPL and gas, and NAPL being the *intermediate wetting phase* if we have a three-phase system.

4.1.2.2 Capillary Pressure

Across the interface between the wetting phase and the non-wetting phase a jump discontinuity occurs in the pressure, because the pressure p_n in the non-wetting phase is larger than the pressure p_w in the wetting phase. This jump is termed *capillary pressure* p_c,

$$p_c := p_n - p_w \geq 0. \tag{4.22}$$

For the idealized situation of two phases in a tube with a small radius r (so that we can neglect gravitational force) we find that

$$p_c = \frac{2\sigma\cos\theta}{r} \tag{4.23}$$

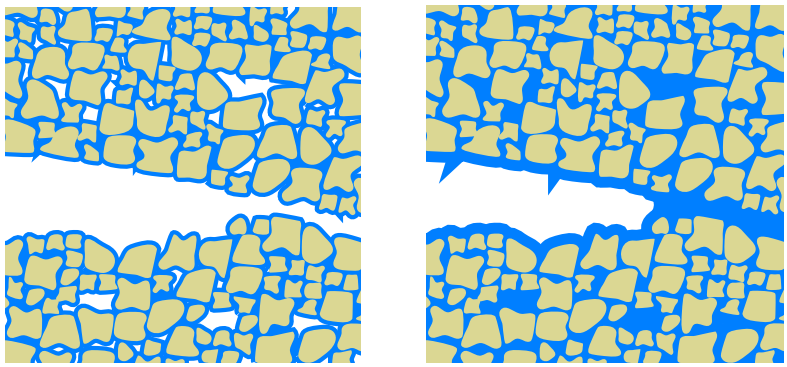

Figure 4.3: Distribution of the wetting phase for high capillary pressure and low capillary pressure.

and the capillary surface has constant mean curvature. σ is the surface tension, the ratio between the amount of work ΔW necessary to enlarge the area of the surface by ΔA, and has the unit $[J/m^2]$.

For more general geometries the Laplace equation describes the capillary pressure as

$$p_c = \sigma \left(\frac{1}{r_1} + \frac{1}{r_2} \right) \tag{4.24}$$

with the mean radii of curvature r_1 and r_2.

These equations allow for a prediction of fluid behavior in the pore space.

4.1.2.3 Capillary Behavior in the Pore Space and in Fractures

From the capillary pressure equations (4.23) and (4.24) we find that for smaller capillary tubes the capillary pressure increases and that for increasing radii of the tube the capillary pressure decreases. The consequence for a porous medium is that if the porous medium is not fully water-saturated, the water will retreat from the largest pores and reside in the small pores of the medium and that large pores of the medium will only be filled when more water is present. The static situation is described in figure 4.3; on the left only a small amount of water is present in the volume and the water is in the small pores and it is spread as a thin film over the grains. Capillary pressure is high, and little water flow can take place because the water phase is largely disconnected. The open fracture can be considered as a large pore. Consequently it contains no water. It may strike as counterintuitive, but fractures act as barriers for water flow in this situation. If large amounts of water are present, the non-wetting phase retreats to the largest pores, as shown on the right of figure 4.3. The capillary pressure is small and water flow can easily take place, especially in the fractures.

The same considerations are in principle valid for flow in a single fracture, too. However, the processes in a single fracture are complex and not yet fully understood.

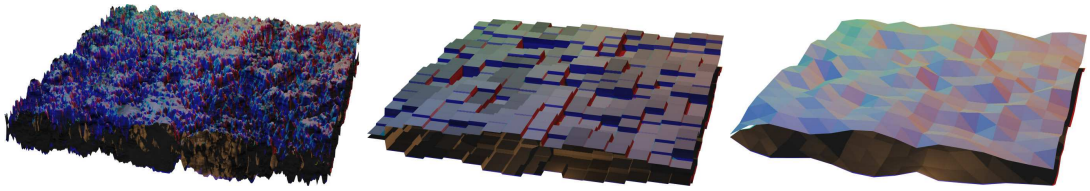

Figure 4.4: Parallel plate and sawtooth approximation of fracture walls.

A discussion of all issues concerning this problem is beyond the scope of this work; Berkowitz (2002) explains some of the difficulties.

One large complexity is introduced by fracture wall roughness. The *parallel plate model* starts by approximating fracture walls by regions of parallel plates with varying widths, see figure 4.4. For parallel plates the capillary pressure is

$$p_c = \frac{4\sigma\cos\theta}{b}, \quad \text{and} \quad b_c := \frac{4\sigma\cos\theta}{p_c}$$

is the *cut-off fracture aperture* which indicates if (for fixed p_c) the wetting phase is present ($b \leq b_c$) or if the non-wetting is present ($b > b_c$).

Recent results have shown, that this model is too simple and that wetting phase can also be present at regions of the fracture with greater width; see Jakobs (2003).

4.1.2.4 Dynamic Processes at the Micro-scale

So far we only considered equilibrium situations. If a water-saturated soil is drained (*drainage*) or if the soil is filled again with water (*imbibition*) the processes are more complex. These dynamic processes introduce *hysteresis* into the system: For an accurate description we need to take the history of a porous medium into account. The question whether we are in a drainage or imbibition process is important and has a significant influence on the flow.

We will only consider processes in one direction, i. e. only drainage or imbibition, and we assume that appropriate parameters for this process are known. If, however, we would like to explore processes where drainage and imbibition alternate hysteresis would become important and our model would have to be extended.

Contact angle hysteresis Depending on the direction of displacement, the contact angle and the capillary pressure changes. This is called *contact angle hysteresis*. Figure 4.5 shows the shape of the capillary surface for drainage, equilibrium and imbibition.

Ink bottle effect Due to the variability of the pore channel width, the fluid volume can be different for the same capillary pressure, depending on whether drainage or imbibition takes place.

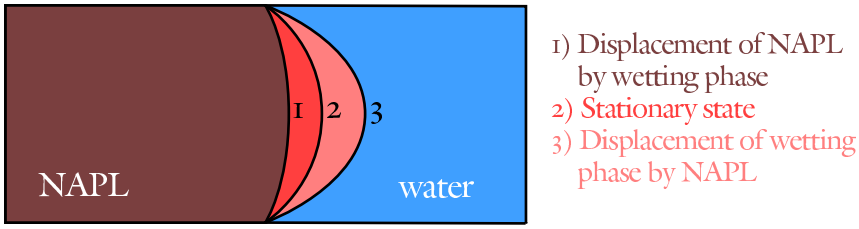

Figure 4.5: Contact angle hysteresis. The contact angle depends on the flow direction.

RESIDUAL SATURATION The displacement of one fluid phase by another may not result in complete removal of the displaced phase from the pore space. During drainage, the wetting phase retracts to smaller pores until the situation on the left in figure 4.3 is reached. The remaining wetting phase volume can not be displaced by advective processes and is called *residual saturation* (a rigorous definition is given in section 4.1.3). Phase transitions (like vaporization) can reduce the water volume below the residual saturation; however, phase transitions are not considered in this work. For the treatment of phase transitions see Ippisch (2001), Helmig (1997), Class (2001).

The similar phenomenon can be observed during imbibition where the non-wetting phase can become entrapped in large pores of the porous medium.

ENTRY PRESSURE If a porous medium is water-filled, then a certain pressure must be reached in the non-wetting phase before it can penetrate the sample. This is called the *entry pressure*, sometimes also *threshold pressure* or *bubbling pressure*. Consequently the capillary pressure must reach a certain level before displacement can take place. This effect is also important at media continuities and will be discussed later.

4.1.3 THE TRANSITION TO THE MACRO-SCALE

The sharp separation between phases at the microscopic scale does not exist on the macroscopic scale. On this scale, we employ a continuum model through averaging like in the case of the Darcy law for a single fluid phase.

Let us consider two fluid phases in the void space of a porous medium[1]. The phases are denoted by lower index w for the wetting phase and lower index n for the non-wetting phase. If we consider water-gas systems, we sometimes use lower index g to indicate the gas phase. For general phases we use greek symbols $\alpha, \beta, \gamma, \ldots$.

4.1.3.1 SATURATION

The *saturation* of a fluid phase α in the void space of an REV is

$$S_\alpha := \frac{\text{volume of fluid within the REV}}{\text{volume of voids in the REV}}. \tag{4.25}$$

[1]The discussion of more than two fluid phases can be found in Helmig (1997).

This can also be expressed by employing a phase indicator function for each point $\mathbf{x}$ in the porous media domain Ω (after Gray and Lee (1977)),

$$\gamma_\alpha(\mathbf{x},t) := \begin{cases} 1 & \mathbf{x} \in \text{phase } \alpha \text{ at time } t, \\ 0 & \text{else.} \end{cases} \tag{4.26}$$

The saturation in an REV $\Omega_0(\mathbf{x}_0)$ around $\mathbf{x}_0$ is then

$$S_\alpha(\mathbf{x}_0,t) := \int_{\Omega_0(\mathbf{x}_0)} \gamma_\alpha(\mathbf{x},t)\,d\mathbf{x} \Big/ \int_{\Omega_0(\mathbf{x}_0)} \gamma(\mathbf{x})\,d\mathbf{x}\,, \tag{4.27}$$

with the void space indicator function

$$\gamma(\mathbf{x}) = \begin{cases} 1 & \text{if } \mathbf{x} \in \text{void space} \\ 0 & \text{if } \mathbf{x} \in \text{solid matrix} \end{cases}. \tag{4.28}$$

Note the dependence on time t for $\gamma_\alpha(\mathbf{x},t)$ and $S_\alpha(\mathbf{x},t)$.

The phases fill the void space,

$$\sum_\alpha S_\alpha(\mathbf{x},t) = 1, \tag{4.29}$$

and this implies

$$S_n = 1 - S_w \quad \text{and} \quad S_w = 1 - S_n \tag{4.30}$$

in the case of two phases w and n.

4.1.3.2 Multiphase Flow Equations

For a multiphase system in a porous medium which fills the domain $\Omega \subset \mathbb{R}^3$ we require conservation of mass for each phase α separately:

$$\frac{\partial(\Phi \rho_\alpha S_\alpha)}{\partial t} + \nabla \cdot (\rho_\alpha \boldsymbol{v}_\alpha) = \rho_\alpha q_\alpha. \tag{4.31}$$

ρ_α is the density of phase α, q_α is the source term of phase α and $\boldsymbol{v}_\alpha$ is the Darcy velocity of phase α.

Under the assumption that momentum transfer between phases is negligible it can be shown by homogenization or volume averaging techniques (see Hornung (1997)) that an extension of Darcy's law holds for each phase,

$$\boldsymbol{v}_\alpha = -\frac{K_\alpha}{\mu_\alpha}(\nabla p_\alpha - \rho_\alpha \mathbf{g}) \tag{4.32}$$

The Darcy velocity now only depends on the macroscopic phase pressure p_α.

In the presence of two fluids the movement of one fluid interferes with the other, so we can expect the *phase permeability* K_α to be smaller than the absolute permeability K,

since only a smaller portion of the void space is available for fluid flow. This requires that the phase permeability depends on the saturation. The common technique to introduce this dependence into the model is by the definition of the *relative permeability* $k_{r\alpha}$. The relative permeability is used together with the absolute permeability to yield the phase permeability K_α:

$$K_\alpha = k_{r\alpha}(S_\alpha)K. \tag{4.33}$$

The relative permeability is a dimensionless factor. Functions for $k_{r\alpha}(S_\alpha)$ are given below.

4.1.3.3 Capillary Pressure Functions

The capillary pressure is also part of the macroscopic description of multiphase flow and is defined as

$$p_c(S_w) = p_n - p_w \tag{4.34}$$

for the pressure of the wetting phase p_w and the non-wetting phase p_w. From the microscopic considerations we expect that the capillary pressure is small when the porous medium is fully saturated with water. During drainage, capillary pressure increases as the water retreats to the smaller pores, until all water is removed from the the pore space or until the residual saturation S_{wr} is reached. Here we neglect the influence of temperature and fluid composition on the capillary pressure. We expect p_c to be a monotonically decreasing function which depends solely on the saturation of the wetting phase S_w. Of course we could make it also depend on S_n, since we know $S_w = 1 - S_n$ from equation (4.30).

The shape of the function depends on the pore space geometry. For very well graded materials, we observe almost linear behavior of the function, while for poorly graded media a strong nonlinearity develops. In figure 4.6, the curves for $n = 2$ (left) and $\lambda = 1/2$ (right) correspond to well sorted materials while the curves for $n = 5$ (left) and $\lambda = 4$ (right) correspond to poorly sorted material.

Two capillary pressure functions are most commonly used, which both employ the *effective saturation* S_e of the wetting phase,

$$S_e := \frac{S_w - S_{wr}}{1 - S_{wr}} \qquad S_{wr} \le S_w \le 1. \tag{4.35}$$

The effective saturation can also be defined for each phase α as

$$S_{e\alpha} := \frac{S_\alpha - S_{\alpha r}}{1 - S_{wr} - S_{nr}} \qquad S_{wr} \le S_w \le 1 - S_{rn}. \tag{4.36}$$

The decision, if S_e or $S_{e\alpha}$ is appropriate depends on the processes which take place in the porous medium. See (Helmig, 1997, pp. 66) for a discussion of this matter. We employ (4.36) throughout this work.

The first function is the *Van Genuchten capillary pressure function*, which was derived for water-gas systems:

$$p_c(S_w) = \frac{1}{\alpha}\left(S_e^{-\frac{1}{m}} - 1\right)^{\frac{1}{n}}, \tag{4.37}$$

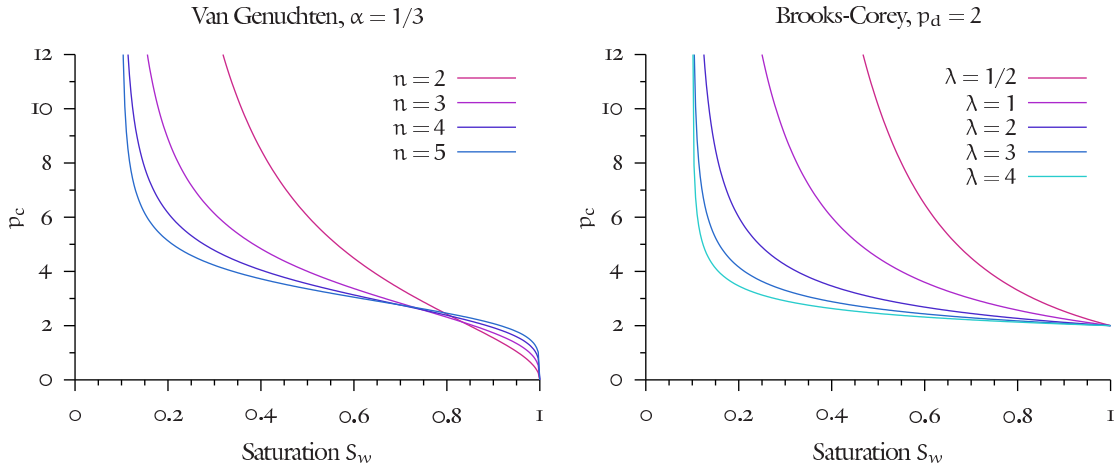

Figure 4.6: Capillary pressure functions after Van Genuchten and Brooks-Corey

with parameters α, n and m which have to be fitted to the data. m is often chosen as $m = 1 - 1/n$. α is related to the entry pressure.

The *Brooks-Corey capillary pressure function* is

$$p_c(S_w) = p_d S_e^{-\frac{1}{\lambda}}. \tag{4.38}$$

p_d is the entry pressure, and λ is related to the pore size distribution: Materials with small variations in pore size have a small λ value while materials with very different pore sizes have large λ values. Usually λ is in the range $0.2 \leq \lambda \leq 4$.

Figure 4.6 shows some examples of capillary pressure functions. Different correlations between the Brooks-Corey capillary pressure function and the Van Genuchten capillary pressure functions for equal physical conditions are compared in Ma et al. (1999). They found the correlation presented by Lenhard et al. (1989b) to be the most accurate:

$$\lambda = (n-1)\left(1 - (1/2)^{\frac{n}{n-1}}\right) \tag{4.39}$$

$$p_d = \frac{1}{\alpha}\left(0.72 - 0.35e^{-n^4}\right)^{\frac{1}{\lambda}}\left(\left(0.72 - 0.35e^{-n^4}\right)^{\frac{n}{1-n}} - 1\right)^{\frac{1}{n}} \tag{4.40}$$

The models of Brooks-Corey and van Genuchten were developed for porous media and we assume that a similar capillary pressure function exists also for fractures, either filled or open. However, the capillary pressure in a single open fracture was experimentally investigated in Bertels et al. (2001) by means of computed tomography (CT) scanning to measure aperture distribution and saturation along with capillary pressure and relative permeability. They found that the capillary pressure curve shows non-monotonic behavior, contrary to the above model. After an initial increase of capillary pressure with increased gas saturation, the capillary pressure decreases in with increasing gas saturation, probably due to local rearrangement of fluid under the influence of

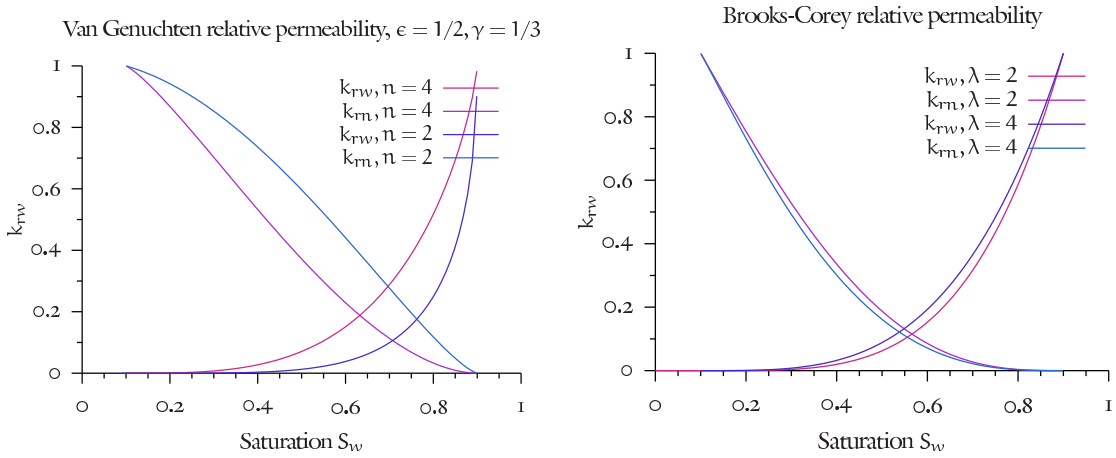

Figure 4.7: Relative permeability functions after Van Genuchten and Brooks-Corey

both capillary and viscous forces. This indicates that a macroscopic description of capillary pressure in open fractures may be inadequate.

4.1.3.4 Relative Permeability Functions

For the relative permeability $k_{r\alpha}$ we present the two models that describe $k_{r\alpha}$ as a function of S_α which are most commonly used. The *Van Genuchten relative permeability functions* are

$$k_{rw} = S_{we}^{\varepsilon}\left(1-\left(1-S_{we}^{\frac{n}{n-1}}\right)^{\frac{n-1}{n}}\right)^2, \tag{4.41}$$

$$k_{rn} = S_{ne}^{\gamma}\left(1-(1-S_{ne})^{\frac{n}{n-1}}\right)^{\frac{2(n-1)}{n}}. \tag{4.42}$$

with parameters ε and γ which are usually chosen $\varepsilon = 1/2$ and $\gamma = 1/3$.

The relative permeability functions after Brooks-Corey are

$$k_{rw}(S_w) = S_{we}^{\frac{2+3\lambda}{\lambda}}, \tag{4.43}$$

$$k_{rn}(S_w) = S_{ne}^2\left(1-(1-S_{ne})^{\frac{2+\lambda}{\lambda}}\right) = (1-S_e)^2(1-S_e^{\frac{2+\lambda}{\lambda}}). \tag{4.44}$$

The function $k_{rw}(S_w)$ increases only slowly for small saturations, because the wetting phase fills the smallest pores first where fluid flow is hindered by the strong molecular adhesion forces. Only for large values of S_w the large pores will be filled and enable easier flow, i. e. a larger k_{rw} value.

For the non-wetting fluid the increase of $k_{rn}(S_n)$ for small S_n is faster because the fluid fills the largest pores first where the fluid can flow easily. For increasing S_n values the non-wetting fluid phase fills also the smaller pores which contribute less to the overall flux rate, hence the smaller increase in the function.

4.1.3.5 The Model for Two-Phase Flow in Porous Media

The model for the flow of a wetting fluid phase w and a non-wetting fluid phase n in a porous medium which fills the domain $\Omega \subset \mathbb{R}^3$ is

$$\frac{\partial \Phi \rho_w S_w}{\partial t} + \nabla \cdot (\rho_w \boldsymbol{\nu}_w) = \rho_w q_w \quad \text{in } \Omega, \tag{4.45a}$$

$$\frac{\partial \Phi \rho_n S_n}{\partial t} + \nabla \cdot (\rho_n \boldsymbol{\nu}_n) = \rho_n q_n \quad \text{in } \Omega, \tag{4.45b}$$

$$\boldsymbol{\nu}_w = -\frac{k_{rw}}{\mu_w} K(\nabla p_w - \rho_w \mathbf{g}), \tag{4.45c}$$

$$\boldsymbol{\nu}_n = -\frac{k_{rn}}{\mu_n} K(\nabla p_n - \rho_n \mathbf{g}). \tag{4.45d}$$

This model will be used for the rest of this work. Saturation and pressure are coupled by

$$S_w + S_n = 1, \qquad \text{and} \tag{4.46}$$

$$p_n - p_w = p_c, \tag{4.47}$$

which makes only two out of the four variables p_w, p_n, S_w, and S_n independent variables.

The model has to be completed by appropriate boundary conditions and initial conditions.

$$S_w(\mathbf{x}, t) = S_{wd}(\mathbf{x}, t) \quad \text{on } \Gamma^S_{wd} \quad \text{Dirichlet BC for saturation} \tag{4.48a}$$

$$S_n(\mathbf{x}, t) = S_{nd}(\mathbf{x}, t) \quad \text{on } \Gamma^S_{nd} \tag{4.48b}$$

$$p_w(\mathbf{x}, t) = p_{wd}(\mathbf{x}, t) \quad \text{on } \Gamma^p_{wd} \quad \text{Dirichlet BC for pressure} \tag{4.48c}$$

$$p_n(\mathbf{x}, t) = p_{nd}(\mathbf{x}, t) \quad \text{on } \Gamma^p_{nd} \tag{4.48d}$$

$$\rho_w \boldsymbol{\nu}_w \cdot \mathbf{n} = \phi_w \quad \text{on } \Gamma_{wn} \quad \text{Neumann boundary condition} \tag{4.48e}$$

$$\rho_n \boldsymbol{\nu}_n \cdot \mathbf{n} = \phi_n \quad \text{on } \Gamma_{nn} \tag{4.48f}$$

$$S_w(\mathbf{x}, 0) = S_{w0}(\mathbf{x}) \quad \text{in } \Omega \quad \text{initial conditions} \tag{4.48g}$$

$$S_n(\mathbf{x}, 0) = S_{n0}(\mathbf{x}) \quad \text{in } \Omega \tag{4.48h}$$

$$p_w(\mathbf{x}, 0) = p_{w0}(\mathbf{x}) \quad \text{in } \Omega \tag{4.48i}$$

$$p_n(\mathbf{x}, 0) = p_{n0}(\mathbf{x}) \quad \text{in } \Omega \tag{4.48j}$$

4.1.3.6 Discrete Modeling and Numerical Simulation

An important reason for the development of equivalence models was the desire to make the problems accessible to numerical simulation. An important concept is the usage of lower-dimensional elements in the finite element method for the numerical solution of fluid flow. Lower-dimensional elements, called Indshell elements, have found widespread acceptance for many problems in mechanical engineering (Ciarlet, 1978). This concept has been applied for the numerical simulation of fracture networks which

neglect the influence of the matrix altogether and only model fluid flow in the fracture network. Apart from this approach, which is only justified for rocks with very small matrix conductivity, there have been finite element models which employ elements of different dimensionality. The term *discrete model* can be found in the literature for both approaches; to distinguish both we refer to the former by *discrete fracture network model*. The combination of discrete fracture network models with a continuum model is also known as hybrid models. We employ the term discrete model for our approach. Wilson and Witherspoon (1974) was one of the earliest papers on numerical simulation of water flow in fractured porous media. It contains two finite element models, one with two-dimensional elements for rock matrix and fractures and one model with one-dimensional elements for the fracture network which does not take the rock matrix into account. Gureghian (1975) formulated a finite element model in three space dimensions with tetrahedral elements in the rock matrix and triangular elements in the fractures; a similar approach is presented in Baca et al. (1984) and in Eaton and Bixler (1987). The approach of element types of different dimension is also pursued in Woodbury and Zhang (2001), Sudicky and McLaren (1998).

The investigation of unsaturated flow received less attention in the past. J. S. Y. Wang and T. N. Narasimhan (1985) modeled unsaturated flow with a discrete fracture approach. Berkowitz et al. (1988) considered solute transport in a fractured porous medium with discrete fractures modeled by one-dimensional equations and the matrix modeled by two-dimensional equations, coupled by exchange terms. In Helmig (1993) mixed-dimensional elements were employed for two-phase flow; see also ROCKFLOW (1986–2003).

4.1.4 Numerical Solution Schemes for the Two-Phase Equations

There are several difficulties which have to be dealt with in approaches to the numerical simulation for subsurface problems. We draw from the accurate description of Ewing (1983) and Bastian (1999a) and give a short overview over some of the available numerical schemes. Based on the difficulties we must expect to encounter and the properties of the available schemes, we motivate our choice.

The analysis of the two-phase flow equations in section 4.1.5 reveals the nonlinear convection-diffusion nature of the saturation equation. This is the more demanding part in the simulation process, the treatment of the elliptic equation (the pressure equation) is comparatively easy. Application of centered differences or standard Galerkin finite element methods to *transport-dominated parabolic equations* yields second order accurate schemes, but the solution can contain oscillations for non-smooth solutions. Stabilization by upwinding makes the solution monotone, but it reduces the approximation order, introduces grid dependencies into the solution and smears out sharp fronts appearing in the solution.

Capillary effects are normally neglected in reservoir engineering applications, but they play an important role on a smaller scale. For non-vanishing capillary pressure effects, the saturation equation is of *degenerate parabolic type* (instead of hyperbolic) and the numerical scheme must appropriately handle the free boundary in the solution.

Capillary pressure effects become especially apparent in the *treatment of media discontinuities* (to which we count fractures). Many numerical methods fail to reproduce the behavior of pooling, entrapment and discontinuous saturations at media discontinuities (Helmig, 1997).

In the formulation in section 4.1.5, the saturation equation is coupled to the pressure equation by the velocity derived from the pressure. An *accurate calculation of the fluid velocities* is therefore crucial for the numerical scheme.

If the frontal mobility ratio is greater than one, the macroscopic equations are unstable and *fingering* develops. This is due to numerical errors, and does not approximate the fingering process which occurs in the physical problem due to microscopic instabilities.

The *time differencing scheme* influences the solution behavior and a balanced choice between efficiency and accuracy is difficult and very problem-dependent. Explicit and implicit methods and combinations thereof are available for two-phase flow equations. With implicit schemes, fast solvers for the arising systems of nonlinear equations have to be devised. Since the pressure equation is elliptic, a fully explicit treatment of the two-phase flow problem is not possible.

Numerical simulation of multiphase flow problems has a long and remarkable history (Douglas Jr. et al., 1959, for the first numerical simulator). A widespread approach is the splitting of the treatment of the saturation equation and the pressure equation. After solving the pressure equations (with coefficients depending on saturation), one or several time steps are computed for the saturation equation with a fixed velocity field. The name IMPES (*implicit pressure, explicit saturation*) is employed for schemes which use explicit time differencing schemes for the saturation equation.

In the convection-dominated case, standard finite difference, finite element or finite volume methods have difficulties, arising either from the temporal discretization error of the backward Euler method, or from the time step size restrictions due to stability problems of the higher order Crank-Nicholson or BDF(2) schemes. An attractive alternative is the strongly stable *fractional-step-*θ *scheme*, which captures sharp fronts better than the backward Euler scheme.

High-order explicit finite volume schemes (Le Veque, 2002) have a Courant number limitation, but their evaluation is cheap. They have been applied to two-phase flow with and without capillary pressure by Durlofsky (1993) and Helmig and Huber (1999), respectively. The Essentially Non-oscillatory (ENO) and Weighted Essentially Non-oscillatory Schemes (WENO) (Shu, 1999, 1998) are based on the idea to choose an adaptive stencil which guarantees high-order approximation in regions where the solution is smooth. Then the oscillations near shocks decay with the order $O(\Delta x^k)$ for kth order approximation. However, they have not seen application to complex realistic problems yet.

An appealing approach is offered by the *characteristic methods*, which consider the characteristics of the hyperbolic part. The *modified method of characteristics* (MMOC) of Douglas Jr. and Russel (1982) interprets the temporal derivative and the advective part together as a directional derivative in the characteristic direction and then discretizes by a backward difference quotient. The method is capable of very large time

steps, but does not conserve mass and has difficulties handling Dirichlet boundary conditions. Non-mass conserving schemes can lead to false predictions of the front position (Hou and LeFloch, 1994). For nonlinear problems, the large time steps can not be taken. Another approach to characteristic methods is offered by the *Eulerian-Lagrangian localized adjoint method* (ELLAM) of Celia et al. (1990). ELLAM-type methods are mass-conservative and can treat all kinds of boundary conditions. The method uses a weighted residual formulation and chooses weight functions which have local support and solve the homogeneous adjoint equations in the interior of each space-time element. Treatment of multiphase flow problems with ELLAM is explained in Binning and Celia (1994), Ewing (1991), but no numerical results are given. It turns out that the implementation of the characteristic tracking algorithm necessary for ELLAM schemes is already very difficult for general domains in two space dimensions.

The upcoming class of discretization methods by the name *discontinuous Galerkin methods* is reviewed in chapter 4.7. See the introductions by Cockburn (1999, 1998) and the articles in Cockburn et al. (2000b) for an overview.

If the numerical simulator is supposed to handle a wide range of applications, fully coupled and fully implicit schemes which employ implicit time differencing schemes on the full system of equations are known to be very robust. The resulting equations have to be solved with a Newton method or quasi-Newton method. The robustness of the method makes it very attractive for our fields of application.

The number of discretization methods that have been combined with the fully coupled, fully implicit approach is far too large to allow a complete presentation. Apart from standard finite element methods and hp-finite element methods (Schwab, 1999), there are *control-volume finite elements* (Forsyth, 1991) and *streamline diffusion methods* (Brooks and Hughes, 1982). Highly popular, due to their mass conserving and monotone behavior, are *finite volume methods*. An overview can be found in Michev (1996). Different fully implicit methods were compared in Helmig (1997).

The choice of our method was directed by the following considerations:

- The simulator should be applied to problems in fractured porous media from the laboratory scale to the field scale. We need to be able to capture the effects of capillary pressure; this is done by including the *extended capillary pressure condition* of van Duijn et al. (1995). The simulator should be able to handle a compressible gas phase. An extension of the functionality to three-phase flow, multicomponent flow, isothermal problems,... should be possible.

- The domains we encounter are usually very complex and *unstructured meshes* are absolutely necessary. This precludes schemes which only work on structured grids.

- The numerical scheme should be *stable*, *consistent*, *monotone* and *mass conservative*. Monotonicity is important because the saturation values must lie between 0 and 1. Methods which are not locally mass conservative can fail to predict the correct location of shocks or sharp fronts (Hou and LeFloch, 1994, Le Veque, 2002).

- ▷ For the time discretization we employ the backward Euler method and the fractional-step-θ method. Both methods are strongly A-stable.
- ▷ The key ingredient for an efficient implicit scheme is the fast solution of the nonlinear systems of equations. We use an *inexact Newton scheme*. The scheme is inexact in that it only solves the arising linear systems of equations up to a given tolerance. Global convergence of the Newton method is achieved by a *line-search* algorithm. The linear systems of equations are solved with a *multigrid method*.
- ▷ Efficiency and the memory requirements of realistic applications demand to run the simulator on parallel computers with message passing architecture. *Adaptivity* can greatly reduce run-time and memory requirements.
- ▷ The software complexity of a project with the mentioned features is by orders of magnitude too large to be handled by a single person. We based our development on the software toolkit UG (Bastian et al., 1997b).

4.1.5 Character of the Equations

A successful numerical scheme for the solution of the two-phase flow equations can not be designed without careful consideration of the character of the equations. A first look at equations (4.45) seems to show two parabolic equations with diffusion-like properties. But the character is more complex, as a transformation by Chavent (1976, 1981) revealed. The transformation assumes that the densities of both phases and the porosity are constants—akin to the assumption that fluids and rock are incompressible—and that there are no gravity terms. It then defines the *total mobility*

$$\lambda(S_w, S_n) = \frac{k_{rn}}{\rho_n} + \frac{k_{rw}}{\rho_w} = \frac{k_{rn}(S_n)}{\rho_n} + \frac{k_{rw}(S_w)}{\rho_w}, \tag{4.49}$$

the phase mobility for the phases $\alpha = n, w$

$$\lambda_\alpha(S_w, S_n) = \frac{k_{r\alpha}}{\lambda \rho_\alpha} = \frac{k_{r\alpha}(S_\alpha)}{\lambda(S_w, S_n)\rho_\alpha}, \tag{4.50}$$

the *average pressure*

$$p = \frac{1}{2}(p_w + p_n) + \frac{1}{2}\int_0^{p_c} (\lambda_n(\xi) - \lambda_w(\xi))\, d\xi, \tag{4.51}$$

and the *total fluid velocity*

$$\tilde{u} = -K(x)\lambda(S_w, S_n)\nabla p. \tag{4.52}$$

If we add and subtract the two-phase flow equations (4.45) and collect terms as in Douglas jr. (1983), we arrive at the system

$$\nabla \cdot \tilde{u} \equiv -K(x)\lambda(S_w, S_n)\nabla p = \frac{q_n}{\rho_n} + \frac{q_w}{\rho_w}, \tag{4.53a}$$

$$\Phi \frac{\partial S_w}{\partial t} - \nabla \cdot (K\lambda\lambda_w\lambda_n \frac{dp_c}{dS_w} \nabla S_w) + \lambda_w \tilde{u} \cdot \nabla S_w = f(q_w, \rho_w, \lambda_w, q_n, \rho_n, \lambda_n). \tag{4.53b}$$

f is a linear function of the flow properties.

Equation (4.53a) is of elliptic type. Without the assumption that the densities of both phases and the porosity are constants, the equation takes the form of a parabolic equation, where the total compressibility of the system enters in the time derivative term; if the total compressibility is very small (as is often the case), the character of the equation is elliptic or almost elliptic.

Equation (4.53b) looks like a nonlinear convection-diffusion equation. If $S_w = 0$ or $S_n = 0$ the corresponding mobilities λ_w and λ_n vanish and the coefficients of the diffusion term degenerate in this case. The diffusion term also degenerates if capillary effects are small. In both cases the equation is of degenerate parabolic type. Degenerate parabolic equations have some of the same properties as hyperbolic equations, such as traveling wave fronts. Fronts moving through the medium will be slightly diffused by capillary pressure effects, and fingering can occur as a result of viscosity differences.

If the capillary pressure gradient dp_c/dS_w is zero, the equation (4.53b) is nonlinear hyperbolic. Since the treatment of the capillary pressure is a key component of this work, we will only briefly comment on this case.

The determination of the character of the equations does not answer the question if a solution to the equations exists. Theoretical analysis of the two-phase flow equations is in most cases done for the *global pressure formulation*. This formulation is discussed in detail in Chavent and Jaffré (1978), where also solutions to some variational formulations of the global pressure formulation are presented for the degenerate and non-degenerate incompressible case. Also in Chavent and Jaffré (1978), uniqueness was shown in the case of complete decoupling of pressure and saturation. Solutions to the degenerate parabolic equation have very low regularity (Yotov, 1997). In Schroll and Tveito (1997) the existence of classical solutions for the incompressible elliptic-hyperbolic system (with $p_c \equiv 0$) was shown. Existence of a weak solution to (4.45) was shown in Kroener and Luckhaus (1984) under the assumption that S_e is bounded away from 0 for Dirichlet and mixed boundary conditions.

4.1.6 Numerical methods for hyperbolic and degenerate parabolic equations

4.1.6.1 Nonlinear Hyperbolic Equations

The *global pressure formulation* can be reduced in the case of two incompressible fluids in one space dimension without gravity and source terms. By imposing the boundary and initial conditions

$$S_w(0,t) = S \qquad S_w(x,0) = S_{w0}(x) \tag{4.54}$$

the problem can be written in the form known as the *Buckley-Leverett equation*:

$$\frac{\partial S_w}{\partial t} + \frac{\partial}{\partial x} f(S_w) = 0 \tag{4.55}$$

with the nonlinear *fractional flow function* f,

$$f(S_w) = \frac{U}{\Phi} \frac{k_{rw}(S_w)}{k_{rw}(S_w) + \frac{\mu_w}{\mu_g} k_{rg}(1 - S_w)} \tag{4.56}$$

U is the constant *total velocity*. The Buckley-Leverett problem as a simple example of a nonlinear hyperbolic equation gets extensive treatment in several excellent sources: Le Veque (1992) and the recent, largely upgraded monograph Le Veque (2002) are devoted to hyperbolic equations. See also Bear (1972), Renardy and Rogers (1993), Bastian (1999a).

Some of the important insights gained from the hyperbolic case, which are covered in the above references, are as follows.

FRONT CAPTURING. Solutions to hyperbolic equations can contain discontinuities, which in the case of nonlinear hyperbolic equations can arise even from smooth initial data. Much of the work on the numerical solution of hyperbolic equations is concerned with the treatment of discontinuities or *sharp fronts*. A successful numerical schemes should be able to represent the sharp front without the addition of artificial diffusion and it should avoid to produce oscillations near the shock. Oscillations occur for higher order methods, and many high resolution methods have been developed based on flux limiters (Le Veque, 2002). In the case of nonlinear hyperbolic equations the smearing of sharp fronts in the numerical solution can be weakened due to the self-sharpening effect arising from the nonlinearities. An important concept is the TVD property (*total variation diminishing*), which—if satisfied—prevents oscillations near a shock.

STABILITY. A necessary (though not sufficient) condition for the stability of a numerical scheme for the solution of hyperbolic equations was presented in the landmark paper by Courant et al. (1928) and is named Courant-Friedrichs-Lewy condition or *CFL condition*:

$$\frac{|v_{max}| \Delta t}{\Delta x} < 1. \tag{4.57}$$

It describes the maximal possible time step Δt. $|v_{max}|$ is the maximum velocity.

ENTROPY SOLUTIONS AND JUMP CONDITIONS In some situations the weak solution to a hyperbolic equation is not unique and an additional condition is required to find the physically relevant solution. This is the *vanishing viscosity solution* which is the solution obtained by considering an additional viscosity term and choosing the limiting solution for vanishing viscosity. Convergence to this solution can be obtained by imposing an *entropy condition*; the resulting solution is called the *entropy solution*. An additional requirement in the case of nonlinear hyperbolic equations is that the shock jump must obey the *Rankine-Hugoniot condition*.

FINGERING. The *frontal mobility ratio* is defined by

$$M = \frac{k_{r\alpha}(S\triangleright)}{k_{r\beta}(\triangleright S)} \cdot \frac{\mu_\beta}{\mu_\alpha}, \tag{4.58}$$

where α denotes the displacing fluid and β the displaced fluid. $S\triangleright$ is the saturation of the displacing fluid behind the front, $\triangleright S$ is the saturation of the displaced fluid ahead of the front. If $M > 1$, the position of the shock front is unstable in the multidimensional case (Bear, 1972, Kueper and Frind, 1988, Glimm et al., 1981, 1983). This leads to the effect of *fingering* in the solution.

4.1.6.2 DEGENERATE PARABOLIC EQUATIONS

A simple example for a degenerate parabolic equation is the *porous medium equation* (Evans, 1998). It has the form of a nonlinear diffusion equation,

$$\partial_t u - \Delta(u^\gamma) = 0 \qquad \text{in } \mathbb{R}^d \times (0,\infty) \tag{4.59}$$

with $u \geq 0$ and $\gamma > 1$. An analytic solution to this equation can be found by separation of variables, which yields the solution

$$\alpha = \frac{2}{\gamma - 1} \qquad \mu = \alpha\gamma(\alpha\gamma + d - 2) \tag{4.60}$$

$$u(x,t) = ((1-\gamma)\mu t + \lambda)^{\frac{1}{1-\gamma}} |x|^\alpha, \tag{4.61}$$

with a constant $\lambda > 0$. Another solution was found by Barenblatt,

$$\alpha = \frac{d}{d(\gamma-1)+2} \qquad \beta = \frac{1}{d(\gamma-1)+2} \tag{4.62}$$

$$u(x,t) = \frac{1}{t^\alpha}\left(b - \frac{\gamma-1}{2\gamma}\beta\frac{|x|}{t^{2\beta}}\right)^{\frac{1}{1-\gamma}}, \tag{4.63}$$

with a constant b. In figure 4.8 the solution curves for $\gamma = 7/8$, $d = 2$, $b = 1$, $\lambda = 2$, $t = 1, 10, 100$ are plotted. A feature of the solution u of (4.59) is that it has compact support for $t > 0$ and that the partial differential equation becomes degenerate for $u = 0$. The set $\{u > 0\}$ moves with finite propagation speed, which is why it is sometimes considered a better model of diffusive spreading than the linear heat equation (according to which an infinite information propagation speed is possible).

An example for a parabolic equation that can be derived from the two-phase flow equations (4.45) is the *McWhorter problem* by McWhorter and Sunada (1990); it is also treated in Bastian (1999a), Helmig (1997). For the unknown S_w the McWhorter problem reads

$$\Phi\frac{\partial S_w}{\partial t} + \frac{\partial}{\partial x}\left(\lambda_n f_w \frac{dp_c}{dS_w} K \frac{\partial S_w}{\partial x}\right) \tag{4.64}$$

The numerical treatment of parabolic equations is presented in Thomée (1997).

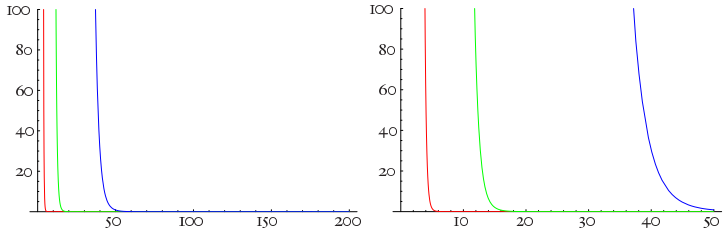

Figure 4.8: Solutions to the porous medium equation (4.59) by separation of variables (left) and Barenblatt's solution (right) for $t = 1, 10, 100$.

4.1.7 Phase Pressure-Saturation Formulation

The transformation of the multi-phase flow equations (4.45) in section 4.1.5 is not applicable to our field of investigation, because the gas phase is compressible. Instead we choose a fully coupled approach based on the Phase pressure-Saturation formulation. As already mentioned, only two out of the four variables p_w, p_g, S_w, and S_g in the two equations (4.45) can be chosen as independent variables. We choose the substitutions

$$S_w = 1 - S_g, \qquad p_g = p_w + p_c(1 - S_g) \tag{4.65}$$

to obtain the (p_w, S_g) *formulation*. Other choices are possible, see Helmig (1997). We would like to note that the difference between the (p_w, S_g) formulation and the (p_w, S_w) formulation reduces to inserting $1 - S_w$ for S_g. Because of this, we write S_w and S_g in the following to facilitate reading. Of course the same argumentation is not applicable for p_w and p_g, because the choice of p_w as an independent variable has larger implications. Formulations based on p_w assume that the water phase is present everywhere in the domain. Because we consider problems in initially fully water-saturated domains with a residual water saturation (i. e. the water phase is never completely replaced by gas) this is the appropriate choice.

The equations now read

$$\frac{\partial(\Phi\rho_w(S_w))}{\partial t} - \nabla\cdot(\rho_w\frac{k_{rw}}{\mu_w}K(\nabla p_w - \rho_w\mathbf{g})) \qquad -\rho_w q_w = 0, \tag{4.66a}$$

$$\frac{\partial(\Phi\rho_g(S_g))}{\partial t} - \nabla\cdot(\rho_g\frac{k_{rg}}{\mu_g}K(\nabla p_w + \nabla p_c(S_w) - \rho_g\mathbf{g})) \; -\rho_g q_g = 0, \tag{4.66b}$$

where we used S_w for $1 - S_g$. We consider these equations in $(0,T)\times\Omega$. $\Omega \subset \mathbb{R}^d, (d = 2,3)$ is a domain with polygonal or polyhedral boundary for $d = 2$ and $d = 3$ respectively. The equations are complemented with initial conditions and boundary conditions of Neumann or Dirichlet type

$$p_w(\mathbf{x},0) = p_{w0}(\mathbf{x}) \qquad S_g(\mathbf{x},0) = S_{g0}(\mathbf{x}) \quad \forall \mathbf{x} \in \Omega\,, \tag{4.67a}$$

$$p_w(\mathbf{x},t) = p_{wd}(\mathbf{x},t) \text{ on } \Gamma_{wd} \qquad S_g(\mathbf{x},t) = S_{gd}(\mathbf{x},t) \text{ on } \Gamma_{gd}\,, \tag{4.67b}$$

$$\rho_w\boldsymbol{\nu}_w\cdot\mathbf{n} = \phi_w(\mathbf{x},t) \text{ on } \Gamma_{wn} \qquad \rho_g\boldsymbol{\nu}_n\cdot\mathbf{n} = \phi_g(\mathbf{x},t) \text{ on } \Gamma_{gn}. \tag{4.67c}$$

If both phases are incompressible no initial condition for p_w is required. Γ^p_{wd} should have positive measure to determine p_w uniquely.

In the following we assume the dependencies

$$\begin{array}{llll} g = & \text{constant} & q_\alpha = & q_\alpha(x,t) \\ p_c = & p_c(x,S_w) & k_{r\alpha} = & k_{r\alpha}(x,S_\alpha) \\ \rho_\alpha = & \rho_\alpha(p_\alpha) & \mu_\alpha = & \mu_\alpha(p_\alpha) \\ \Phi = & \Phi(x) & & \end{array} \tag{4.68}$$

The influence of fractures on the fluid flow is included through the dependency of the quantities in equation (4.68) on the position, i. e. the values are different depending on whether they are evaluated in a fracture or in the rock matrix.

A similar derivation as the one leading to (4.66) produces the (p_g, S_w) *formulation*. This is the appropriate formulation if S_g is bounded away from 0. The choice of (p_w, p_g) as the primary unknowns is called the *pressure-pressure formulation* or (p_w, S_g) *formulation*. In the (p_w, S_g) formulation the saturation is computed from the capillary pressure function by inversion, $S_w = p_c^{-1}(p_n - p_w)$. Obviously, the pressure-pressure formulation requires that S_w *and* S_g are bounded away from 0.

4.2 The Finite Volume Method

In this section we describe the vertex-centered *finite volume method* which was devised after the considerations in section 4.1.4. The method is based on the finite volume method in Bastian (1999a) and is extended for fully coupled treatment of volumetric matrix elements and lower-dimensional fracture elements. Finite volume methods are presented in Michev (1996), Bey (1998). Their close relation to the finite element method was revealed in Hackbusch (1989). A recent application to two-phase flow can be found in Michel (2003). The finite volume method is sometimes called finite volume element method. In the engineering literature it is often called *Control Volume FEM*, Bank and Rose (1987), Hackbusch (1989) use the term *box method*.

4.2.1 Geometry of the Problem and the Primary and Secondary Mesh

In the previous section the domain was only specified with respect to the shape of its boundary and without the description of fractures. Some assumptions on the fracture network which are essential for the discretization method are described. In the following superscript m notation denotes entities in the volumetric rock matrix and superscript f denotes entities in the fracture network.

Let $\Omega \subset \mathbb{R}^d$ be a polygonal or polyhedral domain for $d = 2$ or $d = 3$, respectively. The domain contains a nonempty set of fractures $\{f_1, \ldots, f_F\}$. Each fracture f_i is a $(d-1)$-dimensional object—i. e. we identify each fracture with its middle surface—and each fracture f_i has a width w_i associated with it, which may be variable in the fracture. For simplicity we assume the fractures to have a planar geometry: In a two-dimensional

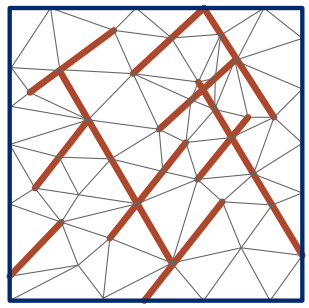

Figure 4.9: Example domain with fractures and mesh resolving the fracture network geometry.

domain the fractures are line segments and in a three-dimensional domain we assume polygonal shape of the fractures (although circular or elliptic shapes can also be treated by the method, as well as non-planar shapes). The union of the fractures constitutes the fracture network

$$\Omega^f = \bigcup_{i=1}^{F} f_i \subset \Omega. \tag{4.69}$$

The domain of the rock matrix Ω^m is the whole domain,

$$\Omega^m = \Omega. \tag{4.70}$$

This means that the domains of the fracture network and the rock matrix overlap.

The discretization method requires a mesh for Ω^m and Ω^f. For the volumetric mesh we consider a *subdivision* E_h^m of Ω^m into K elements e, $E_h^m = \{e_1, \dots, e_K\}$. By Ω_e we denote the sub-domain covered by element e and we require $\bigcup_e \overline{\Omega_e} = \overline{\Omega}$ and $\Omega_e \cap \Omega_f = \emptyset$ for $e \neq f$. h denotes the diameter of the largest element. The subdivision has to resolve the geometry of the fractures f_i, comparable to domains with inner boundaries. Figure 4.9 shows an example for a two-dimensional mesh. The volumetric elements Ω_e of E_h^m are triangles or quadrilaterals in two dimensions and tetrahedra, pyramids, prisms, or hexahedra in three dimensions. Hybrid grids, i. e. grids of mixed element type are admissible, for any grid we require that E_h^m is a *triangulation*: No vertex of an element lies in the interior of a side of another element.

The volumetric elements are complemented with lower dimensional elements on the fractures which are line elements for two-dimensional problems and triangles or quadrilaterals for three-dimensional problems. The fracture elements constitute a mesh $E_h^f = \{f_1, \dots, f_{K^f}\}$ which is conforming with the volumetric mesh, i. e. each Ω_e^f is an element side or face for the two-dimensional and three-dimensional case, respectively.

The vertex centered finite volume method requires the construction of a secondary mesh B_h^m. For the volumetric mesh it is constructed by connecting element barycenters with edge midpoints as shown in figure 4.10 in two dimensions. In three dimensions, first the element barycenters are connected to element face barycenters and then these are connected with edge midpoints. Vertices of the grid are denoted by v_i and their corresponding coordinate vector by $\mathbf{x}_i$. By construction each *control volume* contains exactly

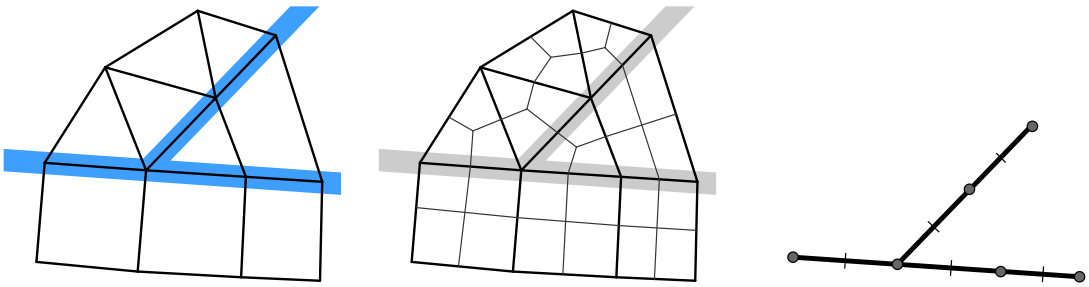

Figure 4.10: Mesh, dual grid and fracture elements/volumes.

one vertex, and the control volume containing vertex v_i is denoted by b_i^m. The generation of the dual grid for the fractures happens in the same way for two-dimensional fractures. One-dimensional elements are simply divided into equal parts. This construction results in a conforming dual mesh for volumetric and fracture elements. The fracture dual mesh is denoted B_h^f.

The construction of the dual grid can happen in alternative ways and the requirements on the dual grid are quite general (Bey, 1998, Michev, 1996).

The *internal skeleton* of the volumetric dual grid consists of the sides of the control volumes. The edge between control volume b and b' inside of element e is denoted by

$$\gamma_{e,b,b'} = \overline{\Omega}_e \cap \overline{\Omega}_b \cap \overline{\Omega}_{b'} \quad \text{for } e \in E_h^m,\ b, b' \in B_h^m \tag{4.71}$$

and the union of all internal edges of the volumetric dual grid is denoted by

$$\Gamma_{int}^m = \{\gamma_{e,b,b'} \mid e \in E_h^m,\ b, b' \in B_h^m\}. \tag{4.72}$$

For the fracture dual grid the intersection of control volume b and b' on the edge between elements e and f is

$$\gamma_{e,f,b,b'} = \overline{\Omega}_e \cap \overline{\Omega}_f \cap \overline{\Omega}_b \cap \overline{\Omega}_{b'} \quad \text{for } e, f \in E_h^f,\ b, b' \in B_h^f \tag{4.73}$$

and the union of all internal control volume intersections (which are points for one-dimensional fractures and edges for two-dimensional fractures) of the fracture dual grid is denoted by

$$\Gamma_{int}^f = \{\gamma_{e,f,b,b'} \mid e, f \in E_h^f,\ b, b' \in B_h^f\}. \tag{4.74}$$

In the two-dimensional case, $\gamma_{e,f,b,b'}$ is already determined uniquely by e and f (or b and b'), but in the three-dimensional case all four are needed.

The external skeleton is the union of the element sides on the domain boundary, defined for the volumetric dual mesh and the fracture dual mesh,

$$\Gamma_{ext}^m = \{\gamma_{e,b} \mid \gamma_{e,b} = \partial\Omega_e \cap \partial\Omega_b \cap \partial\Omega \text{ for } e \in E_h^m,\ b \in B_h^m\}, \tag{4.75}$$

$$\Gamma_{ext}^f = \{\gamma_{e,f,b} \mid \gamma_{e,f,b} = \partial\Omega_e \cap \partial\Omega_f \cap \partial\Omega_b \cap \partial\Omega \text{ for } e \in E_h^f,\ b \in B_h^f\}. \tag{4.76}$$

With each element of the skeleton we associate a fixed unit normal $\mathbf{n}$. For $\gamma \in \Gamma_{ext}^{m}$ and $\gamma \in \Gamma_{ext}^{f}$ we choose the outward unit normal. For interior sides the direction of $\mathbf{n}$ is chosen arbitrarily, but fixed.

For any function f defined on Ω, which may be discontinuous on Γ_{int}^{m} and Γ_{int}^{f}, we define the jump of f at $\mathbf{x} \in \gamma \in \Gamma_{int}$ to be

$$[v](\mathbf{x}) = \lim_{\epsilon \to 0+} v(\mathbf{x} + \epsilon \mathbf{n}) - \lim_{\epsilon \to 0+} v(\mathbf{x} - \epsilon \mathbf{n}). \tag{4.77}$$

4.2.2 The Approximation Spaces

For the discretization we introduce the standard conforming, piecewise linear finite element spaces in the matrix and fracture domain

$$V_h^m = \{v \in C^0(\overline{\Omega^m}) \mid v \text{ is linear on } \overline{\Omega}_e \in E_h^m\}, \tag{4.78}$$

$$V_h^f = \{v \in C^0(\overline{\Omega^f}) \mid v \text{ is linear on } \overline{\Omega}_e \in E_h^f\}, \tag{4.79}$$

and the non-conforming test space W_h (based on the secondary mesh)

$$W_h = \{w \in L^2(\Omega^m) \mid w \text{ is constant on each } b_i \in B_h^m\}, \tag{4.80}$$

$$W_h^f = \{w \in L^2(\Omega^f) \mid w \text{ is constant on each } b_i^f \in B_h^f\}. \tag{4.81}$$

Figure 4.11 shows two basis functions for V_h^m and V_h^f. Depending on the element type, the term *linear* has to be replaced by *multi-linear* in (4.78),(4.79) as well as in the following (e.g. for quadrilaterals).

We will only describe the treatment of homogeneous Dirichlet-type boundary conditions to keep the presentation free from notational abundance. The subspaces for homogeneous Dirichlet boundary conditions for fracture and matrix and the both phases $\alpha = g, w$

$$V_{h\alpha 0}^{\tau} = \{v \in V_h^{\tau} \mid v|_{\Gamma_{\alpha d}} = 0\}, \tag{4.82}$$

$$W_{h\alpha 0}^{\tau} = \{w \in W_h^{\tau} \mid w|_{\Gamma_{\alpha d}} = 0\}, \tag{4.83}$$

with $\tau = m, f$. General Dirichlet boundary conditions can be treated as in Bastian (1999a). In the case of inhomogeneous Dirichlet boundary conditions it is necessary to employ separate function spaces for water pressure and gas saturation, which adhere to the respective boundary conditions. These spaces can also depend on time, a feature which is also not treated here. This is only a notational convenience and at all times $V_{h\alpha 0}^{\tau}$ and $W_{h\alpha 0}^{\tau}$ should be thought of as $V_{h\alpha 0}^{\tau}(t)$ and $W_{h\alpha 0}^{\tau}(t)$.

The phase saturations S_n and S_w are a discontinuous quantity at interfaces between media with different properties as well as at all vertices $\mathbf{v}_i \in \Omega_h^f$, because these vertices are shared by the rock matrix and the fracture network. A discontinuous saturation can not be represented by the standard conforming finite element spaces V_h^m and V_h^f so instead we choose discontinuous saturation spaces

$$S_h^m = \{v \in L^2(\Omega^m) \mid v|_{\Omega_e} \text{ linear for } \Omega_e \in E_h^m\}, \tag{4.84}$$

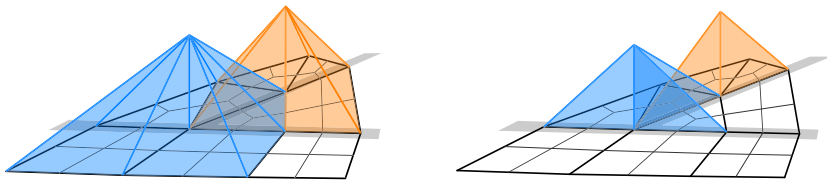

Figure 4.11: Basis functions for volumetric elements and fracture elements.

$$S_h^f = \{v \in L^2(\Omega^f) \mid v|_{\Omega_e} \text{ linear for } \Omega_e \in E_h^f\}. \tag{4.85}$$

By means of the mappings Π^m and Π^f,

$$\Pi^m : V_h^m \to S_h^m, \tag{4.86}$$
$$\Pi^f : V_h^f \to S_h^f, \tag{4.87}$$

it is possible to formulate the discretization by the conforming finite element functions from the previous section, but to employ the correct discontinuous saturation function wherever appropriate. These mappings employ the extended interface conditions from section 4.1.1.3.

S_h^m is only continuous within elements so we define the mapping for a given $\mathbf{x} \in \Omega_e$. The values of the function

$$s_h^m = \Pi^m v_h \quad v_h \in V_h^m,\, s_h \in S_h^m \tag{4.88}$$

are uniquely determined by the values of s_h in the corners of Ω_e by

$$s_h(\mathbf{x}) = \Pi^m v_h(\mathbf{x}) = \sum_{i \in V(e)} S_i^e \varphi_i^m(\mathbf{x}) \tag{4.89}$$

where $V(e)$ is the set of indices of the corner vertices of Ω_e and the value S_i^e at corner vertex v_i is found by

$$S_i^e = \begin{cases} v(\mathbf{x}_i) & \text{if } p_c(\mathbf{x}^e, 1 - v(\mathbf{x}_i)) = p_{cmin}(\mathbf{x}_i), \\ 0 & \text{if } p_{cmin}(\mathbf{x}_i) < p_c(\mathbf{x}^e, 1), \\ 1 - S & \text{else, with } S \text{ from } p_c(\mathbf{x}^e, S) = p_{cmin}(\mathbf{x}_i). \end{cases} \tag{4.90}$$

Here we employ the *minimal capillary pressure function* $p_{cmin}(\mathbf{x})$ defined as

$$p_{cmin}(\mathbf{x}) = \min_{\Omega_e \in E(\mathbf{x})} p_c(\mathbf{x}^e, 1 - v(\mathbf{x})). \tag{4.91}$$

$E(\mathbf{x})$ is the set of elements which contain $\mathbf{x}$ in their closure,

$$E(\mathbf{x}) = \{\Omega_e \in \Omega^m \cup \Omega^f \mid \mathbf{x} \in \overline{\Omega_e}\}. \tag{4.92}$$

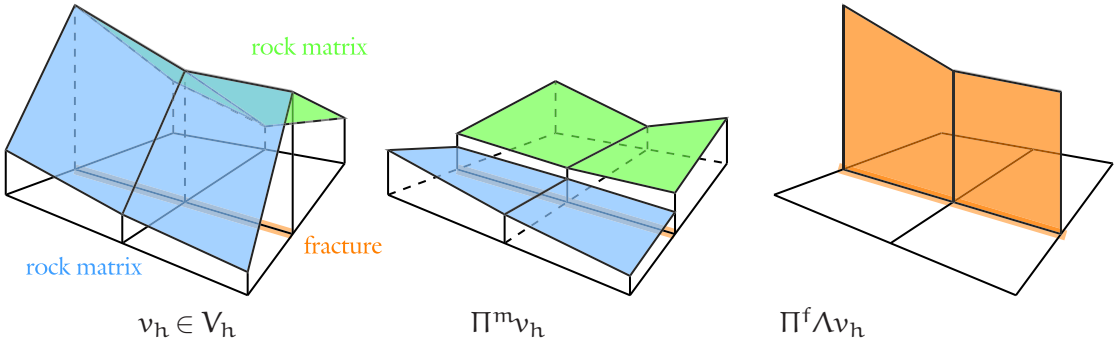

Figure 4.12: A function $v_h \in V_h$ and the mapping into the saturation spaces, $\Pi^m v_h$ and $\Pi^f \Lambda v_h$.

For fractures the same construction is employed, only that the fracture basis functions are used instead of matrix basis functions,

$$s_h(\mathbf{x}) = \Pi^f v_h(\mathbf{x}) = \sum_{i \in V(e)} S_i^e \varphi_i^f(\mathbf{x}) \quad \text{for } s_h \in S_h^f, v_h \in V_h^f \tag{4.93}$$

The connection between the spaces V_h^m and V_h^f is created by the projection Λ. So far, V_h^m and V_h^f have been treated as separate spaces with separate unknowns in the vertices of the grid. The projection

$$\begin{aligned} \Lambda : V_h^m &\to V_h^f \\ v_h^m &\mapsto v_h^f \quad \text{with } v_h^m(\mathbf{x}) = v_h^f(\mathbf{x}) \text{ for all } \mathbf{x} \in \Omega^f. \end{aligned} \tag{4.94}$$

is the function which maps the finite element function v_h^m defined in the matrix to the finite element function v_h^f defined in the fracture network whose values coincide in the fracture network. Figure 4.12 shows a function $v_h \in V_h$ and the mappings $\Pi^m v_h$ into the matrix space and $\Pi^m \Lambda v_h$ into the fracture space.

4.2.3 Weak Formulation

The weak formulation of equations (4.66) for the rock matrix is found by multiplying with the test functions and integration by parts. The resulting weak formulation of the two-phase flow problem in the matrix is (we suppress the time dependencies for notational convenience, and write p_{wh}, S_{gh} for $p_{wh}(t)$, $S_{gh}(t)$):

Find $p_{wh} \in V_{hw0}$ *and* $S_{gh} \in V_{hg0}$ *such that for all* $w_{gh}^m \in W_{hg0}^m$, $w_{wh}^m \in W_{hw0}^m$ *and* $0 < t < T$

$$\begin{aligned} \frac{\partial}{\partial t} \sum_{b \in B_h^m} \int_b \Phi \rho_w (1 - \Pi^m S_{gh}) \, d\mathbf{x} + \sum_{\gamma \in \Gamma_{int}^m} \int_\gamma \rho_w \mathbf{v}_w \cdot \mathbf{n} [w_{wh}^m] \, ds \\ + \sum_{\gamma \in \Gamma_{ext}^m \cap \Gamma_{wn}} \phi_w w_{wh}^m \, ds - \sum_{b \in B_h^m} \int_b \rho_w q_w \, d\mathbf{x} = 0 \end{aligned} \tag{4.95a}$$

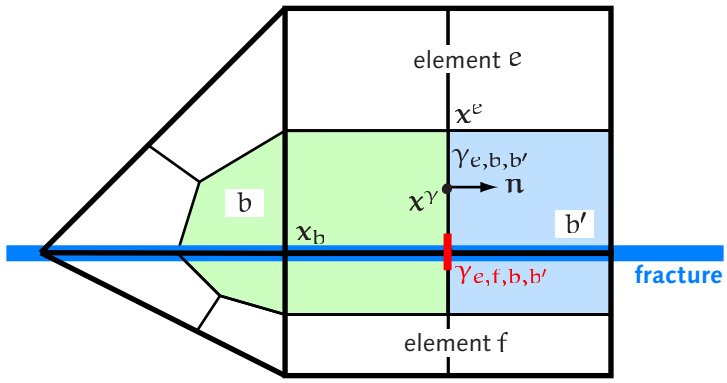

Figure 4.13: Notation for control volumes

$$\begin{aligned}\frac{\partial}{\partial t}\sum_{b\in B_h^m}\int_b \Phi\rho_g\Pi^m S_{gh}\,dx + \sum_{\gamma\in\Gamma_{int}^m}\int_\gamma \rho_g v_g\cdot n[w_{gh}^m]\,ds \\ + \sum_{\gamma\in\Gamma_{ext}^m\cap\Gamma_{gn}}\phi_g w_{gh}^m\,ds - \sum_{b\in B_h^m}\int_b \rho_g q_g\,dx = 0\end{aligned} \tag{4.95b}$$

In the equations the first term is called the accumulation term, the second term is the internal flux term, the third is the boundary flux term and the fourth the source and sink term. For the numerical evaluation of the accumulation term we employ a midpoint rule, which corresponds to the mass lumping approach in the finite element method. The Darcy velocities in the interior flux terms are evaluated with an upwind scheme. For the water phase this is for a given side $\gamma = \gamma_{e,b,b'}$

$$\int_\gamma \rho_w v_w\cdot n[w_h]\,ds = \int_\gamma \rho_w \lambda_{w\gamma}^\star \tilde{v}_w\cdot n[w_h]\,ds \tag{4.96}$$

with the upwind evaluation of the mobility

$$\lambda_{w\gamma}^\star = (1-\beta)\lambda_{wh}(x^\gamma) + \beta\cdot\begin{cases}\lambda_{wh}(x_b) & \text{if } \tilde{v}_w\cdot n \geq 0\\ \lambda_{wh}(x_{b'}) & \text{else}\end{cases} \tag{4.97}$$

and the directional part of the velocity

$$\tilde{v}_w = -K(x^e)(\nabla p(x^\gamma) - \rho_w(x^\gamma)g) \tag{4.98}$$

x^γ is the center of γ and x_b is the grid vertex inside control volume b. The source and sink terms and the boundary flux terms are evaluated by the midpoint rule. The same evaluation scheme is employed for the gas phase saturation. The parameter β controls the upwinding strategy. For $\beta = 1$ fully upwinding is achieved, while $\beta = 0$ results in a central differencing scheme. We employ a fixed β, but adaptive choices depending on the local Peclet number are possible (Michev, 1996). There is also the possibility to

choose fixed, but different β for fracture and matrix discretization, akin to the assumption that the flow processes in the matrix are not convection dominated opposed to the fractures. The full-upwinding scheme is known to introduce grid-dependencies into the solution, which disappear if sufficiently fine grids are employed. Unfortunately, this resolution is extremely small for gas-water problems and some numerical artifacts must be expected.

The forms defined in (4.95) can be abbreviated as the vector-valued form

$$m^m(p_{wh}, S_{gh}, w^m_{wh}, w^m_{gh}) + a^m(p_{wh}, S_{gh}, w^m_{wh}, w^m_{gh}) = 0,$$

where we collect the accumulation terms in $m^m(\cdot,\cdot,\cdot,\cdot)$ and the internal and boundary flux terms and source and sink terms in $a^m(\cdot,\cdot,\cdot,\cdot)$. Note that both w^m_{wh} and w^m_{gh} are only necessary if Dirichlet boundary conditions are present in different parts of the boundary for p_w and S_g.

The corresponding form for the fracture space $m^f(\cdot,\cdot,\cdot,\cdot) + a^f(\cdot,\cdot,\cdot,\cdot)$ is derived by replacing superscript m with f and not using p_w and S_g directly in $m^f(\cdot,\cdot,\cdot,\cdot) + a^f(\cdot,\cdot,\cdot,\cdot)$, but using their projections to the fracture space. The weak formulation is: *Find* $p_{wh} \in V_{hw0}$ *and* $S_{gh} \in V_{hg0}$ *such that for all* $w^f_{gh} \in W^f_{hg0}$, $w^f_{wh} \in W^f_{hw0}$ *and* $0 < t < T$

$$m^f(\Lambda p_{wh}, \Lambda S_{gh}, w^f_{wh}, w^f_{gh}) + a^f(\Lambda p_{wh}, \Lambda S_{gh}, w^f_{wh}, w^f_{gh}) = 0.$$

Note that w^f_{wh} and w^f_{gh} are just a notational convenience: The fracture space test functions are related to the matrix space test functions by the projection $\Xi : w^m_{\alpha h} \mapsto w^f_{\alpha h}$.

The final formulation of the coupled scheme is now found by adding the two bilinear forms: *Find* $p_{wh} \in V_{hw0}$ *and* $S_{gh} \in V_{hg0}$ *such that for all* $w_{gh} \in W^m_{hg0}$, $w_{wh} \in W^m_{hw0}$ *and* $0 < t < T$

$$m(p_{wh}, S_{gh}, w_{wh}, w_{gh}) + a(\Lambda p_{wh}, \Lambda S_{gh}, \Xi w_{wh}, \Xi w_{gh}) = 0 \tag{4.99}$$

where $m(\cdot,\cdot,\cdot,\cdot) = m^m(\cdot,\cdot,\cdot,\cdot) + m^f(\cdot,\cdot,\cdot,\cdot)$ and $a(\cdot,\cdot,\cdot,\cdot) = a^m(\cdot,\cdot,\cdot,\cdot) + a^f(\cdot,\cdot,\cdot,\cdot)$.

4.2.4 Implementation

The implementations of finite volume codes often use a loop over all elements and calculate the contribution of the dual grid skeleton from inside each element. The implementation of the presented method for rock matrix and fractures can be done based on a volumetric element code without the need to introduce the notion of lower-dimensional elements into the code, if fractures are represented as inner boundaries and if each element calculates not only the contributions from Γ^m_{int}, but also from Γ^f_{int}. Calculation of the contribution to the stiffness matrix and the defect from $\gamma_{e,f,b,b'}$ is done by element Ω_e and Ω_f which each contribute half of the value. This approach is advantageous, because it stays within the element-wise implementation paradigm and doesn't require boundary-communications if the method is implemented on parallel computers with a domain decomposition approach.

4.3 Time Discretization

The traditional approach to the numerical solution of time-dependent partial differential equations is by the *method of lines*. First, a spatial discretization is applied to the problem (e. g. a finite element method or a finite volume method), which leads to a system of ordinary differential equations. This system is then solved by a time differencing scheme which can be chosen from the wide range of available methods, see Hairer and Wanner (1996), Thomée (1997).

The opposite approach is taken by the Rothe method, which first applies a time differencing scheme and then approaches the resulting problem by a spatial discretization. The advantage of this method is that different spatial discretizations can be applied during the time stepping process.

In the context of finite element methods and finite volume methods we have to deal with *stiff* systems of ordinary differential equations. The first definition of the term *stiff* was rather pragmatic: *"stiff equations are equations where certain implicit methods, in particular BDF, perform better, usually tremendously better, than explicit ones"* (Curtiss and Hirschfelder, 1952). We will indeed focus our attention on implicit methods.

We divide the time interval $(0,T)$ into discrete time steps

$$0 = t^0, \dots, t^k, t^{k+1} = t^k + \Delta t^k, \dots, t^M = T$$

of variable or fixed size. Superscript n notation

$$p_{wh}(t^n) = p_{wh}^n \quad \text{and} \quad \mathbf{S}_{gh}(t^n) = \mathbf{S}_{gh}^n$$

for functions and coefficient vectors denotes values at time step t^n. The coefficient vectors $\boldsymbol{\nu} \in \mathbb{R}^N$ are related to the discrete solution function $v_h \in V_h$ by the mapping $\mathcal{C} : \mathbb{R}^N \to V_h$ in this way:

$$\mathcal{C}(\boldsymbol{\nu}) = v_h, \qquad v_h(\mathbf{x}) = \sum_{i \in I} \boldsymbol{\nu}_i \varphi_i(\mathbf{x}).$$

The application of the finite volume discretization scheme leads to the semi-discretization

$$\frac{\partial}{\partial t}\mathbf{M}_w(\mathbf{p}_w(t), \mathbf{S}_g(t)) + \mathbf{A}_w(\mathbf{p}_w(t), \mathbf{S}_g(t)) = 0, \tag{4.100}$$

$$\frac{\partial}{\partial t}\mathbf{M}_g(\mathbf{p}_w(t), \mathbf{S}_g(t)) + \mathbf{A}_g(\mathbf{p}_w(t), \mathbf{S}_g(t)) = 0, \tag{4.101}$$

where $\mathbf{M}$ corresponds to m and $\mathbf{A}$ corresponds to a. The system can be written as

$$\begin{pmatrix} \mathbf{M}_{ww} & \mathbf{M}_{wn} \\ \mathbf{M}_{nw} & \mathbf{M}_{nn} \end{pmatrix} \begin{pmatrix} \frac{\partial \mathbf{p}_w(t)}{\partial t} \\ \frac{\partial \mathbf{S}_g(t)}{\partial t} \end{pmatrix} + \begin{pmatrix} \mathbf{A}_w(\mathbf{p}_w, \mathbf{S}_g) \\ \mathbf{A}_n(\mathbf{p}_w, \mathbf{S}_g) \end{pmatrix} = 0 \tag{4.102}$$

with the submatrices

$$(\mathbf{M}_{\alpha w})_{ij} = \frac{\partial \mathbf{M}_{\alpha w,i}}{\partial \mathbf{p}_{w,j}} \qquad (\mathbf{M}_{\alpha g})_{ij} = \frac{\partial \mathbf{M}_{\alpha g,i}}{\partial \mathbf{S}_{g,j}}. \tag{4.103}$$

This results in a system of *differential algebraic equations* (DAE) of index 1 in implicit form. The matrix $\mathbf{M}$,

$$\mathbf{M} = \begin{pmatrix} \mathbf{M}_{ww} & \mathbf{M}_{wn} \\ \mathbf{M}_{nw} & \mathbf{M}_{nn} \end{pmatrix}, \tag{4.104}$$

is singular in the incompressible case. An analysis for the incompressible case shows that a discrete form of the elliptic equation has to be satisfied. This is called the implicit constraint. It is shown, that a backward Euler step guarantees the validity of the implicit constraint. Further time-steps can be chosen from a different method—the constraint is satisfied if it has been satisfied on the previous time level. For this reason, we always employ one backward Euler step as the first time step, regardless of the time differencing scheme of the subsequent steps.

The time step scheme reads in the *one-step*-θ notation: *For* $n = 0, 1, \ldots, M-1$ *find* $\mathbf{p}_w^n$, $\mathbf{S}_n^n$ *such that*

$$\mathbf{M}_w^{n+1} - \mathbf{M}_w^n + \Delta t^n \theta \mathbf{A}_w^{n+1} + \Delta t^n (1-\theta) \mathbf{A}_w^n = 0, \tag{4.105}$$

$$\mathbf{M}_g^{n+1} - \mathbf{M}_g^n + \Delta t^n \theta \mathbf{A}_g^{n+1} + \Delta t^n (1-\theta) \mathbf{A}_g^n = 0. \tag{4.106}$$

For $\theta = 0$ this is the *forward Euler scheme* or *explicit Euler scheme*, for $\theta = 1/2$ the *Crank-Nicholson scheme*, and for $\theta = 1$ the *backward Euler scheme* or *implicit Euler scheme*,

The explicit Euler scheme is first-order accurate, but subject to severe time step size restrictions, so we don't consider this or other explicit schemes any further. The implicit Euler scheme is first-order accurate and strongly A-stable, the Crank-Nicholson scheme is second order accurate and A-stable. Stability is defined by considering the Dahlquist equation $y' = \lambda y, y(0) = 1$, and then deriving the stability function $R(z)$ for the calculation rule

$$y^{k+1} = R(h\lambda) y^k. \tag{4.107}$$

R is a polynomial for explicit methods and a rational function for implicit methods. The *stability domain* of a method with stability function $R(z)$ is

$$S = \{z \in \mathbb{C} \mid |R(z)| \leq 1\} \tag{4.108}$$

A method is called *A-stable* if its stability domain satisfies

$$\mathbb{C}^- \subset S, \qquad \mathbb{C}^- = \{z \mid \operatorname{Re} z \leq 0\} \tag{4.109}$$

If $|R(\infty)| < 1$ the method is called *strongly A-stable*. The one-step-θ scheme has the stability function

$$R(-\lambda) = \frac{1 - (\theta - \frac{1}{2})\lambda}{1 + \theta\lambda} = e^{-\lambda} + O((\theta - \frac{1}{2})|\lambda|^2 + |\lambda|^3)), \quad |\lambda| \leq 1. \tag{4.110}$$

A time differencing scheme should posess these properties (Rannacher, 1999):

A-stability to ensure local convergence

$$|R(-\lambda)| \leq 1$$

Global stability to ensure global convergence

$$\overline{\lim}_{\mathrm{Re}\,\lambda\to\infty}|R(-\lambda)| \leq 1 - O(\Delta t^k)$$

Strong A-stability to ensure the smoothing property

$$\overline{\lim}_{\mathrm{Re}\,\lambda\to\infty}|R(-\lambda)| \leq 1 - \delta < 0$$

Low dissipation to ensure energy preservation

$$|R(-\lambda)| = 1 - O(\mathrm{Im}\,\lambda), \quad \text{for } \mathrm{Re}\,\lambda \to 0$$

The implicit Euler scheme is very stable and damps out perturbations in the data, but it is also very dissipative and will smear out sharp fronts in a solution. The Crank-Nicholson scheme is far less dissipative, but it lacks the stability of the implicit Euler method towards perturbations in the solution. By adapting the time step size this stability concern can be met, but the necessary time step size may be prohibitively small.

The backward-differencing formulæ (BDF) are a family of schemes, including the popular second order BDF(2) method. But BDF(2) it is not globally mass conservative in the case of variable time step sizes—a property posessed by the implicit Euler scheme and the Crank-Nicholson scheme. Also of second order is the *singly diagonally implicit Runge-Kutta scheme* SDIRK(2) (Alexander, 1977).

The *fractional-step-θ scheme* was originally developed as an operator splitting scheme for the incompressible Navier-Stokes equations. It consists of three substeps $t^n \to t^{n+\alpha} \to t^{n+1-\alpha} \to t^{n+1}$, where each substep k is a one-step-θ step with θ_k and Δt^k chosen as

$$\begin{aligned}
\theta_1 &= 2-\sqrt{2} \qquad \Delta t^1 = (1-\sqrt{2}/2)\Delta t = \alpha\Delta t,\\
\theta_2 &= \sqrt{2}-1 \qquad \Delta t^2 = (\sqrt{2}-1)\Delta t = (1-\alpha)\Delta t,\\
\theta_3 &= 2-\sqrt{2} \qquad \Delta t^3 = (1-\sqrt{2}/2)\Delta t = \alpha\Delta t
\end{aligned}$$

The θ_i can be chosen different than above as long as $\theta_1 = \theta_3 = \theta \in (1/2, 1]$, and $\theta_2 = 1-\theta$ holds. The fractional-step-θ scheme is of second order for $\alpha = 1-\sqrt{2}/2$ and strongly A-stable for any $\theta \in (1/2, 1]$. Its stability function is

$$R(z) = \left(\frac{1+\alpha z(1-\theta)}{1-\alpha z\theta}\right)^2 \left(\frac{1+(1-2\alpha)z(1-\theta_2)}{1-(1-2\alpha)z\theta_2}\right) \tag{4.111}$$

The scheme posesses, other than the Crank-Nicholson scheme, the full smoothing property in case of rough initial data. Note that the substepping does not result in higher

computational cost since the step size Δt can be chosen three times larger than for the single-step-θ scheme.

Finally, an interesting time differencing scheme is the *discontinuous Galerkin method* (not to be confused with the class of spatial discretization methods by the same name), see Thomée (1997), Eriksson et al. (1996). It is derived by applying a Galerkin finite element method to the time variable, which has the advantage that if Galerkin finite element methods are used for spatial discretization, the resulting method treats time and space variables similarly. The approximate solution in t will be sought from the space of piecewise polynomial functions, which are not necessarily continuous at the nodes.

4.4 Nonlinear System Solution

In the fully coupled, fully implicit discretization, a large system of nonlinear equations has to be solved in each time step and an accurate solution of the equations is necessary, because otherwise the local mass conservation could be destroyed. The nonlinear system solution is done with an inexact Newton method, where the linearized systems arising in each step of the Newton method are solved iteratively with a multigrid method. Without exact solution of the linearized systems, the quadratic convergence of the Newtons method is reduced, but since quadratic convergence can only be observed in a close neighboorhood of the solution, where the error is already much smaller than the discretization error, this is not a disadvantage in practice. To ensure global convergence, a line search algorithm is applied in the Newton steps (Braess, 1992).

The discretization scheme leads to a system of nonlinear algebraic equations

$$\mathbf{F}(\mathbf{z}) = \mathbf{0} \tag{4.112}$$

with a vector $\mathbf{z}$ which contains pressure and saturation unknowns,

$$\mathbf{z} = (\mathbf{p}_{w,1}, \ldots, \mathbf{p}_{w,N}, \mathbf{S}_{n,1}, \ldots, \mathbf{S}_{n,N})^T \tag{4.113}$$

and a vector function $\mathbf{F}$ with components

$$\mathbf{F} = (\mathbf{F}_{w,1}, \ldots, \mathbf{F}_{w,N}, \mathbf{F}_{n,1}, \ldots, \mathbf{F}_{n,N})^T. \tag{4.114}$$

For the one step θ scheme the components are given by

$$\mathbf{F}_\alpha = \mathbf{M}_\alpha^{n+1} - \mathbf{M}_\alpha^n + \Delta t^n \theta(\mathbf{A}_\alpha^{n+1}) + \Delta t^n (1-\theta)(\mathbf{A}_\alpha^n). \tag{4.115}$$

Dirichlet values are included in the equation system and treated by inserting a trivial equation.

The linearized equations are described by the Jacobian matrix $\mathbf{J}$ of $\mathbf{F}$ at point $\mathbf{z}$,

$$(\mathbf{J}(\mathbf{z}))_{ij} = \frac{\partial \mathbf{F}_i}{\partial \mathbf{z}_j}(\mathbf{z}). \tag{4.116}$$

The entries of $\mathbf{A}$ are computed by numerical differentiation,

$$\frac{\partial \mathbf{J}_i}{\partial z_j}(z) = \frac{\mathbf{F}_i(z + \Delta z_j \mathbf{e}_j) - \mathbf{F}_i(z)}{\Delta z_j} + (O)(\Delta z_j) \tag{4.117}$$

```
    NEWTON(F, z, ε_nl)
1     κ = 0; z^0 = z;
2   while ( ||F(z^κ)||_2 ≥ ε_nl ||F(z^0)||_2 ) {
3       Choose ε_lin^κ ∈ (0, 1];
4       Find s^κ such that ||F(z^κ) + A(z^κ) s^κ||_2 ≥ ε_nl^κ ||F(z^0)||_2;
5       Choose λ_lin^κ ∈ (0, 1];
6       z^{κ+1} = z^κ + λ^κ s^κ;
7       κ = κ + 1;
8   }
```

Algorithm NEWTON($\mathbf{F}, z, \varepsilon_{nl}$) describes the nonlinear systems solution process. In the description, $\|\cdot\|_2$ is the Euclidean vector norm. Line 6 of the Newton iteration algorithm implements a simple line search strategy (Braess, 1992), which helps to achieve global convergence of the Newton method. The damping factor λ^κ is chosen as the maximum of $\{1, \frac{1}{2}, \frac{1}{4}, \dots\}$ such that

$$\|\mathbf{F}(z^\kappa + \lambda^\kappa \mathbf{s}^\kappa)\|_2 \leq \left(1 - \frac{1}{4}\lambda^\kappa\right) \|\mathbf{F}(z^\kappa)\|_2. \tag{4.118}$$

The error in the solution of the linearized equations, which is monitored in the forcing term ε_{lin}^κ, should be sufficiently small because otherwise saturation values can lie outside the intervall $[0, 1]$.

Initial guesses for the solution can be the solution from the last time step—which usually gives good initial guesses as long as the time step size is not too large—or by a hierarchical strategy, where the nonlinear system is solved on the coarsest mesh, interpolated to the next finer mesh and taken as the initial guess. The process is repeated up to the finest grid level. This is an effective strategy for the first time step, where no previous solution is available. A combination of both approaches is possible and advantageous for large time steps, where the initial solution on level 0 uses the solution from the previous time step as an initial guess.

Nonlinear systems can also be solved by *nonlinear multigrid methods* where the smoother in the multigrid method (see next section) is replaced by a nonlinear version. We did not apply this method, because it is usually less efficient than multigrid methods combined with the Newton method and because only Jacobi- and Gauß-Seidel type smoothers are available, while for the linear multigrid method more robust smoothers exist.

In the context of this work it is well known that the nonlinear systems resulting from discretization schemes with the extended capillary pressure condition are more difficult

to solve than systems from discretization schemes without the extended capillary pressure condition Jakobs et al. (2003b). The solution gets increasingly difficult for smaller viscosities and for steep capillary pressure and relative permeability functions. This situation arises when gas saturation increases at the end of a fracture and has to reach the entry pressure before entering the matrix. Since this configuration is found at many places throughout a fracture network, the convergence of the nonlinear solver is of crucial quantity for the overall efficiency.

4.5 Linear System Solution: The Multigrid Method

The solution of the linear systems arising in the implicit time discretization is usually the computationally most expensive part of the numerical solution of partial differential equations. In the present setting, the linear system

$$A\boldsymbol{x} = \mathbf{b}, \qquad A \in \mathbb{R}^{N\times N}, \mathbf{b}, \mathbf{x} \in \mathbb{R}^{N} \tag{4.119}$$

arises from the fully coupled Newton solution of the nonlinear equations, where A is the Jacobian and $\mathbf{b}$ the nonlinear defect. Direct solution of (4.119) requires $O(N^3)$ arithmetical operations (Golub and van Loan, 1996), which can be reduced by banded elimination to $O(N^2)$ or by nesteed disection to $O(N^{1.5})$ for two-dimensional problems arising from the discretization of partial differential equations. This makes the solution of equations with some hundred thousand unknowns possible. In three space dimension, the operations can not be reduced so substantially and $O(N^{2.33})$ or $O(N^2)$ operations for the mentioned techniques remain. This complexity is by far too large for the considered complex three-dimensional systems where several million unknowns must be expected.

A more efficient solution method for systems of linear equations is offered by iterative schemes. We consider *relaxation methods*, where the matrix A is split into two matrices M and N,

$$A = M - N. \tag{4.120}$$

M is chosen as an approximation to A which is easy to invert. From a given initial guess $\boldsymbol{x}^0$, a sequence of iterations is computed by

$$\boldsymbol{x}^{k+1} = \mathbf{b}^k + M^{-1}\mathbf{d}^k, \qquad \mathbf{d}^k = (\mathbf{b} - A\boldsymbol{x}^k). \tag{4.121}$$

$\mathbf{d}^k$ is the *defect* in step k. Choices of M which allow for an easy inversion are the diagonal of A, which gives the *Jacobi method*, and the lower triangle of A, for which the *Gauß-Seidel method* results. The *symmetric Gauß-Seidel method* consists of one forward step of the Gauß-Seidel method (i. e. with the lower triangle of A) followed by a backward step of Gauß-Seidel (i. e. with the upper triangle of A). Another popular method is the *incomplete LU factorization* (ILU), where

$$M = LU \tag{4.122}$$

is the LU factorization of A in which the sparsity pattern of A is kept for L and U, in order to avoid the fill-in which could lead to dense matrices—this would not only jeopardize the efficiency of the method but also the memory requirements of the algorithm.

The convergence of a method can be measured by the factor ρ

$$\|\boldsymbol{x} - \boldsymbol{x}^{k+1}\| \leq \rho \|\boldsymbol{x} - \boldsymbol{x}^{k}\| \tag{4.123}$$

with a suitable norm $\|\cdot\|$. A method is convergent if and only if for the matrix

$$B = I - M^{-1}A = M^{-1}N \tag{4.124}$$

the spectral radius of B of is smaller than one,

$$\mu(B) < 1. \tag{4.125}$$

Reducing the error by a factor ε requires at most $\lceil \log \varepsilon / \log \rho \rceil$ iterations. For these results and an excellent overview of iterative methods see the monograph by Hackbusch (1994).

For systems arising from the discretization of partial differential equations on a grid with mesh size h, a convergence factor of

$$\rho = 1 - O(h^2) \tag{4.126}$$

is common. By the succesive overrelaxation method (SOR), this can be enhanced to $\rho = 1 - O(h)$, but the SOR method relies on a problem-dependent parameter which is normally not known. Convergence of the form (4.126) means that halfing the mesh size h leads to a fourfold increase in the necessary number of iterations.

Convergence theory for the presented relaxation methods is available for many classes of matrices, including positive definite matrices, diagonally dominant matrices and M-matrices (Hackbusch, 1994). However, the Jacobian arising in the solution of the multiphase flow equations as presented above does not fall into any of these classes.

A very efficient class of iterative schemes are *Krylov subspace methods*. These methods look for optimal approximations of $\boldsymbol{x} - \boldsymbol{x}^0$ in the m-dimensional Krylov subspace K_m,

$$K_m(A, \boldsymbol{x}^0) = \operatorname{span}\{\boldsymbol{x}^0, A\boldsymbol{x}^0, A^2\boldsymbol{x}^0, \ldots, A^{m-1}\boldsymbol{x}^0\}. \tag{4.127}$$

Introductions to Krylov subspace methods can be found in Hackbusch (1994), Barrett et al. (1994), and Golub and van Loan (1996). There are many ways to specify optimal approximations, and consequently there is a large range of methods based on the Krylov subspace principle. Among the most popular are the *conjugate gradient method (CG method)*, the *generalized conjugate residuals method* (GCR method), the *generalized minimal residual method* (GMRES), and the *bi-conjugate gradient stabilized* method (Bi-CGSTAB). Of these methods, Bi-CGSTAB and GMRES are especially popular in fluid mechanics. For general matrices A, Bi-CGSTAB is less robust than GMRES, but in practice Bi-CGSTAB is often much more efficient because it is cheaper in each step. Bi-CGSTAB also requires less memory than GMRES. In this work we only use Bi-CGSTAB out of the available Krylov subspace methods.

Krylov subspace methods benefit greatly from preconditioning, either by one of the relaxation schemes mentioned above (ILU is a popular choice), or by the multigrid method discussed below.

Multigrid methods are a very important class of iterative methods. Their impact has been so large that their discovery 'is the most significant development in numerial analysis in the last 25 years' (Wesseling, 2001). Among the many introductions and overviews to the subject we mention Hackbusch (1985), Wesseling (1992), Bramble (1993), and Briggs et al. (2000). Multigrid methods are based on the observation that relaxation methods applied to the model equation $-\Delta u = f$ damp high oscillatory errors more effectively than the low frequency error components. A coarse grid correction step in the multigrid method reduces these low frequency errors and leads to a very efficient scheme.

The multigrid method is of optimal order $O(N)$ for elliptic model problems and the convergence factor ρ is independent of the mesh size. There is no other method which achieves the same convergence rate. The convergence theory for elliptic problems with full regularity assumptions had reached a mature status by the mid 1980s, culminating in the book of Hackbusch (1985). Further developments included regularity perturbations into the theory (Xu, 1992, Bramble, 1993) and led to convergence proofs for complex problems like the Stokes equations (Wittum, 1990, Verfürth, 1988). Multigrid methods have been used for the solution of two-phase flow problems in an IMPES formulation (Scott, 1985, Dendy Jr., 1987), but there the multigrid method was only applied to the scalar elliptic pressure equation. Brakhagen and Fogwell (1990) and Molenaar (1995) applied multigrid methods to the fully implicit, fully coupled formulation, but restricted themselves to the incompressible case on structured meshes in two space dimensions. The first application of multigrid to the fully implicit, fully coupled approach on general meshes in two and three space dimensions was done by Bastian (1999a), Bastian and Helmig (1999).

4.5.1 The Multigrid Algorithm

The multigrid algorithm operates on a sequence of meshes

$$E_0, E_1, \ldots, E_J, \tag{4.128}$$

which are generated from the initial coarse mesh E_0 by uniform or adaptive refinement. For the refinement we employ the stable grid refinement algorithm of Lang (2000) (see also Bastian (1996) and Bey (1998)), which creates grids without hanging nodes.

On each grid level, the discretized equations are now given by

$$A_l \boldsymbol{x}_l = \mathbf{b}_l, \qquad l = 0, \ldots, J, \qquad A \in \mathbb{R}^{N_l \times N_l}, b, x \in \mathbb{R}^{N_l}. \tag{4.129}$$

A *restriction* operator R and a *prolongation* operator P are responsible for the grid transfer between the different grid levels,

$$R_l : \quad \mathbb{R}^{N_l} \to \mathbb{R}^{N_{l-1}}, \tag{4.130}$$

Algorithm 1: The standard multigrid algorithm for one iteration from the finest level l applied to $\mathbf{x}_l$ with right hand side $\mathbf{b}_l$.

```
MGC(l, x_l, b_l)
1     if (l = 0)
2         x_0 := A_0^{-1} b_0;
3     else
4         {
5         Apply ν_1 iterations of S to A_l x_l = b_l
6         d_l := b_l − A_l x_l;
7         d_{l−1} := R_l d_l;
8         c_{l−1} := 0;
9         for (k = 1, ..., γ) mgc(l − 1, c_{l−1}, d_{l−1})
10        c_l := P_l c_{l−1};
11        x_l := x_l + c_l;
12        Apply ν_2 iterations of S to A_l x_l = b_l
13        }
```

$$R_l : \mathbb{R}^{N_{l-1}} \to \mathbb{R}^{N_l}. \tag{4.131}$$

For conforming finite element methods the prolongation can be defined by finite element interpolation ,

$$(P_l \mathbf{c}_{l-1}) = \sum_{j=1}^{N_{l-1}} \mathbf{c}_{l-1,j} \varphi_{l-1,j}(\mathbf{x}_{l-1,i}). \tag{4.132}$$

Here $\varphi_{l-1,j}$ is the finite element basis function corresponding to vertex $\mathbf{x}_{l,j}$ on level j. P_l is a sparse matrix (due to the local support of the basis functions) of rectangular form. The restriction matrix R_l is chosen as

$$R_l = P_l^T. \tag{4.133}$$

On each grid level a relaxation scheme can be applied; in the context of multigrid methods it is referred to as a *smoother*, due to is effect on the high oscillatory error components.

The coarse grid matrices A_l can either be constructed by discretization of the continuous problem on the individual grids (the approach taken in this work), or by the Galerkin coarse grid operator approach

$$A_{l-1} = R_l A_l P_l. \tag{4.134}$$

The parameter γ in line 9 of the multigrid algorithm mgc determines the cycle form, for $\gamma = 1$ the V-cycle and for $\gamma = 2$ the W-cycle results. The parameters ν_1, ν_2 determine the number of pre- and post-smoothing steps.

4.5.2 Robust Multigrid Algorithms

A multigrid algorithm is considered *robust* if its convergence rate does not depend on the coefficients of the discretized partial differential equation. In practice, difficulties with multigrid convergence usually arises from *interface problems*, *anisotropic problems* or convection dominated *convection-diffusion problems*. We comment on the types of problems and the solution apporaches that have been developed to overcome these difficulties.

Interface problems can be studied with the groundwater equation

$$-\nabla \cdot (K \nabla u) = f. \tag{4.135}$$

If the coefficient $K = K(x)$ is smooth or even constant across the domain, multigrid converges with a convergence rate independent of h. But for many problems, the variation in K is not smooth and instead exhibits discontinuities of several orders of magnitude (e. g. between a fracture and the rock matrix). In this case we can distinguish between discontinuities which are resolved by the coarse grid and discontinuities which arise inside elements. In the first case, multigrid converges well and it is possible to prove almost optimal convergence in the two-dimensional case (Bramble et al., 1991), but in three space dimensions coefficient distributions which deteriorate multigrid convergence are possible (Dryja et al., 1996). If the discontinuities are not aligned with the coarse grid, special prolongation operators have to be employed which are constructed from A_l and the Galerkin coarse grid operator (4.134), see Hackbusch (1985). Wagner et al. (1997) use a coarse grid operator based on the Schur complement.

Anisotropic problems arise from an anisotropic diffusion tensor in

$$-\nabla \cdot (K \nabla u) = f \quad \text{with } K = \begin{pmatrix} 1 & 0 \\ 0 & \varepsilon \end{pmatrix}. \tag{4.136}$$

Note that this equation changes it's elliptic character when $\varepsilon = 0$ and is then of parabolic type. For $\varepsilon \ll 1$ or $\varepsilon \gg 1$, the convergence of multigrid with Jacobi- or Gauß-Seidel smoothers deteriorates quickly. One possible solution approach is called *semi-coarsening*, where the mesh is only refined in the direction of the strong coupling. This approach is attractive because it is possible for grids in two and three space dimensions, although the implementation requires a considerable effort for hybrid grids.

Another approach works by constructing robust smoothers for the problem. Block-line smoothers or modified ILU smoothers with an appropriate ordering of the unknowns have been proven to be very efficient (Wittum, 1989). They are, however, not well suited for three-dimensional problems, as the approach requires the solution of two-dimensional subproblems in the smoother.

Convection-diffusion problems with dominating convection pose the most difficult challenge to multigrid convergence theory and practice. They can be studied from the model problem

$$-\nabla \cdot (ru - \varepsilon \nabla u) = f. \tag{4.137}$$

with a flow field $\mathbf{r}$. A very effective solution strategy is available for the case of pure convection ($\varepsilon = 0$) and flow fields without recirculation. In this case the stiffness matrix A has lower triangular form if the unknowns are ordered in a downwind direction and an appropriate upwind scheme is chosen. The approach has been extended to flow fields with recirculation zones by several authors (Hackbusch, 1997, Bey and Wittum, 1997, Bey, 1998, Rentz-Reichert, 1996). It is also possible to approach the problem by constructing improved coarse grid correction matrices; see Reusken (2002) and the citations therein.

An increasingly popular class of multigrid methods are the *algebraic multigrid methods*, which do not rely on a given hierarchy of refined grids, but instead construct the grid hierarchy themselves from the given fine grid stiffness matrix. We did not pursue this research direction in this work, but we applied algebraic multigrid to some of the presented problems with good success. The work on algebraic multigrid methods was initiated by Ruge and Stüben (1987); of the large number of subsequent publications we mention Vaněk et al. (1996), Raw (1996), Braess (1995), Bank and Wagner (1999). To distinguish algebraic multigrid from the geometry-based multigrid algorithms, the latter is sometimes referred to as *geometric multigrid*.

An application of multigrid to a problem which bears some resemblance with our setting is the treatment of crack singularities in Brenner and Sung (1997). This can be considered the case of a lower-dimensional modeling of blocking fractures.

4.5.3 Parallel and Adaptive Multigrid

The numerical solution of linear systems of equations is accessible to acceleration by *adaptivity* and *parallelization*. Both approaches are employed for the presented discretization scheme to speed up the solution process. We do not comment extensively on this topic, because it can be implemented in a problem-independent way and has received careful attention in Bastian (1996, 1999a), Lang (2000)

It is possible to refine the initial coarse mesh either by error indicators (Verfürth, 1996) or by prescribed refinement in specified regions. Two-phase flow problems are very well suited for adaptive refinement due to the local nature of fronts travelling through a medium, but we did not consider error estimation in this work. In figure 4.14 an adaptive refinement of a domain with eight fractures is shown on six grid levels. Starting at level 1 only the elements which share a vertex with a fracture are refined. As the refinement proceeds, the geometry of the fractures becomes visible. The refinement algorithm is rather complex, especially when combined with a parallel implementation. It is implemented in the toolbox UG as described in Lang (2000). The multigrid algorithm needs to be adjusted to the locally refined hierarchy. An analysis of the specific local multigrid method used here is given in Neuss and Wieners (2003); see also Bastian (1996).

The parallelization of the multigrid method is described in Bastian (1999a). The implementation is done for MIMD parallel computers, because this is the only architecture offering scalability up to thousands of processors. Starting with a coarse grid stored on

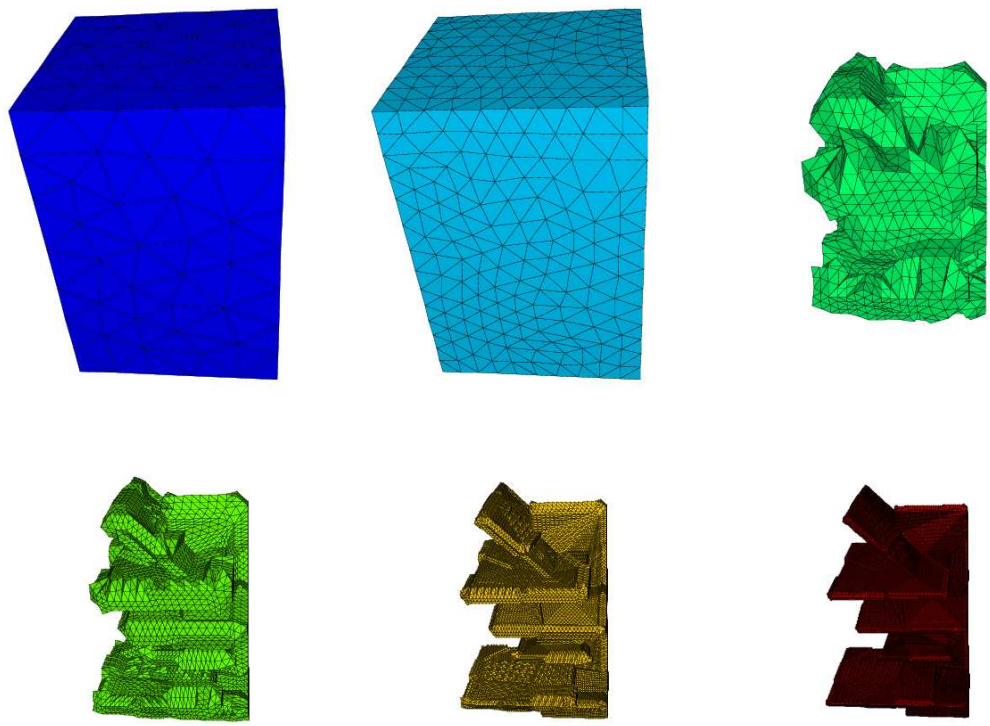

Figure 4.14: Example of adaptive grid refinement of a fractured domain.

one processor, on each grid level a balanced mapping of elements to processors needs to be calculated. This is the *load balancing problem*. The distribution phase or *load migration* phase distributes elements to the processors. In the case of unstructured grids this involves the identification and consistent storage of dependencies among the geometrical objects nodes, edges, faces, and elements. The interaction of the components involved in the parallelization is described in Lang (2000)

4.5.4 Multigrid for Systems

The standard multigrid smoothers are not directly applicable to the Jacobian system, because some rows in the A_{ww} block of the matrix may vanish. This problem of point-wise smoothers can be circumvented by using a *point-block ordering* and block variants of the smoothers. This approach was used in Bastian (1999a), Bastian and Helmig (1999). We order the unknowns belonging to one vertex together, resulting in an ordering

$$\tilde{\boldsymbol{z}} = (\mathbf{p}_{w,1}, \mathbf{S}_{n,1}, \ldots, \mathbf{p}_{w,N}, \mathbf{S}_{n,N})^T \tag{4.138}$$

which corresponds to a permutation of $\boldsymbol{z}$ with the permutation matrix Q,

$$\tilde{\boldsymbol{z}} = Q\boldsymbol{z}. \tag{4.139}$$

Q transforms the system into the equivalent system

$$\tilde{A}\tilde{\boldsymbol{z}} = \tilde{\mathbf{b}} \tag{4.140}$$

with

$$\tilde{A} = QAQ^T, \quad \tilde{\boldsymbol{z}} = Q\boldsymbol{z}, \quad \tilde{\mathbf{b}} = Q\mathbf{b}. \tag{4.141}$$

The matrix A has a block structure with $N \times N$ blocks $\tilde{A}_{ij}$ of size 2×2,

$$\tilde{A} = \begin{pmatrix} \tilde{A}_{11} & \cdots & \tilde{A}_{1N} \\ \vdots & & \vdots \\ \tilde{A}_{N1} & \cdots & \tilde{A}_{NN} \end{pmatrix}. \tag{4.142}$$

We may now ask under what conditions block variants of Jacobi, Gauß-Seidel and ILU iterations (which operate on the 2×2 blocks) can be applied. The only situation in which a block $\tilde{A}_{ij}$ can become singular is at boundaries where

$$\rho_w \boldsymbol{v}_w \cdot \mathbf{n} = \phi_w, \qquad S_n(\mathbf{x}, t) = 1. \tag{4.143}$$

This boundary condition is not physically meaningful, since no water phase exists at points where $S_n = 1$ holds, and consequently no condition can be imposed on the water flux.

The properties of the blocked versions of the smoothers are similar to the point-wise variants (Hackbusch, 1994), but convergence of the Jacobi and the Gauß-Seidel iteration have not been proven for the considered problems. Convergence results are also missing for the ILU iteration, where even the existence of the ILU decomposition remains to be proven.

4.5.5 Truncated Restriction for Discontinuous Problems

Bastian (1999a) considers the case of a discontinuous diffusion coefficient which is 1 in one part of the domain and $\varepsilon \ll 1$ in the other. Application of the standard grid transfer operators in the multigrid algorithm results in divergence if the jump in the discontinuity is large enough, because for nodes near the interface a correction on the order of $O(1/\varepsilon)$ will be computed. In the *truncated restriction*, the restriction operator R_l is replaced by

$$(\tilde{R}_l)_{ij} = (R_l)_{ij} \cdot \min\left(c, \frac{(A_l)_{ij}}{(A_{l-1})_{ij}}\right), \tag{4.144}$$

with a constant c. Note that the modified restriction operator $(\tilde{R}_l)_{ij} = (R_l)_{ij}(A_l)_{ij}/(A_{l-1})_{ij}$ results from a scaling of the equation $Ax = b$ with $D = \mathrm{diag}(A)$. The additional choice of the minimum prevents exactly the problems at interior discontinuous boundaries. By choosing $c \geq 1$ the standard restriction operator results for constant coefficients, since in this case $(A_l)_{ij}/(A_{l-1})_{ij} \leq 1$ holds at all interior vertices. At restrictions of interior vertices to Neumann boundary vertices, $(A_l)_{ij}/(A_{l-1})_{ij}$ may be larger than 1, so we choose $c = 2$ in all subsequent computations. Numerical experiments indicate that the choice of c is not crucial as long as it is smaller than 5. This method is called the *diagonally scaled/truncated restriction multigrid algorithm*, DSTR-MG. Bastian (1999a) contains examples for which the standard multigrid iteration diverges, but the modified multigrid iteration with truncated restriction shows grid independent convergence or $O(J)$ behaviour (with the number of grid levels J).

The extension to systems is done for the point-block ordered system. Instead of scaling with the diagonal matrix, the system is scaled with the point-block diagonal matrix $\hat{D}$, and the resulting restriction is

$$\hat{R}_l = \hat{D}_{l-1}^{-1} R_l \hat{D}_l. \tag{4.145}$$

The 2×2 blocks which constitute $\hat{R}_l$ are determined by

$$(\hat{R}_l)_{ij} = (R_l)_{ij}(\hat{D}_{l-1}^{-1})_{ij}(\hat{D}_l)_{ij}. \tag{4.146}$$

The truncated restriction for systems is defined as

$$\left((\hat{R}_l)_{ij}\right)_{\alpha\beta} = (R_l)_{ij} \cdot \max\left(0, \min\left(c, ((\hat{D}_{l-1})_{ij}^{-1}(\hat{D}_l)_{ij})_{\alpha\beta}\right)\right). \tag{4.147}$$

4.6 Computer Program MUFTE-UG

4.6.1 The Simulation Environment

The numerical simulation of multi-phase flow in fractured porous media requires several software components which need to interact as depicted in figure 4.15. The components in figure 4.15 are employed in many different application fields and we want to comment on the special requirements of the present application.

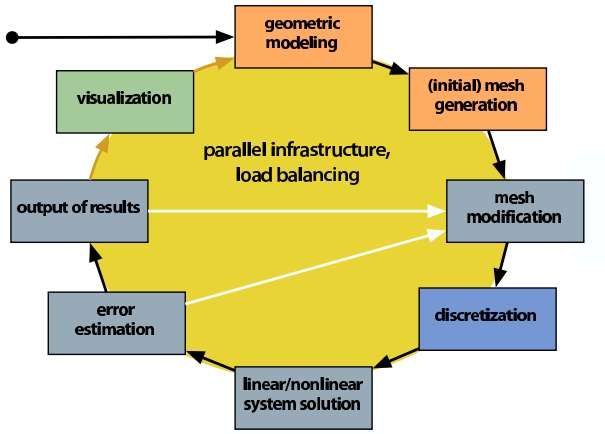

Figure 4.15: The components of a numerical simulation environment and their interaction.

The geometry of domains in the subsurface can be very complex and can in all but the simplest cases only be resolved by unstructured grids. The occurrence of sharp front suggests that adaptive grid refinement is employed near the front. A combination of both features is complicated to implement, but for detailed simulations it is even necessary to run simulations on parallel computers with distributed memory. The combination of *unstructured grids*, *adaptivity* and *parallelization* introduces complexity into the code development which is by orders of magnitude greater than for structured, uniformly refined grids on a single processor computer. Since it is not reasonable to implement this functionality individually for each application domain, the framework UG (Bastian et al., 1997b) was developed, which provides the mentioned functionality in a problem-independent way. The code developed for the solution of the two-phase equations is part of a larger simulation environment, which contains different models for subsurface flow and transport.

In this chapter we describe some core features of the framework UG and explain how the implementation of the module for fractured porous media is done based on this framework. We also explain some crucial components of the discretization process, namely the generation of fractured domains in a pre-processing step and the visualization of fractured domains in post-processing.

4.6.2 MUFTE-UG

In this section, the modeling system MUFTE-UG, especially the processing part, is introduced as an example of a numerical simulator in environment water. MUFTE-UG is a combination of MUFTE and UG. MUFTE stands for MUltiphase Flow, Transport and Energy model, and this software toolbox mainly contains the physical model concepts and discretization methods for isothermal and non-isothermal multiphase–multicomponent flow and transport processes in porous and fractured-porous media (see Helmig (1997), Helmig et al. (1998), Breiting et al. (2000)). UG is the abbreviation for

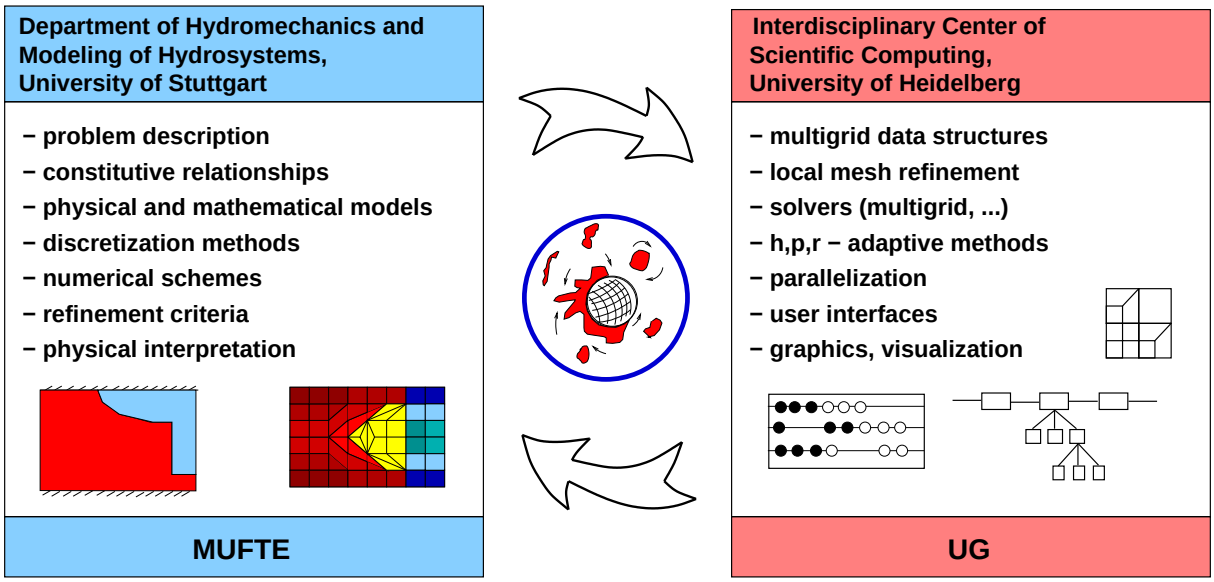

Figure 4.16: Numerical simulator MUFTE-UG

Unstructured Grids, and this toolbox provides the data structures and fast solvers for the discretization of partial differential equations based on parallel, adaptive multigrid methods (see Bastian et al. (1997b), Bastian (1996), Bastian et al. (1997a), Lang (2000)). MUFTE is implemented based on UG. Figures 4.17 and 4.16 present an overview of the modeling system with its pre- and postprocessors as well as interfaces.

4.6.3 The Numerical Framework UG

UG (Bastian et al., 1997b) was written to provide a framework on which state-of-the-art simulation environments can be built. Many components that are required for the finite element or finite volume simulation of processes described by partial differential equations are independent of the problem, but are so complex that they cannot be implemented by one developer alone. With a framework like UG, developers can focus on modeling, discretization or solvers and don't need to know how load balancing, parallel load migration work in detail.

Domain Module The domain module can represent two-dimensional and three-dimensional geometries. With the domain manager module domain boundaries can be defined by means of boundary patches and domains can be split into several subdomains (with different material properties). It also handles the treatment of boundary conditions, so that for given nodes or element sides of the grid the user program can determine which boundary condition is valid in a given location. This works also if the grid is distributed over several processors. Inner boundaries are used to describe fractures and to associate a virtual width with each point on the fractures.

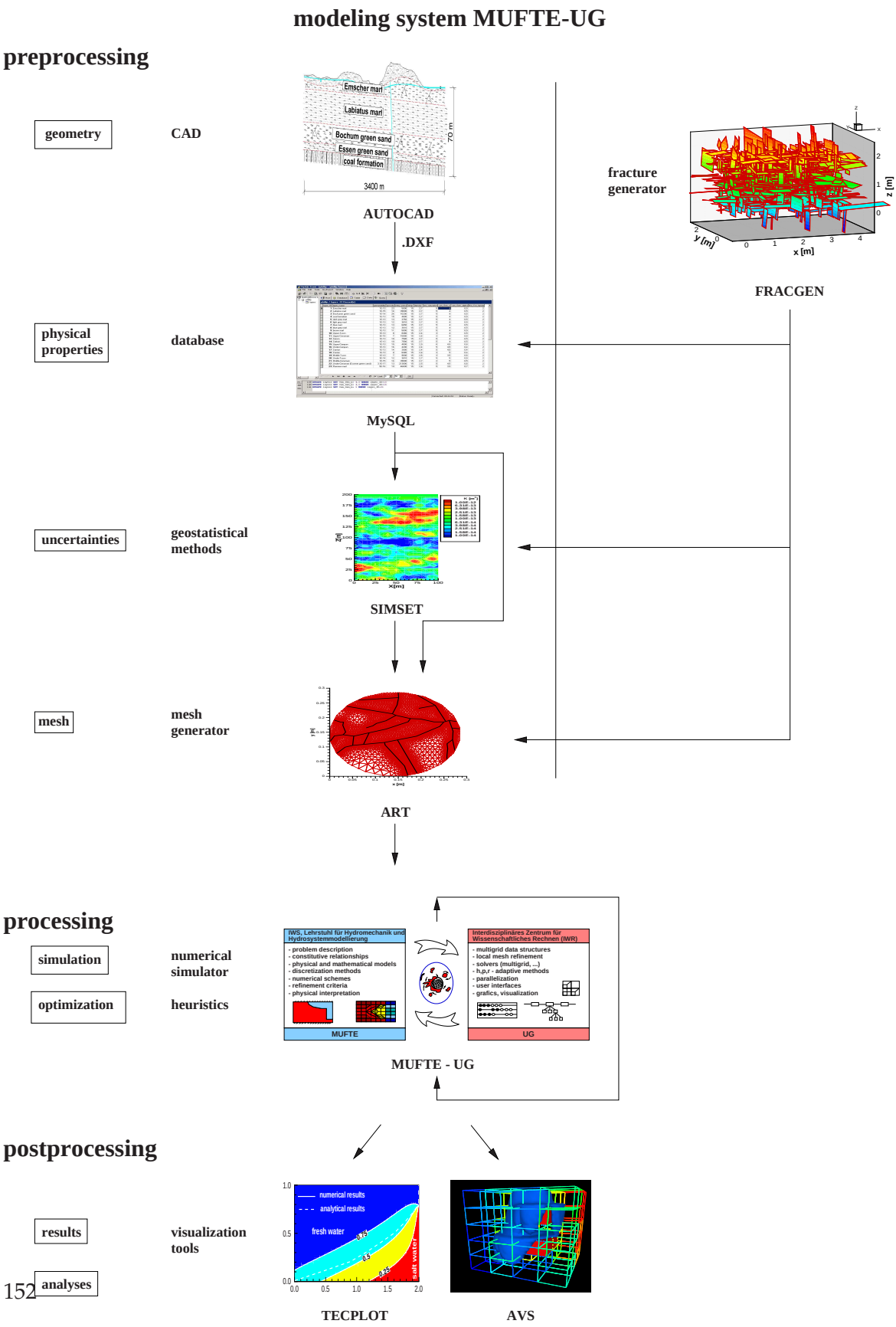

Figure 4.17: Modeling system MUFTE-UG with its pre- and postprocessors

Grid Manager UG can handle triangles and quadrilaterals for two-dimensional geometries and tetrahedrons, pyramids, prisms and hexahedrons for three-dimensional geometries. This variety of element types is necessary to maintain consistent grids in adaptive refinement (i. e. no hanging nodes will occur). The different element types also offer flexibility in the triangulation of complicated geometries.

Local grid refinement greatly reduces storage requirements for problems where sharp fronts or singularities in the solution require grid refinement only in certain regions of the domain.

Grids are stored in a hierarchical fashion. The hierarchical viewpoint is maintained throughout all components of the UG framework and is used to ensure scalability of all components.

Automatic Grid Generation Interfaces to different grid generator softwares exist as well as two grid generators which are included with UG, one for two-dimensional domains and one for three-dimensional domains. Additionally there are interfaces to several other grid generators.

User Data Manager The basic vector-matrix data structure is very flexible and allows for the attachment of degrees of freedom with nodes, edges, faces or elements. Based on the user data managers functionality, finite element methods and finite volume methods can be implemented, from simple node based schemes to complex higher-order methods.

Numerical Algorithms The numerical algorithms for the solution of linear and nonlinear systems as well as the time-stepping schemes are organized in a class hierarchy. The object-oriented approach makes designs of solutions schemes possible which are structurally clear, easily configurable and extensible. The algorithms are implemented in a problem-independent way. Components of a solution scheme can be chosen from a wide range of implemented classes.

Skript Language UG applications are driven by a script language. Its syntax is similar to C. UG applications can either be run in batch mode by executing scripts, or interactively.

Visualization module The visualization module of UG was designed in a scalable way, so that large parallel simulations can be visualized in an efficient way. It employs the hierarchical data structure and is parallelized, thus avoiding unnecessary calculations in the process. Output can be drawn to the screen or to PostScript or PPM files (as well as to a native picture format).

For more sophisticated visualization it is possible to write data in several visualization program formats: OpenDX/DataExplorer, TecPlot, GRAPE and AVS

I/O and restart In long simulation runs it is often necessary to save intermediate results from which the calculation can be restarted if a hardware error occurs and prevents the simulation from finishing. On parallel computers with several hundreds

of processors, this event is much more common than scientists would hope, and on many large computers there is a time limit for individual jobs which is easily exceeded by large simulation runs. In both cases the restart functionality is necessary.

Message Passing Parallelization UG is parallelized by a domain decomposition approach. An underlying framework, DDD (Dynamic Distributed Data) is responsible for the consistency of the data structures during all stages of the lifetime of an application, especially after modification and distribution of the grid. DDD is also responsible for packing messages, sending them to processors and unpacking them. The passing of messages is done with the functionality of the underlying Parallel Processor Interface (PPIF), which uses MPI, PVM or vendor-dependent message passing mechanisms.

Software Engineering The large complexity of UG results in a code basis of over 350.000 lines which were written in more than twelve years by seven main developers and numerous other contributors.

All these components work regardless of the underlying physical problem. If solver components are not suitable for the underlying problem it is usually easy to extend the concerning module by inheriting from the solver class and then modifying or extending its functionality.

Knowledge about the physical problem is part of the *problem classes*. These modules are implemented on top of UG and contain one or several discretizations of the mathematical description of the physical problem along with problem specific functionality (like e. g. constitutive relationships.

4.6.3.1 Pre- and post-processing

Although the simulation environment contains all components mentioned in figure 4.15, the components *geometric modeling*, *mesh generation*, and *visualization* are more loosely coupled to the simulation environment than the others. It is easier to use different visualization programs or grid generators since they can normally be connected by a file interchange format.

Domain generation In fractured systems the exact location of the fractures is often not known, but a realistic approximation of the fracture network is crucial for the simulation process. In these situations a fracture generator can be employed to generate fracture networks based on prescribed geological data. The program FRAC3D (Silberhorn-Hemminger, 2002), developed by A. Hemminger at the IWS, Stuttgart, can create a discrete structural model of a fractured domain based on data collected in the laboratory or the field. Domains created by FRAC3D can be converted to a format readable by UG.

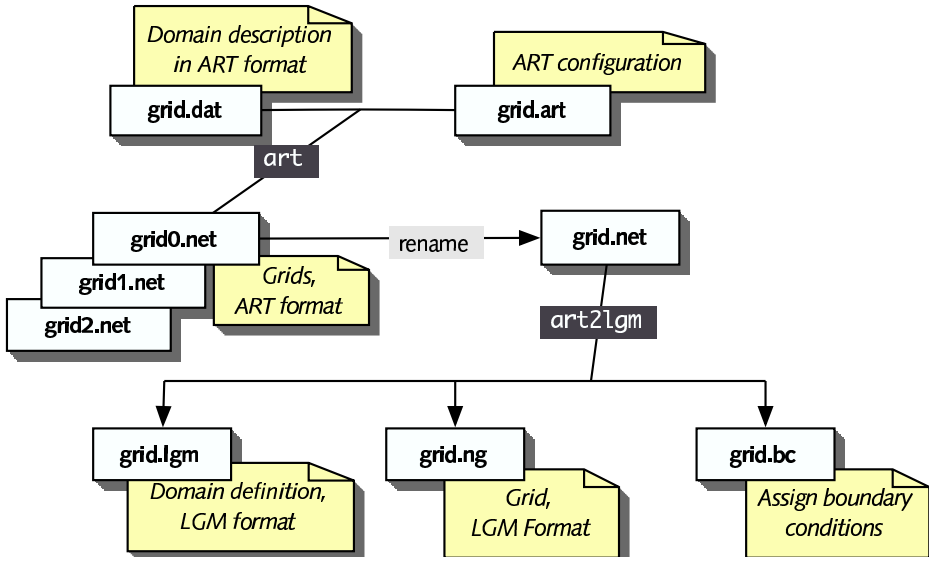

Figure 4.18: The grid generator ART creates grids from domains descriptions generated with the fractured domain generator FRAC3D. The resulting grid file is used for conversion to the LGM-Domain format. Domain as well as grid representation are taken from the grid file.

MESH GENERATION The next step in the simulation process is the creation of an intial mesh. For the geometric multigrid method it is advantageous to have a coarse initial mesh, but without degenerate elements (i. e. elements with large aspect ratios or large inner angles). The amount of work necessary to create these meshes by hand is prohibitive, so automatic grid generation has to be employed. Fuchs (1999) developed the grid generator ART3D in close collaboration with the research groups in Heidelberg and Stuttgart to meet the special demands of these problems. The lower-dimensional modeling of the fractures is advantegous in the grid generation process, because fractures have only to be treated like inner boundaries. This is much easier than the mesh generation for fracture-matrix systems which are represented as thin layers. In the latter case, adaptive grid generation has to be employed to avoid the creation of excessively many elements in the surrounding rock matrix. An interesting concept was introduced by Kornhuber (e. g. Neunhäuserer et al. (2002)), who proposed to employ mesh generation for the domain with fractures represented as inner boundaries, and in a post-processing step to extend the fractures to the full dimensionality. This has to be done carefully in order not to deteriorate the element quality in fracture intersections. The numerical results presented later suggest that the different possible shapes of the fracture ends (triangles or quadrilaterals in two space dimensions) obtained by this procedure have a significant influence on fluid flow and transport.

Figure 4.18 explains the process of how a mesh is created from the domain description file and how domain description and mesh are converted to LGM format (a UG-native domain and grid format). The converter `art2lgm` is a PERL-script, which reads

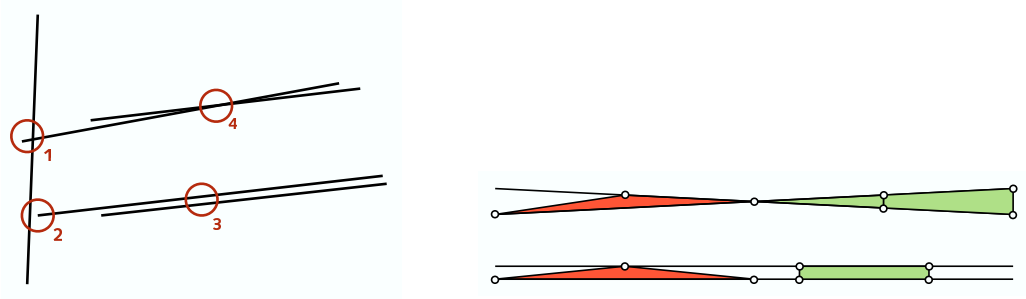

Figure 4.19: Four domain features which are difficult for automatic mesh generation (left) and possible elements of good quality (green) and poor quality (red) for parallel and almost parallel fractures (right).

the grid file created by ART3D and produces an LGM-domain description file and an LGM-grid description file. Only the ART3D-grid file is used for conversion, because this circumvents some complex geometrical calculations which would otherwise be necessary to determine the orientation of the domain boundaries. `art2lgm` uses all element sides on the domain boundary to create a triangulated boundary description. These boundary sides are used as boundary patches in UG. The third file that is created associates the boundary patches with the appropriate boundary conditions.

The automatic generation of meshes has persisted as one of the most challenging tasks of the simulation process. The mesh generation for fractured porous media has to treat four situations which are especially difficult. They are depicted in figure 4.19 for a two-dimensional domain, but the even more severe difficulties for three-dimensional domains can be traced back to these fundamental situations:

1. Fracture intersections, where one fracture end protrudes only slightly from the intersection. A fine mesh is required in the vicinity of this region, which should coarsen rapidly outside this region. In three-dimensional domains, the protruding fracture end can have a "difficult" shape, e. g. a very flat triangle.

2. Almost meeting fractures, where one fracture ends in close proximity to the other. The mesh should also be of high resolution only near this region.

3. Parallel fractures very close to each other should be meshed with quadrilaterals in two space dimensions and with hexahedrons or prisms in three space dimensions, because they can prevent the generation of elements with large inner angles.

4. Fractures intersecting at a very small angle can lead to the generation of elements with very large angles.

In both latter cases, automatic mesh generation of Delaunay-type is especially susceptible, because the mesh generation algorithm minimalizes a penalty functional which places vertices as far apart from each other as possible. In the case of parallel or almost parallel fractures this leads necessarily to large angles, where two vertices on the two

fractures, placed close to each other, would produce preferable elements. This is illustrated on the right in figure 4.19. Even if the green quadrilateral elements are divided into triangles, their largest angles are still close to 90°, while the red elements largest angles are close to 180°.

VISUALIZATION The visualization of fractured porous media problems requires the representation of lower-dimensional elements. We implemented an interface to the visualization software OpenDX, in which lower-dimensional elements can be realized and which can be combined in the visualization with volumetric elements. We also realized an interface to the visualization environment COVISE, where the virtual reality capabilities have been very helpful in discovering features of the solution which are otherwise difficult to detect.

4.6.4 SOFTWARE TOOLBOX MUFTE

MUFTE provides several modules for the numerical simulation of isothermal and non-isothermal multiphase / multicomponent flow and transport processes in porous and fractured-porous media:

- single-phase systems
  - single-phase flow: liquids, e.g. water, NAPLs, ...; gases , e.g. air, methane,...;
    incompressible, compressible
  - single- and multicomponent transport: e.g. contaminants, salt, dissolved gases, ...
  - fractures
  - 2D, 3D
- two-phase systems
  - two-phase flow: liquid / liquid, e.g. water / NAPL, water / oil, ...; liquid / gas, e.g. water / air, water / methane, ...;
    incompressible, compressible
  - two- and multicomponent transport: e.g. salt, dissolved gases, contaminants, ...
  - isothermal and non-isothermal (including phase transitions)
  - fractures
  - 2D, 3D
- three-phase systems
  - three-phase flow: liquid / liquid / gas, e.g. water / NAPL / air, ...;
    incompressible, compressible

- three- and multicomponent transport: e.g. contaminants, wator vapor, dissolved gases, ...
- isothermal and non-isothermal (including phase transitions)
- 2D

The model concepts include the extended *Darcy* law for the movement of multiple phases in isotropic or anisotropic, homogeneous or heterogeneous porous media. For the flow through fault zones and fractures, different flow laws and modeling techniques are available. Moreover, a large set of constitutive relationships for the relative permeability and the capillary pressure as well as state equations for densities, viscosities etc. are provided.

The two most common discretization techniques are the Fully Upwind Box Method, which is a Finite-Volume formulation with piecewise linear shape functions including fully upwinding of the upstream mobilities, and a Control-Volume Finite-Element Method, which is a mass-conservative formulation on a discrete patch including a first-order upwinding scheme. The time integration employs the Finite Difference method, and the temporal discretization is carried out fully implicitly. The development of *optimization methods* is underway (see Kobayashi et al. (2002)) to extend MUFTE-UG to a *decision-support system*.

A software versioning tool is strongly recommended for the development of large, complex software systems where different groups with a large number of scientists are involved. The *Concurrent Version System (CVS)* is used for the development of MUFTE-UG.

4.7 The Discontinuous Galerkin Method for Elliptic problems

The *discontinuous Galerkin method* (DG) is an attractive discretization scheme for fluid flow problems in porous media, because it is locally mass conservative like the finite volume method but also allows for higher order approximation and has relaxed requirements on the mesh. There is a large number of discretization methods which are all titled discontinuous Galerkin methods and they have been applied to such diverse problems as ground-water flow and multiphase flow (on which we will comment below), Euler and Navier-Stokes equations (Oden and Baumann, 2000, Bassi and Rebay, 1997b, 2000), semiconductor device simulation (Chen et al., 1995a,b), Maxwell's equations (Warburton and Karniadakis, 1999, Warburton, 2000), Hamilton-Jacobi equation (Hu and Shu, 2000) and neutron transport (Reed and Hill, 1973). We apply one discontinuous Galerkin method to the ground-water flow equation and compare its performance for fractured domains with the finite volume method of the previous chapter. The element type in the fractures are volumetric elements, not lower-dimensional elements as for the multiphase flow discretization.

The next section contains a short overview of (some) discontinuous Galerkin methods. Then we present the bilinear form employed for our discretization, explain the fast

multigrid solution of the systems and present numerical results.

4.7.1 Development of the Discontinuous Galerkin Method

Discontinuous Galerkin methods derive their name from the choice of trial and test functions which are discontinuous across element boundaries and continuous within elements. The development of the discontinuous Galerkin method is reviewed in Cockburn et al. (2000a); an overview of the state of the art in 2000 is the collection Cockburn et al. (2000b).

The original discontinuous Galerkin method was presented by Reed and Hill (1973) for the solution of the neutron transport equation, a stationary linear hyperbolic problem of the form

$$\nabla \cdot \{\mathbf{a}u\} + \sigma u = f \qquad \text{in } \Omega. \tag{4.148}$$

σ is a real number and $\mathbf{a}$ is a constant vector. If we multiply the equation by a test function v and integrate over the element domain Ω_e of an element e from a triangulation E_h of Ω, we get after integration by parts

$$-\int_{\Omega_e} u\mathbf{a}\cdot\nabla v \, d\mathbf{x} + \int_{\partial\Omega_e} \mathbf{a}\cdot\mathbf{n}uv \, ds + \sigma \int_{\Omega_e} uv \, d\mathbf{x} = \int_{\Omega_e} fv \, d\mathbf{x}. \tag{4.149}$$

$\mathbf{n}$ is the outward unit normal to element e. To get an approximation u_h of u, we choose the test functions to be polynomials of degree at most k on the elements of the triangulation. The space of polynomials of degree at most k on element e is denoted by $P_k(\Omega_e)$. Now we determine u_h as the solution of: *Find* u_h *such that for all* $e \in E_h$ *and all* $v \in V \in P_k(\Omega_e)$

$$-\int_{\Omega_e} u_h\mathbf{a}\cdot\nabla v \, d\mathbf{x} + \int_{\partial\Omega_e} \mathbf{a}\cdot\mathbf{n}_e\hat{u}_h v \, ds + \sigma \int_{\Omega_e} u_h v \, d\mathbf{x} = \int_{\Omega_e} fv \, d\mathbf{x} \tag{4.150}$$

with the *numerical flux*

$$\hat{u}_h(\mathbf{x}) = \lim_{s\to 0+} u_h(\mathbf{x} - s\mathbf{a}). \tag{4.151}$$

The value $\hat{u}_h(\mathbf{x})$ is the *upwind* value of u_h upstream of the characteristic direction $\mathbf{a}$. When the elements are ordered according to the characteristic direction of $\mathbf{a}$, the u_h values can be computed element by element from the upstream values of u_h hitting $\partial\Omega_e$.

The discontinuous Galerkin can be employed as a time differencing scheme as well, see Thomée (1997) and Eriksson et al. (1996). The first analysis of the discontinuous Galerkin method as a time differencing scheme was done in Lesaint and Raviart (1974) and Jamet (1978), Eriksson et al. (1985) studied the method for parabolic equations. In the context of ordinary differential equations the first analysis was done by Delfour et al. (1981). A posteriori error control was pioneered by Johnson et al. (1990).

A series of papers by Cockburn and Shu (Cockburn and Shu, 1991, 1989, Cockburn et al., 1989, 1990, Cockburn and Shu, 1998b), where the discontinuous

Galerkin method was employed for nonlinear time-dependent hyperbolic problems, propelled the interest in the method. They investigated the discontinuous Galerkin discretization in space with the explicit TVD Runge-Kutta time discretizations by Shu (1988), together with limiter methods in the multidimensional case to ensure nonlinear stability and convergence to the entropy solution.

In 1998, Cockburn and Shu (1998a) introduced the *local discontinuous Galerkin method* (LDG), based on the work of Bassi and Rebay (1997a) for the compressible Navier-Stokes equations, and proved stability and error estimates for this method which is suited for convection-dominated convection-diffusion problems. The LDG method is based on rewriting the equation as a first order system and then discretizing by the DG method. Nonlinear stability without flux limiters can be achieved for this method by a careful choice of the rewriting and the numerical fluxes. The LDG method is locally mass conservative, which is a property that in general is difficult to achieve for higher-order finite element methods. If LDG is applied to elliptic equations the method can be ill-posed for some choices of the numerical fluxes (e. g. the choice by Bassi and Rebay in their original DG scheme).

A discontinuous Galerkin method suitable for elliptic problems was introduced in Baumann (1997), Oden et al. (1998), Baumann and Oden (1999). This is the method we are going to employ below and we would like to explain the evolution of this method. The ingredient with the oldest roots is the incorporation of Dirichlet boundary conditions in a weak form through *penalty terms* in the standard finite element method (Nitsche, 1971, Lions, 1968). In order to solve

$$-\Delta u = f \text{ in } \Omega, \qquad u = g \text{ on } \partial\Omega \tag{4.152}$$

one uses the weak form

$$\int_\Omega \nabla u \cdot \nabla v \, d\boldsymbol{x} + \int_{\partial\Omega} \mu(u-g)v \, ds = \int_\Omega f v \, d\boldsymbol{x} \qquad \forall v \in H^1(\Omega). \tag{4.153}$$

The traditional way to impose Dirichlet boundary conditions is by an appropriate choice of the trial functions. Note that the trial functions above are not zero at the Dirichlet boundary. The penalty parameter μ is mesh-dependent.

In this setting the trial and test functions are still continuous. The *interior penalty* Galerkin finite element method (IP) (Wheeler, 1978, Percell and Wheeler, 1978) uses discontinuous basis and trial functions and ensures continuity of the solution at inter element boundaries by penalties. The method was extended to nonlinear elliptic and parabolic equations in Arnold (1979, 1982). The IP method is symmetric and locally mass conservative, and optimal error estimates could be proven, but it hasn't found much practical application because the resulting systems are indefinite and very difficult to solve, and because there is no way to find an optimal choice of the penalty parameter μ for particular problems; it has to be chosen large enough to make the bilinear form coercive.

In his thesis, Baumann (1997) proposed a new stabilization. It is non-symmetric and does not require a penalty term. It was analyzed in Oden et al. (1998) and Rivière (2000),

Rivière et al. (1999), Rivière and Wheeler (2000), where also the *non-symmetric interior penalty method* (NIPG) was introduced which contains an additional penalty term. The relations between LDG, Baumann-Oden DG, IP and NIPG are explored in Arnold et al. (2002); their performance is assessed in Castillo (2002). Applications to porous medium problems can be found in Rivière (2000), Rivière et al. (2000), Aizinger et al. (2001). The DG method presented here has been extended to transport in Bastian and Lang (2002) and two-phase flow in an IMPES formulation in Bastian (2002).

The discontinuous Galerkin methods developed in recent years have several advantages which make them competitive or even superior to standard finite element methods.

- ▷ Given that the problem possesses enough regularity, the methods are higher order convergent. For many methods, the convergence rates are optimal in the L_2 and H^1 norm.discontinuos Galerkin
- ▷ The methods can be applied to elliptic, parabolic and hyperbolic problems.
- ▷ The methods are locally mass conservative.
- ▷ For elliptic problems fast multigrid solvers are available (Bastian and Reichenberger, 2000, Gopalakrishnan and Kanschat, 2003, Hemker and van Raalte, 2002).
- ▷ The methods can be employed on unstructured, non-matching grids, which makes them very flexible and easy to implement. This makes h-adaptivity particularly easy. Additionally, they provide an easy access to hp-adaptive methods, given the availability of a p-estimator.
- ▷ For time-dependent problems suitable high-order explicit as well as implicit time discretizations are available.
- ▷ Modern, cache-based computer architectures are utilized efficiently since matrices with small dense blocks arise and the method is not limited as much by memory throughput as is the case for low-order unstructured finite element and finite volume methods.

4.7.2 Formulation of the Bilinear Form

We consider the ground-water equation (4.6) with constant density and viscosity,

$$-\nabla\cdot\left(\rho\frac{K}{\mu}\nabla p\right) = \rho q \qquad \text{in } \Omega\subset\mathbb{R}^d,\ d=2,3. \tag{4.154a}$$

$$p = p_d \qquad \text{on } \Gamma_d \tag{4.154b}$$

$$\mathbf{u}\cdot\mathbf{n} = \phi \qquad \text{on } \Gamma_n \quad \text{with} \quad \mathbf{u} = -\rho\frac{K}{\mu}\nabla p \tag{4.154c}$$

	k =	0	1	2	3	4	5	6	7	8
d = 2	P_k	1	3	6	10	15	21	28	36	45
	Q_k	1	4	9	16	25	36	49	64	81
d = 3	P_k	1	4	10	20	35	56	84	120	165
	Q_k	1	8	27	64	125	216	343	512	729

Table 4.1: Number of unknowns in one element for the DG method.

Let E_h denote a subdivision of Ω, which does not have to be a triangulation (i. e. *hanging nodes* are allowed) and which may contain elements of mixed type. An example for an admissible mesh is shown here. For the basis and test functions we choose the space of polynomial functions of degree k on element $e \in E_h$

$$P_k(\Omega_e) = \{p : \Omega_e \to \mathbb{R} \mid p(x,y) = \sum_{0 \le a+b \le k} c_{ab}\, x^a y^b\}. \tag{4.155}$$

P_k can be used as the basis for triangles and quadrilaterals; alternatively we can choose the basis functions from the polynomial space

$$Q_k(\Omega_e) = \{p : \Omega_e \to \mathbb{R} \mid p(x,y) = \sum_{0 \le a,b \le k} c_{ab}\, x^a y^b\}, \tag{4.156}$$

which is the more natural choice for quadrilaterals. The extension to three space dimensions is obvious.

In the implementation of our computer program the bases of P_k and Q_k are chosen as L_2-orthonormal polynomials, which are generated from the monomials by Gram-Schmidt orthonormalization. The shape of the resulting functions is depicted in figure 4.20. The dimension of the space spanned by the basis functions for a choice of the degree k—i. e. the number of unknowns per element—is shown in table 4.1.

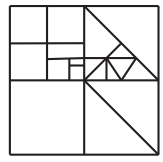

Admissible mesh

We choose the space of trial functions to be

$$V^k(E_h) = \prod_{e \in E_h} P_k(\Omega_e). \tag{4.157}$$

The interior boundary between element e and f (edges in 2D and faces in 3D) is denoted by

$$\Gamma_{ef} = \partial\Omega_e \cap \partial\Omega_f.$$

The set of all interior edges is

$$\Gamma_{int} = \bigcup_{e,f \in E_h, e \neq f} \Gamma_{ef}. \tag{4.158}$$

With every interior edge Γ_{ef} we associate a unique unit normal vector $\mathbf{n}$. A possible choice is to let $\mathbf{n}$ point from element e to f if $e > f$ and from f to e otherwise. For any

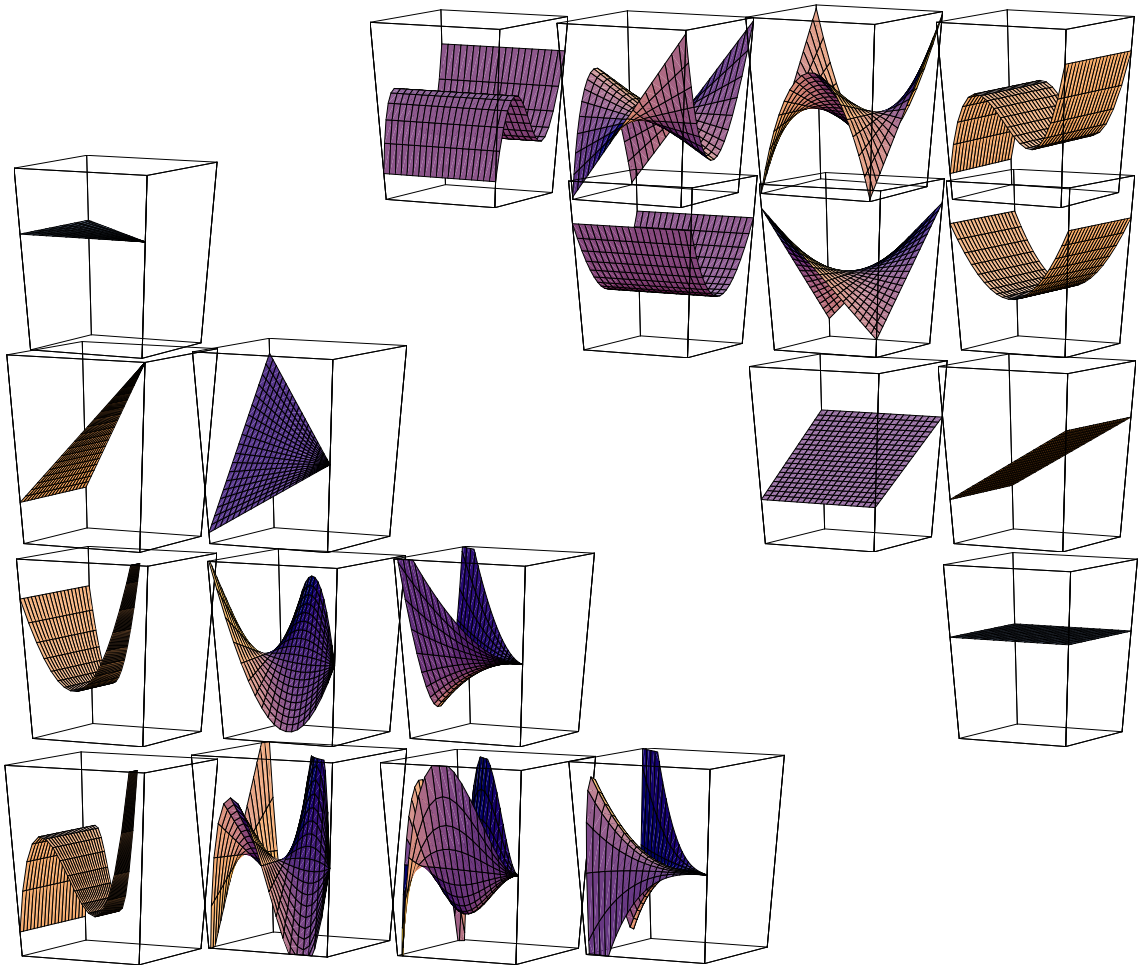

Figure 4.20: Discontinuous Galerkin method basis functions. In the upper triangle are the P_2 basis functions on the quadrilateral element, in the lower triangle the P_2 basis functions for the triangular element.

point $\mathbf{x} \in \Gamma_{ef}$ we define the *jump* of a function $v \in V^k(E_h)$ by

$$[v](x) = \lim_{\varepsilon \to 0+} v(x + \varepsilon n_{ef}) - \lim_{\varepsilon \to 0+} v(x - \varepsilon n_{ef}) \tag{4.159}$$

and the average by

$$\langle v \rangle(x) = \frac{1}{2} \left(\lim_{\varepsilon \to 0+} v(x + \varepsilon \mathbf{n}) + \lim_{\varepsilon \to 0+} v(x - \varepsilon \mathbf{n}) \right). \tag{4.160}$$

The identity

$$[vw] = [v]\langle w \rangle + \langle v \rangle [w] \tag{4.161}$$

is easily verified.

Let us now go back to (4.154a) and derive the bilinear form for the discretization. We consider one element $e \in E_h$ and multiply with a test function $v \in P_k(\Omega_e)$. After integration by parts we get

$$\int_{\Omega_e} \rho \frac{K}{\mu} \nabla p \cdot \nabla v \, d\mathbf{x} - \int_{\partial\Omega_e} \rho \frac{K}{\mu} \nabla p \cdot \mathbf{n} \, v \, ds = \int_{\Omega_e} q v \, d\mathbf{x} \qquad \forall v \in P_k(\Omega_e) \tag{4.162}$$

Summation over all elements in E_h and collecting the boundary integrals into interior and exterior edges results in

$$\begin{aligned} -\sum_{e \in E_h} \int_{\Omega_e} \rho \frac{K}{\mu} \nabla p \cdot \nabla v \, d\mathbf{x} + \sum_{\Gamma_{ef} \in \Gamma_{int}} \int_{\Gamma_{ef}} [\rho \frac{K}{\mu} \nabla p \cdot \mathbf{n} \, v] ds \\ + \sum_{\Gamma_e \in \partial\Omega} \int_{\Gamma_e} \rho \frac{K}{\mu} \nabla p \cdot \mathbf{n} \, v \, ds = \sum_{e \in E_h} \int_{\Omega_e} q v \, d\mathbf{x} \qquad \forall v \in V^k(E_h) \end{aligned} \tag{4.163}$$

The interface between two neighboring elements is handled by the second term on the left side. For second order elliptic problems there are two interface conditions: The first interface condition is continuity of the pressure, $[p] = 0$. Second, the normal flux should be continuous, which can be expressed as

$$[\rho \frac{K}{\mu} \nabla p \cdot \mathbf{n}] = 0 \tag{4.164}$$

and which is incorporated into the second term by

$$[\rho \frac{K}{\mu} \nabla p \cdot \mathbf{n} \, v] = [\rho \frac{K}{\mu} \nabla p \cdot \mathbf{n}] \langle v \rangle + \langle \rho \frac{K}{\mu} \nabla p \cdot \mathbf{n} \rangle [v] = \langle \rho \frac{K}{\mu} \nabla p \cdot \mathbf{n} \rangle [v]. \tag{4.165}$$

The bilinear form for the discontinuous Galerkin method follows from (4.163) by inserting the flux boundary conditions, splitting the boundary term into Dirichlet and Neumann parts and collecting terms independent of p on the right hand side. The penalty on the jump of p at interior edges is included in the second sum of a_h.

$$a_h(p, v) = \sum_{e \in E_h} \int_{\Omega_e} \rho \frac{K}{\mu} \nabla p \cdot \nabla v \, d\mathbf{x} \tag{4.166}$$

$$+\sum_{\Gamma_{ef}\in\Gamma_{int}}\int_{\Gamma_{ef}}\left\langle\rho\frac{K}{\mu}\nabla v\cdot\mathbf{n}\right\rangle[p]-[v]\left\langle\rho\frac{K}{\mu}\nabla p\cdot\mathbf{n}\right\rangle\,ds$$
$$+\sum_{\Gamma_e\in\Gamma_d}\int_{\Gamma_e}(\rho\frac{K}{\mu}\nabla v\cdot\mathbf{n})p-v(\rho\frac{K}{\mu}\nabla p\cdot\mathbf{n})\,ds.$$
$$l_h(v)=\sum_{e\in E_h}\int_{\Omega_e}qv\,d\mathbf{x}+\sum_{\Gamma_e\in\Gamma_d}\int_{\Gamma_e}(\rho\frac{K}{\mu}\nabla v\cdot\mathbf{n})p_d\,ds+\sum_{\Gamma_e\in\Gamma_n}\int_{\Gamma_e}v\phi\,ds$$

The Baumann-Oden discontinuous Galerkin method by Baumann and Oden (1999), Baumann (1997), Oden et al. (1998) is: *Find* $p\in V^k(E_h)$ *such that for all* $v\in V^k(E_h)$

$$a_h(p,v)=l(v). \tag{4.167}$$

The NIPG method by Riviére and Wheeler employs the additional penalty term

$$J_0^{\sigma,\beta}(u,v)=\sum_{\Gamma_{ef}\in\Gamma_{int}}\frac{\sigma_{ef}}{|\Gamma_{ef}|^\beta}\int_{\Gamma_{ef}}[u][v]\,ds+\sum_{\Gamma_e\in\Gamma_{wd}}\frac{\sigma_e}{|\Gamma_e|^\beta}\int_{\Gamma_e}uv\,ds. \tag{4.168}$$

with user-defined parameters σ and β; this penalty was employed in the original IP method. The formulation of the NIPG method is: *Find* $p\in V^k(E_h)$ *such that for all* $v\in V^k(E_h)$

$$a_h(p,v)+J_0^{\sigma,\beta}(p,v)=l(v)+\sum_{\Gamma_e\in\Gamma_{wd}}\frac{\sigma_e}{|\Gamma_e|^\beta}\int_{\Gamma_e}vp\,ds. \tag{4.169}$$

Both the Baumann-Oden method and the NIPG method are unsymmetric, even if the underlying continuous problem is symmetric. The Baumann-Oden method requires $k\geq 2$ to be stable, for the NIPG method $k\geq 1$ is sufficient. Both methods are locally conservative. This can be verified for the Baumann-Oden method by inserting a test function that is constant on each element into (4.167),

$$\sum_{\Gamma_{ef}\in\Gamma_{int}}\int_{\Gamma_{ef}}[v]\,\langle\rho\frac{K}{\mu}\nabla p\cdot\mathbf{n}\rangle ds+\sum_{\Gamma_e\in\partial\Omega}\int_{\Gamma_e}\rho\frac{K}{\mu}\nabla p\cdot\mathbf{n}\,v\,ds=\sum_{e\in E_h}\int_{\Omega_e}qv\,d\mathbf{x}, \tag{4.170}$$

which reduces (4.167) to a flux balance equation. The close relation of the DG schemes to finite volume methods is apparent.

The Baumann-Oden DG method exhibits optimal order convergence in the H^1-norm, i. e. $O(h^k)$ for polynomials of degree k, provided that the solution is sufficiently regular. Convergence in L_2 is $O(h^{k+1})$ for k odd and (suboptimal) $O(h^k)$ for k even for the Baumann-Oden DG method. The NIPG is optimal in the L_2 norm for odd and even choices of k. The suboptimal convergence of the Baumann-Oden method is due to the absence of a stabilizing penalty term.

We prefer the Baumann-Oden DG method over the NIPG method because of its lack of user-defined parameters, because it is computationally cheaper, and because the suboptimal convergence in the L_2 norm does not harm the efficiency of the method for

ground-water flow equations, where the gradient of p—measured in the H^1 norm—is the relevant quantity.

The DG method can be extended to handle lower-dimensional elements and hence fractures in a similar way as described for the finite volume method. This would require the implementation of degrees of freedom on these boundary sides which are part of the fracture network. Another interesting potential of the method is the choice of basis functions for volumetric fracture elements, which are adjusted to the anisotropy and contain more degrees of freedom in one direction than in the other.

4.7.3 Multigrid Solution

After inserting a basis into (4.167), a large system of linear equations has to be solved. The multigrid method, explained in section 4.5, can be used to solve these systems with optimal complexity.

We assume a hierarchy of nested triangulations $E_0, \dots, E_L$, with n_l elements on grid level l. On every grid level the discrete spaces $V_l^k = V^k(E_l)$ is equipped with the basis

$$\mathcal{B}_l = \{\varphi_1^l, \dots, \varphi_{n_l}^l\}. \tag{4.171}$$

φ_i^l has support in exactly one element. The indices of the basis functions associated with element Ω_e are

$$I_e^l = \{j \mid \operatorname{supp} \varphi_j^l \subseteq \overline{\Omega_e}\}. \tag{4.172}$$

Since the triangulations are nested, the according discrete spaces are also nested,

$$V_0^k \subseteq \cdots \subseteq V_L^k, \tag{4.173}$$

and coarse grid basis functions can be represented in the fine grid basis functions

$$\varphi_i^l = \sum_{j=1}^{n_{l+1}} \omega_{ij}^{l+1} \varphi_j^{l+1}. \tag{4.174}$$

The factors ω_{ij}^{l+1} can be computed as follows. Let φ_i^l be the basis function with support in Ω_e, $e \in E_l$ and Ω_f be an element obtained from the subdivision of Ω_e. By $\hat{\varphi}_i^l$ and $\hat{\varphi}_j^{l+1}$ we denote basis functions on the reference element that are mapped to the global basis functions φ_i^l and φ_j^{l+1}. The restriction of φ_i^l to Ω_f is a polynomial of degree k and can be represented uniquely with the basis functions on Ω_f. The representation can be computed on the reference element $\hat{\Omega}$ using

$$\varphi_i^l|_{\Omega_f} = \sum_{j \in I_f^{l+1}} \omega_{ij}^{l+1} \varphi_j^{l+1}$$

$$\Leftrightarrow \qquad \hat{\varphi}_i^l \circ T_{\Omega_e}^{-1} \circ T_{\Omega_f} = \sum_{j \in I_f^{l+1}} \omega_{ij}^{l+1} \hat{\varphi}_j^{l+1}$$

$$\Leftrightarrow \qquad \forall m \in I_f^{l+1} : \quad (\hat{\varphi}_i^l \circ T_{\Omega_e}^{-1} \circ T_{\Omega_f}, \hat{\varphi}_m^{l+1})_{\hat{\Omega}} = \sum_{j \in I_f^{l+1}} \omega_{ij}^{l+1} (\hat{\varphi}_j^{l+1}, \hat{\varphi}_m^{l+1})_{\hat{\Omega}}. \quad (4.175)$$

Here $(\cdot,\cdot)_{\hat{\Omega}}$ is the L_2 scalar product and T_{Ω_f} is the mapping from the reference element to Ω_f. We can now employ the L_2 orthonormality of the basis, due to which the mass matrix is the identity, and get

$$\omega_{ij}^{l+1} = (\hat{\varphi}_i^l \circ T_{\Omega_e}^{-1} \circ T_{\Omega_f}, \hat{\varphi}_m^{l+1})_{\hat{\Omega}}. \quad (4.176)$$

The factors ω_{ij}^{l+1} can be precomputed, because the transformation $T_{\Omega_e}^{-1} \circ T_{\Omega_f} : \hat{\Omega} \to \hat{\Omega}$ depends only on the type of refinement and not on the shape of individual elements. However, since a large number of refinement rules are necessary for hybrid grids in three dimensions, we evaluate (4.176) using numerical quadrature. The factors ω_{ij}^l are the entries of the restriction and prolongation matrices.

The smoother should remove all algebraic errors that are not handled by the coarse grid correction. In that sense it is complementary to the coarse grid correction. The point-wise Jacobi and Gauß-Seidel iterations are not applicable since the matrix A is only positive semi-definite ($x^T A x \geq 0$). Zero diagonal elements are obtained for inserting into the bilinear form a function that is constant on an element. For this reason one has to use block iterations. The most natural block structure is given by combining all degrees of freedom corresponding to one element

$$A^{l,e,f} = \left(A_{ij}^l\right)_{i \in I_e^l, j \in I_f^l} \quad (4.177)$$

and A^l being the block matrix

$$A^l = \left(A^{l,e,f}\right)_{\Omega_e, \Omega_f,\, e,f \in E_l}. \quad (4.178)$$

Unfortunately, Jacobi and Gauß-Seidel iterations with respect to this block structure are not effective smoothers. This can be explained as follows: The diagonal block $A^{l,e,f}$ corresponds to a discretization of the flow equation on element Ω_e including a weak form of continuity of pressure over $\partial\Omega_e$. Because neighboring elements fix the "boundary conditions" for the current element, the error on the inter-element boundaries is only removed very slowly. The situation can be remedied by an overlapping patch smoother, where, for every element Ω_e, all degrees of freedom of Ω_e and some neighborhood are updated. This iteration is an effective smoother but has a high operation count.

The incomplete LU-decomposition on the block structure is a very effective smoother and has a low operation count. The only drawback of ILU is that an additional matrix has to be stored. Note that the ordering of the blocks is not important unless some robustness with respect to discontinuous or anisotropic permeability is required.

If the permeability K is very different from element to element we observe the following problem: Assume that element Ω_e has permeability $K = \varepsilon I$ and all neighboring elements Ω_f have permeability $K = I$ where I is the identity. Then all entries of the diagonal block $A^{l,e,e}$ will have size $O(\varepsilon)$ and all off-diagonal blocks $A^{l,e,f}$ will have entries of

size $O(1)$. The patch-wise smoothers do not work in this case. The ILU-smoother works if blocks corresponding to low permeability elements are ordered first. Therefore, for general permeability fields, we order the blocks with respect to increasing permeability.

Choosing k equal for all grid levels is not necessary; the low-frequency errors on the coarser levels can be represented with polynomials of lower order. On the other hand, an implementation with equal polynomial degree on all grid levels is easier to implement and does not harm the overall performance.

Recently, a different approach to multigrid for the Baumann-Oden method has been proposed by Hemker et al. (2002b), Hemker et al. (2002a), Hemker and van Raalte (2002), for which convergence of the multigrid method with Jacobi and Gauß-Seidel smoothers could be shown for the Poisson equation in one and two space dimensions. They employed a point-wise block-partitioning, which gives better results than the cell-wise partitioning.

4.7.4 Numerical Results for the Multigrid Solution of Discontinuous Galerkin Methods

We investigate the efficiency of the multigrid algorithm for the Baumann-Oden method on several examples, where we compare them to the cell-centered finite volume method. The examples are chosen as a problem with full regularity, a problem with a reentrant corner and a problem with a heterogeneous permeability field with discontinuous coefficients. More applications, including unstructured grids in a complex geometry, are considered in Bastian and Reichenberger (2000). The last example is a comparison of the Baumann-Oden DG method and the finite volume method for a problem with a fracture. The fracture is modeled as a thin layer with different material properties.

We refrain from a description of the cell-centered finite volume method for single phase flow. The solution of the single phase flow equation would be possible with the finite volume method for two-phase flow, if $S_g = 0$ is chosen throughout the domain. Due to its simplicity we implemented the finite volume scheme for single phase flow in porous media as well as in fractured porous media with mixed-dimensional elements.

4.7.4.1 Single Phase Flow in Homogeneous Media

The first example treats a problem with full regularity. For these kinds of problems the higher-order DG method should be clearly superior to the finite volume method. We solve the Poisson equation on the unit square

$$-\Delta p = f \text{ in } \Omega = (0,1)^2 \qquad p = p_0 \text{ on } \partial\Omega$$

and choose f and p_0 such that the exact solution

$$p(x,y) = e^{-\left((x-1/2)^2+(y-1/2)^2\right)}$$

h^{-1}	FV	$r=2$	$r=3$	$r=4$	$r=5$	$r=6$
4	3	5	5	5	5	4
8	4	7	6	6	5	6
16	4	7	6	6	5	6
32	4	7	6	6	5	6
64	4	7	6	6	5	6
128	4	6	6	6		
256	4					
512	4					

Table 4.2: Number of multigrid iterations for the fully regular model problem.

is obtained. In figure 4.21 the error in the L_2 and H^1 norms are plotted. Note that the x-axis does not show the necessary number of iterations but the wall clock computation time, which is the more interesting quantity in practice. The number of multigrid iterations are displayed in table 4.2, which shows the h-independence of the method. We compared the finite volume method (FV) and the DG method with polynomials up to degree six for a multigrid V-cycle with one ILU pre- and post-smoothing step and list iteration numbers for a 10^{-8} reduction of the initial residual.

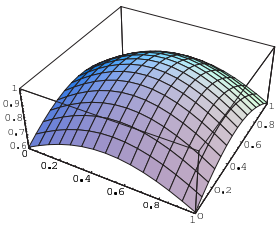

$p(x,y) = e^{-((x-1/2)^2+(y-1/2)^2)}$

The DG method is clearly superior for this example. The sub-optimal convergence $O(h^k)$ in the L_2 norm for even degrees k is confirmed by the numerical experiment. For odd polynomial degrees k the convergence is optimal ($O(h^{k+1})$) in the L_2 norm, and optimal convergence of $O(h^k)$ in the H^1-norm is obtained for all degrees of k.

4.7.4.2 Single Phase Flow in Heterogeneous Media

The second example is taken from Durlofsky (1994). It explores the quality of the DG solutions for elliptic problems with highly discontinuous coefficients for the problem

$$-\nabla \cdot (K \nabla p) = f \quad \text{in } \Omega = (0,1)^2. \tag{4.179}$$

The boundary conditions are chosen as $p = 1$ for $x = 0$, $p = 0$ for $x = 1$ and no flow boundary conditions for $y = 0$ and $y = 1$. The permeability field is defined on a regular 20×20 mesh and is shown in Fig. 4.22 on the left. In dark areas the permeability is $K = 10^{-6} \cdot I$, elsewhere it is $K = I$. We employ a coarse grid with $20 \cdot 20 \cdot 2$ triangular elements. The coarse grid resolves the discontinuities in the permeability field, finer grids are obtained by regular refinement. Fig. 4.22 shows on the right the flow field computed with degree $k = 3$ on the coarsest mesh.

Durlofsky (1994) gave a reference solution for the total flux through the system, based on computing approximations on a sequence of meshes up to 200×200 with a cell centered finite volume scheme and extrapolation to $h = 0$. The "exact" value is 0.5205. We

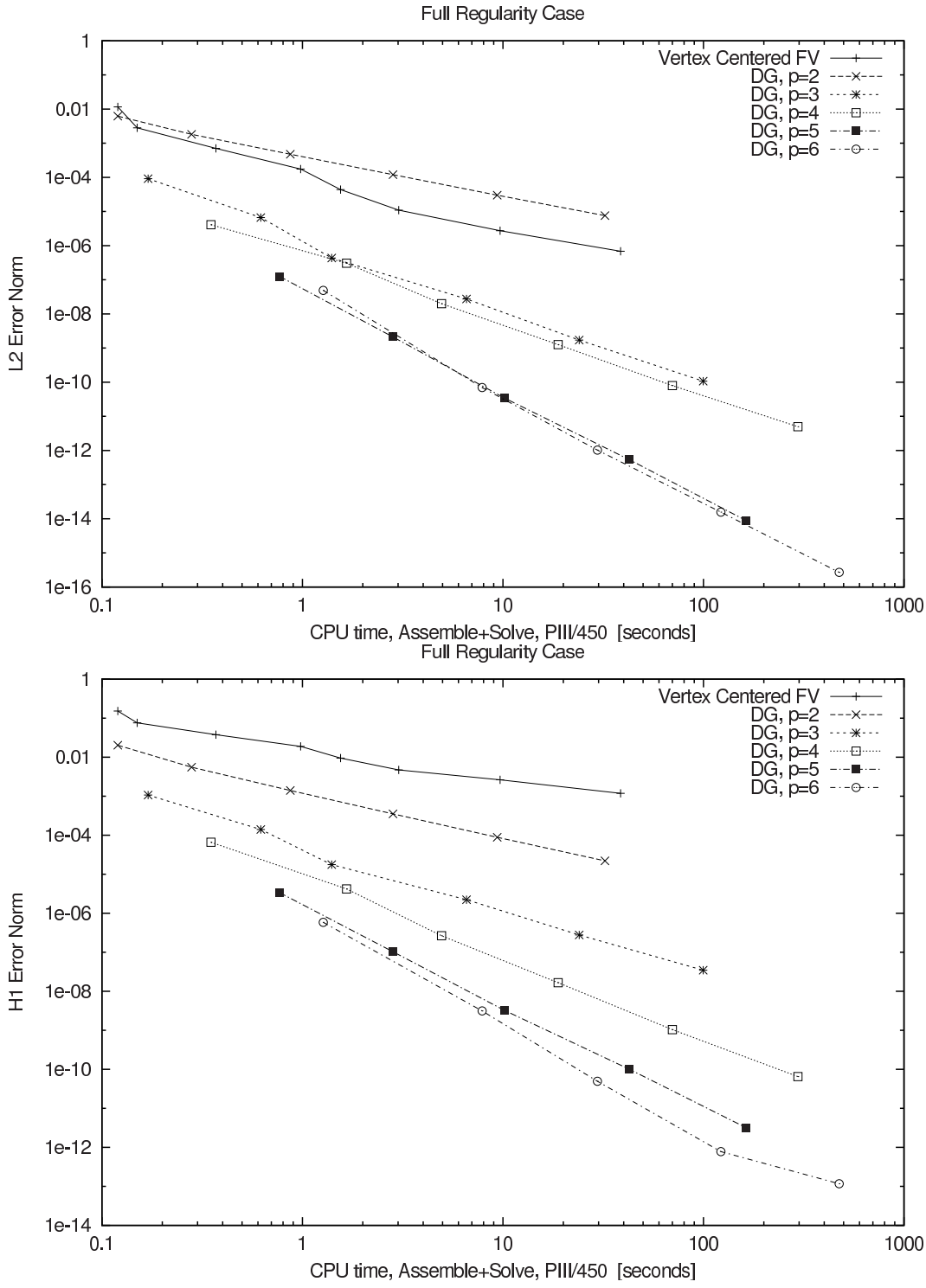

Figure 4.21: L_2 and H^1 error for the full regularity problem.

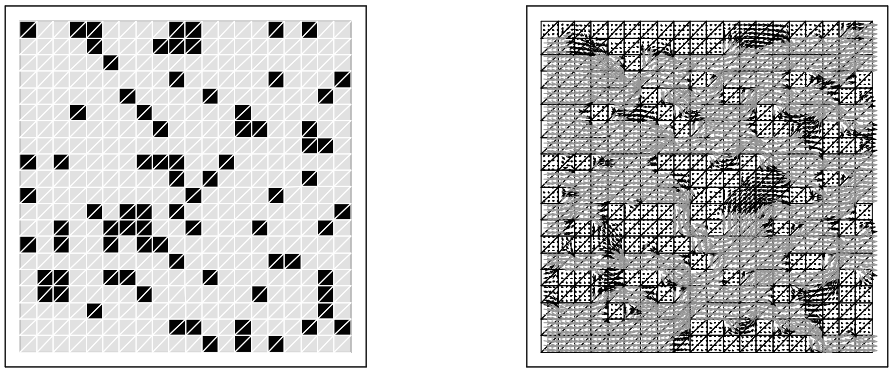

Figure 4.22: Permeability and flow field for the discontinuous coefficient example computed with DG(3). Permeability 1 is shown in light gray and 10^{-6} in black. Vectors not drawn to scale are indicated by gray color in the vector plot.

h^{-1}	FV	$k=2$	$k=3$	$kk=4$	$k=5$	$k=6$	MFE
20	0.6991	0.5094	0.5152	0.5174	0.5232	0.5152	0.4508
40	0.6466	0.5179	0.5181	0.5208	0.5206		
80	0.6170	0.5194	0.5192	0.5201			
160	0.5998	0.5199	0.5198				
320	0.5890						
640	0.5816						

Table 4.3: Total flux through the system for discontinuous coefficient example.

l	h^{-1}	FV	$k=2$	$k=3$	$k=4$
1	40	6	14	14	16
2	80	7	14	12	15
3	160	7	13	12	
4	320	8			
5	640	9			

Table 4.4: Number of multigrid cycles in the discontinuous coefficient example.

compare the vertex centered finite volume method—which in this case is identical to P1 conforming finite elements— and DG with $k=2,\ldots,6$. The values for the mixed finite element method are taken from Durlofsky (1994). The results show that the conforming finite volume/finite element method is not well suited for this problem. The error in the mixed finite element solution on the coarsest mesh is approximately a factor six larger than the error in the DG result on the same mesh, but we note that the number of

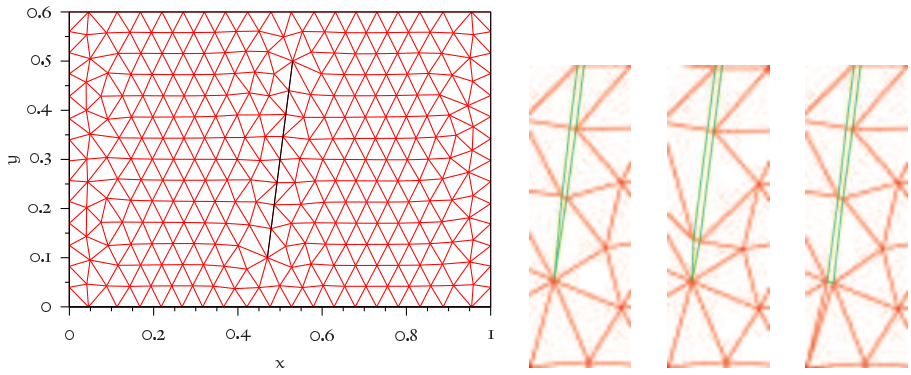

Figure 4.23: Domain with one fracture. On the left is the domain with the one-dimensional fracture, on the right grid details of the volumetric fracture ends `l3`, `l3h`, `l3q`.

unknowns for the DG method (4800) is 2.4 times larger than the number of unknowns for the mixed finite element method (2000). The mixed finite element method is considered optimal for this kind of problem, and the results of the DG method show that it is very well suited for this problem.

The performance of the multigrid method for the discontinuous coefficient example is shown in table 4.4. We use a multigrid V-cycle with $\nu_1 = \nu_2 = 2$ ILU smoothing steps as a preconditioner in the BiCGSTAB-method (van der Vorst, 1992). The table shows the number of preconditioner evaluations needed to reduce the norm of the defect by 10^{-8}. Again the iteration numbers seem to be independent of h and k.

4.7.5 Single Phase Flow in Fractured Media

The third example considers a domain with a single fracture. We compare the behavior of the DG method with the behavior of a vertex-centered finite volume method which discretizes fractures either by one-dimensional or two-dimensional elements. The grids with the volumetric mesh were created from the coarse grid of the domain denoted by `l3-1d` with the one-dimensional fracture by the methods described in Neunhäuserer (2002). The coarse grid for domain `l3-1d` is shown in figure 4.23. There are three variants of the volumetric fracture: In two domains `l3` and `l3h` the fracture has triangular ends, `l3q` has quadrilateral elements throughout the whole fracture. In domain `l3h` the fracture end triangles were reduced in length to enlarge the very small angle at the fracture end.

In the domains we solve the ground-water equation

$$-\nabla \cdot \left(\rho \frac{K}{\mu} \nabla p \right) = \rho q \qquad \text{in } \Omega. \tag{4.180a}$$

$$p = 10^5 \text{ [Pa]} \qquad \text{on } 0 \times [0, 0.6] \tag{4.180b}$$

$$p = 0.999 \cdot 10^5 \text{ [Pa]} \qquad \text{on } 0 \times [1, 0.6] \tag{4.180c}$$

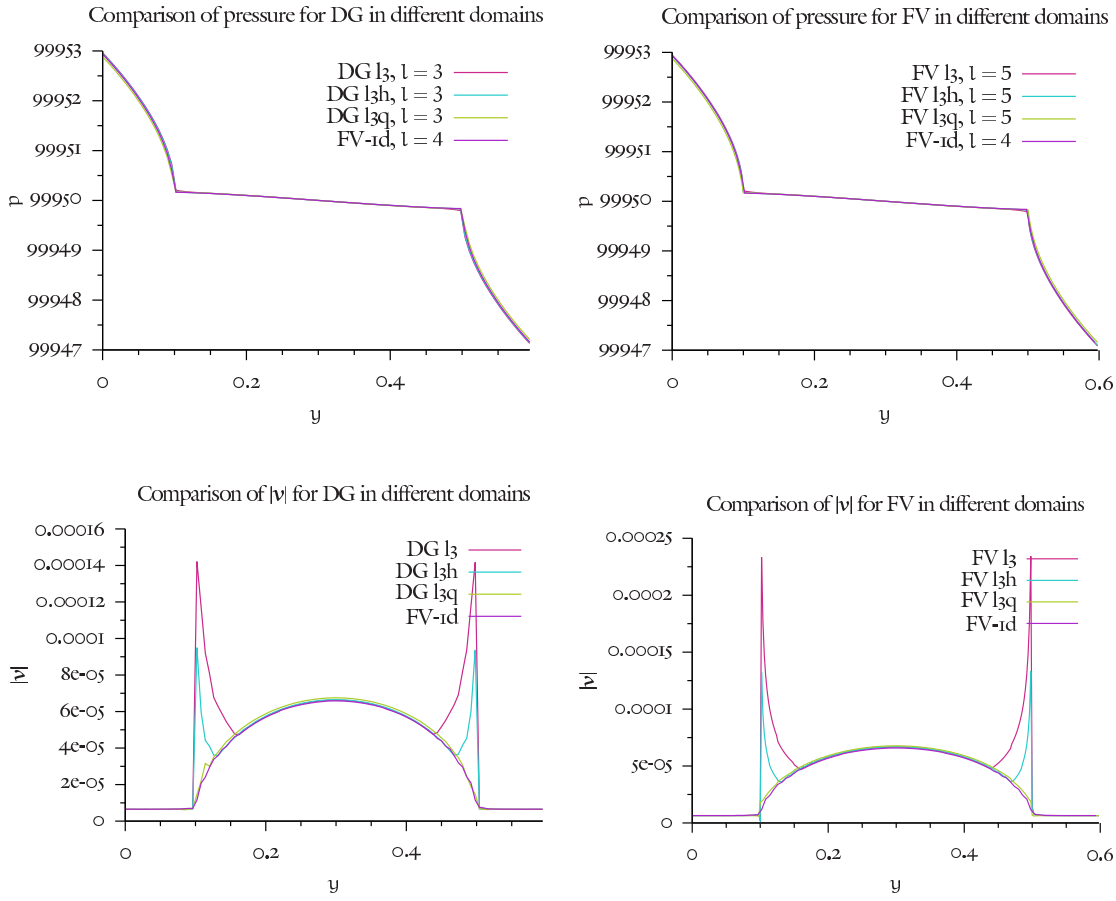

Figure 4.24: Pressure distribution along a line through the fracture for different fracture realizations (above) and the corresponding absolute value of the velocity.

with parameters

$$\rho = 1000\ [\mathrm{kg/m^3}] \qquad \mu = 0.0013\ [\mathrm{kg/(ms)}]$$
$$K^m = 8.3333 \cdot 10^{-11}\ [\mathrm{m^2}] \qquad K^f = 8.3333 \cdot 10^{-8}\ [\mathrm{m^2}]$$
$$b = 5 \cdot 10^{-3}\ [\mathrm{m}]$$

As in the previous chapters we denote quantities in the matrix with superscript m and quantities in the fracture with superscript f.

Numerical solutions to (4.180) are obtained by the methods:

FV-1d The finite volume method with one-dimensional fractures.

FV The finite volume method with two-dimensional fractures.

DG The Baumann-Oden DG method with two-dimensional fractures. The choice of basis functions is indicated by P_k and Q_k.

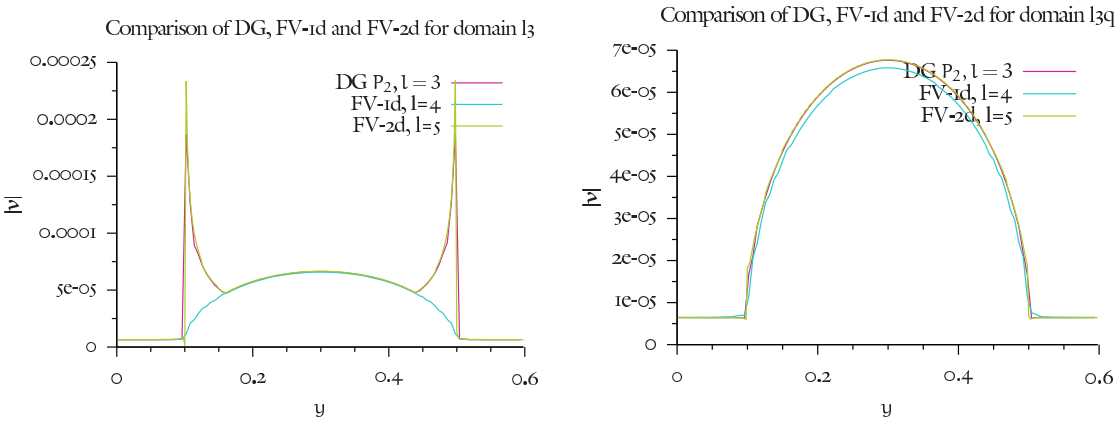

Figure 4.25: Comparison of the DG, FV and FV-1d method.

The number of unknowns for the different meshes on level l are:

l	FV-1d	FV	DG-P_2	DG-P_3	DG-Q_2
0	305	312	3300	5500	4950
1	1151	1179	13200	22000	19800
2	4469	4581	52800	88000	79200
3	17609	18057	211200	352000	316800
4	69905	71697			
5		285729			

For the finite volume methods, the number of unknowns is equal to the number of nodes in the grid, for the DG method the number of unknowns is equal to the number of elements times the dimension of the space of basis functions.

The comparison of the method is done by extracting the values along the line from $(0.455, 0)$ to $(0.545, 0.6)$—this is the line along the fracture middle surface. Along this line we compare the pressure p and the absolute value of the Darcy velocity, $|\mathbf{v}|$.

In figure 4.24 we compare how the different fracture realizations—one-dimensional, with triangles and with quadrilaterals—affect the solution. The figure shows on the left the results for the DG method with P_k on level 3 and the FV-1d method on level 4. On the right the results for the FV method on level 5 are compared to the FV-1d method on level 4. The differences in the pressure are very small. We can get more insight from the plot of the absolute value of the Darcy velocity below. Here it is obvious that the choice for the fracture ends has a significant influence on the velocity distribution. While the realization with quadrilateral ends agrees nicely with the lower-dimensional approximation, the velocity in the region of the fracture end triangle on the coarsest mesh introduces an increase in the velocity toward the fracture end. The velocity peaks

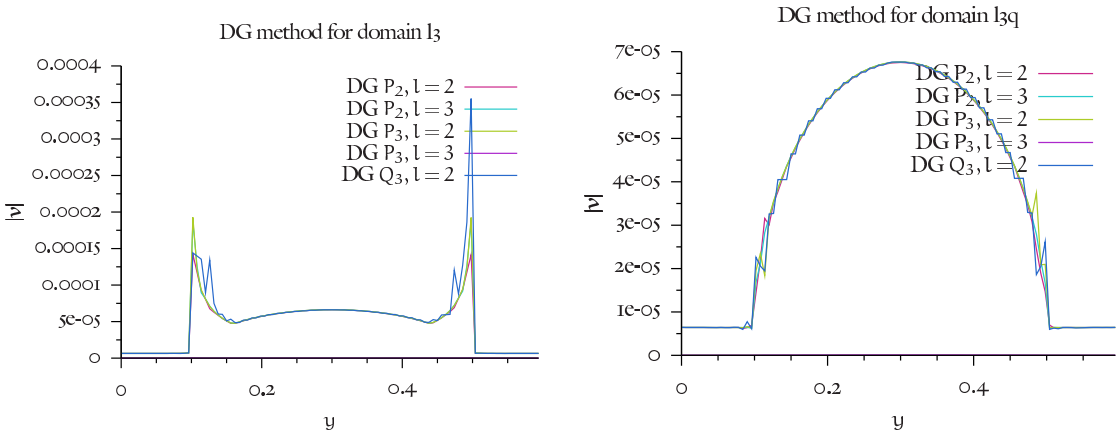

Figure 4.26: h and p convergence of the DG method.

appear for the DG method and the FV method, for the FV method they are more developed.

The discretization methods are compared once more in figure 4.25, to make the difference between the methods more visible. The FV-1d method solution is included as a "reference" solution. In the case of the quadrilateral fracture ends, the FV method and the DG method solutions are almost identical. The DG method shows some minor discontinuities in the elements at the fracture ends. The FV-1d method has a smoother progression which is explainable because a node shared by a fracture and the matrix carries an averaging solution. Due to this averaging the total velocity in the fracture is smaller than for the other methods, which have degrees of freedom entirely inside the fracture.

Figure 4.26 compares DG solutions for P_2 and P_3 on grid levels 2 and 3, and for Q_3 on level 3. The P_2 solution on level 3 and the P_3 solution on level 2 are almost identical. The Q_3 solution has strong oscillations in the region where triangular elements are employed; in the case of the quadrilateral fracture ends (l3q) the oscillations are less pronounced. The quadrilateral case also shows non-monotone behavior for the methods with $k = 3$, while the $k = 2$ solutions are monotone. This suggests that the problem does not possess the required regularity near the fracture-matrix interface that makes higher order methods applicable.

Figure 4.27 shows development of sharp velocity peaks for the FV-2d method, which reach their maximum for level 4 and decay afterwards. They are not present in the case of the fracture with quadrilateral ends (as shown in figure 4.25).

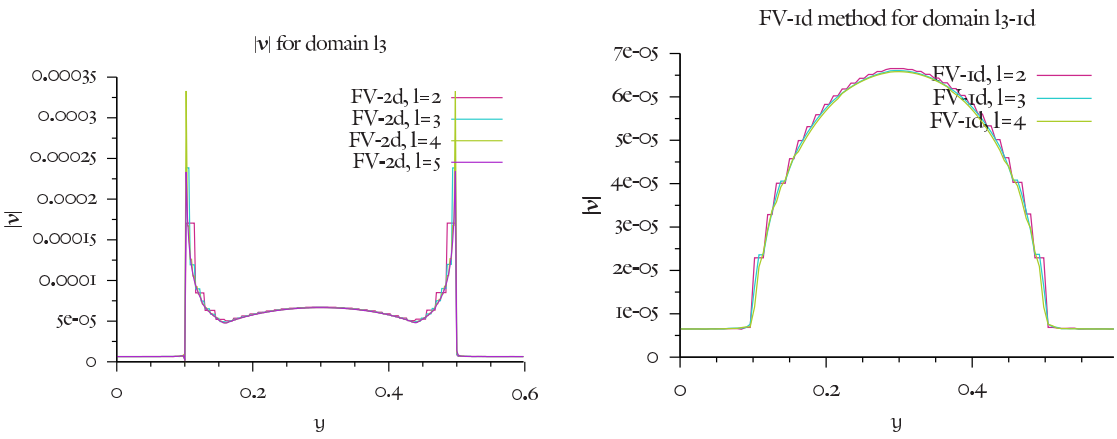

Figure 4.27: Convergence of the FV-1d and FV-2d methods.

5 Computation Examples for Degassing Processes

5.1 Description of the Degassing Field Experiment of Jarsjö (1998)

Geller and Jarsjö (1995) carried out a degassing experiment in the Äspö rock laboratory about 300 m below the groundwater level. They wanted to find out, if a pressure decrease would lead to the creation of a gas phase and thus to a decrease of hydraulic conductivity. For this purpose, the pressure in a drilling of a single fracture was fixed and the resuling fluxes were measured. However, no decrease of conductivity due to degassing effects could be stated. Geller and Jarsjö (1995) give the very low volumetric gas concentrations of 0.5% to 1% as a reason.

Jarsjö and Destouni (2000) carried through further experiments in the Äspö rock laboratory 450 m below the water level. Their experiments are different from the one of Geller and Jarsjö (1995) in two points:

1. A hydraulical test series of gas-saturated water was injected into the fracture.
2. The pressure in the drilling hole was decreased down to values below the atmospheric pressure.

A schematic illustration of the degassing field experiment can be seen in Figure 5.1. By these measures, the degassing effects in the fracture were increased.

The following hydraulic tests were subdivided into three phases as can also be taken from Figure 5.2.

1. For the first phase, the pressure in the drilling hole was kept above the degassing pressure. Thus, we have single-phase conditions.
2. In the second phase, the pressure in the drilling hole was decreased down to a value below the atmosheric pressure. For the degassing, we get two-phase conditions depending on the pressure.
3. For the third phase, the pressure in the drilling hole was increased up to a value above the degassing pressure. Under the assumption of a thermodynamic equilibrium, we regain single-phase conditions.

These experiments were carried through for different drilling holes. Single-drilling hole investigations as well as dipole investigations with two drilling holes were carried through. As for the dipole experiment the system is continuously infiltrated by

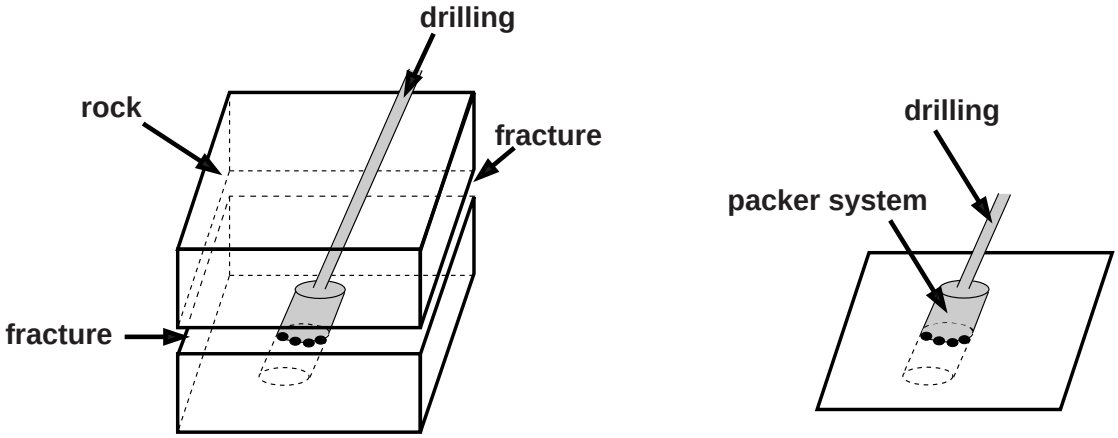

Figure 5.1: Schematic illustration of the degassing field experiment

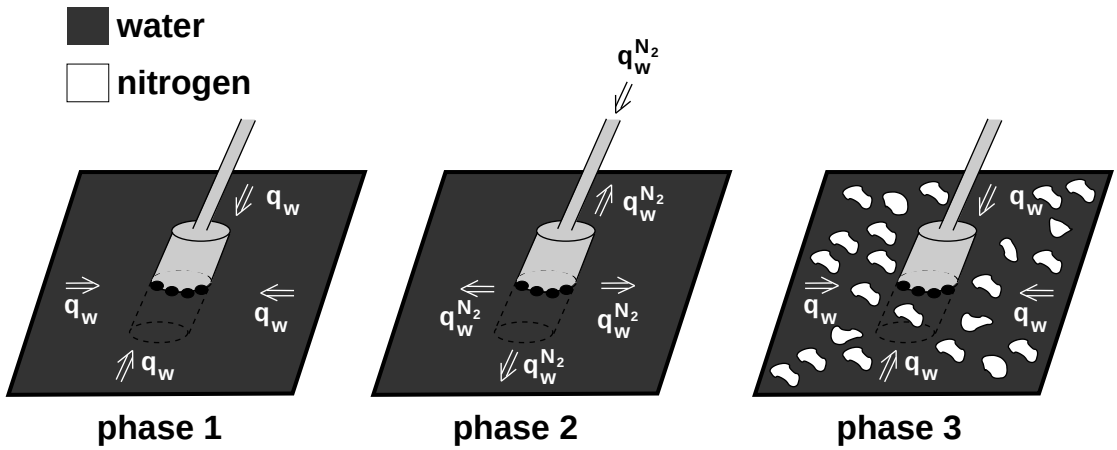

Figure 5.2: The three phases of the degassing field experiment

gas-saturated water, and this water is again withdrawn in a certain distance, we cannot assume a thermodynamic equilibrium in this experiment. The gas content of water is for an extraction about as high as for the injection of water. For this reason, we restrict ourselves to the consideration of the single borehole investigations. For these investigations, Jarsjö and Destouni (2000) give a reduction of the hydraulic conductivity by a factor between 0.89 and 0.90.

Jarsjö and Destouni (2000) injected nitrogen-saturated gas into the fracture. They give a value for the volumetric concentration of about 17%, however, for the water actually injected they only measured a volume concentration of only 13%. For our considerations we refer to the latter. In Table 5.1, the respective values for the molar concentration and the mole fractions are listed under the assumption of isothermal conditions and a temperature of 13°C, as given by Liedtke et al. (2001).

experiment	field experiment Äspö–HRL
θ_g [%]	0.13
molar concentration [mole /m^3]	6.245
mole fraction	0.0001124
degassing pressure p_b [Pa]	867283

Table 5.1: Volume concentration θ_g, molar concentration, mole fraction and degassing pressure of the experiments described by Jarsjö and Destouni (2000) for nitrogen as desolved gas

We assume a distribution of the fracture opening width as can be seen in Figure 3.34. For the identification of effective parameters we proceed as in Section 3.6, however, we consider only the temperature of 13°C. The corresponding input parameters for the percolation algorithm can be found in Table 5.2. Thus, we get a relative permeability–pressure relationship as illustrated in Figure 5.3.

5.2 1D Study for a Degassing Experiment

First, we will carry through a simple 1D simulation in order to check the acquired relative permeability–pressure function. Therefore, the pressure was fixed at 1 million Pa at the one end, and at 0.8 million Pa at the other end. Then, the pressure is reduced at both ends by 0.1 million Pa. The pressure gradient, however, remains constant. This continues, until the lower pressure of 100000 Pa is reached. The velocities in dependence of the pressures can be taken from Table 5.3. Figures 5.4 and 5.5 show the pressure fields and velocities for the highest and the lowest pressure of the simulation. The quotient of the velocities and the lowest pressure and the velocity and the highest pressure which lies above the degassing pressure, is about 0.82. This is a higher reduction of conductivity than Jarsjö and Destouni (2000) have determined.

This results, however, from the experimental arrangement which cannot be captured by the one-dimensional build-up. Therefore, the results, cannot be compared to the

Henry coefficient K^{N_2}	9228100000 [Pa]
temperature	298.15 [K]
initial mole fraction $x_{start^{N_2}}$	0.0001124 [-]
molar mass M^{N_2}	0.028 [kg]
$Enthsol^{N_2}$	1300
density of the fluid phase ρ_{fl}	1000 [kg/m^3]
factor for hydraulically active fracture	1.0
thickness of the wetting water film	0.000001 [m]
residual saturation S_{wr} due to fracture roughness	0.2
surface tension for the gas - water system σ_{gw}	0.0727 [Nm]
initial pressure	101325 [Pa]
final pressure	1000000 [Pa]
pressure iterations	200
initial temperature	286.3
final temperature	288.3
temperature iterations	2

Table 5.2: Parameters for the percolation model with N_2 as desolved gas according to the experiment of Jarsjö and Destouni (2000).

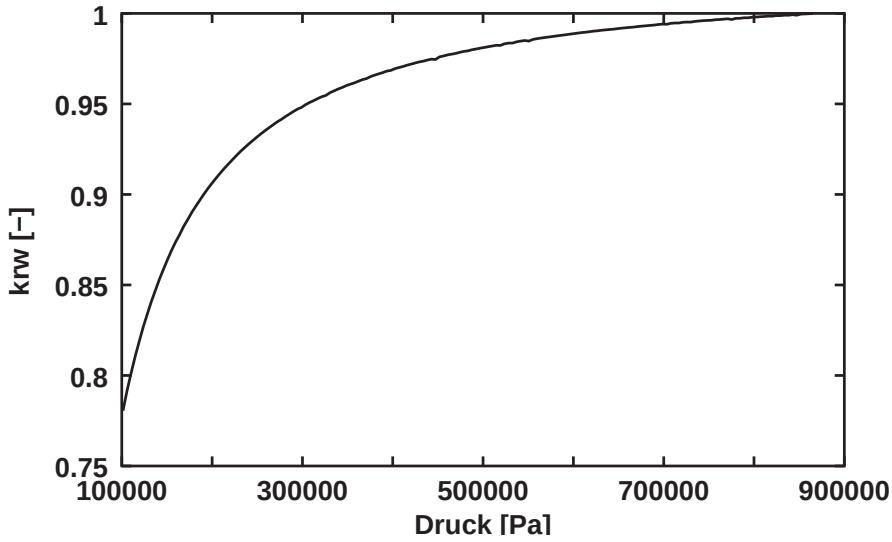

Figure 5.3: Relative permeability–pressure relationship for the simulation of the field experiment of Jarsjö and Destouni (2000)

experimental results and serve only as principal illustration of the degassing effects.

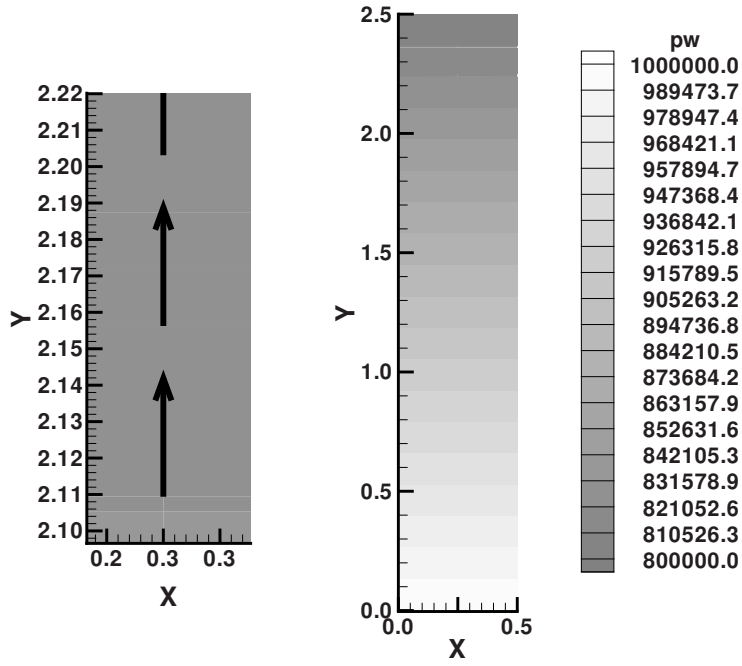

Figure 5.4: Simulation results for 1D model example for degassing processes; $p_{w,\mathrm{top}} = 8 * 10^5$ Pa, $p_{w,\mathrm{bottom}} = 10^6$ Pa

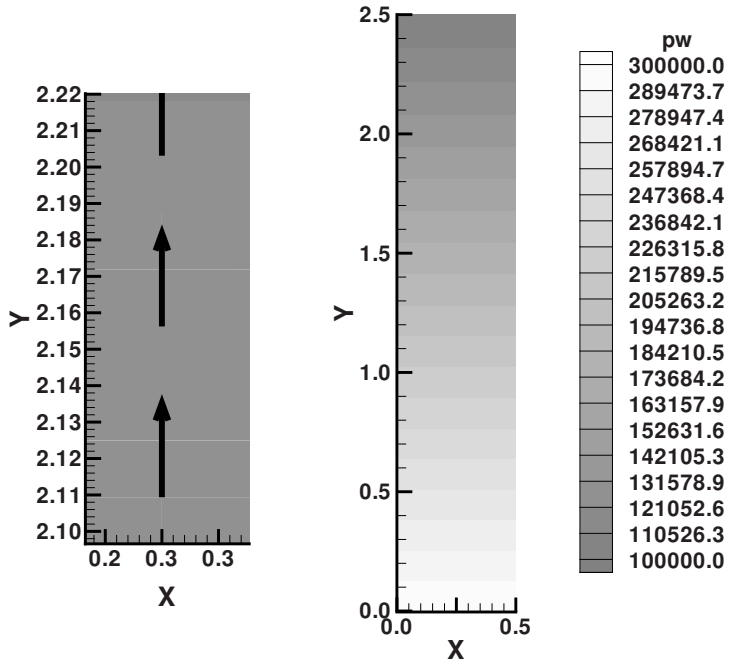

Figure 5.5: Simulation results for the 1D principle example of degassing processes;
upper picture: $p_{w,\mathrm{top}} = 8 * 10^5$ Pa, $p_{w,\mathrm{bottom}} = 10^6$ Pa;
lower picture: $p_{w,\mathrm{top}} = 10^5$ Pa, $p_{w,\mathrm{bottom}} = 3 * 10^5$ Pa

p_{max} [Pa]	p_{min} [Pa]	v_w [m/s]
1000000	800000	0.0325395
900000	700000	0.0323764
800000	600000	0.0321949
700000	500000	0.0319527
600000	400000	0.0315615
500000	300000	0.0309441
400000	200000	0.0297279
300000	100000	0.0265736

Table 5.3: Pressures and velocities for the 1D simulation

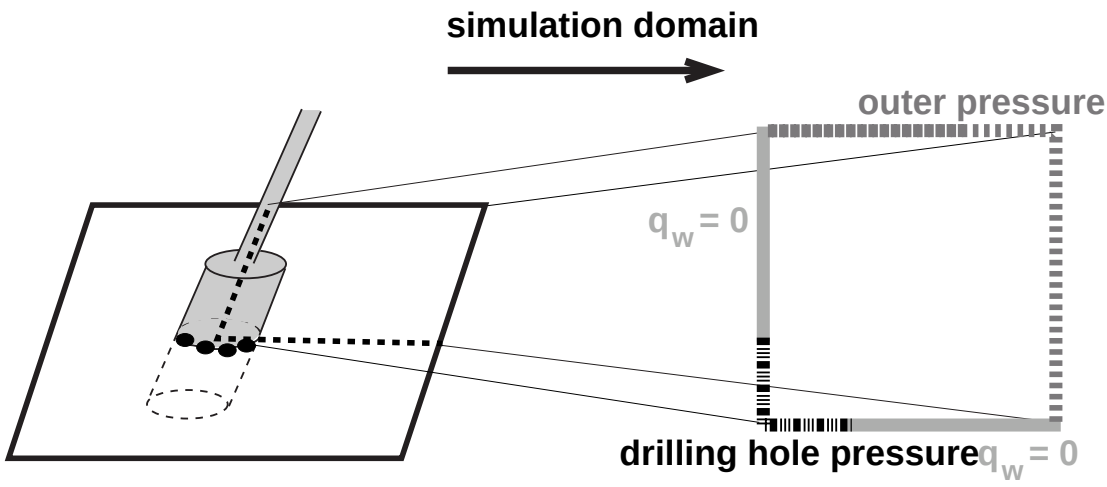

Figure 5.6: Boundary conditions for the simulation of the degassing field experiment

5.3 Simulation of a Field Experiment

For the simulation of the field experiment of Jarsjö and Destouni (2000), an area of 10 m $\times$ 10 m was chosen. As illustrated in Figure 5.6, we have chosen the pressure in a depth of 500 meters below the groundwater level of 5 million Pa for two sides. The boundary conditions for the drilling hole are set to a value of 100,000 Pa. This corresponds about to the value set by Jarsjö and Destouni (2000) for a drilling hole in phase 2 of the field degassing experiment. The boundary condition for the drilling hole is set for a region of 10 cm (as can be seen from Figure 5.6) for two sides. For the rest of length of the sides, the flux was set to zero for reasons of symmetry.

Neither the pressure fields nor the velocity fields differ optically, from Table 5.4, however, we can see that taking into account the degassing effects leads to a reduction of the maximum velocity by 4.33%, i.e. a factor of 0.9567. For increasing refinement of the domain around the drilling hole (see Figure 5.6), this factor gets smaller and smaller. A finer mesh than given in Figure 5.7, could not be computed due to a lack of stor-

age. Therefore, a smaller domain was chosen (1 m $\times$ 1 m) and the pressure at the outer boundary was set to 3 million Pa. For the boundary condition of the drilling hole, we chose again 10 cm. For this simulation, mesh convergence could be achieved. The results for pressure p_w and velocity v_w can be seen in Figures 5.11 and 5.12. As a result, the maximum velocity was reduced by 12.5%, i.e. with a factor of 0.875. This reduction is slightly larger than the reductions according to Jarsjö and Destouni (2000) by 10% to 11%, i.e. with a factor of 0.89 to 0.90.

This good agreement has not been expected in this form. The transfer of the parameters from the micro-scale to the macro-scale is afflicted with numerous uncertainties. Especially the thickness of the boundary layer is only a roughly estimated paramter, which, however, has a decisive influence (see Jakobs and Helmig (2000)). The overestimation of the degassing effects can also be explained by the fact that the water flowing out of a fracture, still has a volumetric gas concentration of more than 1%. Thus, the thermodynamic equilibrium is not yet entirely reached in the experiment. For a closer verification of the model, further measurements are needed. As such measurements are time intensive and costly, we have to content ourselves with the statement, that the introduced model does well represent the existing experimental results.

simulation domain, $p_{boundary}$	$v_{w,max}$ with degassing effects [m/s]	$v_{w,max}$ without degassing effects [m/s]
10 m $\times$ 10 m, $5 \cdot 10^6$Pa	0.0007547	0.000789
1 m $\times$ 1 m, $3 \cdot 10^6$Pa	0.0021	0.0024

Table 5.4: Maximum velocity with and without taking into account degassing effects

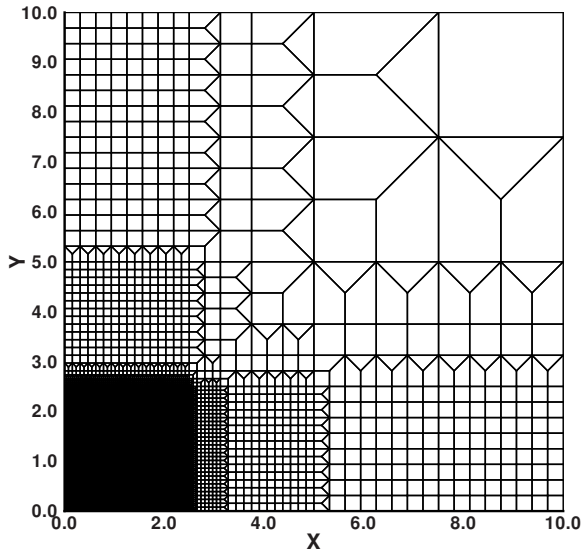

Figure 5.7: Mesh used for the simulation of the field experiment

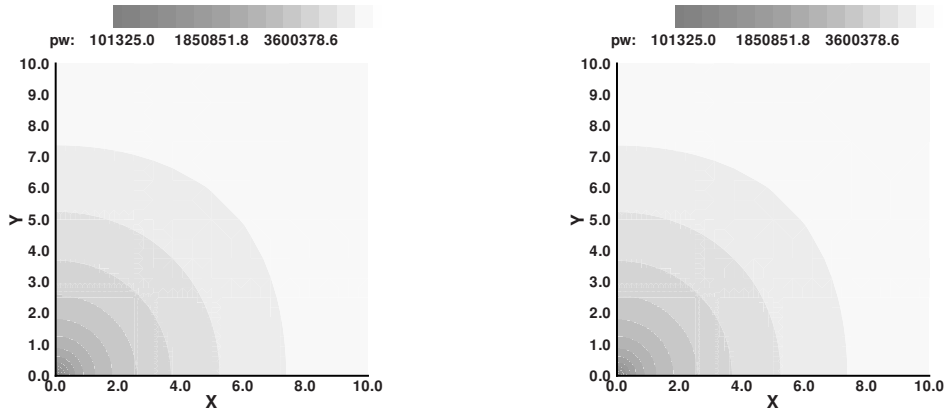

Figure 5.8: The pressure fields with and without the degassing effect are almost identical

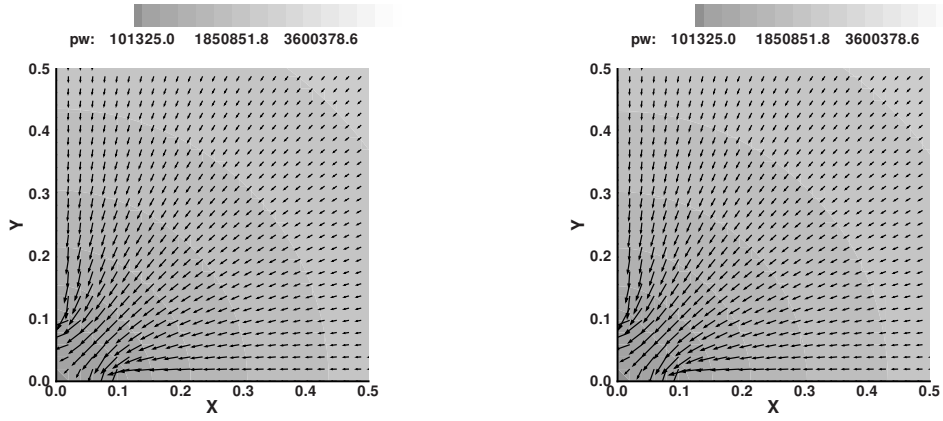

Figure 5.9: The velocity fields in the nearfield of the boundary conditions of the drilling hole almost cannot be distinguished optically

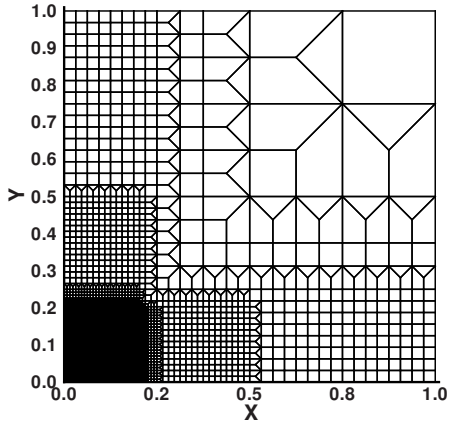

Figure 5.10: Mesh for the (1 m $\times$ 1 m) cut-out of the fracture

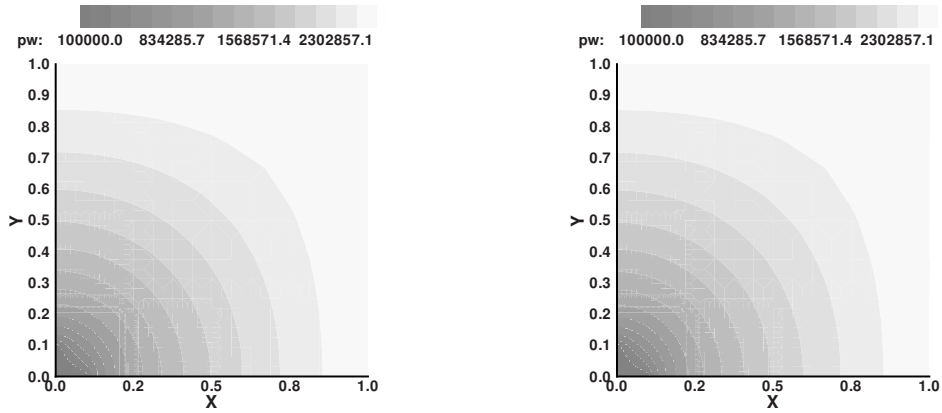

Figure 5.11: Pressure field with and without degassing effects for a domain of (1 m $\times$ 1 m)

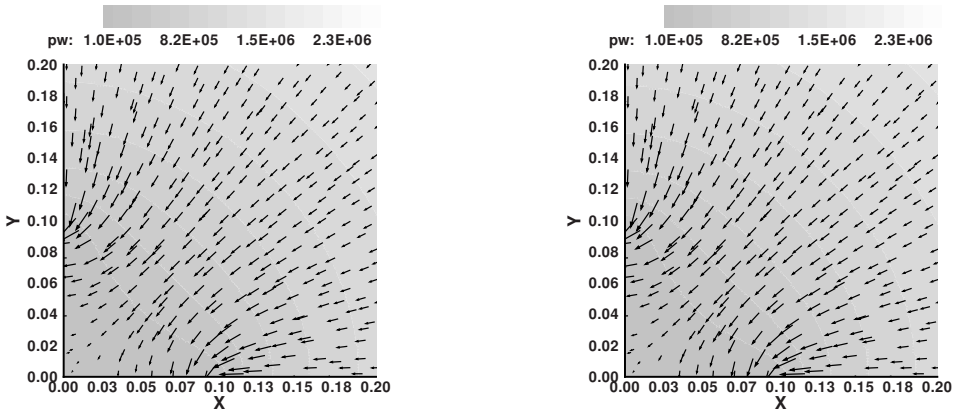

Figure 5.12: For the (1 m $\times$ 1 m) cut-out of the fracture, the velocity fields with and without degassing effects can only hardly be distinguished

6 Numerical experiments

6.1 Vertical Water–Gas Flow

The first numerical experiment with two-phase flow is set up to assess the difference between a lower-dimensional fracture approach and a fracture with volumetric elements. We choose a simple configuration with only one fracture in order not to include too many different effects into the solution. The setup includes one vertical fracture inside a domain of 1m $\times$ 1m, a sketch is displayed in figure 6.1. The fracture is located along the line from $(0.5, 0.2)$ to $(0.5, 0.8)$. We consider inflow of a compressible gas phase at the south boundary.

The parameters of the simulation are artificially chosen but give a representative picture of fracture-matrix interaction. The parameters are

$$\rho_w = 1000 \text{ [kg/m}^3\text{]} \qquad \rho_g = \frac{p_n}{84149.6} \text{ [kg/m}^3\text{]}$$
$$\mu_w = 10^{-3} \text{ [Pa s]} \qquad \mu_g = 1.65 \cdot 10^{-5} \text{ [Pa s]}$$
$$\Phi^f = 0.3 \qquad \Phi^m = 0.1$$
$$K^f = 10^{-8} \qquad K^m = 10^{-12}$$
$$S^f_{wr} = 0 \qquad S^m_{wr} = 0$$
$$S^f_{gr} = 0 \qquad S^m_{gr} = 0$$
$$\lambda^f = 2 \qquad \lambda^m = 2$$
$$\lambda^f = 1000 \text{ [Pa]} \qquad \lambda^m = 2000 \text{ [Pa]}$$

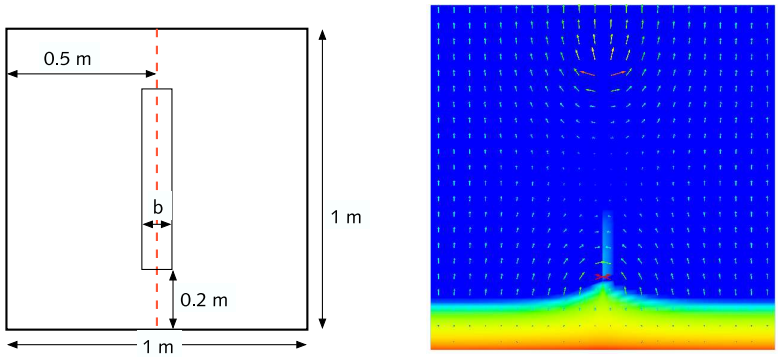

Figure 6.1: Sketch of the domain for the vertical water-gas flow example and S_g and $\mathbf{u}_w$ at $t = 70$ s.

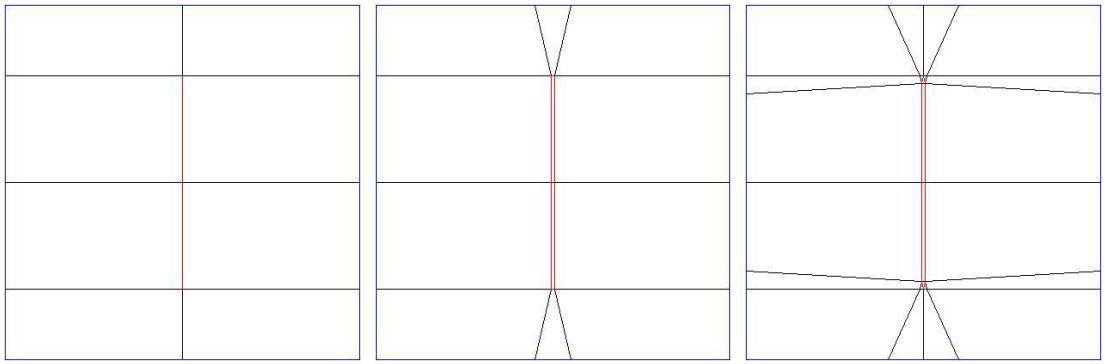

Figure 6.2: Coarse grids of the vertical water-gas flow simulation for the one-dimensional fracture (left) and the two-dimensional fractures with rectangular ends (middle) and triangular ends (right).

The fracture width b is chosen from $\{0.01, 0.005, 0.001\}$ [m], to determine the influence of the fracture width on the solution and on the solution efficiency. Boundary conditions are $S_g = p_w = 0$ on the north boundary, and Neumann boundary conditions elsewhere. At the south boundary the value of the Neumann boundary condition for the saturation is $-2.5 \cdot 10^{-5}$ [kg/m^2], all remaining Neumann boundary condition values are 0.

Without the fracture, the problem would be quasi one-dimensional, but a look at the flow field reveals how the influence of the fracture affects the solution behavior (figure 6.1, right). We choose a vertical fracture in order to exclude grid dependent phenomena from the experiment.

Three different coarse grids are employed, depicted in figure 6.2. The first grid (left) employs the mixed dimensional finite volume method and models the fracture by one-dimensional elements. The other grids resolve the fracture with two-dimensional elements. The grid in the middle uses only quadrilateral elements, the grid on the right has a triangular element at both fracture ends. It should be obvious from this example that grid generation for fractures with volumetric elements is much more difficult than for lower-dimensional fractures.

For the simulation we employed the backward Euler scheme with fixed time steps. The nonlinear equations were solved with inexact Newton method with line search. The linear systems were solved with the V(2,2)-cycle multigrid method with ILU smoothing, accelerated with Bi-CGSTAB. Additional properties of the solution process can be found in table 6.1.

We compared the discretization schemes by plotting the values for S_g and p_w at different time steps along the line from $(0.5, 0)$ to $(0.5, 1)$. The time steps are chosen as $t = 50$ s, 74 s, 100 s. At $t = 50$ s the gas has not reached the fracture yet, at $t = 74$ s some

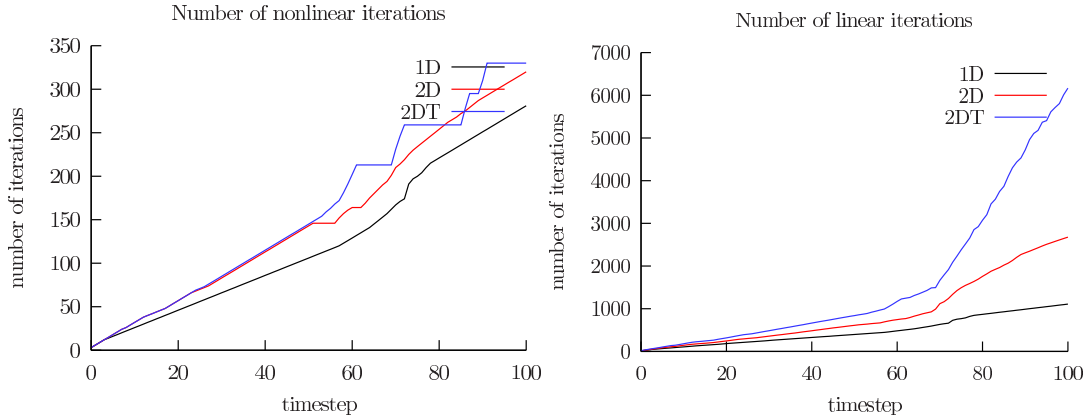

Figure 6.3: Linear and nonlinear iterations for vertical infiltration problem with $b = 0.005$ on level $l = 3$.

gas is inside the fracture and at $t = 100$ s the gas has reached the fracture end and has penetrated the matrix. The series of figures 6.4–6.6 reveals the slow grid convergence which is typical for gas-water problems. This is especially pronounced at $t = 74$ s, where the fast movement in the fracture amplifies the effect. The plot at the top right of figure 6.5 shows a study on six of eight refinement levels (level 0 is the coarse grid). Only for this refinement can we start to speak of grid convergence.

The influence of the type of fracture realization (lower-dimensional, with quadrilateral or triangular fracture ends) has already been observed for single phase flow in chapter 4.7. In figure 6.8 we display the shape of the saturation curve for the three discretizations at $t = 74$ s and $t = 100$ s. This is an interesting comparison, because it compares the mixed-dimensional model with a "trusted one", the model with only two-dimensional elements. First, we would like to point out that the total mass in the system is the same in all realizations. A contradicting impression could arise because

		one-dimensional		two-dimensional		two-dimensional, triangle	
Level l	Δt [s]	#E	#N	#E	#N	#E	#N
2	2	153	128	221	192	384	377
3	1	561	512	825	768	1536	1425
4	0.5	2145	2048	3185	3072	6144	5537
5	0.25	8385	8192	12513	12288	24576	21825
6	0.5	33153	32768				
7	0.25	131841	131072				

Table 6.1: Time step Δt, number of elements #E and nodes #N for grids of the vertical gas flow problem

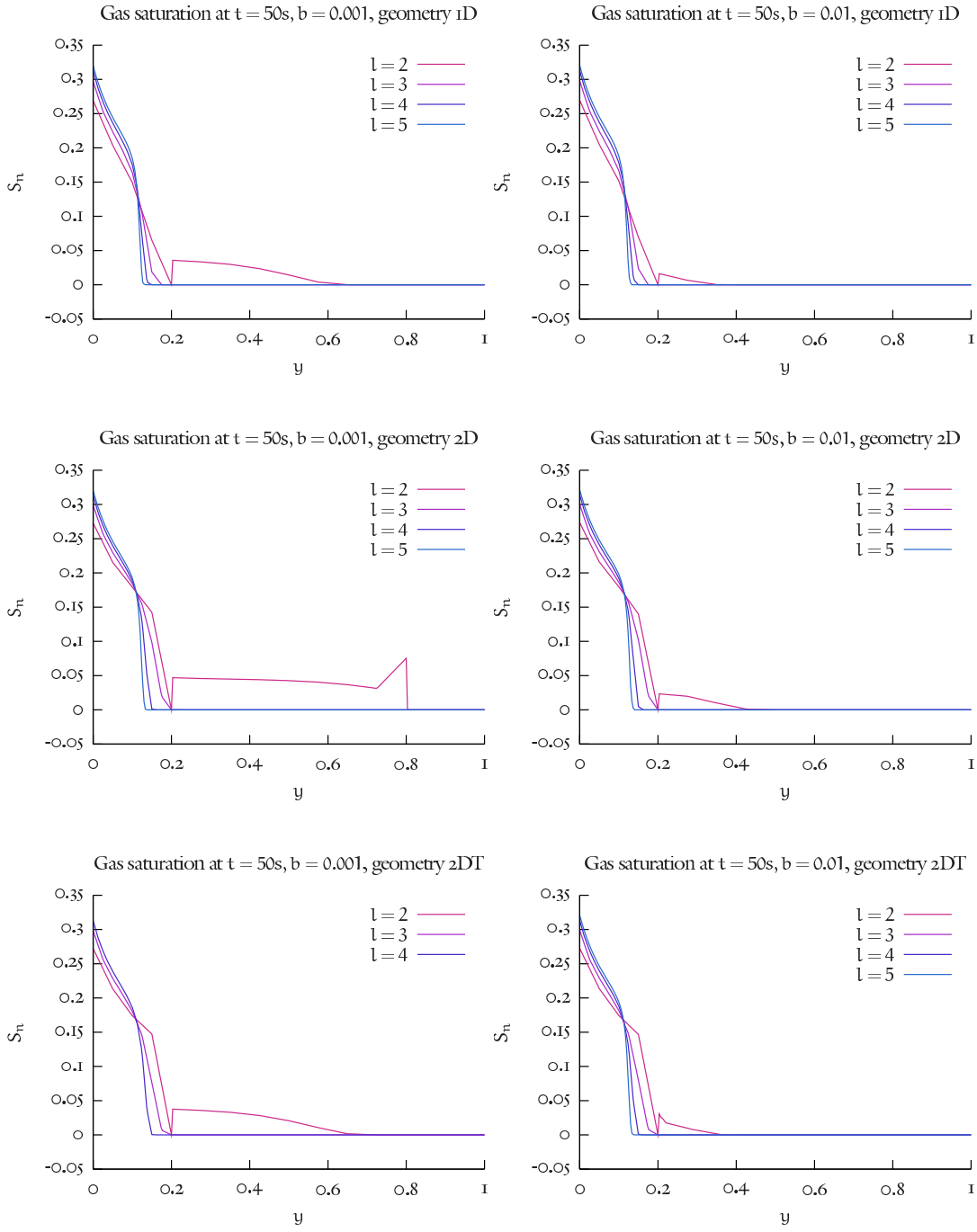

Figure 6.4: Grid convergence of vertical gas-water flow test case for $t = 50s$. The gas saturation along the line in y-direction is plotted for grid level l and the fracture widths $b = 0.001$ (left) and $b = 0.01$ (right). Results in the first row are for the one-dimensional fracture geometry, the middle row for the two-dimensional fracture geometry with rectangular ends and the last row for the two-dimensional fracture geometry with triangular ends.

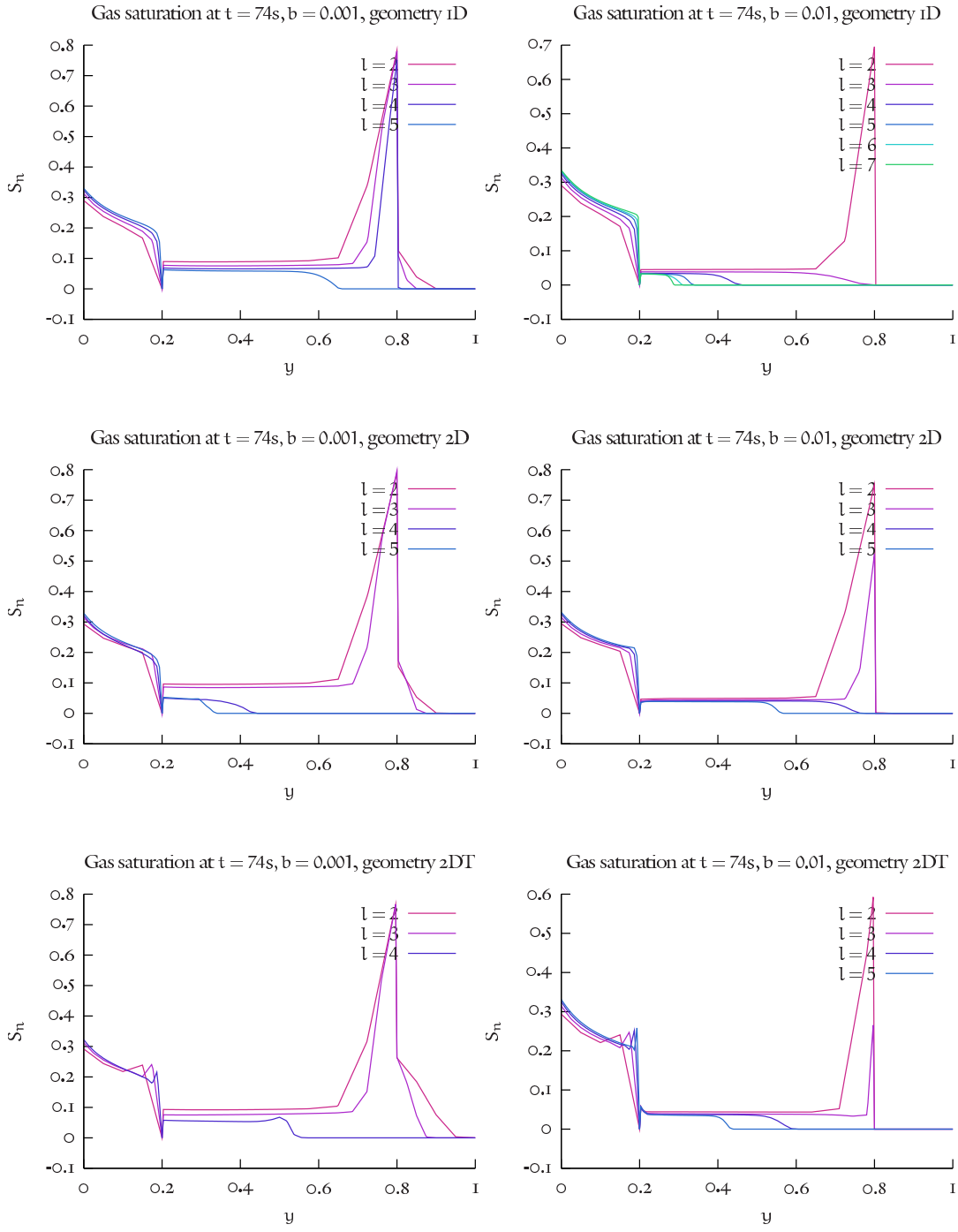

Figure 6.5: Grid convergence of vertical gas-water flow test case for $t = 74s$. The gas saturation along the line in y-direction is plotted for grid level l and the fracture widths $b = 0.001$ (left) and $b = 0.01$ (right). Results in the first row are for the one-dimensional fracture geometry, the middle row for the two-dimensional fracture geometry with rectangular ends and the last row for the two-dimensional fracture geometry with triangular ends.

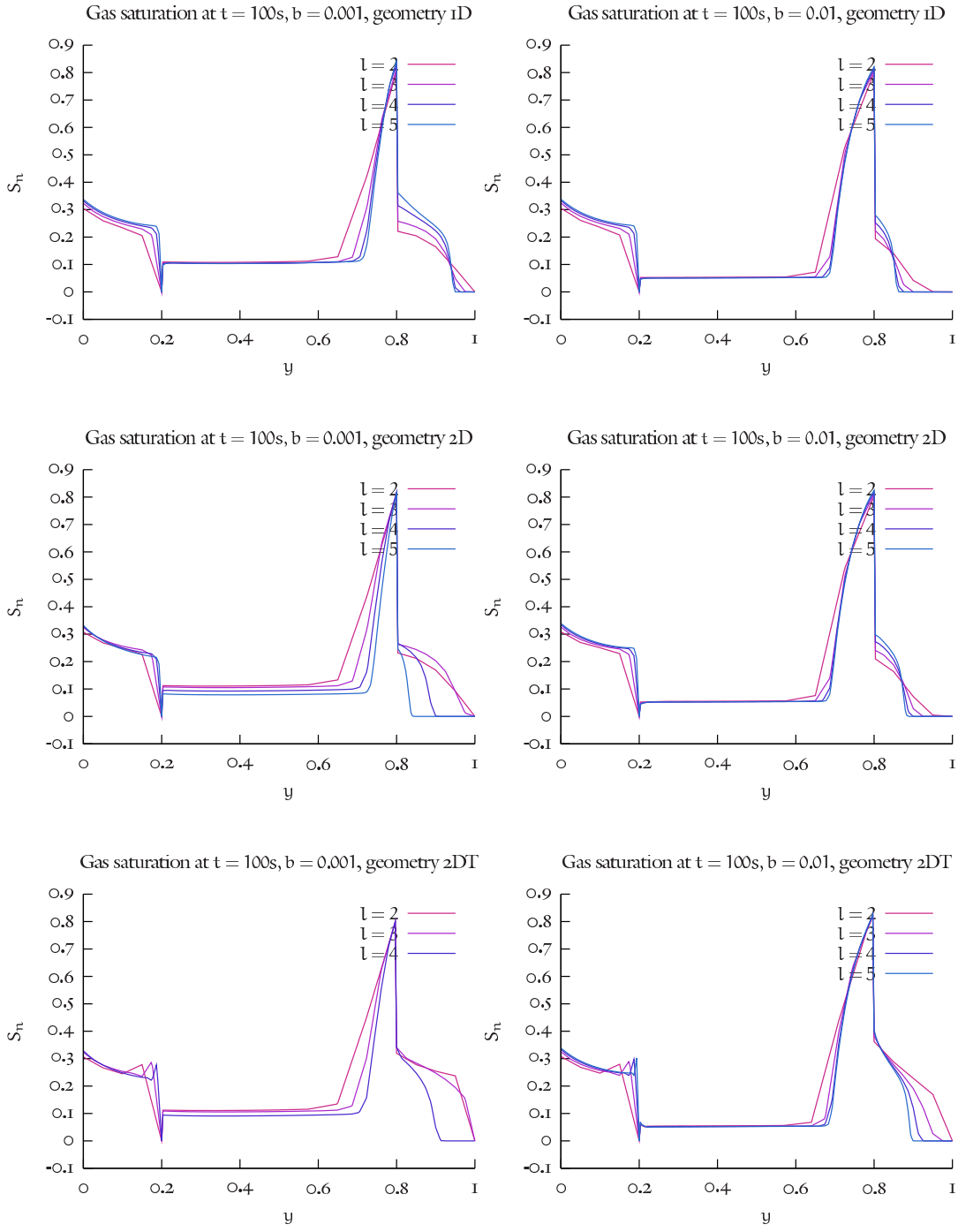

Figure 6.6: Grid convergence of vertical gas-water flow test case for $t = 100s$. The gas saturation along the line in y-direction is plotted for grid level l and the fracture widths $b = 0.001$ (left) and $b = 0.01$ (right). Results in the first row are for the one-dimensional fracture geometry, the middle row for the two-dimensional fracture geometry with rectangular ends and the last row for the two-dimensional fracture geometry with triangular ends.

the saturation curve resembles a one-dimensional model problem and seems to reveal that in the lower-dimensional case less mass is present. This is *not* the case—only the mass in the fracture is different.

Apparently, the fracture geometry has a notable influence on the solution. The difference is, however, small enough to be of relatively small significance when compared to other uncertainties associated with the modeling and simulation process.

If the differences in the solution are small, the differences in obtaining the solution are quite remarkable. In figure 6.3 we plot the number of linear multigrid cycles and nonlinear Newton steps necessary for the simulation with 100 time steps. Note that in some cases the convergence requirements had to be relaxed if convergence could not be reached to the desired level. In these cases the counted total number of Newton steps is not increased, and this accounts for the behavior of the 2DT case. The systems in the lower-dimensional realization are easier to solve and require less iterations than the two-dimensional realization. The curves also reveal that the system solution only starts to get difficult when the gas has reached the fracture and the nonlinearities in the constitutive relations in combination with the discontinuous material properties make the systems more difficult to solve.

We include only one figure (6.7) with the values of p_w at $t = 74$ s for all three fracture realizations, because the differences in the pressure are small and the interesting quantity is the gas saturation.

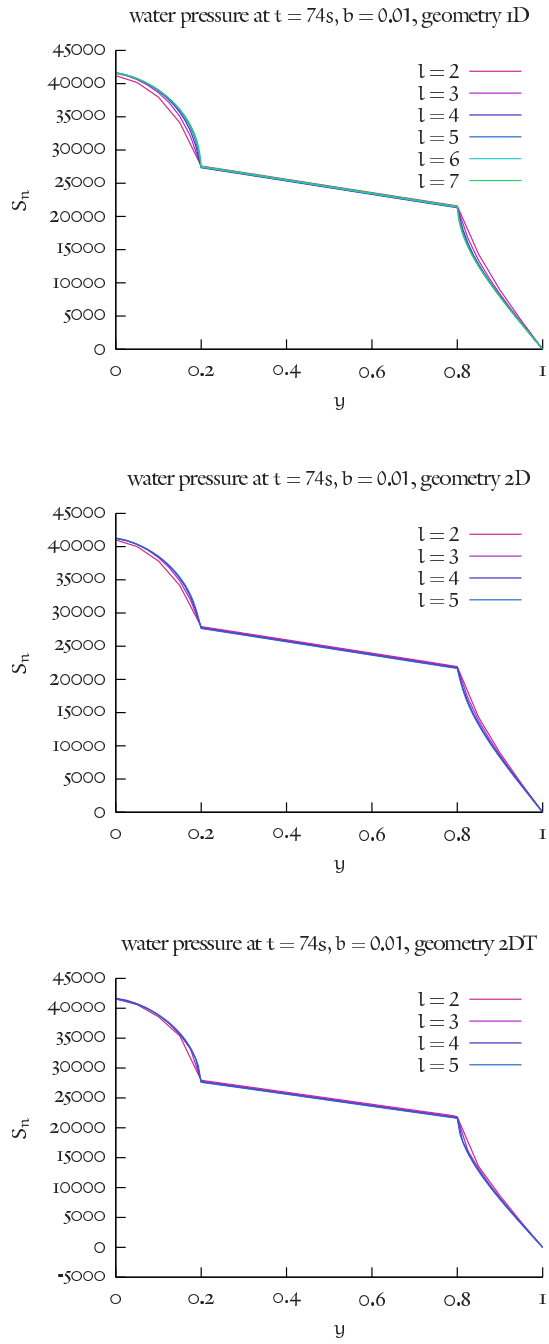

Figure 6.7: Grid convergence of vertical gas-water flow test case for $t = 74s$. The *water pressure* (labeling of the y-axis is wrong) along the line in y-direction is plotted for grid level l and the fracture width $b = 0.01$. Results at the top are for the one-dimensional fracture geometry, in the middle for the two-dimensional fracture geometry with rectangular ends and the bottom for the two-dimensional fracture geometry with triangular ends.

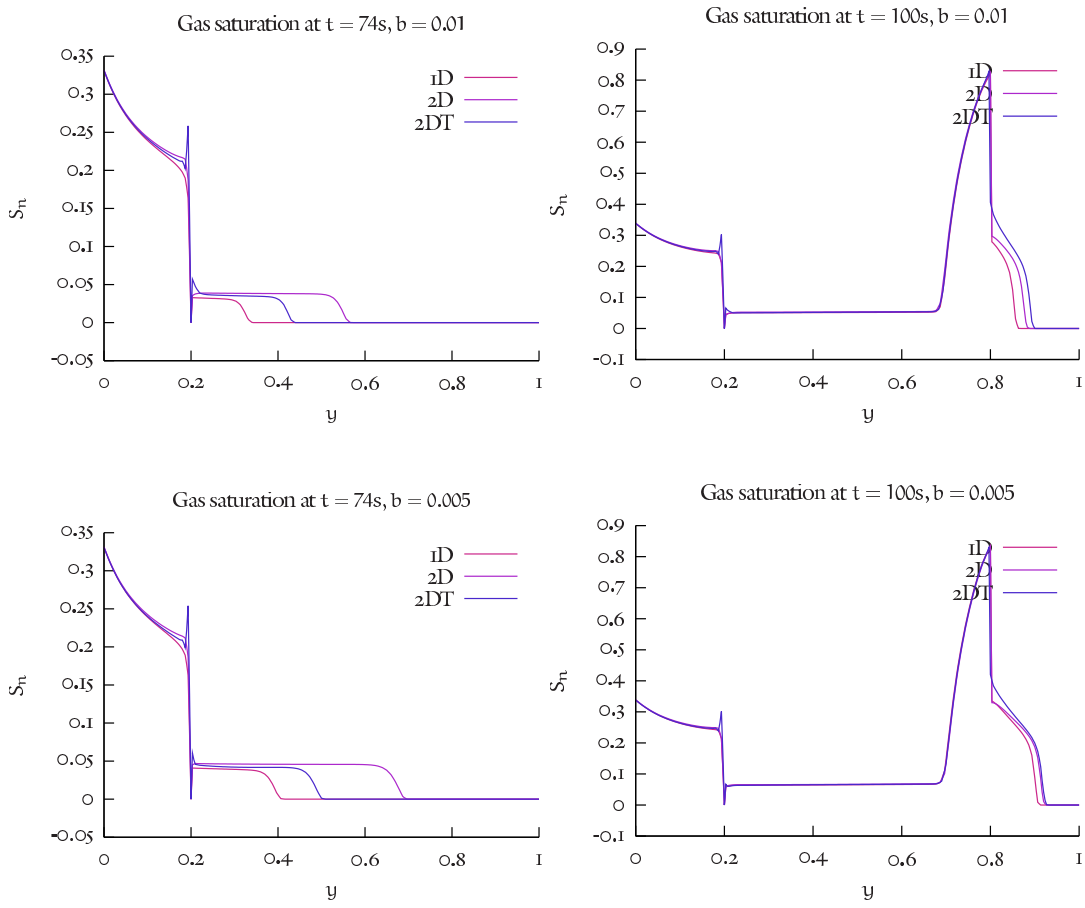

Figure 6.8: Comparison of the gas saturation value along the vertical axis of the domain on grid level 3. Results in the first row, second, and third row are for fracture widths $b = 0.01$, $b = 0.005$ resp., with $t = 74s$ in the left column, $t = 100s$ in the right column.

6.2 Three-Dimensional Gas-Water Simulation

The enclosing domain for the gas-water flow simulation has a size of $12 \times 12 \times 12$ [m] and contains an interconnected fracture network with eight fractures. Two fractures are connected to the domain boundary, it is through these fractures that the compressible gas phase enters the system.

The parameters of the simulation are

$$\begin{aligned}
\rho_w &= 1000\ [\mathrm{kg/m^3}] & \rho_g &= p_n/84149.6\ [\mathrm{kg/m^3}] \\
\mu_w &= 10^{-3}\ [\mathrm{Pa\ s}] & \mu_g &= 1.65 \cdot 10^{-5}\ [\mathrm{Pa\ s}] \\
\Phi^f &= 0.3 & \Phi^m &= 0.1 \\
K^f &= 10^{-8} & K^m &= 10^{-12} \\
S^f_{wr} &= 0 & S^m_{wr} &= 0 \\
S^f_{gr} &= 0 & S^m_{gr} &= 0 \\
\lambda^f &= 2 & \lambda^m &= 2 \\
\lambda^f &= 1000\ [\mathrm{Pa}] & \lambda^m &= 2000\ [\mathrm{Pa}]
\end{aligned}$$

We prescribe a hydrostatic pressure at the boundaries with $p_w = 9810$ at the north boundary. The boundary condition for the saturation is $Sn = 0$, except for the south boundary with Neumann boundary conditions $\phi = 0$ except for the lines where the fractures intersect the domain boundary. There we set $\phi = -2.4 \cdot 10^{-4}$.

Figure 6.9 shows the time step size development for the problem. Again, the Courant number is very large and makes the system difficult to solve. The fractional-step-θ scheme has three sub steps, so the numbers have to be divided by three for comparison with other time stepping schemes.

The simulation uses the finite volume scheme with full upwinding and the fractional-step-θ scheme. In each Newton step a defect reduction of 10^{-5} is prescribed, and a linear defect reduction of 10^{-5}. The multigrid method uses a V(2,2)-cycle with symmetric Gauß-Seidel smoothing. The smoothing is damped with a factor 0.8. The time step size changes depending on the number of required nonlinear iterations.

In figure 6.10 we show visualizations for the time steps $t = 40$s, $t = 60$s, $t = 80$s. The gas saturation is small in these examples. The large picture shows the gas saturation for $t = 80$s. Contrary to the Water-Oil problem the gas spreads into a very thin layer along the fracture end which is hardly visible. This is due to the smaller amount of mass that has entered the system and due to the substantial viscosity and density differences between gas and water.

We ran the simulation on 64 processors of the HELICS cluster (HEidelberg LInux Cluster System) consisting of AMD Athlon 1.3 GHz processors connected by a Myrinet 2000 interconnect.

The large number of Newton iterations stems from the large Peclet numbers which arise in the current configuration. We assume that the Peclet number is approximately

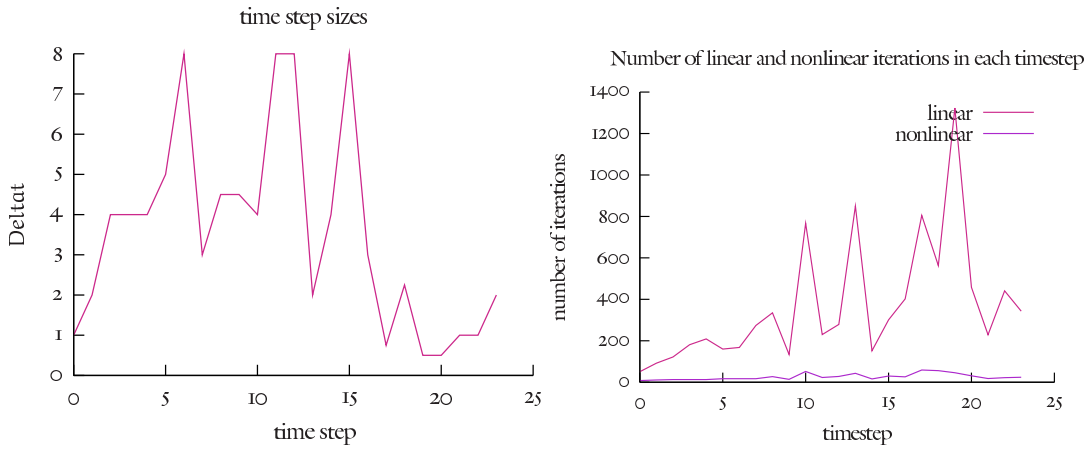

Figure 6.9: 3D Water-Gas simulation

10, which proves the robustness of the algorithm. It is also clear that for accuracy reasons smaller time steps should be employed. Note also that the fractional-step-θ scheme has three sub steps.

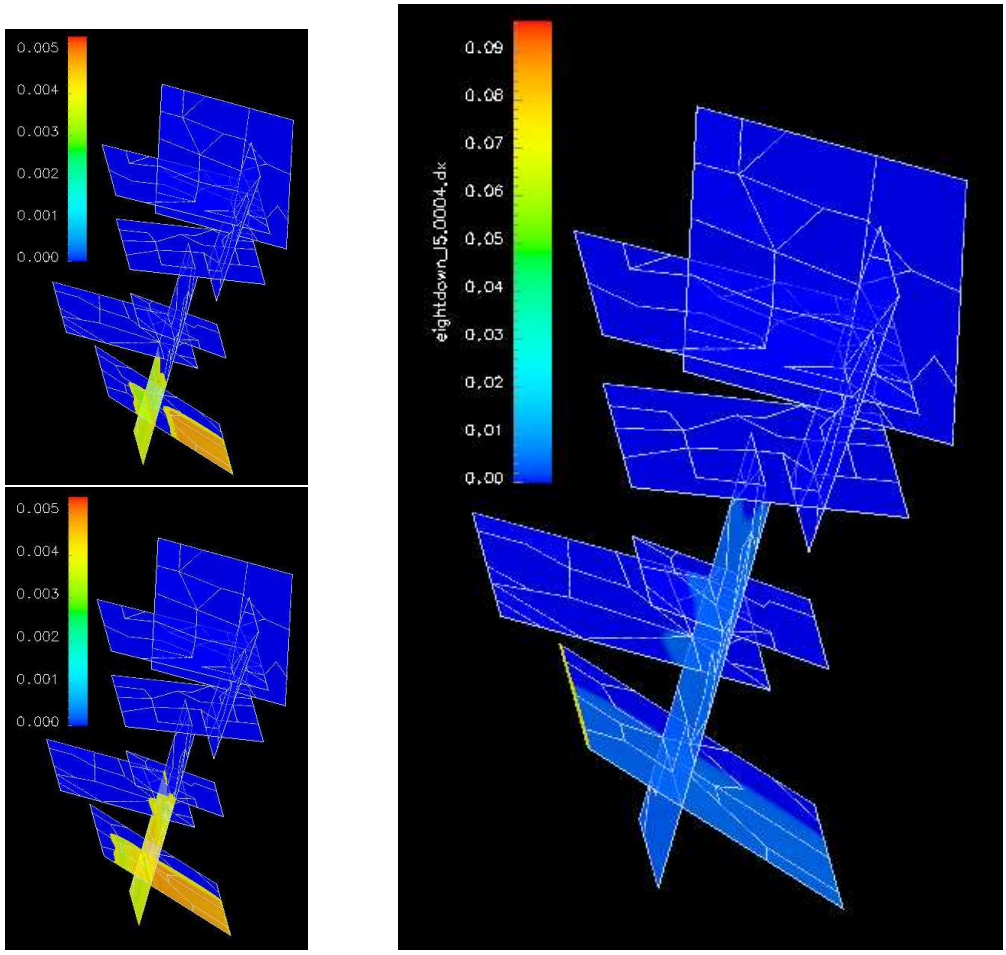

Figure 6.10: 3D Water-Gas simulation at t = 40s (upper left), t = 60s (lower left), t = 80s (right).

BIBLIOGRAPHY

H. Abelin, L. Birgersson, T. Agren, and I. Neretnieks. A channeling experiment to study flow and transport in natural fractures. In *Proceedings Scientific Basis of Nuclear Waste Management, XII, Mater. Res. Soc. Symp. Proc.*, volume 127, pages 661–668, Elsevier Sci., New York, 1988. L. Lutze and R. C. Ewing.

H. Abelin, L. Birgersson, J. Gidlund, L. Moreno, T. Agren, H. Widen, and I. Neretnieks. 3-D migration experiment in sparsely fractured crystalline rock. In *Proceedings Scientific Basis of Nuclear Waste Management, XI, Mater. Res. Soc. Symp. Proc.*, volume 112, pages 199–207, Elsevier Sci., New York, 1987. M. J. Apted and R.F. Westerman.

H. Abelin, L. Birgersson, H. Wilen, T. Agren, L. Moreno, and I. Neretnieks. Channeling experiment. Stripa Proj. Tech. Rep.90–13, Nucl. Field Safety Proj., Swed. Nucl. Fuel and Waste Manage, 1990.

H. Abelin, I. Neretnieks, S. Tunbrant, and L. Moreno. Final report of the migration in a single fracture, experimental results and evaluation. Stripa Proj. Tech. Rep.85–103, Nucl. Field Safety Proj., Swed. Nucl. Fuel and Waste Manage, 1985.

V. Aizinger, C. Dawson, B. Cockburn, and P. Castillo. The local discontinuous Galerkin method for contaminant transport. *Advances in Water Resources*, 24:73–87, 2001.

A. Al-Yaarubi, C. Pain, and R. Zimmerman. Navier-Stokes Simulations of Fluid Flow in Rock Fractures. Perm affiliates meeting, Royal School of Mines, Imperial College, 2001.

R. Alexander. Diagonally implicit Runge-Kutta methods for stiff O.D.E's. *SIAM J. Sci. Comput.*, 14:1006–1021, 1977.

J.-E. Andersson, L. Ekman, E. Gustafsson, R. Nordqvist, and S. Tiren. Hydraulic interference tests and tracer test within the brndan area, finnsj?n study site: The fracture zone project phase 3. SKB Prog. Rep.89–12, Swed. Nucl. Fuel and Waste Manage. Co., 1989.

J.-E. Andersson, L. Ekman, and A. Winberg. Detailed investigations of frature zones in the brndan area, finnsj?n study site: Single hole water injection tests in detailed sections, analysis of conductive fracture frequency. SKB Proj. Rep.88–08, Swed. Nucl. Fuel and Waste Manage. Co., 1988.

P. Andersson, E. G. C. O. Eriksson, and T. Ittner. Dipole tracer experiment in a low-angle fracture zone at the finnsj?n site, central sweden – experimental design and preliminary results. SKB Prog. Rep.90–24, Swed. Nucl. Fuel and Waste Manage. Co., 1990.

L. Anton and R. Hilfer. Trapping and mobilization of residual fluid during capillary desaturation. *Physical Review E*, 59, 1999.

D. Arnold. *An interior penalty finite element method with discontinuous elements*. PhD thesis, University of Chicago, 1979.

D. Arnold. An interior penalty finite element method with discontinuous elements. *SIAM J. Numer. Anal.*, 19(4):742–760, 1982.

D. Arnold, F. Brezzi, B. Cockburn, and L. Marini. Unified analysis of discontinuous Galerkin methods for elliptic problems. *SIAM J. Numer. Anal.*, 39(5):1749–1779, 2002.

B. Ataie-Ashtiani, S. Hassanizadeh, and M. Celia. Effects of heterogeneities on capillary pressure-saturation-relative permeability relationships. *Journal of Contaminant Hydrology*, 56:175–192, 2002.

R. G. Baca, R. C. Arnett, and I. P. King. Modeling of fluid flow in fractured-porous rock masses by finite-element techniques. *Int. J. Num. Meth. Fluids*, 4:337–348, 1984.

R. Bank and C. Wagner. Multilevel ILU decomposition. *Numerische Mathematik*, 82: 543–576, 1999.

R. E. Bank and D. J. Rose. Some error estimates for the box scheme. *SIAM J. Numer. Anal.*, 24:777–787, 1987.

A. Barbreau, M. C. Cacas, E. Durand, and B. Feuga. Hydrodynamic characterization of a fractured granite body at various scales. In *6th International Congress on Rock Mechanics, Int. Soc. for Rock Mech.*, Monreal, Canada, 1987.

A. Bardossy. Introduction to Geostatistics. Vorlesungsskript, Universität Stuttgart, Institut für Wasserbau, 2002.

R. Barrett, M. Berry, T. Chan, J. Demmel, J. Donato, J. Dongarra, V. Eijkhout, R. Pozo, C. Romine, and H. van der Vorst. *Templates for the Solution of Linear Systems: Building Blocks for Iterative Methods*. SIAM, 1994.

F. Bassi and R. Rebay. A high-order accurate discontinuous finite element method for the numerical solution of the compressible Navier-Stokes equations. *J. Comput. Phys.*, 131:267–279, 1997a.

F. Bassi and S. Rebay. High-order accurate discontinuous finite element solution of the 2D Euler equations. *J. Comput. Phys.*, 138:251–285, 1997b.

F. Bassi and S. Rebay. GMRES Discontinuous Galerkin Solution of the Compressible Navier-Stokes Equations. In B. Cockburn, G. E. Karniadakis, and C. Shu, editors, *Discontinuous Galerkin Methods: Theory, Computation and Applications*, volume 11 of *Lecture Notes in Computational Science and Engineering*. Springer-Verlag, Berlin, Heidelberg, New York, 2000.

P. Bastian. *Parallele adaptive Mehrgitterverfahren*. Teubner-Verlag, 1996.

P. Bastian. Numerical Computation of Multiphase Flow in Porous Media, 1999a. Habilitationsschrift, Universität Kiel.

P. Bastian. Numerical computation of multiphase flows in porous media, 1999b. Habilitation thesis, Christian-Albrechts-Universität Kiel.

P. Bastian. Higher Order Discontinuous Galerkin Methods for Flow and Transport in Porous Media. Technical Report 2002-33, IWR (SFB 359), Universität Heidelberg, 2002. to appear in Lecture Notes in Computational Science and Engineering.

P. Bastian, K. Birken, K. Johannsen, S. Lang, K. Eckstein, N. Neuss, H. Rentz-Reichert, and C. Wieners. UG – A Flexible Software Toolbox for Solving Partial Differential Equations. *Computing and Visualization in Science*, 1997a. to appear in.

P. Bastian, K. Birken, S. Lang, K. Johannsen, N. Neuß, H. Rentz-Reichert, and C. Wieners. UG: A flexible software toolbox for solving partial differential equations. *Computing and Visualization in Science*, 1:27–40, 1997b. `http://cox.iwr.uni-heidelberg.de/~ug`.

P. Bastian and R. Helmig. Efficient fully-coupled solution techniques for two-phase flow in porous media. Parallel multigrid solution and large scale computations. *Advances in Water Resources*, 23:199–216, 1999.

P. Bastian and S. Lang. Couplex Benchmark Computations with UG. Technical Report 2002-31, IWR (SFB 359), Universität Heidelberg, 2002. to appear in Computational Geosciences.

P. Bastian and V. Reichenberger. Multigrid for higher order discontinuous Galerkin finite elements applied to groundwater flow. Technical report, SFB 359, Universität Heidelberg, 2000. Preprint 2000-37.

C. Baumann. *An hp-adaptive discontinuous finite element method for computational fluid dynamics*. PhD thesis, The University of Texas at Austin, 1997.

C. E. Baumann and J. T. Oden. A discontinuous hp finite element method for convection-diffusion problems. *Comput. Methods Appl. Mech. Engrg.*, 175:311–341, 1999.

J. Bear. *Dynamics of Fluids in Porous Media*. Dover Publications Inc., New York, 1972.

J. Bear. Modeling Flow and Contaminant Transport in Fractured Rocks. In J. Bear, C.-F. Tsang, and G. de Marsily, editors, *Flow and contaminant transport in fractured rock*, pages 1–37. Academic Press, Inc., San Diego, 1993.

B. Berkowitz. Characterizing flow and transport in fractured geological media: A review. *Advances in Water Resources*, 25:861–884, 2002.

B. Berkowitz and I. Balberg. Percolation theory and its application to groundwater hydrology. *Water Resources Research*, 29(4):775–794, 1993.

B. Berkowitz, J. Bear, and C. Braester. Continuum models for contaminant transport in fractured porous formations. *Water Resources Research*, 24(8):1225–1236, 1988.

S. P. Bertels, D. A. DiCarlo, and M. J. Blunt. Measurement of aperture distribution, capillary pressure, relative permeability, and in situ saturation in a rock fracture using computed tomography scanning. *Water Resources Research*, 37(3):649–662, 3 2001.

J. Bey. *Finite-Volumen- und Mehrgitter-Verfahren für elliptische Randwertprobleme*. B. G. Teubner, Stuttgart, Leipzig, 1998. ISBN 3-519-02741-0.

J. Bey and G. Wittum. Downwind numbering: Robust multigrid for convection-diffusion problems. *Appl. Numer. Math.*, 23:177–192, 1997.

D. Billaux. Hydrogèologie des millieux fracturès. Gèomètrie, connectivitè et comportement hydraulique. In *Ph.D. thesis*, Ecole des Mines, Paris, 1990.

P. Binning and M. Celia. Eulerian-Lagrangian localized adjoint methods for contaminant transport simulations. In A. P. et al., editor, *Computational Methods in Water Resources X*. Kluwer Academic Publishers, 1994.

L. Birgersson, L. Moreno, I. Neretnieks, H. Widén, and T. Årgen. A Tracer Migration Experiment in a Small Fracture Zone in Granite. *Water Resources Research*, 29(12): 3867–3878, 1993.

E. Bonnet, O. Bour, E. Odling, P. Davy, I. Main, P. Cowie, and B. Berkowitz. Scaling of fracture systems in geological media. *Reviews of Geophysics*, 39(3):347–383, 2001.

P. J. Bourke. Channeling of flow through fractures in rock. In *GEOVAL-87 International Symposium, Swed. Nucl. Power Insp. (SKI)*, Stockholm, 1987.

D. Braess. *Finite Elemente*. Springer-Lehrbuch. Springer-Verlag, Berlin, Heidelberg, New York, 1992.

D. Braess. Towards algebraic multigrid for elliptic problems of second order. *Computing*, 55:379–393, 1995.

F. Brakhagen and T. Fogwell. Multigrid for the fully implicit formulation of the equations for multiphase flow in porous media. In *Multigrid Methods: Special topics and applications*, volume II, pages 31–42, 1990.

J. Bramble, J. Pasciak, J. Wang, and J. Xu. Convergence estimates for multigrid algorithms without regularity assumptions. *Math. Comput.*, 57:1–22, 1991.

J. H. Bramble. *Multigrid Methods*. Number 294 in Pitman Research Notes in Mathematics. Longman, Essex, 1993. ISBN 0-582-23435-2.

C. Braun. *Ein Upscaling-Verfahren für Mehrphasenströmungen in porösen Medien*. PhD thesis, Institut für Wasserbau, Universität Stuttgart, 2000.

C. Braun, R. Helmig, and S. Manthey. Determination of constitutive relationships for two-phase flow processes in heterogeneous porous media with emphasis on the relative permeability-saturation-relationship. *submitted to Journal of Contaminant Hydrology*, 2002.

J. Braun. Ausbreitung von NAPL in gesättigten und ungesättigten Böden. In *VEGAS-Workshop und BMBF/PWAB-Seminar In-Situ Technologien zur Grundwasser- und Altlastensanierung*, University of Stuttgart, 1996.

T. Breiting, R. Hinkelmann, and R. Helmig. *Modeling of Hydrosystems with MUFTE-UG: Multiphase Flow and Transport Processes in the Subsurface*. Fourth International Conference on Hydroinformatics, Iowa,USA, 2000.

S. C. Brenner and L.-Y. Sung. Multigrid method for the computation of singular solutions and stress intensity factors. II: Crack singularities. *BIT*, 37:623–643, 1997.

W. L. Briggs, V. E. Henson, and S. F. McCormick. *A Multigrid Tutorial*. SIAM Books, Philadelphia, second edition, 2000.

H. C. Brinkman. A calculation of the viscous force exerted by a flowing fluid on a dense swarm of particles. *Appl. Sci. Res.*, A 1:27–34, 1947.

A. Brooks and T. Hughes. Streamline upwind/Petrov-Galerkin formulations for convection dominated flows with particular emphasis on the incompressible Navier-Stokes equation. *Computer Methods in Applied Mechanics and Engineering*, 32:199–259, 1982.

R. Brooks and A. Corey. Hydraulic Properties of Porous Media. In *Hydrol. Pap.*, volume 3, Fort Collins, 1964. Colorado State University.

N. Burdine. Relative permeability calculations from pore-size distribution data. Technical report, Petroleum Transactions, AIME, 1953.

P. Calmels, B. Gaillard, and R. Margrita. Etude de l'effet d'échelle en milieu fissuré, Phase 2B: Etude des migrations, essais de tracages, vols A and B. ORIS/DAMRI/SAR/SAT/RAP/86-14/PCs, Off. des Rayonnements Ionisants, Cent. d'Etudes Nucl. de Grenoble, Grenoble, France, 1986.

P. Castillo. Performance of discontinuous galerkin methods for elliptic pdes. *SIAM Journal on Scientific Computing*, 24(2):524–547, 2002.

M. Celia, T. Russel, I. Herrera, and R. E. Ewing. An Eulerian-Lagrangian localized adjoint method for the advection-diffusion equation. *Advances in Water Resources*, 13 (4):187–206, 1990.

G. Chavent. A new formulation of diphasic incompressible flows in porous media. volume 503 of *Lecture Notes in Mathematics*, pages 258–270. Springer-Verlag, Berlin, Heidelberg, New York, 1976.

G. Chavent. The global pressure, a new concept for mobilization of compressible two phase flow in porous media. In A. Verruyt and F. B. J. Barends, editors, *Flow and Transport in Porous Media*. Balkema, Rotterdam, 1981.

G. Chavent and J. Jaffré. *Mathematical Models and Finite Elements for Reservoir Simulation*. North-Holland, New York, 1978.

Z. Chen, B. Cockburn, C. Gardner, and J. Jerome. Quantum hydrodynamic simulation of hysteresis in the resonant tunneling diode. *J. Comput. Phys.*, 117:274–280, 1995a.

Z. Chen, B. Cockburn, J. Jerome, and C. Shu. Mixed-RKDG finite element methods for the 2-D hydrodynamic model for semiconductor device simulation. *VLSI Design*, 3: 145–158, 1995b.

J.-P. Chilès and P. Delfiner. *Geostatistics: Modeling Spatial Uncertainty*. Wiley, New York, 1999.

P. Ciarlet. *The finite element method for elliptic problems*. North-Holland, New York, 1978. Republished as vol. 40 in *Classics in Applied Mathematics*, Society for Industrial & Applied Mathematics. Philadelphia, 2002.

O. Cirpka. Macrotransport theory. Vorlesungsskript, Institut fr Wasserbau, Universitt Stuttgart, 2001.

O. Cirpka. Parameter Estimation and Inverse Modeling. Vorlesungsskript, Institut fr Wasserbau, Universitt Stuttgart, 2002.

H. Class. *Theorie und numerische Modellierung nichtisothermer Mehrphasenprozesse in NAPL-kontaminierten porösen Medien*. PhD thesis, Mitteilungsheft 105, Institut für Wasserbau, Universität Stuttgart, 2001.

B. Cockburn. An Introduction to the Discontinuous Galerkin Method for Convection-Diffusion Laws. In B. Cockburn, C. Johnson, C.-W. Shu, and E. Tadmor, editors, *Advanced Numerical Approximation of Nonlinear Hyperbolic Equations*, volume 1687 of *Lecture Notes in Mathematics*, pages 151–268. Springer-Verlag, Berlin, Heidelberg, New York, 1998.

B. Cockburn. Discontinuous Galerkin Methods for Convection-Dominated Problems. In T. J. Barth and H. Deconinck, editors, *High-Order Methods for Computational Physics*, volume 9 of *Lecture Notes in Computational Engineering*, pages 69–225. Springer-Verlag, Berlin, Heidelberg, New York, 1999.

B. Cockburn, S. Hou, and C. Shu. TVB Runge-Kutta local projection discontinuous Galerkin finite element method for conservation laws III: One-dimensional systems. *J. Comput. Phys.*, 84:90, 1989.

B. Cockburn, S. Hou, and C. Shu. TVB Runge-Kutta local projection discontinuous Galerkin finite element method for conservation laws IV: The multidimensional case. *Math. Comput.*, 54:545, 1990.

B. Cockburn, G. Karniadakis, and C. Shu. The Development of Discontinuous Galerkin Methods. In B. Cockburn, G. E. Karniadakis, and C. Shu, editors, *Discontinuous Galerkin Methods: Theory, Computation and Applications*, volume 11 of *Lecture Notes in Computational Science and Engineering*, pages 3–50. Springer-Verlag, Berlin, Heidelberg, New York, 2000a.

B. Cockburn, G. E. Karniadakis, and C. Shu, editors. *Discontinuous Galerkin Methods: Theory, Computation and Applications*, volume 11 of *Lecture Notes in Computational Science and Engineering*. Springer-Verlag, Berlin, Heidelberg, New York, 2000b.

B. Cockburn and C. Shu. TVB Runge-Kutta local projection discontinuous Galerkin finite element method for conservation laws II: Gerneral framework. *Math. Comput.*, 52(186):411–435, 1989.

B. Cockburn and C. Shu. The Runge-Kutta local projection P^1-discontinuous Galerkin method for scalar conservation laws. M^2 AN, 25:337, 1991.

B. Cockburn and C. Shu. The local discontinuous Galerkin finite element method for convection-diffusion systems. *SIAM J. Numer. Anal.*, 35:2440–2463, 1998a.

B. Cockburn and C. Shu. The Runge-Kutta discontinuous Galerkin method for conservation laws V: Multidimensional systems. *J. Comput. Phys.*, 141:199–224, 1998b.

R. Courant, K. O. Friedrichs, and H. Lewy. Über die partiellen Differentialgleichungen der mathematischen Physik. *Math. Ann.*, 100:32–74, 1928.

COVISE. Collaborative Visualization and Simulation Environment. `http://www.hlrs.de/organization/vis/covise/`.

C. F. Curtiss and J. O. Hirschfelder. Integration of stiff equations. *Proc. Nat. Acas. Sci.*, 38:235–243, 1952.

G. Dagan. *Flow and transport in porous formations*. Springer-Verlag, Berlin, 1989.

H. Darcy. *Les Fontaines Publiques de la Vilee de Dijon*. Dalmont, Paris, 1856.

S. Dasberg and F. N. Dalton. Time domain reflectometry field measurements of soil water content and electrical conductivity. *Soil Sci. Soc. Am. J.*, 49:293–297, 1985.

R. A. Dawe, M. R. Wheat, and M. S. Bidner. Experimental investigation of capillary pressure effects on immiscible displacement in lensed and layered porous media. *Transport in porous media.*, 7(9):83–101, 1992.

M. Delfour, W. Hager, and F. Trochu. Discontinuous Galerkin methods for ordinary differential equations. *Math. Comp.*, 36:453–473, 1981.

G. Demny, M. Spiller, J. Köngeter, and C. Forkel. Modelluntersuchungen zum Strömungs- und Transportverhalten in Kluftflächen mit stark variierenden Öffnungsweiten. Abschlussbericht 10/2000, Institut für Wasserbau und Wasserwirtschaft, RWTH Aachen, 2000. DFG – Projekt Nr. Ko 1573/3-3.

J. Dendy Jr. Two multigrid methods for three-dimensional problems with discontinuous and anisotropic coefficients. *SIAM J. Sci. Stat. Comput.*, 8:673–685, 1987.

W. Dershowitz and H. Einstein. Charaterizing Rock Joint Geometry with Joint System Models. *Rock Mechanics and Rock Engineering*, 21:21–51, 1988.

M. M. Dias and A. C. Payatakes. Network models for two-phase flow in porous media, part 1. immiscible microdisplacement of non-wetting fluids. *Journal of Fluid Mechanics*, 164:305–336, 1986.

J. Douglas jr. Finite difference methods for two-phase incompressible flow in porous media. *SIAM J. Numer. Anal.*, 20(4):681–696, August 1983.

J. Douglas Jr., D. Peaceman, and H. Rachford Jr. A method for calculating multidimensional displacement. *Trans. AIME*, 216:297–308, 1959.

J. Douglas Jr. and T. Russel. Numerical methods for convection dominated diffusion problems based on combining the method of characteristics with finite element or finite difference procedures. *SIAM J. Numer. Anal.*, 19(5):871–885, 1982.

M. Dryja, M. Sarkin, and O. Widlund. Multilevel Schwartz methods for elliptic problems with discontinuous coefficients in three space dimensions. *Numer. Math.*, 72: 313–348, 1996.

L. Durlofsky. A triangle based mixed finite element-finite volume technique for modeling two-phase flow through porous media. *Journal of Computational Physics*, 105: 252–266, 1993.

L. Durlofsky. Accuracy of mixed and control volume finite element approximations to Darcy velocity and related quantities. *Water Resources Research*, 30(4):965–973, 1994.

R. R. Eaton and N. E. Bixler. Analysis of a multiphase, porous-flow imbibition experiment in a fractured volcanic tuff. In D. D. Evans, editor, *Flow and Transport through Unsaturated Fractured Rock*, pages 91–97. Geophysical Monograph 42, 1987.

J. Eikenberg, E. Hoehn, T. Fierz, and U. Frick. Grimsel test site: Preparation and performance of migration experiments with radio isotopes of sodium, strontium and iodine. In *PSI Ber. 94-11, Paul-Scherrer-Inst.*, Villingen, Schwitzerland, 1994.

D. Elsworth and R. Goodman. Hydro-mechanical characterisation of rock fissures of idealised sawtooth or sinussiudal form. *International Symposium on Fundamentals of Rock Joints*, pages 259–268, 1985.

M. Emmert. *Numerische Modellierung nichtisothermer Gas-Wasser Systeme in porösen Medien*. PhD thesis, Universität Stuttgart, Stuttgart, 1996.

K. Eriksson, D. Estep, P. Hansbo, and C. Johnson. *Computational Differential Equations*. Cambridge University Press, 1996.

K. Eriksson, C. Johnson, and V. Thomeée. Time discretization of parabolic problems by the discontinuous Galerkin method. *RAIRO Modél. Math. Anal. Numér.*, 19:611–643, 1985.

L. C. Evans. *Partial Differential Equations*, volume 19 of *Graduate Studies in Mathematics*. American Mathematical Society, Providence, Rhode Island, 1998.

R. E. Ewing. Problems arising in the modeling of processes for hydrocarbon recovery. In R. E. Ewing, editor, *Research Frontiers in Applied Mathematics*, volume 1, pages 3–34. SIAM, 1983.

R. E. Ewing. Operator splitting and Eulerian-Lagrangian localized adjoint methods for multiphase flow. In *The Mathematics of Finite Elements and Applications VII*, 1991.

A. Färber and C. Betz. Thermisch unterstützte Bodenluftabsaugung (TUBA): Planung, Aufbau und Messtechnik der Versuchsstände. Technical report, Institut für Wasserbau, Universität Stuttgart, 1995.

U. Fischer and M. A. Celia. Prediction of relative and absolute permeabilities for gas and water from soil water retention curves using a pore-scale network model. *Water Resources Research*, 35(4):1089–1100, 1999.

P. Forchheimer. Wasserbewegung durch Boden. *Zeit. Ver. deut. Ing.*, 45:1781– 1788, 1901.

P. Forsyth. A control volume finite element approach to NAPL groundwater contamination. *SIAM J. Sci. Stat. Comput.*, 12(5):1029–1057, 1991.

U. Frick. Grimsel test site: The Radionuclide Migration Experiment – Overview of investigations 1985–1990. In *PSI Ber. 120, Paul-Scherrer-Inst.*, Villingen, Schwitzerland, 1992.

L. H. Frost and C. C. Davison. Summary of the fracture zone 3 groundwater tracer test program at the Underground Research Laboratory. Rep. TR-617, Appl. Geosci. Branch, Whiteshell Lab., Pinawa, Manit., Canada, 1995.

L. H. Frost, N. W. Scheier, E. T. Kozak, and C. C. Davison. Solute transport properties of a major fracture zone in granite. *Tracer Hydrology*, pages 313–320, 1992.

A. Fuchs. *Optimierte Delaunay-Triangulierungen zur Vernetzung getrimmter NURBS-Körper*. PhD thesis, Universität Stuttgart, 1999.

J. Gale. Impact of flow geometry, flow regime, two-phase flow and degassing on the transmissivity of rough fractures. International progress report, Fracflow Consultants Inc., 1999. Äspö Hard Rock Laboratory.

S. Ge. A governing Equation for Fluid Flow in Rough Fractures. *Water Resources Research*, 33(1):53–61, 1997.

L. Gelhar. *Stochastic Subsurface Hydrology*. Wiley, Prentice Hall, 1993.

J. Geller and J. Jarsjö. Groundwater degassing and two-phase flow: Pilot hole test report. Skb Äspö hrl int. coop. rep. 95-03, Swedish Nuclear Fuel and Waste Management Company, 1995.

S. Gentier. Morphologie et comportement hydromécanique d'une fracture naturelle dans un granite sous contrainte normale. *Doctoral thesis, Université d'Orléans, Orléans, France*, 1986.

S. Gentier, D. Billaux, and L. van Vliet. Laboratory Testing of the Voids of a Fracture. *Int. Jour. Rock Mech. and Rock Eng.*, 1989.

J. Glimm, E. Isaacson, B. Lindquist, O. McBryan, and S. Yaniv. Statistical fluid dynamics: The influence of geometry on surface instabilites. In R. E. Ewing, editor, *Research Frontiers in Applied Mathematics*, volume 1, pages 137–160. SIAM, 1983.

J. Glimm, D. Marchesin, and O. McBryan. Unstable fingers in two phase flow. *Comm. Pure Appl. Math.*, 34:53–75, 1981.

G. H. Golub and C. F. van Loan. *Matrix Computations*. Johns Hopkins Series in the Mathematical Sciences. The Johns Hopkins University Press, Baltimore, Maryland, third edition, 1996.

J. Gopalakrishnan and G. Kanschat. A multilevel discontinuous Galerkin method. *Numerische Mathematik*, 95(3):527–550, September 2003.

W. G. Gray and P. C. Y. Lee. On the theorems for local volume averaging of multiphase systems. *International Journal of Multiphase Flow*, 3:333–340, 1977.

A. B. Gureghian. A study by the finite element method of the influence of fractures in confined aquifers. *Soc. Pet. Eng. J.*, 15:181–191, 1975.

W. Hackbusch. *Multi-Grid Methods and Applications*. Springer-Verlag, Berlin, Heidelberg, New York, 1985.

W. Hackbusch. On First and Second Order Box Schemes. *Computing*, 41:277–296, 1989.

W. Hackbusch. *Iterative Solution of Large Sparse Systems of Linear Equations*. Springer-Verlag, New York, 1994.

W. Hackbusch. On the feedback vertex set problem for a planar graph. *Computing*, 58 (2):129–155, 1997.

J. Hadermann and W. Heer. The Grimsel (Switzerland) Migration Experiment – Integrating field experiments, laboratory investigantions and modelling. *J. Contam. Hydrol.*, 21(1-4):87–100, 1996.

Häffner product data base, 2002. WWW: http://www.hugohaeffner.com/haeffnerdatenbank/ (04/02/02).

E. Hairer and G. Wanner. *Solving ordinaray differential equations II. Stiff and differential algebraic problems*, volume 14 of *Springer Series in Computational Mathematics*. Springer-Verlag, Berlin, Heidelberg, New York, 2 edition, 1996. ISBN 3-540-60452-9.

E. Hakami and E. Larsson. Aperture measurements and flow experiments on a single natural fracture. *Int. J. Rock Mech. Min. Sci. Geomech. Abstr.*, 33(4):395–404, 1996.

S. M. Hassanizadeh and W. G. Gray. General conservation equations for multi-phase systems: 1. Averaging procedure. *Advances in Water Resources*, 2:131–144, 1979a.

S. M. Hassanizadeh and W. G. Gray. General conservation equations for multi-phase systems: 2. Mass, momenta, energy, and entropy equations. *Advances in Water Resources*, 2:191–203, 1979b.

S. M. Hassanizadeh and W. G. Gray. General conservation equations for multi-phase systems: 3. Constitutive theory for porous media flow. *Advances in Water Resources*, 3:25–40, 1980.

S. M. Hassanizadeh and W. G. Gray. Mechanics and thermodynamics of multiphase flow in porous media including interphase boundaries. *Advances in Water Resources*, 13(4):169–186, 1990.

S. M. Hassanizadeh and W. G. Gray. Toward an improved description of the physics of two-phase flow. *Advances in Water Resources*, 16(1):53–67, 1993.

S. M. Hassanizadeh and W. G. Gray. Recent advances in theories of two-phase flow in porous media. In J. P. du Plessis, editor, *Fluid Transport in Porous Media*, pages 105–160. Computational Mechanics Publications, Southampton, 1997.

R. D. Hazlett. Statistical characterization and stochastic modeling of pore networks in relation to fluid flow. *Mathematical Geology*, 29(6):801–822, 1997.

R. Helmig. *Theorie und Numerik der Mehrphasenströmungen in geklüftet-porösen Medien*. PhD thesis, Institut für Strömungsmechanik und Elektronisches Rechnen im Bauwesen, Universität Hannover, Bericht Nr. 34, 1993.

R. Helmig. *Multiphase Flow and Transport Processes in the Subsurface. A Contribution to the Modeling of Hydrosystems.* Springer-Verlag, Berlin, Heidelberg, New York, 1997.

R. Helmig, P. Bastian, H. Jakobs, and V. Reichenberger. Multiphase Multicomponent Processes in Fractured Porous Media. Bericht, Institut für ComputerAnwendungen, Universität Braunschweig, Braunschweig, 2000.

R. Helmig, H. Class, R. Huber, H. Sheta, J. Ewing, R. Hinkelmann, H. Jakobs, and P. Bastian. Architecture of the Modular Program System MUFTE_UG for Simulating Multiphase Flow and Transport Processes in Heterogeneous Porous Media. *Mathematische Geologie*, 2, 1998.

R. Helmig and R. Huber. Multiphase flow in heterogeneous porous media: A classical finite element method versus an IMPES-based mixed FE/FV approach. *Int. J. Numer. Meth. in Fluids*, 29:899–920, 1999.

P. W. Hemker, W. Hoffmann, and M. H. van Raalte. Fourier two-level analysis for discontinuous Galerkin discretization with linear elements. Technical Report MAS-R0217, Centrum voor Wiskunde en Informatica (CWI), Modelling, Analysis and Simulation (MAS), Amsterdam, 2002a. URL `www.cwi.nl/ftp/CWIreports/MAS/MAS-R0217.pdf`.

P. W. Hemker, W. Hoffmann, and M. H. van Raalte. Two-level Fourier analysis of a multigrid approach for discontinuous Galerkin discretisation. Technical Report MAS-R0206, Centrum voor Wiskunde en Informatica (CWI), Modelling, Analysis and Simulation (MAS), Amsterdam, 2002b. URL `www.cwi.nl/ftp/CWIreports/MAS/MAS-R0206.pdf`. submitted to SIAM SISC.

P. W. Hemker and M. H. van Raalte. Fourier two-level analysis for higher dimensional discontinuous Galerkin Discretisation. Technical Report MAS-R0227, Centrum voor Wiskunde en Informatica (CWI), Modelling, Analysis and Simulation (MAS), Amsterdam, 2002. URL `www.cwi.nl/ftp/CWIreports/MAS/MAS-R0227.pdf`.

A. Hemminger, L. Neunhäuserer, and R. Helmig. Festgesteins-Aquiferanalog: Experimente und Modellierung – Einsatz von diskreten Modellansätzen. In *3. Workshop Kluftaquifere*, Inst. für Strömungsmechanik und Elektronisches Rechnen im Bauwesen, Univ. Hannover, November 2000.

R. Hilfer and P. E. Oren. Dimensional analysis of pore scale and field scale immiscible displacement. *Transport in Porous Media*, 22(1):53–72, 1996.

M. Hilpert, R. Glantz, W. G. Gray, C. T. Miller, and V. R. Raghu. Calibration of a pore network model. In *American Geophysical Union Fall Meeting*, volume 79(45), page F248, 1998.

M. Hilpert and C. T. Miller. Pore-morphology based calibration of a pore network model. In *American Geophysical Union Spring Meeting*, volume 81(19) of *EOS Transactions*, page S233. American Geophysical Union, 2000.

R. A. Horn and C. R. Johnson. *Matrix Analysis*. Cambridge University Press, 1985.

R. A. Horn and C. R. Johnson. *Topics in Matrix Analysis*. Cambridge University Press, 1991.

U. Hornung, editor. *Homogenization and Porous Media*, volume 6 of *Interdisciplinary Applied Mathematics*. Springer-Verlag, Berlin, Heidelberg, New York, 1997. ISBN 0-387-94786-8.

T. Y. Hou and P. G. LeFloch. Why nonconservative schemes converge to wrong solutions: Error analysis. *Mathematics of Computation*, 62(206):497–530, April 1994.

C. Hu and C. Shu. A discontinuous Galerkin finite element method for Hamilton-Jacobi equations. *SIAM J. Sci. Comput.*, 2000.

I. F. C. IFC. *A Formulation of the Thermodynamic Properties of Ordinary Water Substance*. IFC Secretariat, Düsseldorf, Germany, 1967, 1967.

O. Ippisch. *Coupled Transport in Natural Porous Media.* PhD thesis, Universität Heidelberg, 2001.

E. Isakov, P. Glover, and S. Ogilvie. Use of Synthetic Fractures in the Analysis of Natural Fracture Apertures. In *8th ECS and Image Analysis*, Bordeaux, France, September 2001.

J. S. Y. Wang and T. N. Narasimhan. Hydrologic mechanisms governing fluid flow in a partially saturated fractured prous medium. *Water Resources Research*, 21(12):1861–1874, 1985.

H. Jakobs. *Nicht-isotherme Gas-Wasser-Prozesse in stark heterogenen Medien*. PhD thesis, Universität Stuttgart, Stuttgart, 2003.

H. Jakobs and R. Helmig. Gas-Water Processes in Fractured Porous Media - Comparison of Different Upscaling Methods. In O. Kolditz et al., editor, *Gekoppelte Prozesse in Geosystemen*, pages 267–278. ISEB Hannover, 2000.

H. Jakobs, R. Helmig, C. Miller, H. Class, M. Hilpert, and C. Kees. Modeling of dnapl flow in saturated heterogeneous porous media. preprint for SFB404 – in preparation for Advances in Water Resources, 2003a.

H. Jakobs, R. Helmig, C. Miller, H. Class, M. Hilpert, and C. Kees. Modeling of DNAPL flow in saturated heterogeneous porous media. To appear in Advances in Water Resources, 2003b.

P. Jamet. Galerkin-type approximations which are discontinuous in time for parabolic equations in a variable domain. *SIAM J. Numer. Anal.*, 15:912–928, 1978.

K. Jänich. *Vektoranalysis*. Springer-Lehrbuch. Springer-Verlag, Berlin, Heidelberg, New York, 4 edition, 2003. ISBN 3-540-00392-4.

J. Jarsjö. Hydraulic conductivity relations in soil and fractured rock: Fluid component and phase interaction effects. Technical report, Royal Institute of Technology, Div. of Water Resources Engineering, Stockholm, 1998. Ph.D. thesis.

J. Jarsjö and G. Destouni. Hydraulic conductivity relations in soil and fractured rock: Fluid component and phase interaction effects. Skb technical report, Swedish Nuclear Fuel and Waste Management Company, 1998.

J. Jarsjö and G. Destouni. Degassing of deep groundwater in fractured rock around boreholes and drifts. *Water Resources Research*, 36(9):2477–2492, 2000.

J. Jarsjö and J. Geller. Groundwater degassing: Laboratory experiments in rock fracture replicas with radial flow. Skb Äspö hrl progress report, Swedish Nuclear Fuel and Waste Management Company, 1996.

B. H. J.H. Cushman, L.S. Bennethum. A primer on upscaling tools for porous media. *Advances in Water Resources*, 25:1043–1067, 2002.

M. Jischa. *Konvektiver Impuls-, Wärme- und Stoffaustausch*. Grundlagen der Ingenieurwissenschaften. Vieweg, 1982.

C. Johnson, Y. Nie, and V. Thomeée. Time discretization of parabolic problems by the discontinuous Galerkin method. *SIAM J. Numer. Anal.*, 27:277–291, 1990.

A. Keller, P. Roberts, and M. Blunt. Effect of fracture aperture variations on the dispersion of contaminants. *Water Resources Research*, 35(1):55–63, 1999.

A. A. Keller. High resolution CAT imaging of fractures in consolidated materials. *International Journal of Rock Mechanics and Mining Sciences*, 34(3–4):358–370, 1997.

P. Kitanidis. *Introduction to Geostatistics*. Cambridge University Press, New York, 1997.

K. Kobayashi, R. Hinkelmann, H. Class, C. Shoemaker, and R. Helmig. *Development of an Optimisation Method for Methane Extraction in Subsurface*. 4th Workshop - Porous Media, Blaubeuren, 2002.

D. Kroener and S. Luckhaus. Flow of oil and water in a porous medium. *Journal of Differential Equations*, 55:276–288, 1984.

K.-P. Kröhn. Simulation von Transportvorgängen im klüftigen Gesetin mit der Methode der Finiten Elemente. Technical Report 29, Institut für Strömungsmechanik und Elektronisches Rechnen im Bauwesen, Universität Hannover, 1991.

B. Kueper and E. Frind. An overview of immiscible fingering in porous media. *Journal of Contaminant Hydrology*, 2:95–110, 1988.

B. H. Kueper, W. Abbott, and G. Farquhar. Experimental Observations of Multiphase Flow in Heterogeneous Porous Media. *Journal of Contaminant Hydrology*, 5:83–95, 1989.

S. Lang. *Parallele Numerische Simulation instationärer Probleme mit adaptiven Methoden auf unstrukturierten Gittern*. PhD thesis, Universität Stuttgart, 2000.

R. Lenhard, J. Dane, J. Parker, and J. Kaluarachchi. Measurement and Simulation of One-Dimensional Transient Three-Phase Flow for Monotonic Liquid Drainage. *Water Resources Research*, 24:853–863, 1988.

R. Lenhard and J. Parker. A Model for Hysteric Constitutive Relations Governing Multiphase Flow 3. Refinements and Numerical Simulation. *Water Resources Research*, 25 (7):1727–1736, 1989.

R. Lenhard, J. Parker, and S. Mishra. On the correspondence between Brooks-Corey and Van Genuchten models. *Journal of Irrigation and Drainage Engineering*, 115(4):744–751, 1989a.

R. J. Lenhard, J. C. Parker, and S. Mishra. On the correspondence between Brooks-Corey and van Genuchten models. *J. Irrig. Drain. Eng.*, 115:744–751, 1989b.

P. Lesaint and P. Raviart. On a finite element method for solving the neutron transport equation. In C. de Boor, editor, *Mathematical Aspects of Finite Elements in Partial Differential Equations*, pages 89–123. Academic Press, new York, 1974.

R. J. Le Veque. *Numerical Methods for Conservation Laws*. Lectures in Mathematics: ETH Zürich. Birkhäuser Verlag, Basel, Boston, Berlin, 1992. ISBN 3-7643-2723-5.

R. J. Le Veque. *Finite Volume Methods for Hyperbolic Problems*. Cambridge Texts in Applied Mathematics. Cambridge University Press, Cambridge, 2002. ISBN 0-521-00924-3.

M. Leverett. Capillary behavior in porous solids. *Trans. AIME*, 142:152–169, 1941.

L. Liedtke, I. Engelhardt, M. Fiene, K.-P. Kröhn, H. Kull, H. Jakobs, and C. Thorenz. Two-phase flow in fractured crystalline rock – investigations in niche 2175. Ttigkeitsbericht, Bundesanstalt für Geowissenschaften und Rohstoffe, 2001. BMWi-Projekte 02E9027 und 02E9037.

J. Lions. Problèmes aux limites non homogènes à donées irrégulières: Une méthode d'approximation. In *Numerical Analysis of Partial Differential Equations (C.I.M.E. 2 Ciclo, Ispra, 1967)*, pages 283–292. Rome, 1968. Edizioni Cremonese.

G. M. Lomize. *Flow in fractured rocks (in russian)*. Gosenergoizdat, Moscow, 1951.

S. Lorentz, D. Durnford, and A. Corey. *Liqud retention measurement on porous media using a controlled outflow cell.* Dept. of Chemical and Biorecource Engineering, Colorado state University, Fort Collins, Colorado, 1992. Copy of manuscript submitted to Soil Sci. Soc. Am. J.

C. Louis. A study of groundwater flow in jointed rock and its influence on the stability of rock masses. *Rock Mech. Res. Rep., Imp. Coll.*, 10:90 pp., 1969.

Q. Ma, J. E. Hook, and L. R. Ahuja. Influence of three-parameter conversion methods between van Genuchten and Brooks-Corey functions on soil hydraulic properties and water-balance predictions. *Water Resources Research*, 35(8):2571–2578, August 1999.

B. Mandelbrot. *The Fractal Geometry of Nature*. W.H. Freeman, New York, 1982.

J. E. Marsden and A. Tromba. *Vector Calculus*. W. H. Freeman, New York, April 1996. ISBN 0716724324.

G. Matheron. *Eléments pour une Théorie des Milieux Poreux*. Masson, Paris, 1967.

D. McWhorter and D. Sunada. Exact integral solutions for two-phase flow. *Water Resources Research*, 26(3):399–413, 1990.

A. Michel. A Finite Volume Scheme for Two-Phase Immiscible Flow in Porous Media. *SIAM Journal on Numerical Analysis*, 41(4):1301–1317, 2003.

I. D. Michev. *Finite volume and finite volume element methods for nonsymmetric problems*. PhD thesis, Texas A&M University, College Station, 1996.

J. Molenaar. Multigrid methods for fully implicit oil reservoir simulation. In *Proceedings Copper Mountain Conference on Multigrid Methods*, 1995.

L. Moreno, I. Neretnieks, and T. Eriksen. Analysis of some laboratory tracer transportruns in matural fissues. *Water Resources Research*, 21(7):951–958, 1985.

Y. Mualem. A new model for predicting the hydraulic conductivity of unsaturated porous media. *Water Resources Research*, 12:513–522, 1976.

B. Munson, A. Rangwalla, and J.A.Mann. Low Reynolds number circular Couette flow past a wavy wall. *Phys. Fluid*, 28:2679–2686, 1985.

T. Narasimhan and K. Pruess. MINC: An Approach for Analyzing Transport in Strongly Heterogeneous Systems. In Custodio, E., A. Gurgui, and J. P. L. Ferreira, editors, *Groundwater Flow and Quality Modelling, NATO ASI Series C, Vol. 224*. D. Reidel Publishing Company, Dordrecht, Boston, Lancaster, Tokyo, 1988.

I. Neretnieks. Channeling effects in flow and transport in fractured rocks – Some recent observations and models. In *GEOVAL-87 International Symposium, Swed. Nucl. Power Insp. (SKI)*, Stockholm, 1987.

I. Neretnieks. Nuclear waste repositories in crystalline rock – An overview of nuclide transport mechanisms. In *MRS Meeting on Scientific Basis for Nuclear Waste Management, Mater. Res. Soc.*, Kyoto, Jpn., Oct. 24-26, 1994.

I. Neretnieks, T. Eriksen, and P. Tähtinen. Tracer movement in a single fissure in granitic rock: some experimental results and their interpretation. *Water Resources Research*, 18 (4):849–858, 1982.

L. Neunhäuserer. *Diskretisierungsansätze zur Modellierung von Strömungs- und Transportprozessen in geklüftet-porösen Medien*. PhD thesis, Institut für Wasserbau, Universität Stuttgart, 2002.

L. Neunhäuserer, S. Gebauer, S. Ochs, R. Hinkelmann, R. Kornhuber, and R. Helmig. Equidimensional Modelling of Flow and Transport Processes in Fractured Porous Systems II. In S. M. Hassanizadeh, R. J. Schotting, W. G. Gray, and G. Pinder, editors, *Computational Methods in Water Resources*. Elsevier Science Publishers B.V., Amsterdam, 2002.

N. Neuss and C. Wieners. Criteria for the approximation property for multigrid methods in nonnested spaces. *Mathematics of Computation*, 2003. accepted.

I. Neuweiler. *Macroscopic parameters for two-phase flow*. PhD thesis, E.T.H. Zürich, 1999.

C. Neuzil and J. Tracy. Flow Through Fractures. *Water Resources Research*, 17(1):191–199, 1981.

J. Nitsche. Über ein Variationsprinzip zur Lösung von Dirichlet-Problemen bei Verwendung von Teilräumen, die keinen Randbedingungen unterworfen sind. *Abh. Math. Sem. Univ. Hamburg*, 36:9–15, 1971.

K. S. Novakowski, G. V. Evans, D. A. Lever, and K. G. Raven. A field example of measuring hydrodynamic dispersion in a single fracture. *Water Resources Research*, 24 (8):1165–1174, 1985.

J. Oden, I. Babuška, and C. Baumann. A Discontinuous *hp* Finite Element Method for Diffusion Problems. *Journal of Computational Physics*, 146:491–519, 1998.

J. T. Oden and C. E. Baumann. A conservative DGM for Convection-Diffusion and Navier-Stokes Problems. In B. Cockburn, G. E. Karniadakis, and C. Shu, editors, *Discontinuous Galerkin Methods: Theory, Computation and Applications*, volume 11 of *Lecture Notes in Computational Science and Engineering*, pages 179–196. Springer-Verlag, Berlin, Heidelberg, New York, 2000.

OpenDX. The Open Source Software based on IBM's Visualization Data Explorer. `http://www.opendx.org/`.

A. Oron and B. Berkowitz. Flow in rock fractures: The local cubic law assumption reexamined. *WRR*, 34(11):2811–2825, 1998.

J. Parker and R. Lenhard. A Model for Hysteric Constitutive Relations Governing Multiphase Flow 1. Saturation-Pressure Relations. *Water Resources Research*, 23(12):2187–2196, 1987.

J. Parker, R. Lenhard, and T. Kuppusami. A Parametric Model for Constitutive Properties Governing Multiphase Flow in Porous Media. *Water Resources Research*, 23(4): 618–624, 1987.

P. Percell and M. Wheeler. A local residual finite element procedure for elliptic equations. *SIAM J. Numer. Anal.*, 15(4):705–714, August 1978.

L. J. Pyrak-Nolte, L. Myer, N. W. Cook, and P. A. Witherspoon. Hydraulic and mechanical properties of natureal fractures in low permeability rock. *Proceedings of the Sixth International Congress for Rock Mechanics*, pages 225–231, 1987.

R. Rannacher. Finite Element Methods for the Incompressible Navier-Stokes Equations. Preprint 99–37, IWR, Universität Heidelberg, SFB 359. Published in Special Issue of J. Math. Fluid Mech., September 1999.

K. G. Raven, K. S. Novakowski, and P. A. Lapcevic. Interpretation of field tracer tests of a single fracture using a transient solute storage model. *Water Resources Research*, 24(12):2019–2032, 1988.

M. Raw. Robustness of coupled algebraic multigrid for the Navier-Stokes equations. Technical Report 96–0297, AIAA, 1996.

W. Reed and T. Hill. Triangular mesh methods for the neutron transport equation. Technical report, Los Alamos Scientific Laboratory, 1973.

V. Reichenberger. *Multiphase Flow in Fractured Porous Media*. PhD thesis, IWR, Universität Heidelberg, 2004.

P. Renard and G. de Marsily. Calculating equivalent permeability: a review. *Advances in Water Resources*, 20(5-6):253–278, 1997.

M. Renardy and R. C. Rogers. *An Introduction to Partial Differentail Equations*, volume 13 of *Texts in Applied Mathematics*. Springer-Verlag, Berlin Heidelberg New York, 1993.

H. Rentz-Reichert. *Robuste Mehrgitterverfahren zur Lösung der inkompressiblen Navier-Stokes Gleichung: Ein Vergleich*. PhD thesis, Universität Stuttgart, 1996.

A. Reusken. Convergence analysis of a multigird method for convection diffusion equations. *Numerische Mathematik*, 91:323–349, 2002.

B. Rivière. *Discontinuous Galerkin methods for solving the miscible displacement problem in porous media*. PhD thesis, The University of Texas at Austin, 2000.

B. Rivière and M. Wheeler. A Discontinuous Galerkin Method Applied to Nonlinear Parabolic Equations. In B. Cockburn, G. E. Karniadakis, and C. Shu, editors, *Discontinuous Galerkin Methods: Theory, Computation and Applications*, volume 11 of *Lecture Notes in Computational Science and Engineering*, pages 231–244. Springer-Verlag, Berlin, Heidelberg, New York, 2000.

B. Rivière, M. Wheeler, and K. Banaś. Part II. Discontinuous Galerkin method applied to a single phase flow in porous media. *Comput. Geosci.*, 4:337–349, 2000.

B. Rivière, M. Wheeler, and V. Girault. Improved energy estimates for interior penalty, constrained and discontinuous Galerkin methods for elliptic problems I. *Computational Geosciences*, 3:337–360, 1999.

ROCKFLOW. *Theorie und Benutzeranleitung zum Programmsystem ROCKFLOW*. Institut für Strömungsmechanik und Elektronisches Rechnen im Bauwesen, Universität Hannover, 1986–2003.

E. S. Romm. *Flow Characteristics of Fractured Rocks (in Russian)*. Nedra, Moscow, 1966.

K. Roth, R. Schulin, H. Flühler, and W. Attinger. Calibration of time domain reflectometry for water content measurement using a composite dielectric approach. *Water Resources Research*, 26:2267–2273, 1990.

J. Ruge and K. Stüben. Algebraic multigrid. In S. F. McCormick, editor, *Multigrid Methods*. SIAM, 1987.

M. Sahimi. *Flow and Transport in Porous Media and Fractured Rock: From Classical Methods to Modern Approaches.* VCH, Weinheim, 1995. ISBN 3-527-29260-8.

K. Sato, K. Watanabe, and N. Kotajima. Fundamental study on flow resistance in rock fissure. *Soils and Foundatins, Japanese Society of Soil Mechanics and Foundation Engineering*, 24(1):1–8, 1985.

A. Scheidegger. General Theory of Dispersion in Porous Media. *Journal of Geophysical Research*, 66:3273–3278, 1961.

H. Schroll and A. Tveito. Local existence and stability for a hyperbolic-elliptic system modeling two-phase reservoir flow. Technical Report 136, Institut für Geometrie und Praktische Mathematik, RWTH Aachen, 1997.

H. Schubert. *Kapillarität in porösen Feststoffsystemen*. Springer-Verlag, Berlin, 1982.

C. Schwab. hp-FEM for Fluid Flow Simulation. In T. J. Barth and H. Deconinck, editors, *High-Order Methods for Computational Physics*, volume 9 of *Lecture Notes in Computational Engineering*, pages 325–438. Springer-Verlag, Berlin, Heidelberg, New York, 1999.

T. Scott. Multi-grid methods for oil reservoir simulation in two and three dimensions. *J. Comput. Phys.*, 59:290–307, 1985.

V. Selyakov and V. Kadet. *Percolation Models for Transport in Porous Media – with Applications to Reservoir Engineering*. Theory and Applications of Transport in Porous Media. Kluwer Academic Publishers, 1996.

H. Sheta. *Einfluss der Hysterese bei Infiltrations- und Ausbreitungsvorgängen in der gesättigten und ungesättigten Bodenzone*. PhD thesis, Universität Stuttgart, Institut für Wasserbau, 1999.

C. Shu. Total-variation-diminishing time discretizations. *SIAM J. Sci. Stat. Comput.*, 9 (6):1073–1084, 1988.

C.-W. Shu. Essentially Non-oscillatory and Weighted Essentially Non-oscillatory Schemes for Hyperbolic Conservation Laws. In B. Cockburn, C. Johnson, C.-W. Shu, and E. Tadmor, editors, *Advanced Numerical Approximation of Nonlinear Hyperbolic Equations*, volume 1687 of *Lecture Notes in Mathematics*, pages 325–432. Springer-Verlag, Berlin, Heidelberg, New York, 1998.

C.-W. Shu. High Order ENO and WENO Schemes for Computational Fluid Dynamics. In T. J. Barth and H. Deconinck, editors, *High-Order Methods for Computational Physics*, volume 9 of *Lecture Notes in Computational Engineering*, pages 439–582. Springer-Verlag, Berlin, Heidelberg, New York, 1999.

A. Silberhorn-Hemminger. *Modellierung von Kluftaquifersystemen: Geostatistische Analyse und deterministisch-stochastische Kluftgenerierung*. PhD thesis, IWS, Universität Stuttgart, 2002.

B. Singhal and R. Gupta. *Applied Hydrogeology of Fractured Rocks*. Kluwer Academic Pubplisher, Dordrecht, 1999a.

B. B. S. Singhal and R. P. Gupta. *Applied Hydrogeology of Fractured Rocks*. Kluwer Academic Publishers, Dordrecht, Boston, London, 1999b.

D. Stauffer and A. Aharony. *Perkolationstheorie: eine Einfhrung*. VCH, 1995.

E. A. Sudicky and R. G. McLaren. *FRACTRAN user's guide – an efficient simulator for two-dimensional, saturated groundwater flow and solute transport in Porous or discretely fractured porous formations*. Waterloo Centre for Groundwater Research, University of Waterloo, 1998.

V. Thomée. *Galerkin finite element methods for parabolic problems*. Number 25 in Springer Series in Computational Mathematics. Springer-Verlag, Berlin, Heidelberg, New York, 1997. ISBN 3-540-63236-0.

J. Tiedemann. Geologisch-ingenieurgeologische Untersuchungen zur Abgrenzung von Homogenbereichen innerhalb der Mittleren Siegener Schichten (Ahrtalsattel). In *Mitteilungen Ingenieur- und Hydrogeologisches Heft 16*, 1983.

C. Tsang and I. Neretnieks. Flow channeling in heterogeneous fractured rock. *Reviews of Geophysics*, 36(2):275 –298, 1998.

Y. Tsang. Usage of Equivalent Apertures for Rock Fractures as Derived From Hydraulic and Tracer Tests. *Water Resources Research*, 28(5):1451–1455, 1992.

Y. Tsang and C. Tsang. Channel Model of Flow through Fractured Media. *Water Resources Research*, 23(3):467–479, 1987.

A. Unger and C. Mase. Numerical Study of the Hydromechanical Behavior of Two Rough Fracture Surfaces in Contact. *Water Resources Research*, 29(7):2101–2114, 1993.

H. van der Vorst. Bi-CGSTAB: A fast and smoothly converging variant of BiCG for the solution of nonsymmetric line ar systems. *SIAM J. Sci. Stat. Comp.*, 13:631 – 644, 1992.

C. J. van Duijn, J. Molenaar, and M. J. de Neef. Effects of capillary forces on immiscible two-phase flow in heterogeneous porous media. *Transport in Porous Media*, 21:71–93, 1995.

M. van Genuchten. A closed-form equation for predicting the hydraulic conductivity of unsaturated soils. *Soil Sci. Soc. Am. J.*, 44:892–898, 1980.

P. Vaněk, J. Mandel, and M. Brezina. Algebraic multi-grid by smoothed aggregation for second and forth order elliptic problems. *Computing*, 56:179–196, 1996.

R. Verfürth. Multi-level algorithms for mixed problems II. Treatment of the Mini-Element. *SIAM J. Numer. Anal.*, 25:285–293, 1988.

R. Verfürth. *A Review of* A Posteriori *Error Estimation and Adaptive Mesh-Refinement Techniques*. Advances in Numerical Mathematics. John Wiley & Sons and B. G. Teubner, Chichester, New York, Stuttgart, Leipzig, 1996.

A. Verma. *Effects of phase transformation of steam-water relative permeabilities*. PhD thesis, Lawrence Berkeley National Laboratory report No. LBL-20594, University of California, 1986.

C. Wagner, W. Kinzelbach, and G. Wittum. A robust multigrid method for groundwater flow. *Numer. Math.*, 75:523–545, 1997.

C. Wang. Drag due to a striated boundary in slow Couette flow. *Phys. Fluid*, 21:697–698, 1978.

J. Wang. Flow and Transport in Fractured Rocks. *Reviews of Geophysics, Supplement*, pages 254–262, 1991.

J. Wang and T. Narasimhan. Hydrologic Mechanisms Governing Fluid Flow in a Partially Saturated, Fractured, Porous Medium. *Water Resources Research*, 21:1861–1874, 1985.

T. C. Warburton. Application of the discontinuous Galerkin method to Maxwell's eauations using unstructured polymorphic hp-finite elements. In B. Cockburn, G. E. Karniadakis, and C. Shu, editors, *Discontinuous Galerkin Methods: Theory, Computation and Applications*, volume 11 of *Lecture Notes in Computational Science and Engineering*. Springer-Verlag, Berlin, Heidelberg, New York, 2000.

T. C. Warburton and G. E. Karniadakis. A discontinuous Galerkin merhod for the viscous MHD equations. *J. Comput. Phys.*, 152:1–34, 1999.

P. Wesseling. *An Introduction to Multigrid Methods*. John Wiley & Sons, Chichester, 1992. Reprinted by `www.mgnet.org`.

P. Wesseling. *Principles of Computational Fluid Dynamics*. Springer Series in Computational Mathematics. Springer-Verlag, Berlin, Heidelberg, New York, 2001. ISBN 3-540-67853-0.

M. Wheeler. An elliptic collocation finite element method with interior penalties. *SIAM J. Numer. Anal.*, 15(1):152–161, February 1978.

D. Wilkinson. Percolation effects in immiscible displacement. *Physical Review A*, 34(2): 1380–1391, 1986.

D. Wilkinson and J. F. Willemsen. Invasion percolation: A new form of percolation theory. *J. Phys. A: Math*, 16:3365–3376, 1983.

C. R. Wilson and P. A. Witherspoon. Steady state flow in rigid networks of fracures. *Water Resources Research*, 10(2):328–335, 1974.

K. Wilson. Renormalization group and critical phenomena. *Phys. Rev. B*, 4:3174–3184, 1971.

A. Winkler. *Prozesse des Wärme- und Stofftransports bei der In-situ-Sanierung mit festen Wärmequellen*. PhD thesis, Universität Stuttgart, Stuttgart, 2002.

P. A. Witherspoon, J. S. Y. Wang, K. Iwai, and J. E. Gale. Validity of cubic law for fluid flow in deformable rock fractures. *Water Resources Research*, 6(16):1016–1024, 1980.

G. Wittum. On the robustness of ILU smoothing. *SIAM J. Sci. Stat. Comput.*, 10:699–717, 1989.

G. Wittum. On the convergence of multigrid methods with transforming smoothers. *Numerische Mathematik*, 57:15–38, 1990.

T.-F. Wong, J. Fredrich, and G. Gwanmesia. Crack aperture statistics and pore space fractal geometry of westerly granite and rutland quartzite: Implications for elastic contact models of rock compressibility. *J. Geophys. Res.*, 94:267–278, 1989.

A. Woodbury and K. Zhang. Lanczos method for the solution of groundwater flow in discretely fractured porous media. *Advances in Water Resources*, 24:621–630, 2001.

Y.-S. Wu and K. Pruess. Numerical simulation of non-isothermal multiphase tracer transport in heterogeneous fractured porous media. *Advances in Water Resources*, 23: 699–723, 2000.

J. Xu. Iterative methods by space decomposition and subspace correction: A unifying approach. *SIAM Review*, 34:581–613, 1992.

I. Yotov. A mixed finite element discretization on non-matching multiblock grids for a degenerate parabolic equation arising in porous media flow. *East-West J. Numer. Math.*, 5:211–230, 1997.

E. Zeidler. *Applied Functional Analysis: Main Principles and Their Applications*. Number 109 in Applied Mathematical Sciences. Springer-Verlag, New York, Berlin, Heidelberg, 1995.

A Integral Transformations

In this section we explain how the evaluation of integrals on the reference element is done for lower dimensional elements. The transformation includes only basic vector calculus, but we include the subject since it is seldomly treated in standard finite element literature. As a reminder we repeat how the transformation to the reference element is done in the case of triangular elements in $\mathbb{R}^2$. The transformation to the reference elements uses standard results from vector analysis as they can be found in Jänich (2003) or Marsden and Tromba (1996).

A.1 Two-Dimensional Elements in Two Space Dimensions

We consider a function u on a fracture element Ω_e and the mapping T which maps the reference element $\hat{\Omega}_e$ to the element in $\mathbb{R}^2$. The mapping T is an affine mapping of the form

$$T(\xi,\eta) = B\begin{pmatrix}\xi\\ \eta\end{pmatrix} + d = \begin{pmatrix}x_1-x_0 & x_2-x_0\\ y_1-y_0 & y_2-y_0\end{pmatrix}\begin{pmatrix}\xi\\ \eta\end{pmatrix} + \begin{pmatrix}x_0\\ y_0\end{pmatrix},$$

and the derivatives are transformed as

$$D_{\xi,\eta}u(F(\xi,\eta)) = D_{x,y}u(F(\xi,\eta))\cdot D_{\xi,\eta}F(\xi,\eta) = D_{x,y}u(F(\xi,\eta))\cdot B$$

by the chain rule, where $D_{x,y}$ and $D_{\xi,\eta}$ are the row vectors (∂_x,∂_y) and $(\partial_\xi,\partial_\eta)$, respectively. The gradient of u in x,y-coordinates is then

$$\nabla_{x,y}u(F(\xi,\eta)) = (B^{-1})^T\nabla_{\xi,\eta}F(\xi,\eta).$$

This is used in the evaluation of the integral over the element Ω_e by transformation to the reference element $\hat{\Omega}_e$ where we write B^{-T} for $(B^{-1})^T$.

$$\begin{aligned}\int_{\Omega_e}\nabla_{x,y}u\cdot\nabla_{x,y}v\,dx\,dy &= \int_{\hat{\Omega}_e}\nabla_{x,y}u(F(\xi,\eta))\cdot\nabla_{x,y}v(F(\xi,\eta))|\det(D_{\xi,\eta}F(\xi,\eta))|\,d\xi\,d\eta\\ &= \int_{\hat{\Omega}_e}B^{-T}\nabla_{\xi,\eta}u(F(\xi,\eta))\cdot B^{-T}\nabla_{\xi,\eta}v(F(\xi,\eta))|\det(B)|\,d\xi\,d\eta\\ &= \int_{\hat{\Omega}_e}B^{-T}\nabla_{\xi,\eta}\hat{u}(\xi,\eta)\cdot B^{-T}\nabla_{\xi,\eta}\hat{v}(\xi,\eta)|\det(B)|\,d\xi\,d\eta\\ &= \int_{\hat{\Omega}_e}(B^TB)^{-1}\nabla_{\xi,\eta}\hat{u}(\xi,\eta)\cdot\nabla_{\xi,\eta}\hat{v}(\xi,\eta)|\det(B)|\,d\xi\,d\eta\end{aligned}$$

A.2 One-Dimensional Elements in Two Space Dimensions

Let us now consider the transformation of a line element into $\mathbb{R}^2$. The transformation in this case is

$$T(\xi) = B(\xi) + d = \begin{pmatrix} x_1 - x_0 \\ y_1 - y_0 \end{pmatrix} (\xi) + \begin{pmatrix} x_0 \\ y_0 \end{pmatrix},$$

and the chain rule applies again,

$$\hat{u}' = u'(B\xi + d) \cdot T'(\xi) = (\partial_x u, \partial_y u) \cdot B = B^T \cdot \nabla u. \tag{A.1}$$

(We write ∇u instead of $\nabla_{x,y} u$.) Like in the example above, $\nabla_{x,y} u = B^{-T} \hat{u}'$ holds, but since B is not a square matrix it is not obvious what the inversion means. A geometrically motivated way to determine B^{-T} is as follows. The linear system is underdetermined and can be extendend in a meaningful way. $B^T \cdot \nabla u$ is the directional derivative in direction B^T, i. e. the fracture direction. The function $u(x, y)$ should have no variation in the direction orthogonal to the fracture direction. This leads to the additional requirement

$$0 = (\partial_x u, \partial_y u) \cdot N = (\partial_x u, \partial_y u) \cdot \begin{pmatrix} y_1 - y_0 \\ -(x_1 - x_0) \end{pmatrix}. \tag{A.2}$$

Together, equations (A.1) and (A.2) state

$$\begin{pmatrix} \hat{u}' \\ 0 \end{pmatrix} = \begin{pmatrix} x_1 - x_0 & y_1 - y_0 \\ y_1 - y_0 & -(x_1 - x_0) \end{pmatrix} \begin{pmatrix} \partial_x u \\ \partial_y u \end{pmatrix} = \tilde{A} \begin{pmatrix} \partial_x u \\ \partial_y u \end{pmatrix}. \tag{A.3}$$

The inverse of $\tilde{A}$ is

$$\tilde{A}^{-1} = \frac{1}{(x_1 - x_0)^2 + (y_1 - y_0)^2} \begin{pmatrix} x_1 - x_0 & y_1 - y_0 \\ y_1 - y_0 & -(x_1 - x_0) \end{pmatrix}, \tag{A.4}$$

and it follows that

$$\begin{pmatrix} \partial_x u \\ \partial_y u \end{pmatrix} = \frac{1}{(x_1 - x_0)^2 + (y_1 - y_0)^2} \begin{pmatrix} x_1 - x_0 \\ y_1 - y_0 \end{pmatrix} \hat{u}' = B^+ \hat{u}'. \tag{A.5}$$

Note that we write B^+ for the generalized inverse of B. It is no concidence that this notation resembles the *Moore-Penrose pseudo inverse*: B^+ *is* the pseudo inverse of B (Horn and Johnson, 1985, 1991). The connection is that $A^+ Ax \in (\ker A)^\perp$ (the orthogonal complement of the kernel of A).

For the integral transformation of lines we know from vector analysis that for $T : \hat{\omega}_e \to \omega_e$, $\hat{\omega}_e = (0, 1)$, $\omega_e \subset \mathbb{R}^2$ the integral transforms as

$$\int_\Omega f(s)\,ds = \int_\omega f(T(\xi)) \|T'(\xi)\|\,d\xi = \int_\omega f(T(\xi)) \sqrt{(x_1 - x_0)^2 + (y_1 - y_0)^2}\,d\xi.$$

A.3 Lower-Dimensional Elements in Three Space Dimensions

For two-dimensional triangular elements the transformation rule is

$$\int_{\omega} f(x,y)\,dF = \int_{\hat{\omega}} f(T(\xi,\eta)) \left\| \frac{\partial T}{\partial \xi} \times \frac{\partial T}{\partial \eta} \right\| d\xi\, d\eta \tag{A.6}$$

The transformation is given by

$$T(\xi,\eta) = B(\xi,\eta) + d = \begin{pmatrix} x_1 - x_0 & x_2 - x_0 \\ y_1 - y_0 & y_2 - y_0 \\ z_1 - z_0 & z_2 - z_0 \end{pmatrix} (\xi,\eta) + \begin{pmatrix} x_0 \\ y_0 \\ z_0 \end{pmatrix}. \tag{A.7}$$

The derivation of B^{-T} can be done in the geometrically motivated way as before by considering the matrix C,

$$(\mathbf{a},\mathbf{b}) := \begin{pmatrix} x_1 - x_0 & x_2 - x_0 \\ y_1 - y_0 & y_2 - y_0 \\ z_1 - z_0 & z_2 - z_0 \end{pmatrix} \qquad C = (\mathbf{a},\mathbf{b},\mathbf{a}\times\mathbf{b}) \tag{A.8}$$

Calculating C and selecting the first two columns yields the pseudo inverse B^{+}.

The integral transformation for one-dimensional elements in $\mathbb{R}^3$, which are transformed from the reference element $(0,1)$ by $T : \xi \mapsto (x,y,z)$, is

$$\int_{\omega} f(s)\,ds = \int_{\hat{\omega}} f(T(\xi)) \|T'(\xi)\|\, d\xi = \int_{\hat{\omega}} f(T(\xi)) \sqrt{(x_1 - x_0)^2 + (y_1 - y_0)^2 + (z_1 - z_0)^2}\, d\xi. \tag{A.9}$$

The derivation of the pseudo-inverse is done as before, except that we have to find two normal directions to the fracture direction.

B NOTATION

UPPER CASE LATIN

B_i	control volume, box for vertex v_i
B_h	Dual grid
Bo	bond number [–]
Ca	capillary number [–]
E	set of elements
E_h	Mesh
E_i	set of elements adjoined to vertex v_i
F	defect term
$\mathbf{F}$	equation system
G	domain of interest
Gr	gravitational number [–]
$\mathbf{J}$	Jacobian matrix
K	absolute permeability [m^2]
$\mathbf{K}$	matrix for Jacobian system
$\mathbf{K}_l$	matrix for gridlevel l
L	characteristic length [m]
N_i	shape function of vertex v_i
$\mathbf{P}_l$	prolongation for multigrid method
$\hat{\mathbf{Q}}$	positive definite matrix
R_g	individual gas constant [J/(kgK)]
$\mathbf{R}_l$	restriction for multigrid method
S	saturation [–]
S_e	effective saturation [–]
S_r	residual saturation [–]
S_t	total liquid saturation [–]
S_α	saturation of phase α
$S_{\alpha r}$	residual saturation of phase α

V	set of vertices
V_h	conforming finite volume basis space
W_h	finite volume test space
W_i	weighting function for vertex v_i

Lower case latin

a	range
b	box volume (dual grid)
b_i^k	sub control volume
d	space dimension (2 or 3)
$\mathbf{d}_l$	vector on gridlevel l
$dtscale$	scaling factor for time step
e, f	finite element
$\mathbf{e}_l$	vector on gridlevel l
$\mathbf{f}$	right-hand side for Jacobian system
$\mathbf{f}_l$	vector on gridlevel l
$\mathbf{g}$	gravity vector $[m/s^2]$
$\mathbf{h}$	distance vector
$k_{r,\alpha}$	relative permeability of phase α $[-]$
l	counter
m	Van Genuchten parameter $[-]$, counter; number of elements
n	Van Genuchten parameter $[-]$, counter; number of vertices
n_{ls}	number of line search steps
$\mathbf{n}$	normal vector for box face at integration point
$\mathbf{n}$	normal vector
p	pressure [Pa]
p_c	capillary pressure [Pa]
p_c^*	characteristic capillary pressure [Pa]
p_d	displacement/entry pressure, Brooks–Corey parameter [Pa]
p_e	entry pressure; capillary pressure of the biggest pore [Pa]
p_α	phase pressure, $\alpha = n, w$ [Pa]
q	number of actual line search
q_α	source term for phase α $[kg/m^3]$

q^K	source term for component K [J/s]
r	radius [m]
t	time [s]
$\mathbf{u}$	vector of unknowns for Jacobian system, corrections for primary variables
$\mathbf{u}_l$	vector on gridlevel l
$\boldsymbol{v}_\alpha$	Darcy velocity of phase α [m/s]
v_i	vertex i
$\boldsymbol{v}$	Darcy velocity vector [m/s]
v	basis function
w	test function
$\boldsymbol{x}$	position in $\mathbb{R}^d$
x, y, z	spatial variable [m]
$\boldsymbol{x}$	vector holding the primary variables
$\boldsymbol{x}^k$	barycenter of element e_k

UPPER CASE GREEK

Γ	Boundary between two subdomains of G
Γ_{B_i}	integration path around control volume B_i
$\Gamma_{\alpha,D}$	Dirichlet boundary
$\Gamma_{\alpha,N}$	Neumann boundary
Δh	grid width [m]
Δt	numerical time step [s]
Ω	Domain
Ω^f	Domain of volumetric fractures
Ω^m	Domain of rock matrix
Ω_e	Domain of finite element e
Λ	Projection into fracture space
Π	Mapping into saturation space
Π^c	second rank matrix for capillary pressure saturation relationship
Γ_{int}	interior grid skeleton
Γ_{ext}	interior grid skeleton

LOWER CASE GREEK

α	subscript indicating an arbitrary phase
α	van Genuchten parameter [Pa^{-1}]
β_n	scaling factors for capillary pressure for three phase system [–]
β_{gn}	scaling factors for capillary pressure for three phase system [–]
γ	semivariogram
$\gamma_{ij}^{Flue_l}$	integral over sub-control volume face between vertex v_i and vertex v_j in Element e_l
$\gamma_{e,f}$	Side between elements e and f
δ	Kronecker delta function
ρ	density [kg/m^3]
Φ	effective porosity [-]
p	pressure [Pa]
λ	Brooks-Corey parameter [–]
λ	Brooks–Corey parameter [–], lattice constant of network [m]
λ_α	mobility of phase α [(ms)/kg]
μ	dynamic viscosity [kg/(ms)]
ϕ	Value of Neumann boundary condition [kg/m^2]
ϕ	porosity [–]
μ	viscosity [-]
σ	surface tension [N/m]
θ	time discretization parameter
Δt	time step size

SUBSCRIPT SYMBOLS

G_i	belonging to subdomain G_i; e.g. $x_{G_i} \in G_i$ or $p\|G_i$ for the pressure in subdomain G_i
g	gas phase
h	horizontal
$i, j, k, l, \ldots$	index; counter
n	non-wetting phase
t	throat related
v	vertical
v^hat	unit vector pointing into flow direction
w	wetting phase or water phase

SUPERSCRIPT SYMBOLS

f	A fracture related quantity
h	horizontal
m	A rock matrix related quantity
n	time step
v	vertical

ABBREVIATIONS

BC	Brooks–Corey
DNAPL	non-aqueous phase liquid denser than water
FU	fully upwind
FUB	fully upwind box method (fully upwind finite volume method)
ILU	incomplete decomposition solver
$Inv_{pc}^{G_i}$	inverse capillary pressure saturation relationship for subdomain G_i
NAPL	none-aqueous phase liquid
PPS	phase pressure saturation (formulation); usually $p_w - -S_n$–formulation
PPSIC	Phase Pressure Saturation (formulation) with Interface Condition; usually $p_w - -S_n$–formulation with extended capillary pressure equilibrium condition
REV	Representative Elementary Volume
VG	van Genuchten